



HAL
open science

Etude de l'organisation et de la dynamique du nucléoïde de *Deinococcus radiodurans* par microscopie de fluorescence avancée

Kevin Floc'h

► **To cite this version:**

Kevin Floc'h. Etude de l'organisation et de la dynamique du nucléoïde de *Deinococcus radiodurans* par microscopie de fluorescence avancée. Biologie structurale [q-bio.BM]. Université Grenoble Alpes, 2019. Français. NNT : 2019GREAV007 . tel-02137438

HAL Id: tel-02137438

<https://theses.hal.science/tel-02137438v1>

Submitted on 23 May 2019

HAL is a multi-disciplinary open access archive for the deposit and dissemination of scientific research documents, whether they are published or not. The documents may come from teaching and research institutions in France or abroad, or from public or private research centers.

L'archive ouverte pluridisciplinaire **HAL**, est destinée au dépôt et à la diffusion de documents scientifiques de niveau recherche, publiés ou non, émanant des établissements d'enseignement et de recherche français ou étrangers, des laboratoires publics ou privés.

THÈSE

Pour obtenir le grade de

DOCTEUR DE LA COMMUNAUTE UNIVERSITE GRENOBLE ALPES

Spécialité: **Nanobiologie**

Arrêté ministériel : 25 mai 2016

Présentée par

« **Kevin FLOC'H** »

Thèse dirigée par « **Joanna Timmins** », CR, CNRS et
codirigée par « **Dominique Bourgeois** », DR, CNRS

préparée au sein de l'**Institut de Biologie Structurale**
dans l'**École Doctorale Chimie et Sciences du Vivant**

Cell morphology and nucleoid dynamics during *Deinococcus radiodurans* cell cycle

Thèse soutenue publiquement le **8 février 2019**,
Devant le jury composé de :

Monsieur Franz BRUCKERT

Professeur, Université Grenoble Alpes, Président

Monsieur François-Xavier BARRE

Directeur de Recherche, Institut de Biologie Intégrative de la Cellule,
Rapporteur

Monsieur Christian LESTERLIN

Chargé de recherche, Université Claude Bernard Lyon 1, Rapporteur

Madame Ulrike ENDESFELDER

Chargé de recherche, Institut Max Planck, Examineur

Madame Mariana Gomes de PINHO

Professeur, Universidade Nova de Lisboa, Examineur

Madame Irina GUTSCHE

Directeur de recherche, Institut de Biologie Structurale, Examineur



Table of Contents

Table of Contents	v
Table of Figures	vii
Table of Tables	ix
Table of Abbreviations and Acronyms	x
Chapter I: Introduction	11
1. <i>Deinococcus radiodurans</i>	12
1.1. Overview	12
1.2. Cell wall structure	15
2. Nucleoid organization	17
2.1. Molecular organization by nucleoid-associated proteins	17
2.2. Micro- & macro-domain organization	21
2.3. Spatial organization of the nucleoid	24
2.4. Nucleoid compaction mechanisms	28
2.5. <i>D. radiodurans</i> chromosome organization and condensation	32
3. Chromosome segregation	35
3.1. ParABS system, an active model for origin segregation	35
3.2. Passive model for bulk chromosome segregation	37
3.3. Segregation termination	38
3.4. Segregation in <i>D. radiodurans</i>	40
4. Bacterial cell division	42
4.1. Rod vs. (ovo)cocci division	42
4.2. Division site selection and cytokinesis	44
4.3. <i>D. radiodurans</i> cell division	51
Chapter II: Overview of fluorescence microscopy	55
1. Optical microscopy	56
2. History of fluorescence microscopy	57
3. Fluorescence	58
4. Fluorophores	60
5. Optical resolution principle	62
6. Conventional fluorescence microscopy	64
7. SR fluorescence microscopy	66
7.1. Ensemble	66
7.2. Single-molecule	69

Chapter III: Objectives of the PhD	79
1. Autoblinking: a SR artifact	80
2. <i>D. radiodurans</i> cell and nucleoid dynamics.....	81
3. Dissemination	82
Chapter IV: Autoblinking.....	83
Chapter V: <i>D. radiodurans</i> cell and nucleoid dynamics	119
1. Abstract.....	121
2. Introduction.....	122
3. Results	124
4. Discussion.....	138
5. Methods.....	142
6. References.....	146
7. Supplementary material	151
Chapter VI: Discussion and perspectives	161
1. Autoblinking.....	162
2. <i>D. radiodurans</i> cell and nucleoid dynamics.....	164
2.1. Cell morphology definition.....	164
2.2. Cell growth	165
2.3. Nucleoid organization, segregation and compaction	168
2.4. Perspectives.....	170
3. <i>D. radiodurans</i> imaging	172
Chapter VII: Appendices	175
1. Codes used for analyses.....	176
1.1. Density graph of foci	176
1.2. Perimeter fraction of a phase 1 diad	177
1.3. Translation of trackmate output to trackart input	178
2. Video material.....	179
3. Résumé de la thèse en Français	180
Bibliography.....	185
Acknowledgment.....	200
Resumé.....	202
Summary	202

Table of Figures

Figure 1.1: Morphology of <i>D. radiodurans</i> and its outstanding DNA repair capacity..	13
Figure 1.2: Difference of survival capacities of several bacteria.	14
Figure 1.3: Thin section electron micrograph of <i>D. radiodurans</i>	15
Figure 1.4: Model of <i>D. radiodurans</i> cell walls.....	16
Figure 1.5: Representation of the different activities of HU, IHF, Fis, H-NS and SMC NAPs.....	19
Figure 1.6: Schematic representation of a bacterial nucleoid across different levels of organization (helical structure, macrodomains, high-density regions, chromosomal interaction domains and microdomains).....	21
Figure 1.7: <i>E. coli</i> macrodomain organization, Ori, Ter, Left, Right and the two non- structured region (N-S R) along the origin of replication (<i>ori</i>) and the replication terminus (<i>ter</i>).	23
Figure 1.8: Spatial organization of chromosomes in different organisms:.....	25
Figure 1.9: Schematic representation of the two chromosomes organization in <i>V.</i> <i>cholerae</i>	27
Figure 1.10: Schematic illustration of the depletion forces.	29
Figure 1.11: The coarse-grained model of bacterial chromosome DNA.....	31
Figure 1.12: Optical sections for successive Z-depth, of <i>Deinococcus radiodurans</i>	34
Figure 1.13: Role of FtsK in the decatenation of chromosomes during segregation termination.	39
Figure 1.14: Resolution of chromosome dimers in <i>E. coli</i> , an aberrant chromosome conformation.	40
Figure 1.15: Loci cartography in <i>D. radiodurans</i> cells.....	41
Figure 1.16: Schematic representation of the division site selection process (i.e. the positioning of the Z-ring in violet) by different gradients of FtsZ regulators in <i>E. coli</i> , <i>B. subtilis</i> and <i>C. crescentus</i>	45
Figure 1.17: Schematic representation of Min systems during the cell cycle of <i>E. coli</i> (A) or <i>B. subtilis</i> (B).	47
Figure 1.18: Model of the displacement of MipZ, FtsZ and ParB during the cell cycle of <i>C. crescentus</i>	48
Figure 1.19: Schematic representation of SlmA protein position (in dark gray) during the nucleoid segregation occurring during <i>E. coli</i> cell cycle.....	49
Figure 1.20: <i>D. radiodurans</i> cell growth and schematic representation of the cell wall structure of <i>D. radiodurans</i> . A).....	53
Figure 2.1: General scales of times and sizes in biology.....	56
Figure 2.2: Simplified Perrin-Jablonski diagram.	58
Figure 2.3: Optical resolution and Rayleigh criterion.....	63
Figure 2.4: Effective PSF generation in STED.....	68

Figure 2.5: Illustration of the different type of PTFPs.	70
Figure 2.6: Scheme illustrating the PALM technique using PTFPs.	71
Figure 2.7: Effect of molecular density on super-resolved image.....	72
Figure 2.8: tcPALM analysis of a trimer of proteins labeled with an ideal PAFP.	73
Figure 2.9: Study of molecular dynamics by sptPALM.....	75
Figure 2.10: Principle of PAINT microscopy.	76
Figure 2.11: Spectral-PALM experimental setup.....	77
Figure 6.1: BADA and Nile Red staining of <i>D. radiodurans</i> cell walls.	167
Figure 7.1: Coordination des changements morphologiques du nucléoïde avec le cycle cellulaire de <i>D. radiodurans</i>	183

Table of Tables

Table 1.1: NAP genes found in bacteria.	20
Table 1.2: Summary of the genome organization and characteristics of model bacteria.	24
Table 1.3: Chromosome segregation machinery found in selected bacteria.	35
Table 1.4: Elongation and septation proteins found in selected bacteria.	43
Table 1.5: Shapes and division planes of various bacteria.	44
Table 1.6: Division site selection proteins found in selected bacteria.	46

Table of Abbreviations and Acronyms

- *Biology:*

DNA: Deoxyribonucleic acid
CID: Chromosomal interaction domains
Chr: Chromosome
Dif: Terminal defined site
GFP: Green fluorescent protein
HDR: High-density regions
KOPS: FtsK-orienting polar sequences
NAP: Nucleoid associated protein
NO: Nucleoid occlusion
PBS: Phosphate buffered saline
PFA: Paraformaldehyde
PG: Peptidoglycan
TGY: Tryptone glucose yeast extract
Topo: Topoisomerase
WT: Wild-type

- *Microscopy:*

CSLM: Confocal laser scanning microscopes
dSTORM: Direct stochastic optical reconstruction microscopy
NSOM: near-field scanning optical microscopy
GSD: Ground state depletion
PALM: Photoactivated localization microscopy
PSF: Point spread function
PTFP: Phototransformable protein
RESOLFT: Reversible saturable optical fluorescence transitions
SIM: Structured illumination microscopy
SD: Spinning-disk
SMLM: Single-molecule localization microscopy
sptPALM : Single particle tracking PALM
SR: Super-resolution
STED: Stimulated emission depletion

I

Introduction

This first chapter lays the background on the subjects that were investigated during the course of this PhD project.

As this manuscript focuses on a bacterium called *Deinococcus radiodurans*, we first start by giving an overview on this peculiar and interesting bacterium and some of its characteristics. Then we review our current state of knowledge of (i) nucleoid organization, (ii) chromosome segregation and (iii) bacterial cell morphology during bacterial division. As these studies mostly focus on model bacteria, when available, the knowledge on these topics for *D. radiodurans* is summarized.

Through this review, it appears that the great diversity of bacteria is reflected in the multiplicity of proteins and mechanisms involved in these three processes, which in fact are intimately interlinked. This diversity actually prevents the definition of universal mechanisms for these three processes.

1. *Deinococcus radiodurans*

1.1. Overview

Deinococcus radiodurans (*D. radiodurans*) was discovered in 1956 by Arthur W. Anderson (Anderson et al. 1956) during an attempt to sterilize a can of meat using high doses of gamma radiation, supposed to kill all known forms of life. However, after the experiment the meat spoiled. The researchers were able to isolate the bacterium responsible for the spoil and named it *Micrococcus radiodurans*, later renamed as *Deinococcus radiodurans*.

D. radiodurans has been found in very different places, ranging from meat to sawdust or in the air of clean rooms and in clothes (Slade & Radman 2011). *D. radiodurans* was the first *Deinococcus* isolated, now over 40 of these species have been discovered, in habitats such as hot springs, deserts or Antarctica (De Groot et al. 2005; Ferreira et al. 1997; Hirsch et al. 2004). Among these different species, some present peculiar characteristics directly related to their growth environments (thermophilia, cryophilia) and all present a high resistance to DNA damaging agents.

D. radiodurans is a non-pathogenic, pink-pigmented, 1-3 μm diameter bacterium (Figure 1.1 A), with an outstanding ability to withstand the lethal effects of DNA-damaging events, including ionizing radiation, UV light, and desiccation (Blasius et al. 2008). For example, *D. radiodurans* can survive, without any loss of viability, UV doses up to $500 \text{ J}\cdot\text{m}^{-2}$, a dose that is known to generate $\sim 5,000$ pyrimidine dimers per genome copy. It can also resist an acute dose of 5 kGy γ -irradiation, generating approximately 200 DNA double strand breaks, 3,000 DNA single strand breaks and more than 1,000 damaged bases per genome, a dose representing around 1000 times the maximum dose humans can withstand. *D. radiodurans* is able to reconstruct a functional genome from hundreds of chromosomal fragments induced by exposure to ionizing radiation, whereas the genomes of most organisms are irreversibly shattered under the same conditions (Figure 1.1 B; reviewed in: (Blasius et al. 2008; Makarova et al. 2001; Slade & Radman 2011)). However, *D. radiodurans* is not an extremophilic species per se, as it does not thrive in damaging conditions: it can recover and then replicate in normal growth conditions after being exposed to extreme conditions. For example, 85% of *D. radiodurans* cells survived a 2-year dehydration phase in a desiccator kept below 5% humidity. The ability of *D. radiodurans* to survive long periods of desiccation may actually be its main characteristic, from which the other resistances could have derived (Mattimore & Battista 1996). Cells that have been engineered to impair their radio-resistance were also shown to be more sensitive to desiccation. All of these unusual properties of *D. radiodurans* have lead it to be considered as a potential agent for

digesting toxic materials, such as mercury and solvents (toluene for instance) in highly radioactive sites (Brim et al. 2000).

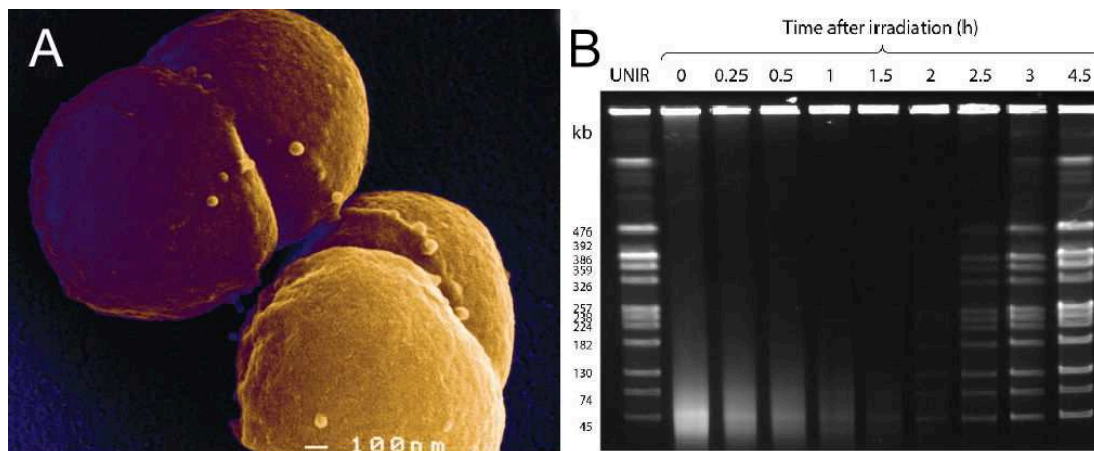


Figure 1.1: Morphology of *D. radiodurans* and its outstanding DNA repair capacity. A) Scanning electron micrographs of *D. radiodurans* tetrads. B) Kinetics of genome reassembly in *D. radiodurans* post 6.8kGy γ -irradiation. The genome is fully shattered directly after irradiation, as shown by the low molecular weight, smeared bands at $t=0$, and fully restored in just 3 hours. Adapted from (Rothfuss et al. 2006; Slade & Radman 2011).

The high resistance of *D. radiodurans* compared to other bacteria (Figure 1.2) has been hypothesized to be due to (i) its ability to protect its proteome, (ii) the efficient repair of its highly shattered genomic information thanks to its protected proteome, (iii) its capacity to export the damaged DNA to the exterior medium.

- (i) It has been proposed that high levels of intracellular antioxidant metabolites protect the proteome from reactive oxygen species or free radicals that are produced during irradiation (Daly 2009; Slade & Radman 2011). Even though their mechanisms of action are not really understood, *D. radiodurans* actually possesses various of these antioxidant metabolites and enzymes, such as Mn- or Fe-superoxide dismutases, Cu/Zn-superoxide dismutases, catalases, peroxidases (Makarova et al. 2001; Wang & Schellhorn 1995), nonenzymic Mn(II) complex (Daly 2009) and carotenoids (Tian et al. 2007). Moreover, *D. radiodurans* is able to shield its different enzymes from oxidative stress thanks to divalent Mn ions (Mn^{2+}), in complex with small metabolites (such as peptides) (Sharma et al. 2017). For example, Daly *et al.* showed that a complex, called Mn^{2+} -decapeptide complex (designed according to compounds found in *D. radiodurans* ultrafiltrates), when injected into mice exposed to 9.5 Gy radiation doses, lead to the 30 days survival of all the mice, whereas only 37% of control mice survived (Gupta et al. 2016).
- (ii) Multiple, robust and efficient DNA repair machineries have been observed in *D. radiodurans* (Daly & Minton 1996; Slade et al. 2009; Zahradka et al. 2006). The different studies of the DNA repair pathways have showed that no “super-proteins” could account for *D. radiodurans* radioresistance. But, these repair enzymes, although they are well conserved, display numerous differences in structure and/or

enzymatic activity compared to their homologues from radio-sensitive bacteria, as reviewed in (Timmins & Moe 2016). These small differences plus the unusual number of DNA glycosylases may add up and significantly contribute to the efficient repair system. The effectiveness of the repair machineries, coupled to the effective protection of the proteome may be key to the resistance of *D. radiodurans*. Indeed, *D. radiodurans* can proceed to the repair of its genome thanks to the well protected, and thus functional and efficient, DNA repair proteins.

- (iii) The export of the damaged DNA to the exterior medium has also been proposed as a key factor of *D. radiodurans* resistance. This expulsion would prevent the reinsertion of damaged bases into the genome (Battista 1997). This export may be mediated by UvrA proteins, as they have a close evolutionary relationship to ABC transporter proteins (Doolittle et al. 1986; Linton & Higgins 1998). In particular, UvrA2 which does not appear to play a direct role in the nucleotide excision repair pathway in *D. radiodurans* may be involved in the export process (White et al. 1999).

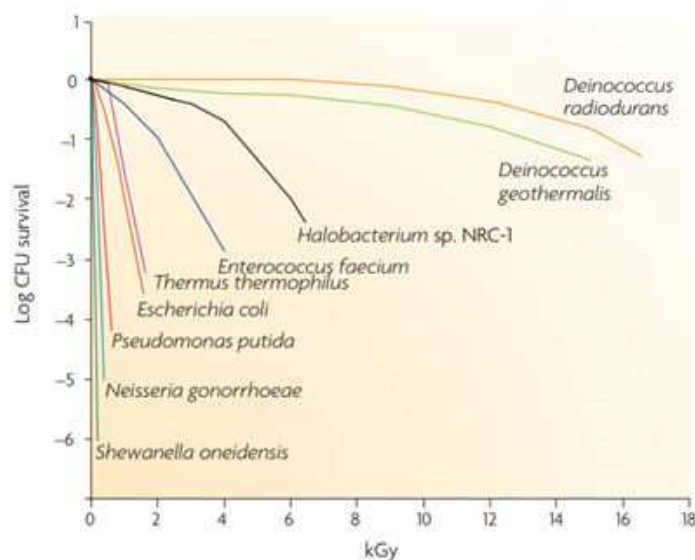


Figure 1.2: Difference of survival capacities of several bacteria. Comparison between different species with similar DNA repair protein repertoire, for different levels of irradiation. Adapted from (Daly 2009).

Other factors contribute to its robust phenotype. Its genome is composed of 4 to up to 10 copies of its different chromosomes, varying during the cell cycle (Battista 1997). This high redundancy of genetic information may therefore ensure the presence, and the availability, of intact DNA template for the restoration of the original genome (Minton & Daly 1995). Moreover, its genome is particularly condensed, which is proposed to prevent the dispersion of free DNA ends (Minsky et al. 2006). Interestingly, *D. radiodurans* genome has been shown to adopt a ring-like structure that is unaffected by high doses of gamma irradiation (Englander et al. 2004; Levin-Zaidman et al. 2003). Condensed genomes appear to be a common feature of a number of radiation resistant bacteria (Zimmerman & Battista 2005). The link between nucleoid organisation and

bacterial radioresistance is further discussed in “2.3 *D. radiodurans* chromosome organization and condensation”.

In addition to this peculiar phenotype, *D. radiodurans* also possesses numerous properties making it suitable for lab work: *D. radiodurans* is a class 1 organism, it can be cultivated in the laboratory in rich medium and a wide range of genetic tools has been developed over the years in particular in Prof. Sommer’s laboratory in Orsay (now directed by Prof. Confalonieri), with whom we collaborated for the work presented in this manuscript (Lecointe et al. 2004).

1.2. Cell wall structure

Even though *D. radiodurans* cell envelope has been investigated in many studies, the exact structure of the cell wall is still not clear yet. As it is much more complex than in other bacteria, it was believed that *D. radiodurans* resistance could hide in this unusual cell envelope.

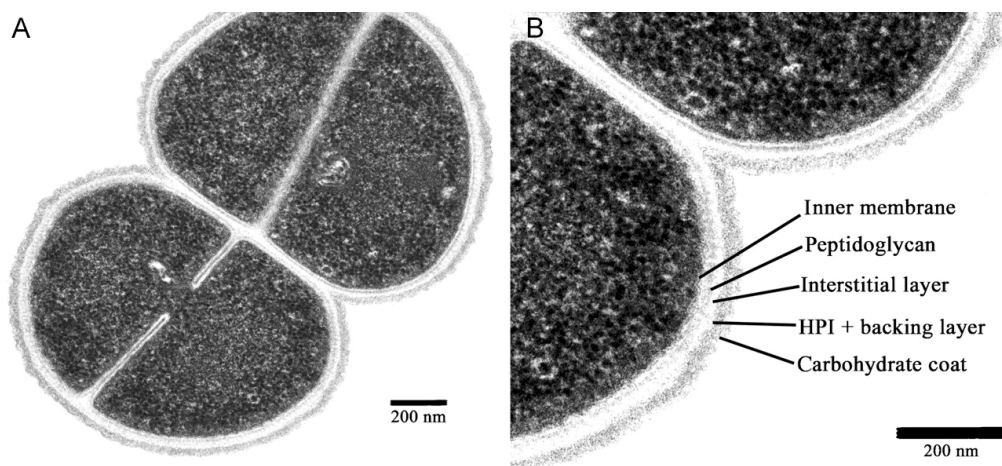


Figure 1.3: Thin section electron micrograph of *D. radiodurans*. *D. radiodurans* tetrad in A) is magnified in B), with the different layers indicated. Adapted from (Rothfuss et al. 2006).

D. radiodurans is a bacterium that stains Gram positive, however, its cell envelope is unusual: it shows similarities to Gram-negative bacteria as it possesses an outer membrane (Battista 1997). Five layers have been identified (Rothfuss et al. 2006), forming a 70nm thick cell wall: (i) the inner cytoplasmic membrane, (ii) the rigid peptidoglycan cell wall, (iii) the interstitial layer, mostly unknown, and supposed to be composed of water soluble proteins, (iv) the Hpi (for Hexagonally Packed Intermediate) and membrane-like backing layer and (v) the carbohydrate coat (Figure 1.3). Part of the cell wall that contains the interstitial layer, the backing layer, the Hpi layer and the carbohydrates coat is referred as the “pink envelope,” due to the color given by carotenoids (identified as deinoxanthin) (Farci et al. 2016) present in the Hpi layer. This pink envelope is composed of carotenoids, lipids, proteins and polysaccharides.

The Hpi layer is structurally organized into a hexagonal network. Two of the most abundant proteins of the Hpi layer are the Hpi proteins and SlpA (Surface Layer Protein A) proteins. Deletion of *Hpi* had almost no impact neither on the structure of the pink envelope nor on the cell viability and response to stress. However, deletion of *SplA* leads to clear changes in cell viability and response to stress; peelings of the outer layers were even observed by electron microscopy (Rothfuss et al. 2006).

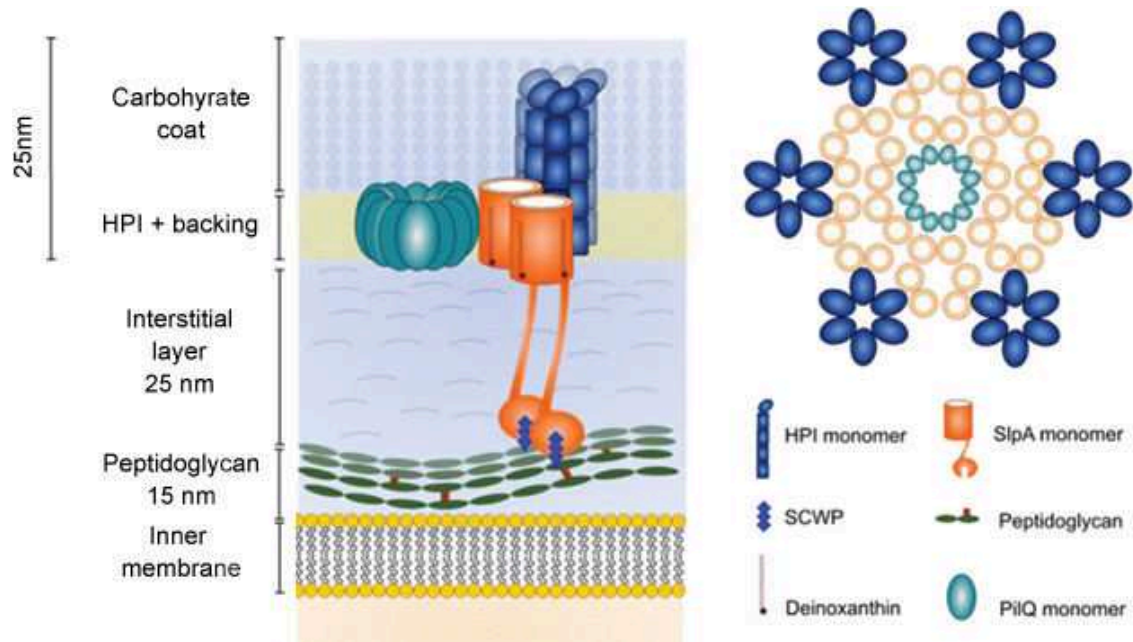


Figure 1.4: Model of *D. radiodurans* cell walls. A) Representation of the five different layers of the cell wall. B) The predicted association of the SlpA dimers with the hexameric Hpi structure and PilQ protein. Adapted from (Ghedira et al. 2016).

Recent investigation on the pink envelope structure proposed that SlpA localizes to the interstitial layer and interacts with the peptidoglycan layer (Misra et al. 2015), the backing layer (Rothfuss et al. 2006), the Hpi protein (Misra et al. 2015) and may associate with the PilQ protein (Farci et al. 2015) (Figure 1.4). Moreover, it has also been shown that SlpA interacts with deinoxanthin (Farci et al. 2016). SlpA proteins are organized as dimers combined in triads that form hexameric structures. A model taking into account these different associations and structural information is presented in Figure 1.4.

2. Nucleoid organization

Genomic DNA supports information that encodes an organism and as such must be easily accessible for essential DNA-related proteins that replicate, repair or transcribe it. Surprisingly, this accessibility of DNA occurs even though DNA forms a compact structure known as chromatin, or nucleoid in bacteria. Each human nucleus, which measures on average about 6 μm in diameter, contains around 2 m of de-compacted DNA, and the unwound DNA of a bacterium like *Caulobacter crescentus* measures 1.3 mm, compacted into a 2 μm long cell. In a bacterium like *E. coli*, it is reported that the nucleoid occupies $\sim 75\%$ of the whole cell volume (Fisher et al. 2013). Thus, the DNA must fit into this restricted space, while remaining accessible for DNA replication (which will double the amount of DNA in the same cell) and subsequent segregation into each daughter cell.

Overall, not much is known on *D. radiodurans* nucleoid organization and the processes underlying chromosome segregation. Thus, the next section will describe the current state-of-the-art on nucleoid organization and chromosome segregation in model bacteria, in order to fully apprehend the differences with *D. radiodurans*. For the sake of clarity, we will explore the organization of the nucleoid and its segregation independently.

As we will see, the organization of the nucleoid can be analyzed at different levels. We will adopt a bottom-up point of view, starting from the molecular level, then the micro and macrodomains level, in order to finish with the global spatial configuration level of the nucleoid. There is a strong interplay between these different levels of organization and all of them contribute to the compaction and architecture of the nucleoid. Moreover, as it will be clear throughout the review of the literature, DNA segregation and its organization are intimately linked.

2.1. Molecular organization by nucleoid-associated proteins

At the molecular level, biochemical factors play an important role in the compaction and organization of the nucleoid. Bacteria produce small, but abundant proteins that associate with the nucleoid (NAPs, nucleoid-associated-proteins). The study of their molecular roles on the compaction and dynamics of DNA has suffered from some of their properties. Indeed, NAPs are redundant and pleiotropic, which complicates *in vivo* studies. Moreover, these biological challenges are also worsened by the technical challenge posed by the small size of bacterial nucleoids ($< 1 \mu\text{m}$). Indeed, it hinders the usability of conventional microscopy techniques (see paragraph “II.5 Optical resolution principle”). Nevertheless, numerous NAPs have been identified and characterized in different bacteria.

The nature and number of NAPs are not conserved across different bacterial species (**Table 1.1**). NAPs can play the role of transcription factors and even impact transcription, replication, and recombination (Dillon & Dorman 2010). In the following, we will briefly summarize the properties of common NAPs such as the small basic ones (HU, IHF, Fis, NH-S) and SMC, a larger one. They are found scattered throughout the nucleoid (Wang et al. 2011) and can have a broad range of effects on the chromosome; if we focus on the topological consequences, three main categories can be drawn: (i) the bending of DNA, (ii) the connection of distant regions and (iii) the coating of DNA strands (Figure 1.5). Interestingly, as we will see, NAPs can belong to multiple categories. More details can be read in these general reviews on nucleoid organization (Badrinarayanan et al. 2015; Surovtsev & Jacobs-Wagner 2018) or in the NAP focused review (Dillon & Dorman 2010).

- (i) Among the NAPs that induce sharp DNA bending are the Fis protein (factor for inversion stimulation), the IHF protein (integration host factor) and the HU protein (Heat unstable). This bending can dramatically change the topology of the DNA and can promote the formation of loops. The HU protein is a small, basic, protein (10 kDa, usually composed of 90 to 99 amino acids (Grove 2011)) that resembles eukaryotic Histone H2B while being present and highly conserved in all bacteria. *E. coli* mutant strains lacking HU have a perturbed cell division, resulting in poor growth and some anucleate cells (Huisman et al. 1989). In *E. coli*, HU has also been proposed to play a role in DNA repair, by reducing the formation of double strand breaks generated by ionizing radiation that occur when lesions are induced in both strands within a distance of a few base pairs (Hashimoto et al. 2003). HU and IHF share some sequence similarities and both bind non-specifically to DNA and are composed of two subunits that interact with the minor groove of the DNA duplex to induce its bending. HU also displays high affinity for specific DNA structures including nicks, gaps, junctions and forks (Balandina et al. 2002).
- (ii) Distant regions of the chromosome can be connected through the action of H-NS (histone-like nucleoid-structuring). This connection can occur for example by bridging into a loop different regions that can span several kilobases. The bridging of DNA by H-NS has been proposed to actually constrain its negative supercoiling by isolating looped regions of DNA. Recently, HU has also been reported to promote long-range contacts in the chromosome, in the megabase range (Lioy et al. 2018).
- (iii) H-NS has also been shown to coat the DNA, which can alter its rigidity. The H-NS is a molecule capable of oligomerization, which spreads on the DNA and can directly occlude different binding sites of the DNA, thereby interfering with transcription, leading to gene expression regulation. At high concentrations, HU heterodimers form rigid filaments *in vitro* where HU and DNA spiral around each other (Luijsterburg et al. 2006). Interestingly, HU possesses a higher affinity for

supercoiled DNA, or for distorted DNA to which it can induce bends or supercoiling (Nguyen et al. 2009).

All the NAPs presented in this section are small basic proteins (10-20 kDa). The SMC complex (structural maintenance of chromosomes) is generally also considered as a NAP and yet it is much larger than previously presented NAPs (>150 kDa) and is analogous to eukaryotic condensins or cohesins. The SMC complex forms a ring-like structure, which can modify the chromosome topology, by encircling the DNA, like a handcuff. It appears that distant regions of the chromosome can be connected through the action of the SMC complex. It is made of an ATPase and two regulatory proteins, named, ScpA and ScpB. In *E. coli*, analogous proteins MukB, MukE, MukF, form the related complex MukBEF.

It is noteworthy that the different NAPs presented above are not as equally abundant in cells. Moreover, in *E. coli* their levels of expression vary during the cell cycle.

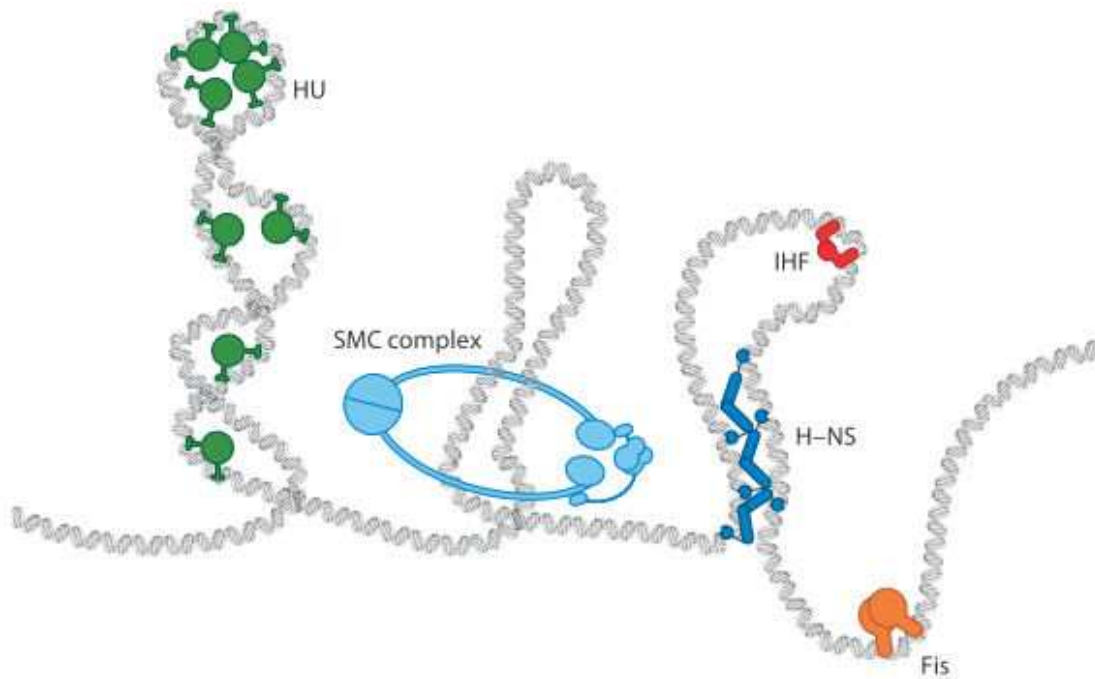


Figure 1.5: Representation of the different activities of HU, IHF, Fis, H-NS and SMC NAPs. HU proteins (in green) can bend or wrap DNA around itself. SMC proteins (in cyan) can form a ring structure that handcuffs the DNA. H-NS (in blue) dimer of dimers can bridge DNA. IHF proteins (in red) can induce U-turn bends to DNA. Fis proteins (in orange) also bend the DNA. From (Badrinarayanan et al. 2015).

Table 1.1: NAP genes found in bacteria. Adapted from (Pinho et al. 2013)

	Nucleoid organisation (NAPs)				
	HU	IHF	Fis	H-NS	Smc
<i>E. coli</i>	+	+	+	+	+ [¶]
<i>B. subtilis</i>	+	-	-	-	+
<i>C. crescentus</i>	+	+	-	-	+
<i>S. aureus</i>	+	+ [#]	-	+	+
<i>D. radiodurans</i>	+	-	-	-	+

[#] In *S. aureus* SarA is a functional analogue of IHF. [¶] In *E. coli* MukBEF is a functional analogue of Smc.

Compared to model bacteria, *D. radiodurans* possesses very few NAPs and some display different properties (see Table 1.1). For example, *D. radiodurans* lacks Fis, H-NS and IHF proteins. SMC proteins also do not appear to play a major role in nucleoid condensation in *D. radiodurans* (La Tour et al. 2009). The major NAP that organizes *D. radiodurans* nucleoid is HU (Passot et al. 2015; Toueille et al. 2012). Its action is facilitated by the DNA gyrase that modulates the extent of supercoiling of the DNA. Both HU and DNA gyrase have been shown to be essential for *D. radiodurans* viability, and the progressive depletion of HU leads to nucleoid decondensation. Interestingly, only one HU protein is produced by *D. radiodurans* unlike *D. deserti* (another *Deinococcus* species) that produces three variants of HU, DdHU1, DdHU2 and DdHU3 (La Tour et al. 2015). The presence of either DdHU1 or DdHU2 is sufficient for survival. These two HU genes can even substitute the sole HU gene in *D. radiodurans* unlike DdHU3.

2.2. Micro- & macro-domain organization

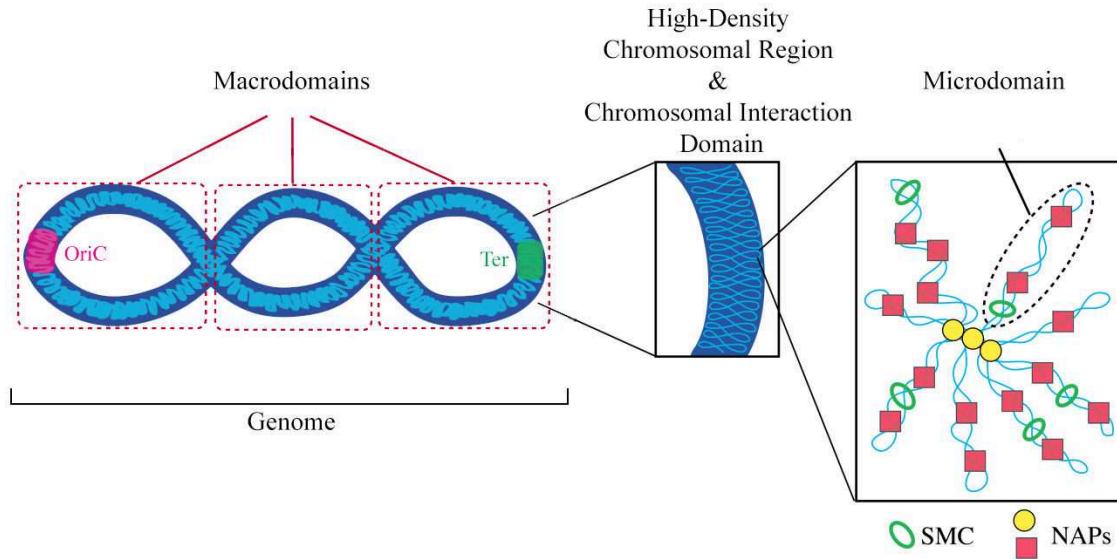


Figure 1.6: Schematic representation of a bacterial nucleoid across different levels of organization (helical structure, macrodomains, high-density regions, chromosomal interaction domains and microdomains).

Relaxed double-stranded DNA (dsDNA) twists around the helical axis every 10.5 base pairs. If dsDNA is closed with covalently linked ends, the shape of the molecule becomes constrained. Different DNA-related mechanisms, such as transcription or DNA repair, will induce positive or negative torsional stress on circular dsDNA, that can induce supercoiling of the DNA. For example, adding or subtracting writhes by enzymes named topoisomerases (either by cutting only one DNA strand, by type I topoisomerases, or by cutting both strands by type II topoisomerases) produces, respectively, positive or negative supercoiled structures.

E. coli chromosomes have been shown to be organized into 50-400 DNA domains of negatively supercoiled loops of ~10 kb. This subdivision of the chromosome into these small independent loops contributes to the compaction of the nucleoid (Luijsterburg et al. 2006). In *E. coli*, the supercoiling of the DNA may be stabilized by different NAPs (see above), such as H-NS and SMC proteins that bind at the base of the loops, in order to topologically isolate them into independent domains (Badrinarayanan et al. 2015).

Despite supercoiled domains being known for a long time, their exact roles and their distribution along the chromosome are not really understood. For example, it is hypothesized that the variation of the supercoiled domain localization in the same population of cells, or throughout the cell cycle could impact the expression of genes (the promoters could be sensitive to the topological state of the DNA) (Badrinarayanan et al. 2015). Lately, bioinformatics studies have focused on the boundaries of the supercoiled

domains, and have shown that they were dynamic, which may suggest again an interplay between gene expression and localization of supercoiled domains (Lioy et al. 2018).

As we have just seen, molecular factors, such as NAPs can induce changes at the molecular scale in the topology of the chromosome, and even at a larger scale by promoting the contact between different regions of the chromosome. These DNA-DNA interactions actually reveal the existence of chromosomal interaction domains (CIDs).

Hi-C analysis (a chromosome conformation capture technique) is capable of generating genome-wide interaction maps of genomic loci (Lieberman-Aiden et al. 2009). Thus, it can reveal the spatial organization of chromatin in a cell, by quantifying the interactions between genomic loci that may not be genomic neighbors, forming spatial domains, the CIDs. These domains represent loci with more frequent DNA-DNA contacts within the domain itself than with any other loci of the rest of the chromosome. CID studies revealed that *C. crescentus*, *B. subtilis* and *E. coli*, possess respectively 23, 20 and 31 CIDs, ranging in size from 20 to 200 kb for *C. crescentus* and *B. subtilis*, and from 40 to 300 kb for *E. coli* (Lioy et al. 2018). Interestingly, the boundaries of these domains often coincide with the presence of highly transcribed genes. It has also been proposed that these domain boundaries could have a link with the previously described supercoiled domains. A potential model linking these last two observations hypothesizes that the highly expressed nature of a gene induces an important decondensation and uncoiling in this region, which would physically separate the different loci upstream and downstream of the particular gene, producing these boundaries (Le et al. 2013). A recent study suggested that the NAPs play an important role in the formation of CIDs. In *E. coli*, MukBEF promotes long-range (>280 kb) DNA contacts along the chromosome outside of the Ter region, a region encompassing the replication terminus (or *ter*). HU would promote even longer range contacts (megabase range) outside of Ter (see macromonains, just below), and around 280 kb range contacts within Ter. In contrary, H-NS was shown to promote short-range DNA-DNA interactions (Lioy et al. 2018).

In *B. subtilis* and *E. coli*, CIDs may randomly associate, creating a higher level of organization, named high-density regions (HDR) (Le Gall et al. 2016; Marbouty et al. 2015). These were seen thanks to 3D structured-illumination microscopy, a super-resolution (SR) microscopy technique (see “II.7 SR fluorescence microscopy”). Moreover, the HDR containing the origin of replication (*ori*) displayed a localization choreography during the cell cycle that was well defined compared to other HDRs in the cell. The authors suggest that this defined choreography might be regulated, maybe in order to play a role in chromosome replication.

Nucleoids can also be divided into larger domains (megabases in size), called macrodomains, corresponding to regions where loci in the same macrodomain interact and recombine more frequently than with loci present in different macrodomains (Valens et al. 2004). *E. coli* was found to be organized into four macrodomains, Ori, Ter, Left

and Right, and two less-structured regions, one positioned in between the Ori and Right regions, the other in between *ori* and Left regions (Figure 1.7). The Ori domain includes the *ori* sequence and the Ter domain includes the *ter* sequence.

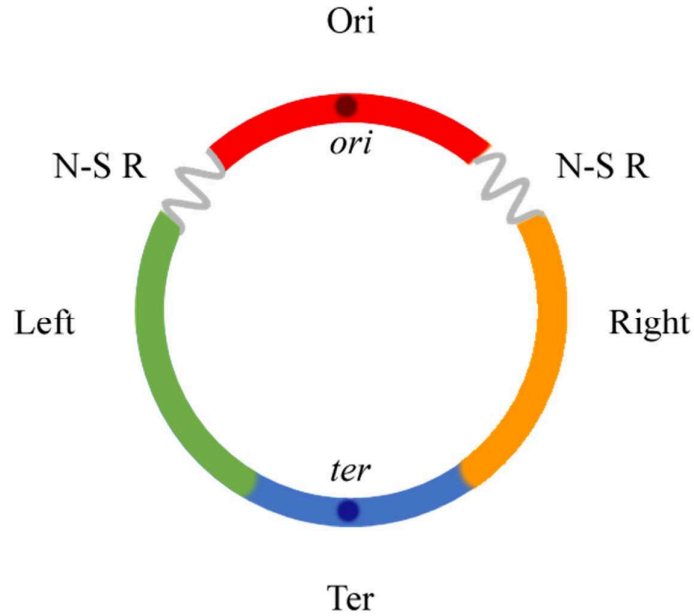


Figure 1.7: *E. coli* macrodomain organization, Ori, Ter, Left, Right and the two non-structured region (N-S R) along the origin of replication (*ori*) and the replication terminus (*ter*).

The most studied macrodomain is the Ter region. In *E. coli*, the *ter* loci are tethered at midcell thanks to the action of MatP protein which also prevent the segregation of the *ter* loci until the end of the cell division. The first studies of MatP protein showed that it was responsible for the condensation of the Ter region (Dupaigne et al. 2012; Mercier et al. 2008) by binding to 23 specific DNA motifs of 13 bp, *matS* (mostly present in the 800 kb long Ter region). However, recent results suggest that MatP promotes a thin Ter region rather than condensing it. Silencing MatP reduced the size of the chromosome by 20% (Wu, Japaridze, et al. 2018; Wu, Swain, et al. 2018). MatP seems to facilitate the association of MukBEF (SMC analogue) with the Ori region (Nolivos et al. 2016) and prevents the MukBEF activity in the Ter region, which might explain the distinct structure of the macrodomain, by hindering the long-distance DNA-DNA contacts induced by MukBEF (Liroy et al. 2018).

Recently, a single specific sequence of 17 bp, *maoS*, and an adjacent gene, *maoP*, both from Ori region, were found in *E. coli*. MaoP seems to organize the Ori region, by an unknown mechanism (Valens et al. 2016). In particular, silencing of MaoP/*maoS* resulted in abnormal cells with altered nucleoid segregation, defects in the control of replication initiation. More generally, MaoP/*maoS* seems to play an important role in Ori positioning and chromosome choreography and also affects the long-distance contacts with loci in the Right macrodomain.

Interestingly, so far, no specific protein was found to bind to the Right and Left macrodomains. On the contrary, it was shown that the position of the Ori region might be the main determinant of the position of the Right and Left regions. Indeed, even when the Ori region is genetically displaced, the two non-structured regions can be observed closely flanking the Ori region. Moreover, the Left or Right macrodomains can also be observed, but further away (regardless of their sequence composition) (Duigou & Boccard 2017). Thus the Ori region also seems to determine the localizations and the structuring of the other macrodomains of the chromosome in *E. coli*.

Finally, the nucleoids in *E. coli*, *B. subtilis* and *C. crescentus* seem to be shaped as a gently curved helical-like conformation (Fisher et al. 2013; Marbouty et al. 2015; Umbarger et al. 2011). This curvature does not appear to have any particular handedness. The nucleoids appear to be organized as a longitudinal pair of parallel bundles.

Table 1.2: Summary of the genome organization and characteristics of model bacteria. Adapted from (Dame & Tark-Dame 2016)

Organization unit	Genome	Macrodomain	Chromosomal Interaction Domain (CID)	High-Density Chromosomal Region (HDR)	Microdomain
Size	≈ 5 Mbp	≈ 1 Mbp	30-500 kbp	200-250 kbp	≈ 10kbp
Characteristics	Helical organization	High intra-domain recombination	High-intra domain interaction frequency	High local DNA density	Possible role in gene expression
Organisms	<i>E. coli</i> <i>B. subtilis</i> <i>C. crescentus</i>	<i>E. coli</i> <i>B. subtilis</i>	<i>E. coli</i> <i>B. subtilis</i> <i>C. crescentus</i>	<i>B. subtilis</i>	<i>E. coli</i>

2.3. Spatial organization of the nucleoid

In bacteria, two stereotypical configurations have been observed for the nucleoid organization: the transversal and the longitudinal one. Interestingly, the very same bacteria, can display both of these configurations during their cell cycle or under different growth conditions (Figure 1.8).

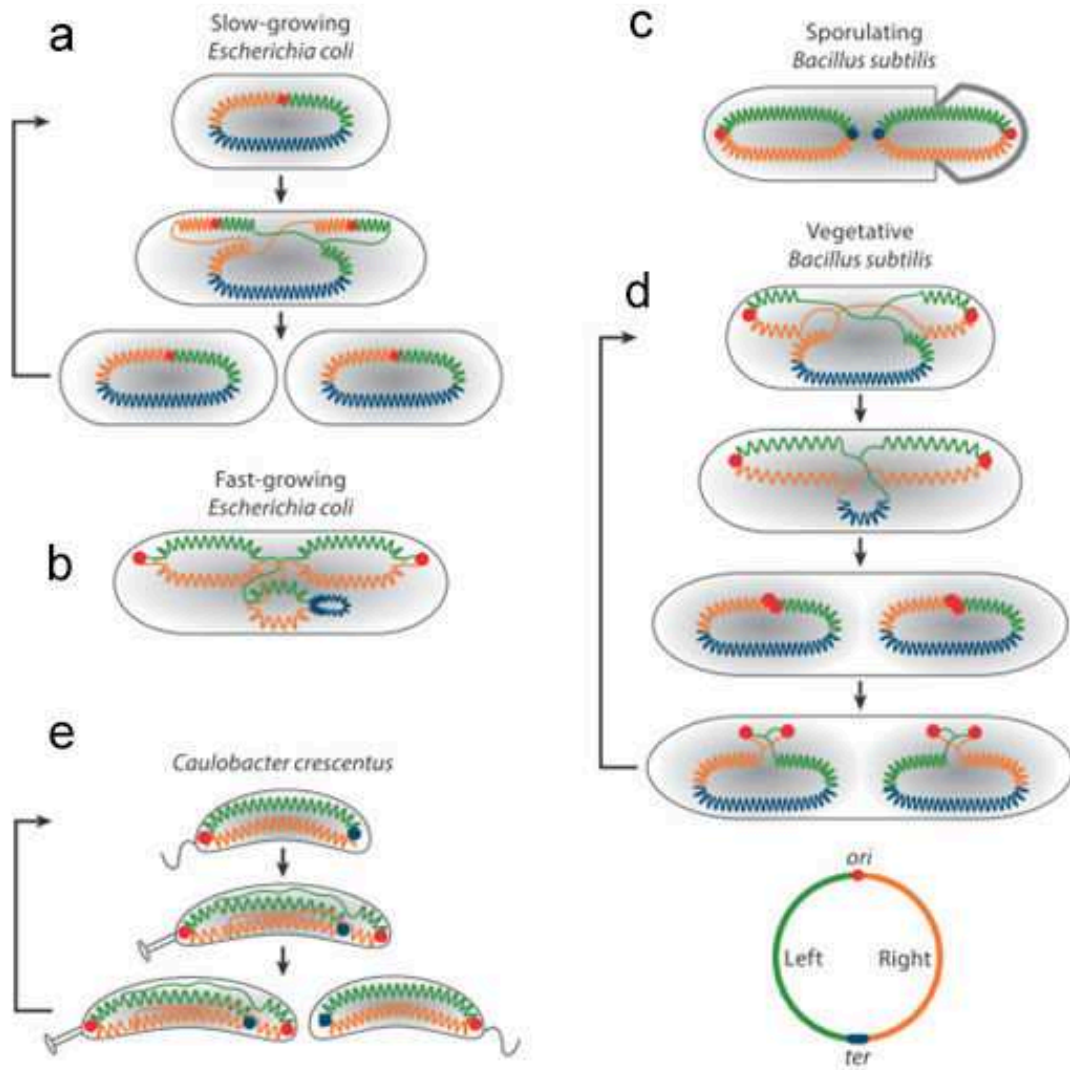


Figure 1.8: Spatial organization of chromosomes in different organisms: (a) Slow-growing *E. coli*, (b) fast-growing *E. coli*, (c) sporulating *B. subtilis* and (d) vegetative *B. subtilis* and (e) *C. crescentus*. The *ori* appears as a red dot, the left arm in green, the right arm in orange and the terminus region as a blue dot. Newly synthesized or less-organized DNA appears as thin lines whereas compacted parts of the chromosomes are shown as zigzag lines. The gray shading represents the overall distribution of the nucleoid, and the black arrow the progression of the cell cycle. Adapted from (Badrinarayanan et al. 2015).

2.3.1. Basic configuration: transversal configuration

Slow-growing *E. coli* cells display a transversal configuration of their chromosomes (named “left-*ori*-right”). On average, *ori* is localized at midcell, while the left branch of the chromosomes is located on one side of the rod and the right branch to the opposite side (see Figure 1.8). The center of the large termination site that links the left and right branches is also around midcell (Toro & Shapiro 2010). After replication of *ori*, the two copies of the chromosomes are segregated to the quarter positions of the cell (1/4 and

3/4), where both copies will adopt again a transversal configuration (Wang & Rudner 2014).

Other bacteria can adopt a transversal configuration of their chromosomes during their cell cycle or under specific conditions (see “More complex” paragraph). Notably, *E. coli* can also adopt a second configuration, the longitudinal one, when fast-growing.

2.3.2. Basic configuration: longitudinal configuration

Other bacteria display a longitudinal configuration of their chromosomes (named “*ori-ter*”), i.e. *ori* is localized on one side of the cell and *ter* is situated at the other pole, inducing the two arms of the chromosomes to lie side-by-side, parallel to the long axis of the cell (Wang & Rudner 2014).

C. crescentus nucleoids adopt a longitudinal configuration, that is dependent on its cell cycle. The *ori* is first localized at the old pole of the cell, whereas *ter* is localized at the newest pole. Once the duplication is initiated at *ori*, the newly duplicated origin moves to the new pole of the cell, where the termination site lied previously. Meanwhile, *ter* is delocalized to midcell. The replication ends with the duplication of *ter*. The two copies of the chromosome will adopt again an *ori-ter* configuration in the daughter cells (Toro & Shapiro 2010).

Fast-growing *E. coli* cells also adopt a longitudinal configuration. In fast-growing conditions, *E. coli* cells continuously replicate their genomes thus, even newborn cells possess an important portion of their chromosomes already replicated. Under these conditions, the newly replicated origins are segregated to the different poles of the cells, with the right and left branches of the cells side-by-side (Youngren et al. 2014). Interestingly, *E. coli* cells lacking MukB protein will adopt an *ori-ter* conformation even if slowly growing (Danilova et al. 2007).

In sporulating *B. subtilis*, despite an asymmetric septum which positions the quarter of one of the two replicated chromosomes inside the pre-spore, the two chromosomes adopt a longitudinal configuration. Notably, the *ter* of the two chromosomes are positioned at midcell, giving a special orientation to the two chromosomes: an *ori-ter/ter-ori* longitudinal configuration (Badrinarayanan et al. 2015).

In *V. cholerae* which possesses two chromosomes, both of them are longitudinally configured (see Figure 1.9) (Espinosa et al. 2017).

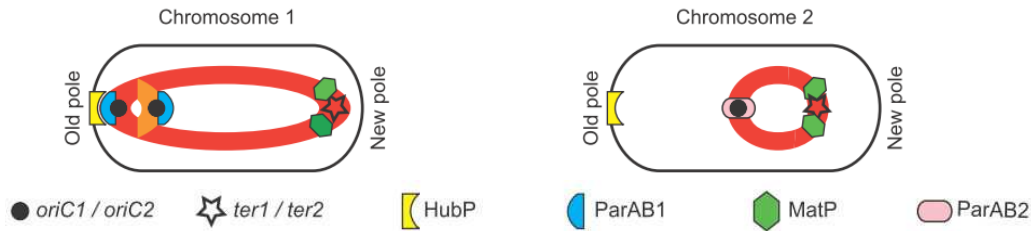


Figure 1.9: Schematic representation of the two chromosomes organization in *V. cholerae*. Adapted from (Espinosa et al. 2017).

2.3.3. Complex configurations

The two previously described configurations are stereotypical, and can be viewed as building blocks to better understand the configuration of other bacteria. Indeed:

- Some bacteria actually display both configurations, but for different growth conditions (as presented for *E. coli* earlier).
- Some bacteria alternate between these two configurations during their cell cycle. For example, vegetative *B. subtilis* organization switches during its cell cycle from an *ori-ter* organization just before division and in newborn cells to a left-*ori*-right configuration just after replication (Figure 1.8) (Wang & Rudner 2014).
- The configuration in the vast majority of bacterial species is still unknown. For example, some bacteria such as *Streptomyces* species do not even possess a circular chromosome but a ~8 Mb linear one. Its loose ends are spatially closed, probably by folding back on themselves with a possible role for Telomere-binding proteins. However, nothing is known regarding the spatial configuration of such a genome (Badrinarayanan et al. 2015).

As we have seen, the two arrangements, the *ori-ter* and left-*ori*-right, are both found in *E. coli* and in *B. subtilis*. This fact actually points towards a possibility that these two distinct organizations might not be so different. Although the underlying mechanisms explaining these two arrangements are still unclear, several factors are believed to influence it: the NAPs, especially the SMCs (see paragraph “2.1 Molecular organization by nucleoid-associated proteins”), the physical properties of the nucleoid itself, the cell shape, but also the mechanisms underlying segregation or anchoring of the chromosomes.

2.3.4. Anchoring of Ori region

Different proteins have been found to anchor the chromosome to the cell pole in bacteria. The presence of these proteins may promote the *ori-ter* configuration (Badrinarayanan et al. 2015). For example, in *C. crescentus*, the chromosome is anchored to the cell pole by the PopZ protein which interacts with ParB a protein that binds to a specific DNA sequence, *parS* (more detail in “3.1 ParABS system, an active

model for origin segregation”). It is noteworthy that, in *C. crescentus*, moving the *parS* sequence away from its original position (close to *ori*) does not affect its position inside the cell, unlike *ori* which shifts away from the pole (Umbarger et al. 2011). In *B. subtilis*, RacA protein is recruited by DivIVA to curved cell poles and is able to bind RacA-binding motif sequences (ram), located near *ori* of the chromosome, anchoring it to the cell pole during sporulation (Badrinarayanan et al. 2015).

Despite the fact that the polar-anchoring proteins presence seems concomitant with an *ori-ter* organization, some organisms adopt an *ori-ter* configuration without their chromosome seemingly anchored to the pole. For example, in newborn cells of *M. xanthus*, the distance chromosome pole / cell wall is about 1 μm (Harms et al. 2013). However, the existence of a possible subpolar anchoring protein exists in this bacterium. Similarly, fast growing *E. coli* adopt an *ori-ter* configuration, but no polar-anchoring proteins have so far been found in *E. coli*.

Finally, for cells that do not seem to possess any anchoring machineries, or cells that display a left-*ori*-right organization, it is still not clear how *ori* loci become localized to midcell. The position of *ori* may be a consequence of other properties of the chromosomes: the distinct properties of the Ter region, the different interaction domains or the polymer nature of the chromosome and the depletion force exerted on it as we will see below.

2.4. Nucleoid compaction mechanisms

Currently, the mechanisms accounting for these changes in chromosome configuration and more generally for the organization of the nucleoid in bacteria are not yet resolved. Some general models try to explain these organizations as a consequence of the remarkable capacities of bacteria to condense their chromosomes into a nucleoid.

As illustrated earlier, NAPs are legitimate candidates to explain the compaction of the nucleoid. However, no clear-cut results on the condensation role of NAPs *in vivo* has emerged, and overexpression of NAPs does not result in over-compaction of bacterial nucleoids (Jun 2015). Therefore, NAPs may indeed account for part of the nucleoid compaction, but do not seem to be fully responsible for the high levels of compaction observed in nucleoids.

A proposed source of compaction forces arises from the concentration of cytoplasmic proteins. For example in *E. coli* growing in rich medium, macromolecule concentrations (RNA + protein + DNA) is estimated to be around 0.3-0.4g/ml (Zimmerman & Trach 1991), which can crowd the cytoplasm, in an effect coined “macromolecular crowding”. At such levels, these proteins occupy around 20% of the whole cell volume and the interprotein distances are about the same size as the proteins themselves. This high concentration of proteins indirectly produces a non-negligible attracting force, the

depletion force, on the DNA strand (Jun 2015; Marenduzzo et al. 2006; Shendruk et al. 2015) (Figure 1.10).

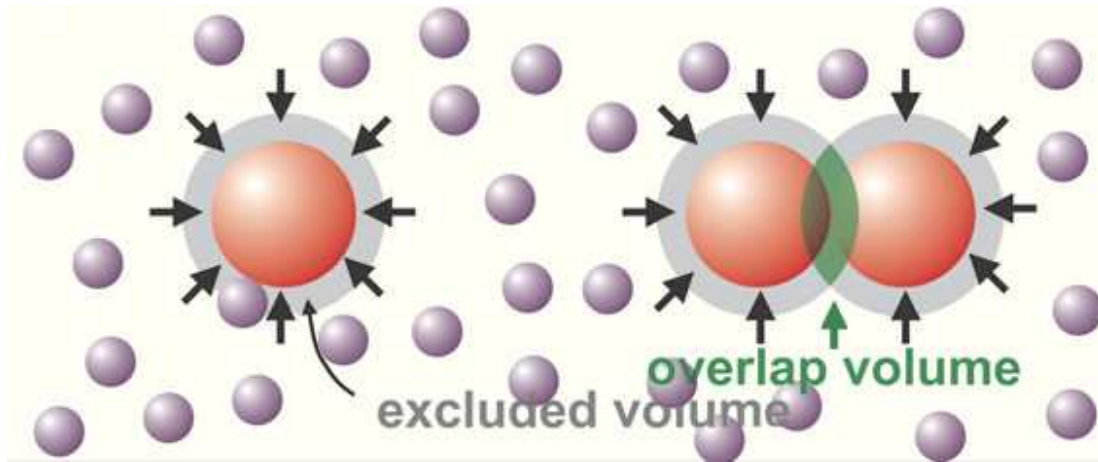


Figure 1.10: Schematic illustration of the depletion forces. A depletion layer forms around the large non-absorbing molecules (in red), generating an excluded volume (gray zone) for the small molecules (in purple), where they tend not to enter due to their loss of entropy in this volume. When two large molecules are close enough, their depletion layer starts to overlap. The small molecules cannot enter the space in between these two large molecules (green zone) and a difference in the osmotic pressures of the small molecules arise between the general surrounding volume and the volume in between the two large spheres. Thus, the small spheres will push the two large spheres together due to this difference in osmotic pressure. This results in an indirect attractive force between the two large molecules due to the depletion force induced by the non-absorbing large molecule on the small ones. Adapted from: (Marenduzzo et al. 2006).

The depletion forces may result in the collapse of the chromosome and induce a phase separation between the DNA and the cytoplasmic proteins. Pelletier et al. (Pelletier et al. 2012) when studying the compaction of the nucleoid at different levels of molecular crowding (using different concentrations of PEGs), observed that at a certain PEG concentration the nucleoid was present in both compact and non-compact phases. In thermodynamics, the transition between two different phases is called a first-order transition. It basically means that the transition from one phase to another is not continuous due to the latent heat during the transition. For example, the transition from ice to liquid water is a first-order transition: when ice is moved from a negative temperature to a positive temperature, at 0°C , both ice and liquid water will coexist and the temperature of the whole system will not increase, until all the ice has melted. By analogy, the coexistence of compacted and non-compact phases of the nucleoid at a precise concentration of macromolecular depletants, indicate a first order transition.

Recent simulation models, based on a coarse-grained model (Figure 1.11), shows that a large molecule like a chromosome when confined in a small volume such as a cylinder, will not adopt a random organization (Jung et al. 2012; Youngren et al. 2014). Instead, adjacent segments of the chromosome will collapse onto each other. Thus the chromosome in *E. coli* can be simulated as a ring-like, soft-spring polymer, made of a string of beads (where the adjacent segments collapse), in a cylindrical space (Pelletier

et al. 2012). The exact constituents of the beads of collapsed segments of DNA is not known, but one can speculate that it could be composed of supercoiled DNA structured into domains due to different NAP effects (Pelletier et al. 2012). This whole structure appears to adopt a donut shape, that basically resembles an elastic bracelet loaded with beads, the diameter of which ranges from 130 to 440 nm. The most recent simulations (reviewed in (Jun 2015)), added to this coarse grained model the possible depletion forces induced by molecular crowding of the cytoplasm and compared it to experimental data (Shendruk et al. 2015). Their results showed that the depletion force induced by crowding was strong enough to account for nucleoid compaction. However, first-order transitions could not be explained by any simulations. This led the authors to postulate that NAPs were possibly responsible for this difference in the phase transition. Thus, according to these theoretical simulations, basal compaction of the nucleoid could be accomplished by the sole presence of depletants plus the polymeric nature of the chromosome and the numerous NAPs would mostly play a role in phase separation between the nucleoid and the cytoplasm (Jun 2015).

Interestingly, in such a model, the strength of depletion forces induced on chromosomes should be higher than the entropic forces that result from the polymer nature of the chromosomes, but much smaller than the forces underlying the various processes that involve DNA transport (ParABS, FtsK...) (Wu, Swain, et al. 2018).

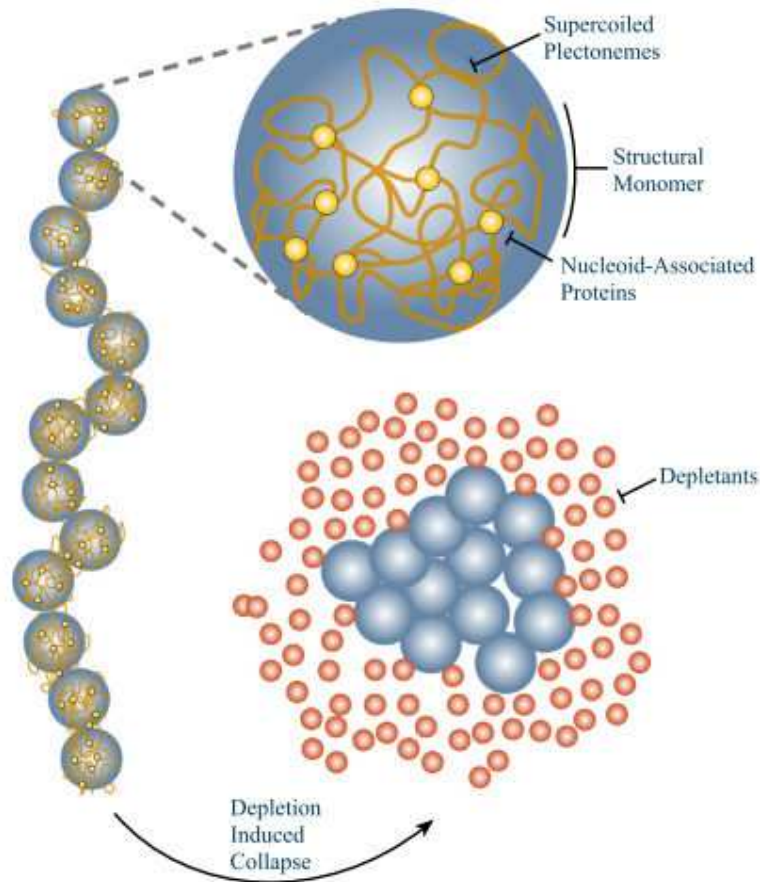


Figure 1.11: The coarse-grained model of bacterial chromosome DNA. The chromosome is considered to be a chain of beads, also named structural monomers, where segments of DNA composed of supercoiled structures and NAPs collapse onto each other. The DNA is surrounded by proteins acting as depletants. Adapted from (Shendruk et al. 2015).

Another factor has been taken into account in different experiments and simulations studies: the cell shape itself. Indeed, as the chromosomes occupy most of the cytoplasm, correlating the cell size/shape to the nucleoid size/shape may be a reasonable working hypothesis.

Experimentally, the influence of cell shape/size on the nucleoid shape/size and compaction in *E. coli* was demonstrated in two recent studies (Wu, Japaridze, et al. 2018; Wu, Swain, et al. 2018). Mutant *E. coli* cells, exhibiting a “lemon” shape (cell with a larger width, but with the same length as wild type strains) and engineered to possess only one chromosome; showed an expanded nucleoid, with a clear toroidal shape (Wu, Japaridze, et al. 2018). Wu et al. also linked the cell shape/size and nucleoid cell size to molecular crowding (Wu, Swain, et al. 2018). They experimentally observed that nucleoids displayed different sizes in engineered *E. coli* cells of various sizes, possessing a single non-replicating chromosome and placed into micro-patterns that force the cells to only grow longitudinally. Using these engineered cells, several observations were made on the link between cell size and the nucleoid size. For example, they observed that the nucleoid size was increasing non-linearly with the cell length. In extreme cases, for cells

that were 10 times longer than usual *E. coli* cells, the nucleoid expanded only by a factor of 4. The deletion of NAPs did not significantly impact the relation dependence between the nucleoid size and the cell size. Their observations were also investigated through simulation, which suggests that the nucleoid is actually adapted to the size of the cell itself via its interactions with the molecular crowders. Indeed, these macromolecules, tend to localize at the peripheries of the cell shape, which exert an inward force on the chromosome, promoting the compact shape of the nucleoid and also its positioning. According to this paper, this entropic dispersion of the crowders inside the cells, coupled to the slow dynamics of chromosomes, might play an important role in nucleoid positioning inside cells, whether at their center, or at their $\frac{1}{4}$ and $\frac{3}{4}$ position in daughter cells.

However, another recent article (Valens et al. 2016), showed that large DNA rings (150–200 kb and 500-600 kb, excised from different chromosomal regions), accumulated at the cell poles of growing cells, throughout multiple generations. This observation actually contradicts the previously described model suggesting that the forces exerted by the entropic dispersion of crowders on DNA viewed as a coil-like polymer were sufficient to account for the choreography of the nucleoid during the cell cycle, especially the positioning of the two newly replicated chromosomes at the $\frac{1}{4}$ and $\frac{3}{4}$ position.

The difference between the longitudinal or transversal organization in fast or slow growing *E. coli* was also studied through simulations. Multiple factors differ between these two different growth conditions of *E. coli*, but the radial width of the cell was shown to be a critical player in these recent simulations based on the coarse-grained model for the chromosomes (Youngren et al. 2014). Slow-growing *E. coli* cells are thinner than fast growing ones. These thinner cells result in the two different arms of the chromosomes not being able to fit along the long axis in a side-by-side fashion (characteristics of a transversal organization), but instead organize as a long linear polymer. In contrast, fast-growing cells are larger and can accommodate the different arms of the chromosome that can lay side-by-side along the long axis in a longitudinal fashion.

2.5. D. radiodurans chromosome organization and condensation

D. radiodurans genome consists of two chromosomes, of 2.65 Mbp and 412 kbp, a mega plasmid of 177.5 kbp and a plasmid of 5.7 kbp, accounting for 3200 genes encoding around 2000 proteins (White et al. 1999). It is a polyploid bacterium, with cells containing between 4 and 10 genome copy number, depending on the culture medium and growth phase (Hansen 1978; Kitayama & Matsuyama 1981). It was hypothesized that these numerous genome copies may be pre-aligned in the nucleoid (Minton 1994; Minton & Daly 1995) to facilitate the homology search and provide near substrate for

the recombination repair of DNA double strand breaks. However, through the study of fluorescently tagged loci of chromosome 1, it was shown that the number of observed fluorescent foci compared to the number of copies of the studied loci could rule out the possibility of chromosome pre-alignment, before irradiation (Passot et al. 2015). Interestingly, it was also shown in the same study that after irradiation, the nucleoid organization of *D. radiodurans* is modified, and loci tend to transiently align, but only in the late stage of DNA repair.

So far, most of the studies of *D. radiodurans* nucleoids were performed in order to better understand *D. radiodurans* remarkable radioresistance. These studies have revealed that *D. radiodurans* nucleoids are highly condensed. The compact nucleoid of *D. radiodurans* has been hypothesized to actually play a role in the radiation resistance capabilities of *D. radiodurans*. While exposed to ionizing radiation, a high number of double strand breaks are generated. The condensed genome may increase the speed of double-strand DNA breaks repair, by preventing the diffusion of the loose DNA ends (Levin-Zaidman et al. 2003; Zimmerman & Battista 2005). However, this compaction of the nucleoid is not a necessary criterion for radiation-resistance, as several radiation-resistant species do not have a compacted nucleoid. In addition, compaction of the nucleoid is not a sufficient criterion for radiation-resistance, as several species with compacted nucleoids do not display particularly high radiation-resistance phenotypes (Zimmerman & Battista 2005).

It has been reported that in its stationary phase, up to 90% of *D. radiodurans* cells display a compact toroid-like nucleoid shape (Minsky et al. 2006) (Figure 1.12). In exponential phase, the nucleoid has been reported to be less compact and more diffused (Eltsov & Dubochet 2005). Interestingly, *in vitro* DNA tends to aggregate into toroids of hexagonal arrangement, in the presence of condensing agents (Hud & Downing 2001; Hud & Vilfan 2005). Ring-like structures were observed with different methods. Cross-sections of highly condensed stationary-phase cells revealed circular-shaped structures (Daly et al. 2004; Murray et al. 1983) in which DNA is folded around a protein core possibly consisting of SMC proteins (Zimmerman & Battista 2005). This unusual morphology was also revealed by transmission electron microscopy (Levin-Zaidman et al. 2003) as well as epifluorescence and deconvolution microscopy (Zimmerman & Battista 2005)

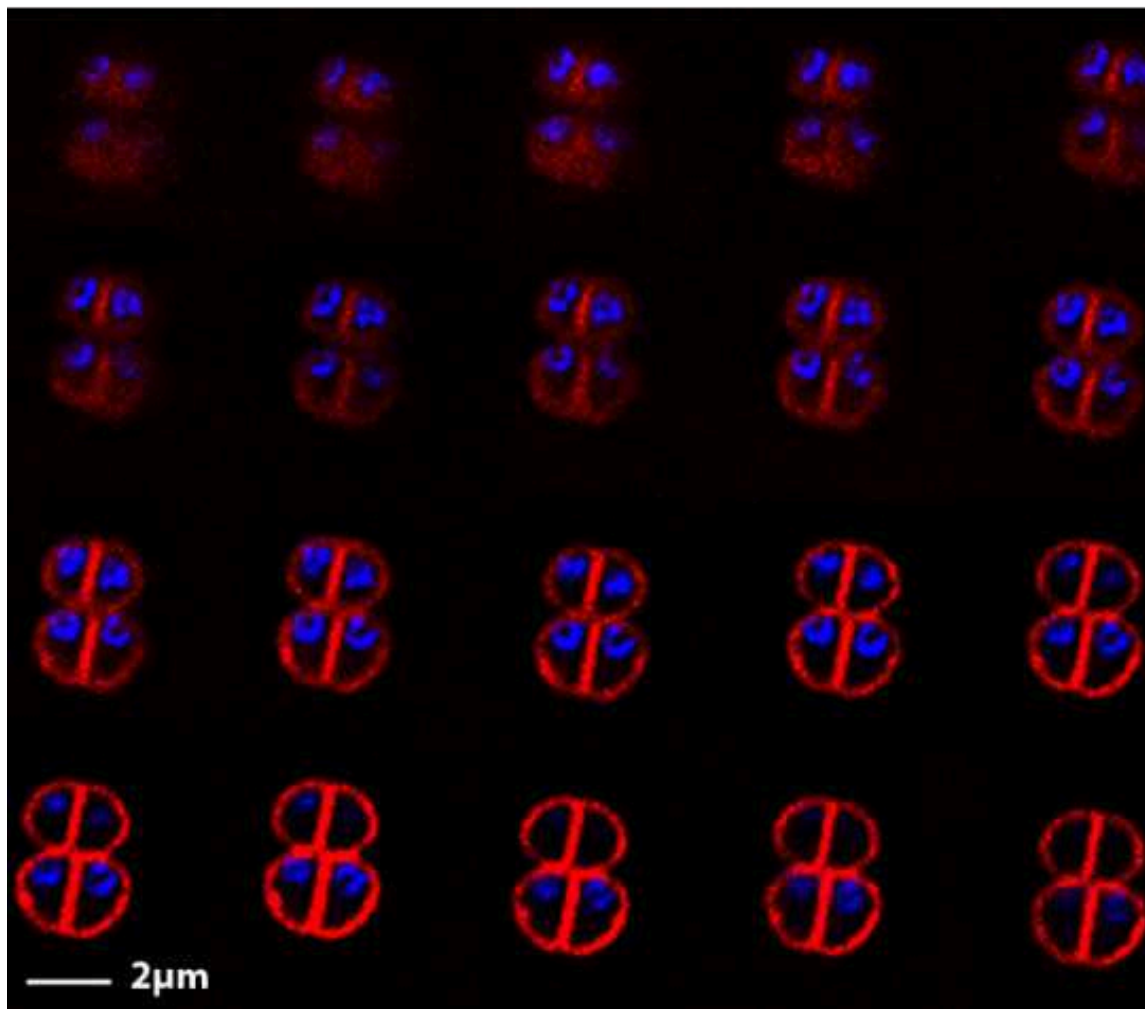


Figure 1.12: Optical sections for successive Z-depth, of *Deinococcus radiodurans*. Series is from left to right, starting from the top left corner with 100nm intervals in Z between each image. The DNA is stained by DAPI and appears in blue, the lipid membrane is stained with FM-4-64 and appears in red. Taken from (Zimmerman & Battista 2005).

3. Chromosome segregation

Every cell must copy its genome with high fidelity and transmit it equally to its two daughter cells, in order to ensure that the genetic material is preserved from one generation to another. In eukaryotes, DNA replication and segregation occur in two distinct phases. In contrast, in bacteria, both occur at the same time. The segregation process in bacteria is less understood than in eukaryotes, partly due to their small size compared to eukaryotic cells, which make them less suited for imaging studies.

Chromosome segregation seems to involve both active and passive mechanisms, both of which have been proposed to be key players in this process. Moreover, there is likely to be some level of interplay between these two systems, making their study more complex. So far, no universal model has emerged to explain chromosome segregation in bacteria. Indeed, not all bacteria encode the same segregation proteins (see Table 1.3) and key players in some bacteria have been shown to be dispensable in others.

Table 1.3: Chromosome segregation machinery found in selected bacteria.
Adapted from (Pinho et al. 2013)

	Chromosome segregation				
	ParA	ParB	FtsK	Smc	MatP
<i>E. coli</i>	-	-	+	+ [¶]	+
<i>B. subtilis</i>	+	+	+	+	-
<i>C. crescentus</i>	+	+	+	+	-
<i>S. aureus</i>	-	+	+	+	-
<i>D. radiodurans</i>	+	+	+	+	-

[¶]In *E. coli* MukBEF is a functional analogue of Smc.

3.1. ParABS system, an active model for origin segregation

In some bacteria the chromosome partitioning system, the ParABS complex, has been identified as playing an active role in the segregation of the nucleoid *ori*-proximal region. Briefly, the canonical ParABS system, is composed of:

- ParB, a dimeric DNA binding protein capable of recognizing and binding to *parS*, forming the partition complex.
- *parS* is a centromere-like DNA palindromic sequence generally located close to the *ori* of chromosomes (Livny et al. 2007). Bacteria can possess from 1 (in *C. crescentus* (Toro et al. 2008)), to up to 24 *parS* sequences (in *M. xanthus* (Harms et al. 2013)). In *C. crescentus*, *parS* may also interact with DnaA. This interaction may alter the structure of DNA and promote ParB binding, thus hinting for a link between DNA replication and proper origin segregation (Mera et al. 2014).
- ParA is a Walker A type ATPase that forms dimers upon ATP binding. ParA-ATP binds DNA nonspecifically. Upon binding to the ParB:*parS* complex, its ATPase activity is stimulated, which releases ParA.

This ParABS system is still not totally characterized. Moreover, among bacteria differences in ParB concentrations, in ParA localization and possibly in function have been observed. Thus, different models of how ParABS system functions in chromosome segregation have been proposed. One of the latest models (Lim et al. 2014), in *C. crescentus*, proposed that the segregating effect of ParABS results from a “DNA-relay”. Simulations of this model relies on the existence of a ParA-concentration gradient in the cell (higher concentration at the new pole) and on the elasticity of the chromosomes. The partition complex will tend to encounter the DNA-bound ParA-ATP as they stretch toward the old pole. The elasticity of the chromosome makes the ParB:*parS* move in the direction of the new pole, similarly to a “sling”, where there is a higher concentration of DNA-bound ParA-ATP. Another model named “hitch-hiking” has been proposed based on 3D SR microscopy data on *B. subtilis* cells (Le Gall et al. 2016). It relies on the assembly of ParA-ATP patches in HDRs (high density chromosomal region, see “2.2 Micro- & macro-domain organization”). Upon binding to the ParB:*parS* complex, ParA patches dissociate from the DNA. The released ParA molecules are then freely diffusing in the cytoplasm until they reload ATP and assemble into new patches in neighbouring HDRs (this jumping of the ParA from one patch to another is the “hitch-hike”). After dissociating from ParA patches, the ParB:*parS* complex will continue to diffuse towards a proximal ParA-rich HDR, driving the segregation of the ParB:*parS* complex and hence of the chromosome.

Studies of the ParABS system also indicate that they may function differently in different bacteria. In some bacteria, the ParABS has been shown to be mandatory for chromosome segregation to proceed correctly. This is the case in *C. crescentus*, where the deletion of the ParABS system, results in an increased number of anucleate cells (Mohl & Gober 1997). In contrast, in *Vibrio cholera*, chromosomes still segregated after silencing of their ParABS system (Yamaichi et al. 2007). Moreover, although rare, some bacteria such as *E. coli* do not possess any ParABS system. A *parS*-like sequence called *migS* has been identified in *E. coli*, that helps chromosome segregation, but it has been shown not to be essential (Yamaichi & Niki 2004).

Interestingly, some coccoid bacteria such as *S. pneumoniae* and *S. aureus* lack the ParA protein. As in other bacteria, their ParB homologue (named Spo0J) localizes to their *ori*, where it binds to *parS* sites. Mutating these proteins induces anucleate cells, thus the ParB:*parS* complex alone can promote chromosome segregation in *S. pneumoniae* and *S. aureus* (Pinho et al. 2013). In *D. radiodurans*, chromosome I appears to encode for a complete ParABS system with 3 possible *parS* sequences (Charaka & Misra 2012), while the chromosome II and the two megaplasmids each encode a ParAB system (ParA2 (DR_A0001)/ ParB2 (DR_A0002); ParA3 (DR_B0001)/ ParB3 (DR_B0002); ParA4 (DR_B0031)/ ParB4 (DR_B0030)) but no *parS* sequences have so far been identified on these DNA replicons (Maurya et al. 2016).

3.2. Passive model for bulk chromosome segregation

The segregation of the just-replicated Ori region to different parts of the cell by the ParABS system might be the driving force (in a passive fashion) of the segregation of the rest of the bulk chromosome. However, as shown above, not all bacteria possess a ParABS system and silenced ParABS systems do not necessarily impair cell viability. These observations suggest the presence of other mechanisms for the segregation of chromosomes. Several hypotheses and factors have been proposed to provide different forces that contribute to chromosome segregation:

- Passive segregation might be a secondary effect of other mechanisms in the bacteria. For example, it has been proposed that the different extrusion forces generated on DNA for example by the replisome might power chromosome segregation (Lemon & Grossman 2001).
- Passive segregation could be a byproduct of cell elongation and anchoring of specific chromosome loci to the membrane. For example, coupled transcription, translation and insertion of an in-translation protein into the membrane (a phenomenon coined “transertion”), can serve as an anchor for the DNA-RNA polymerase-RNA-ribosome-peptide complex at the membrane. However, this anchoring seems unlikely to play an important role in *E. coli*, as no RNA synthesis is needed for the chromosome to segregate in this organism (Wang & Sherratt 2010). Another hypothesis is the coupling of *ori* anchoring to the membrane (as seen previously, PopZ and DivIVA serve as chromosome anchoring proteins in *C. crescentus* and *B. subtilis* respectively) with the growth of specific zones of the cell wall. However, zonal growth of the cell wall is not seen in all species and cannot explain the fast speed of loci movement compared to that of cell growth (Toro & Shapiro 2010).
- Factors affecting chromosome organization might also promote chromosome segregation. For example, the decatenation of interlinked chromosomes, or the

supercoiling of DNA mediated by topoisomerases (Topo) is believed to play a role. Indeed, mutations of Topo IV, Topo I, or DNA gyrase can induce defects in chromosome segregation and increase the proportion of anucleate cells (Badrinarayanan et al. 2015; Nguyen et al. 2009).

- NAPs, such as HU or SMC proteins, that contribute to the compaction of the DNA might also help to separate the newly replicated chromosome copies. In *E. coli*, the absence of HU results in an increased formation of anucleate cells, indicating an impaired chromosome segregation process (Huisman et al. 1989). Moreover, NAPs and SMC complexes might serve as enhancers of an entropy-driven segregation. Thus, replicated daughter chromosomes might spontaneously disentangle and repulse each other, promoting chromosome segregation (Jun & Wright 2010). The SMC complex also seems to play a role in the segregation of *ori* by the partition complex. It has been shown in *E. coli* and *B. subtilis* that the SMC complex colocalizes with regions close to *ori* and seems to be necessary for proper segregation of the origins (Danilova et al. 2007; Sullivan et al. 2009). More recently, in *B. subtilis*, it was shown that the SMC complex actually targets ParB/*parS* loading sites (Minnen et al. 2016). It is also noteworthy that the deletion of genes coding for the components of the SMC complex results in altered viability and poor growth of rod-shaped bacteria (Pinho et al. 2013). However, in cocci, it results in only minor phenotypic alterations and a small fraction of anucleate cells (La Tour et al. 2009; Pinho et al. 2013).

3.3. Segregation termination

We have presented above the different mechanisms that may segregate *ori* and the bulk of the chromosome, however, other mechanisms seem to explain *ter* segregation and its different segregation choreography. During DNA replication, the terminal regions tend to locate at midcell (*i.e.* at the future position of septal division). Improper segregation or chromosome dimerization resulting from homologous recombination events can cause *ter* to remain trapped at midcell (Espinosa et al. 2017). As a result, the terminal regions of chromosomes may be guillotined and broken by the closing septa. Cells have developed two different strategies to prevent this from happening: (i) they possess a mechanism that ensures the synchronization of chromosome segregation and cytokinesis, and (ii) they possess a machinery capable of inducing the segregation of the Ter region just before the final scission of the cells and also capable to eventually correct non-resolved chromosomes.

The first machinery delays the formation of the dividing septum until most of the chromosomal regions have been fully segregated. This delaying mechanism, known as “nucleoid occlusion”, is described later in “4.2.2 Nucleoid Occlusion”.

The second machinery is based on the highly conserved protein FtsK, also known as SpoIIIE in *B. subtilis* (see Table 1.3), which serves as a translocase (Figure 1.13 A). It

can decatenate chromosomes by stimulating Topo IV (Figure 1.13 B) and can activate the recombinase machinery, if needed (Badrinarayanan et al. 2015). The FtsK protein is able to pump the DNA away from the center of the cell, towards daughter cell compartments, just before the final scission. This pumping has been suggested to play a role in bulk chromosome segregation. FtsK is localized at midcell with other cell division proteins, reviewed in (Badrinarayanan et al. 2015; Espinosa et al. 2017). The protein is able to specifically bind to small DNA regions (6-8bp), called FtsK-orienting polar sequences (KOPS), which define the direction of the translocase activity towards a terminal defined site (*dif*). By bringing the different *dif* loci of the chromosomes closer together, FtsK can help decatenate chromosomes (Figure 1.13) as well as resolve aberrant chromosome conformations (Figure 1.14).

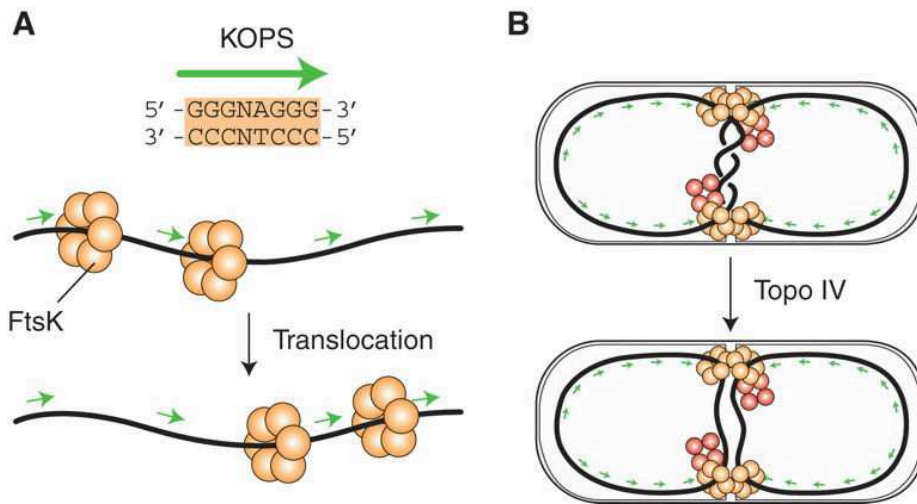


Figure 1.13: Role of FtsK in the decatenation of chromosomes during segregation termination. A) Hexameric rings of FtsK can load on the DNA and translocate in the direction defined by the polarity of KOPS shown as green arrows. B) Due to the translocase activity of FtsK the catenates are located at midcell. FtsK interacts with the tetrameric Topo IV (shown as red disks), which catalyzes the unlinking of the two chromosomes. Adapted from (Thanbichler 2010).

RecA-mediated homologous recombination, which can be induced by DNA damage during the replication, can lead to the formation of chromosome dimers, an aberrant chromosome conformation. **Figure 1.14** illustrates how a chromosome dimer can be resolved through the action of FtsK. Once the *dif* loci are colocalized, FtsK is able to induce the correction of non-resolved chromosomes by activating the XerCD recombinases on the two *dif* sites. In the case of bacteria with multiple chromosomes, like *V. cholera* (2 chromosomes), the different chromosomes harbor different *dif* sites in order to be used by the same Xer/FtsK machinery.

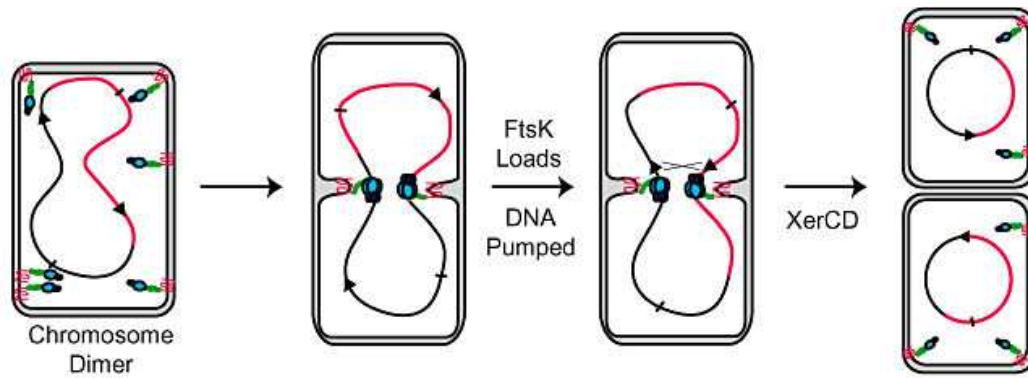


Figure 1.14: Resolution of chromosome dimers in *E. coli*, an aberrant chromosome conformation. The two daughter chromosomes are represented in black and in red. The chromosome dimer is represented as a single large chromosome with a red and a black region. The DNA cannot be resolved until FtsK loads and pumps the DNA through its translocase activity, in order to colocalize the different *dif* sites (represented by an arrow on the DNA), enabling its recombination of the dimer into two monomers by the XerCD recombinases. Adapted from (Kennedy et al. 2008).

3.4. Segregation in *D. radiodurans*

In *D. radiodurans*, little is known regarding chromosome segregation and most of the available knowledge has been provided by a single study (Passot et al. 2015), in which three loci (*ter* and *ori* sites and a defined locus at 268° on the left replicore) of chromosome I were fluorescently tagged and observed as “foci” (Figure 1.15). The authors show that the multipartite genome of *D. radiodurans*, which is present in 4 to 10 copies per cell, displays a variable number of these defined loci, which are dispersed throughout the cell. Multiple (5-9) *ori* and (4-7) 268° foci were seen per cell, in contrast to *ter* sites that were present in fewer copies (2-4). In exponentially growing cells, the number of these foci increased as a function of cell size. During the division into daughter cells, some heterogeneity in the genome ploidy was observed. It was proposed that this results from an uncoordinated segregation of the different chromosome I copies. During cell division, the *ori* and 268° loci seemed to segregate more in the two lobes of the nucleoid which would be separated in the two future daughter cells and to be excluded from the future new septum area. A similar distribution of *ter* sites was also observed in the cells where more than 4 *ter* foci were present. However, in cells with only one or two *ter* foci, the *ter* sites were found to preferentially locate to a region close to the upcoming cell division axis, *i.e.* where the upcoming septum will be formed. Altogether, these observations point towards a progressive duplication and segregation of loci along the chromosomes. Thus, the early loci such as *ori* and the 268° locus are duplicated and even segregated before duplication of *ter*.

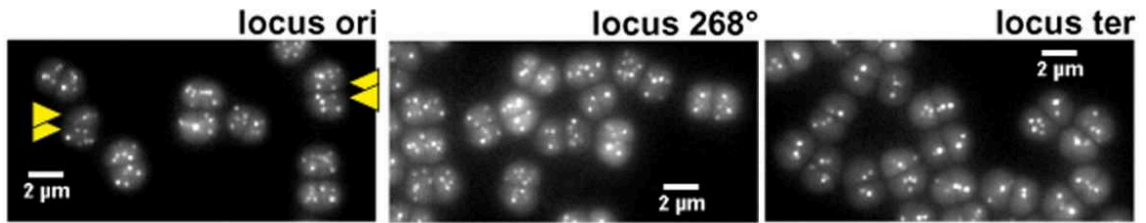


Figure 1.15: Loci cartography in *D. radiodurans* cells. Cells express ParBc2Bc-GFP with *parSc2Bc* inserted at the indicated loci (*ori*, 268° or *ter*). Yellow arrows: daughter or dividing cells containing unequal number of *ori* foci. Adapted from (Passot et al. 2015).

4. Bacterial cell division

4.1. Rod vs. (ovo)cocci division

Most of our knowledge regarding nucleoid organization and segregation comes from the study of model bacteria that are essentially rod-shaped. In contrast, these processes are only poorly characterized in cocci. Similarly, little is known about bacterial cell division in cocci.

- Peptidoglycan synthesis and cell division

Bacterial cell walls are able to withstand the turgor pressure arising from the osmotic flow, due to a difference in solute concentration between the medium and the bacterial cytoplasm. While resisting this pressure, the cell walls need to remain flexible enough to permit cell growth and its associated changes in cell shape. Among the different layers that compose the cell wall, the peptidoglycan (PG) is the major structural component of the cell wall and is responsible for maintaining the cell shape. PG synthesis ensures that the two daughter cells will be identical to the mother cell. This is achieved by two processes: the peripheral growth of the mother cell and the division by septation into two daughters, reviewed in (Pinho et al. 2013).

The elongation in rod-shaped bacteria is responsible for their doubling in size, just before their division by septation. During the elongation, bacteria usually synthesize a new PG layer at the non-polar region. The ATPase, MreB, regulates the molecular machinery that is responsible for PG synthesis during elongation. MreB is an actin homolog that polymerizes upon ATP binding (Jones et al. 2001). MreB forms filaments inside cells, which bind to the cytoplasmic membrane (Dempwolff et al. 2011; Salje et al. 2011). In *B. subtilis*, MreB has been suggested to be coupled with penicillin-binding-proteins (PBPs) through its interactions with the transmembrane proteins MreC and MreD (Leaver & Errington 2005). Interestingly, in *E. coli* cells, MreB has been shown to interact with Topo IV and stimulate its DNA decatenation activity to facilitate chromosome segregation. This clearly illustrates the interplay and synchronization between chromosome segregation and cell division (Madabhushi & Mariani 2009).

In ovococci, such as *Streptococcus pneumoniae*, PG synthesis for cell elongation is less pronounced compared to PG synthesis for the septation. This difference is responsible for the ovoid shape of ovococci (Zapun et al. 2008). PG synthesis for cell elongation occurs at midcell and has been proposed to be regulated by FtsZ, a key GTPase protein that is implicated in septation in many bacteria, including rod-shaped, ovococci and cocci bacteria. FtsZ (Table 1.4) is a tubulin homolog, that polymerizes upon GTP binding into a Z-ring at midcell (Pinho et al. 2013). This Z-ring serves as a scaffold for the binding of the different constituents of the divisome including the PBPs. FtsZ may

serve as an organizer and coordinator of the elongation and septation machinery (Pinho et al. 2013).

Table 1.4: Elongation and septation proteins found in selected bacteria. Adapted from (Pinho et al. 2013)

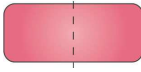

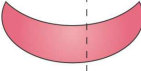
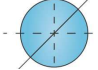
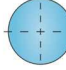
	Elongation and septation			
	MreB	MreC	MreD	FtsZ
<i>E. coli</i>	+	+	+	+
<i>B. subtilis</i>	+	+	+	+
<i>C. crescentus</i>	+	+	+	+
<i>S. aureus</i>	-	+	+	+
<i>D. radiodurans</i>	-	-	-	+

Ovococci thus have an FtsZ-dependent elongation and septation machinery, while cocci seem to possess only the FtsZ-dependent septation machinery. Indeed, cocci do not encode any MreB homologs (see Table 1.4). However, recent studies have shown that in *S. aureus*, PG synthesis does not only take place in the septal region. In fact, its synthesis occurs all over the cell surface and throughout the cell cycle before septation (Monteiro et al. 2015). This actually would translate into cell enlargement before the septation. This has been observed in *S. aureus* thanks to the advent of SR imaging (see “7 SR fluorescence microscopy”). The latest model of *S. aureus* growth suggests that the bacteria possess a single PG synthesis machinery that would move from the cell periphery (where it synthesizes PG during the initial phase of the cell cycle) to the future site of division, where PG will also be synthesized for the septation (Monteiro et al. 2018). In this model, in the initial phase, FtsZ treadmilling would be the force that would induce the initial invagination of the cell wall, whereas PG synthesis during septation would drive cytokinesis.

- Planes of Division

Equatorial division is a common feature of many rod-shaped and ovococci bacteria, occurring over successive division cycles (Pinho et al. 2013) (see Table 1.5). The core mechanisms of this division site placement are described in the following paragraph “I.4.2 Division site selection and cytokinesis”). Unlike other model bacteria, *C. crescentus* does not divide equatorially, but asymmetrically.

Table 1.5: Shapes and division planes of various bacteria. Adapted from (Pinho et al. 2013). Red and blue indicate Gram-negative and Gram-positive species, respectively. The dashed lines represent division planes.

Shape & division planes	
<i>E. coli</i>	
<i>B. subtilis</i>	
<i>C. crescentus</i>	
<i>S. aureus</i>	
<i>D. radiodurans</i>	

Cocci, on the other hand, divide in more than one plane. For example, *S. aureus* divides in three orthogonal planes over the successive division cycles (Monteiro et al. 2015). How *S. aureus* is capable of retaining the information necessary to divide in three successive orthogonal planes is still unclear. One hypothesis relies on the use of the PG “scars” that are visible at the surface of the bacteria as markers. Moreover, in *S. aureus*, the splitting into two daughter cells and the reshaping of the flat septum into a hemisphere is very fast (on the order of milliseconds).

4.2. Division site selection and cytokinesis

As we have seen, cytokinesis requires the assembly of the divisome machinery responsible for septation together with polymerization of FtsZ to form the Z-ring. Bacteria have developed different strategies in order to ensure the precise localization of the division site.

At least three different strategies have been identified so far, relying on independent negative regulators: the Min system, the MipZ system (MipZ has a similar function to Min but is not homologous to Min) and the nucleoid occlusion (NO) system (see Figure 1.16).

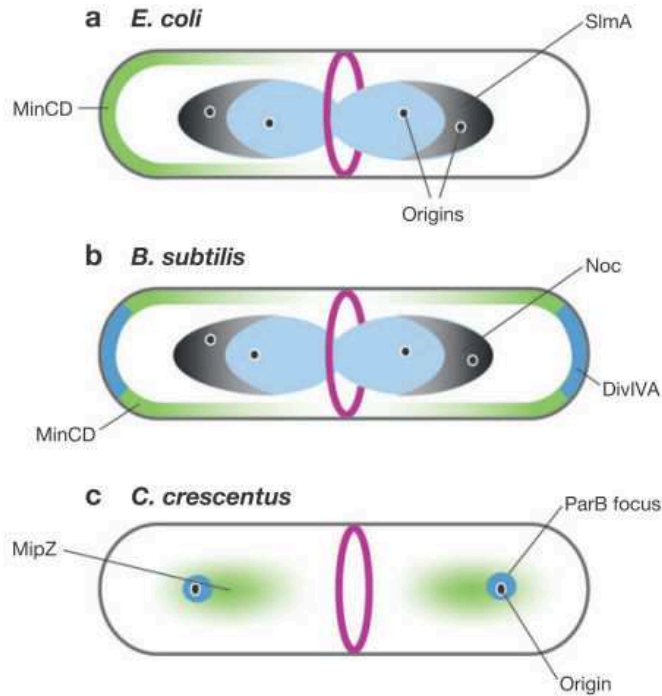


Figure 1.16: Schematic representation of the division site selection process (i.e. the positioning of the Z-ring in violet) by different gradients of FtsZ regulators in *E. coli*, *B. subtilis* and *C. crescentus*. See text for greater detail. Adapted from (Lutkenhaus 2007).

The Min and the MipZ systems prevent the formation of the Z-ring in aberrant locations, such as cell poles, and the NO system prevents the occlusion on the nucleoid. These two different functions cooperate in some cells, in order to ensure that cytokinesis occurs at midcell, once the two duplicated nucleoids are correctly segregated. Bacteria encode different sets of division site proteins (see Table 1.6). For example, in *E. coli*, the division site is regulated by two gradients determined by the MinCDE system (Min system) and the SmlA protein (NO system). In *B. subtilis*, it is regulated by the MinCDJ/DivIVA system (Min system) and the Noc protein (NO system). In *C. crescentus*, only one gradient of MipZ/ParB complex (MipZ system) seems to regulate the division site selection. Thus, bacteria have developed different, but analogous, systems for the selection of the division site, and other unidentified systems may remain to be discovered.

Table 1.6: Division site selection proteins found in selected bacteria. Adapted from (Pinho et al. 2013).

	Division site selection			
	DivIVA	Min*	MipZ	NO
<i>B. subtilis</i>	+	+	-	+
<i>S. aureus</i>	+	-	-	+
<i>E. coli</i>	-	+	-	+
<i>C. crescentus</i>	-	-	+	-
<i>D. radiodurans</i>	+	+	-	-

NO: nucleoid occlusion system involving SlmA in *E. coli* and Noc in *S. aureus* and *B. subtilis*.* In *E. coli* and in *D. radiodurans*, the Min system consists of MinCDE, whereas in *B. subtilis* it consists of MinCDJ.

4.2.1. Min/MipZ System

In *E. coli*, the Min system is the major regulator of division site placement (Figure 1.17 A), by preventing the aberrant polymerization of FtsZ into Z-rings at the poles (Lutkenhaus 2007). The Min system is composed of three proteins of distinct functions:

- MinD, an ATPase, able to bind to the membrane where it recruits MinC.
- MinC is an inhibitor of FtsZ, that blocks the Z-ring formation.
- MinE is the regulator of MinCD, by stimulating the ATPase activity of MinD to release MinD and MinC from the membrane.

MinD binds to the cell membrane at the poles and recruits MinC, which prevents FtsZ polymerization. Then MinE triggers the release of MinCD from the membrane allowing them to diffuse into the cytoplasm, where MinD's ATPase capabilities are regenerated. Then a new cycle can start again. However, a difference exists between two consecutive iterations of the cycle: MinD will bind to the opposite pole of the cell, where the concentration of MinE is lower. Overall, MinCD oscillates from one side of the cell to another on a time scale of seconds (Raskin & De Boer 1999). This creates a gradient of MinC, the FtsZ inhibitor. Thus, the formation of the Z-ring is more prone to occur at midcell than at the poles as the mean concentration of MinC overtime appears to be the lowest in this region.

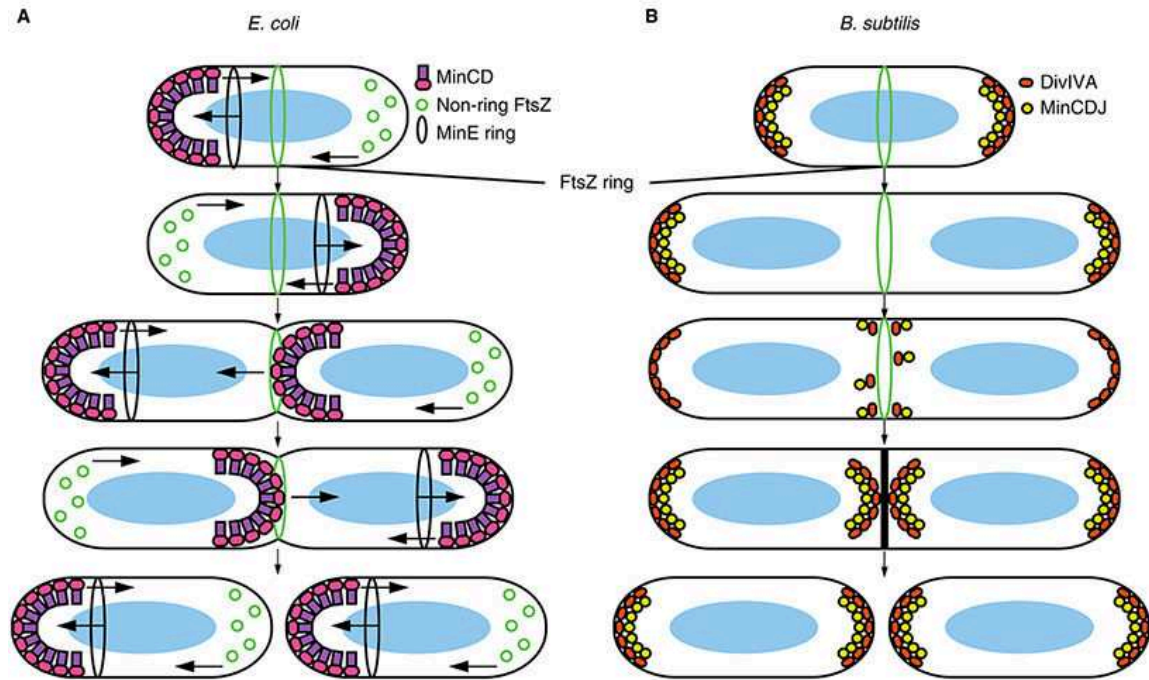


Figure 1.17: Schematic representation of Min systems during the cell cycle of *E. coli* (A) or *B. subtilis* (B). See text for greater detail. Adapted from (Rowlett & Margolin 2013).

During the later stage of cell division, when the newly generated septum is almost closing, MinCD pauses at midcell, possibly to distribute the MinCD material equally in each daughter cells and help the septal constriction. This would also be a means of preventing the formation of additional Z-rings in the proximity of the already existing one. Subsequently, two distinct oscillating MinCD gradients appear in the daughter cells (see Figure 1.17 B) (Rowlett & Margolin 2013).

Interestingly, in *B. subtilis*, MinCD does not oscillate and lacks MinE. MinD is in fact recruited by MinJ protein, which is itself recruited by DivIVA to specific membrane localizations (cell poles, but also at the division septum, as DivIVA is recruited to membranes with high curvature). This results in the formation of two gradients of MinC in *B. subtilis*, that guide FtsZ polymerization at midcell. Moreover, as in *E. coli*, the Min system of *B. subtilis* also prevents the formation of additional Z-rings close to the existing one used for the cell division (Rowlett & Margolin 2013). Defects in MinCD induce Z-ring assembly at the poles leading to anucleate mini-cells. In addition, in *E. coli*, defects in MinE result in long filamentous cells (Boer et al. 1989).

In *C. crescentus*, MipZ is a protein that serves a function similar to that of MinD (both belong to the ParA family of ATPases despite not being homologs). MipZ is an FtsZ polymerization inhibitor that is distributed in a gradient fashion towards the two opposite poles through interactions with ParB during the whole cell cycle of *C. crescentus* (see Figure 1.18) (Thanbichler & Shapiro 2006).

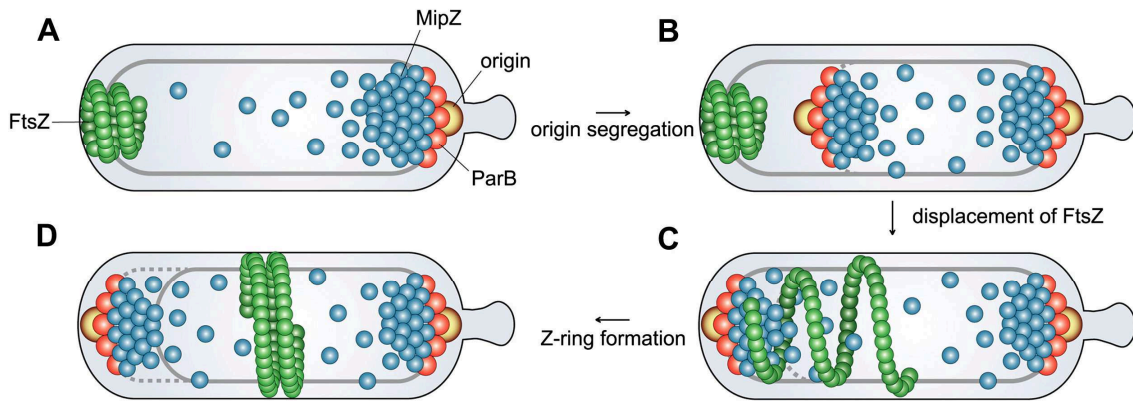


Figure 1.18: Model of the displacement of MipZ, FtsZ and ParB during the cell cycle of *C. crescentus*. A) The *ori*-MipZ-ParB complex is located at one pole while FtsZ is localized at the opposite pole. B) After replication initiation and the duplication of *ori*, one of the *ori*-MipZ-ParB complexes segregates towards the opposite pole. C) As the *ori*-MipZ-ParB complex reaches the other pole, a MipZ concentration gradient appears in the cell, with low levels at the center of the cell and higher levels at the cell poles. This leads to the displacement of FtsZ towards midcell and D), to the formation of the Z-ring. Adapted from (Thanbichler & Shapiro 2006).

4.2.2. Nucleoid Occlusion

One of the systems used by bacteria to accurately direct the localization of the division plane is the nucleoid occlusion (NO) system which prevents the division from occurring over the nucleoid (Wu & Errington 2012). This occlusion is tightly coupled with chromosome segregation, as it delays cytokinesis until most of the chromosome regions have been fully segregated to different compartments of the future cells (*i.e.* not at the midcell anymore). This process limits the risk of breakage of the chromosome by the dividing septum.

E. coli NO prevents the formation of the septum over the bulk chromosome, through the action of the SlmA protein, which is able to block the polymerization of FtsZ (Bernhardt & De Boer 2005). By binding to palindromic DNA sequences mostly scattered in the first half of the chromosomes, SmlA actively delays the assembly of the division machinery at midcell, until most of the chromosomes are also segregated to the opposite poles of the daughter cells (see Figure 1.19).

In *B. subtilis*, a protein Noc, also able to bind a specific DNA sequence (also localized mostly in the first half of the chromosome), plays a similar function, but does not prevent the polymerization of FtsZ. Instead, it seems to form large complexes, which obstruct the formation of the divisome (Badrinarayanan et al. 2015).

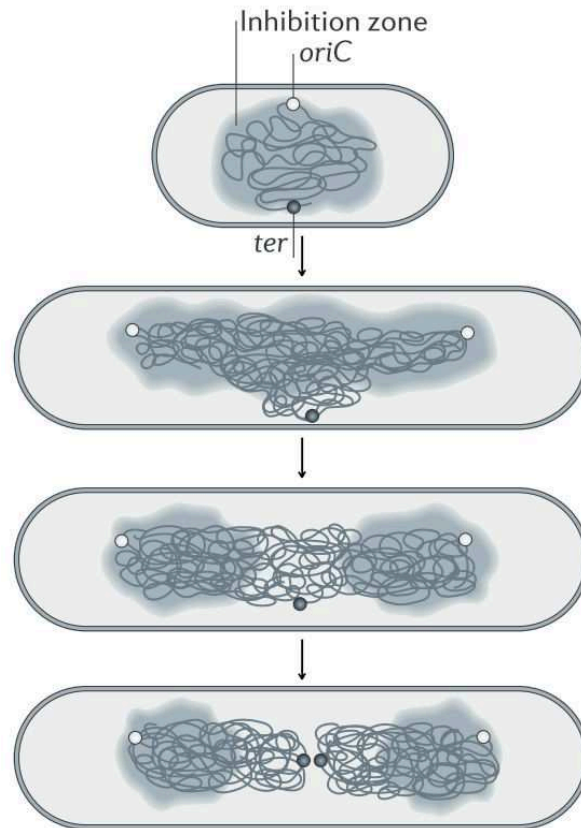


Figure 1.19: Schematic representation of SlmA protein position (in dark gray) during the nucleoid segregation occurring during *E. coli* cell cycle. Adapted from (Pinho et al. 2013)

In *E. coli* or *B. subtilis*, unless combined with other defects in the cell cycle (replication, segregation, division), NO systems are not essential and their inactivation does not lead to noticeable phenotypes (Wu & Errington 2012). As mentioned earlier, defects in Min system, however, induce a loss of cell viability, suggesting that Min systems in rod bacteria might be sufficient for blocking cell division until chromosome segregation is complete and distant from midcell.

S. aureus possesses a NO system, but no Min system, which suggests the NO system (Noc) may play a more important role in the localization of the cell division site in these bacteria. Indeed, its deletion results in some cells presenting multiple Z-rings or oblique Z-rings and an increase in anucleate cells, or in cell size, or in DNA breaks (Veiga et al. 2011). However, these findings also reveal that Noc is not essential for *S. aureus* viability (Pinho et al. 2013), hinting for the possible existence of other unidentified division regulators. Interestingly, in this bacterium, the Noc protein has also been reported to play a role in the initiation of DNA replication as well as in the coordination of chromosome segregation and cell division, which adds another layer of connection between cell division and chromosome dynamics (Pang et al. 2017). It is noteworthy to mention that unlike *S. aureus*, *D. radiodurans* possesses a Min system but no identified

NO system (Table 1.6), which clearly indicates that cocci may have developed different strategies to correctly determine the position of their division sites.

4.2.3. Other Putative Regulators

Interestingly, some bacteria do not possess any of the three systems presented above, others might possess subsets of these three systems, and in some cases these subsets may be dispensable for correct Z-ring placement. Indeed, in cells possessing both a Min system and a NO system (such as *E. coli* or *B. subtilis*), the silencing of both of these systems does not impede the formation of Z-rings around midcell (Bernhardt & De Boer 2005). Altogether, these observations suggest that other unidentified regulators are likely to intervene in the precise Z-ring localization.

A recent study proposed that chromosomal replication/segregation and division site positioning might be even more interconnected than previously thought. For example, in *S. pneumoniae*, it was shown that at the beginning of the replication, the *ori* was localized to the future septum position and that the replication actually initiates at the same time as the Z-ring is formed (Raaphorst et al. 2017). Moreover, this study also showed that SMC was required for the segregation of chromosome origins and was timely coordinated with Z-ring formation. In *S. aureus*, as in *S. pneumoniae*, a direct link between replication, chromosome segregation and cytokinesis was recently found (Pang et al. 2017). These observations regarding the high levels of coordination between different cellular processes suggest that previously characterized factors playing roles in other cellular processes may also be putative regulators of cytokinesis.

The DivIVA-ParB complex in *S. pneumomiae* has also been proposed to regulate division site placement. Indeed, this complex appears to anchor the origin of the just segregated chromosomes to the daughter cell poles (Fadda et al. 2007). This may affect in turn the positional regulation of the Z-ring formation. Interestingly, cocci that lack the Min system, generally possess the DivIVA protein and in the case of *S. pneumomiae*, it is an essential protein: its inactivation leads to a slower growth of the cell, forming chains of cells with some unclosed septa (Fadda et al. 2003).

Study of non-model bacteria also revealed possible regulators. For example, in *Myxococcus xanthus*, unlike all the presented negative regulators presented so far, a positive regulator system was found, PomXYZ. Clusters of PomX/Y act as sinks for PomZ, which binds to the nucleoid. The resulting PomZ flux ultimately leads to the accumulation of the PomXYZ complex at midcell, which stimulates the formation of the Z-ring (the mechanism of stimulation is not yet understood) (Surovtsev & Jacobs-Wagner 2018).

4.2.4. Direction of Division in Cocci

In rod-shaped bacteria, different mechanisms determine the site of division. As a whole plane is devoid of negative regulators of Z-ring formation, this also determines the direction of the division plane. However, determining the division plane direction in cocci is less well understood. Indeed, several cocci only possess one or no negative regulator of Z-ring formation and yet can divide in two or three alternating and orthogonal planes. Importantly, during this process, cocci temporarily lose their spherical symmetry. This is the case in *D. radiodurans*, which remains as diads or tetrads during its cell cycle. Several hypotheses have been proposed to explain these observations:

- As we have seen previously, entropic forces may regulate chromosome segregation. It is possible that these forces are also responsible for the observed alignment of the nucleoid parallel to the newly forming septum. For example, in *S. aureus* which possesses a Noc protein, the alignment of the chromosome to the division septum induces an orthogonal plane to the nucleoid at midcell. This plane has a lower concentration of Noc, which may guide the future orthogonal division plane (Pinho et al. 2013).
- MapZ, a protein that was thought to play the role of a FtsZ regulator is now believed to actually control the perpendicular formation of the division plane in *S. pneumoniae* (Raaphorst et al. 2017).
- In the case of mutant *E. coli* that are engineered into spheres (*rodA* mutants), the oscillations of the Min complex are stochastic in symmetrical cells. However, as soon as an asymmetrical feature appears (for example the beginning of the constriction of the sphere), the MinCD complex moves along the long axis of the cell. At the end of the division, the oscillations are parallel to the growing septum which is now the new long axis of the two daughter cells. An orthogonal plane to this long axis will on average have a lower concentration of Min complex and be the site of the next division. Thus the spherical *E. coli* also display alternating orthogonal division planes (Corbin et al. 2002).

4.3. *D. radiodurans* cell division

D. radiodurans is conventionally grown in tryptone, glucose and yeast extract medium (TGY) at a temperature of 30-32°C, with aeration, leading to a doubling time around 100 min. In TGY, *D. radiodurans* mainly forms dyads in early stages of growth and tetrads in late ones (Daly et al. 2004).

In response to different environmental conditions, *D. radiodurans* displays pleomorphic capabilities as it adopts different morphologies. This variation is attributed to nutrition induced pleomorphism (Joshi & Toleti 2009). For example, the concentration of cations such as Na, Li, Mg and Ca, also plays a role in the population

aggregation. The addition of salt to the culture medium shifts the diad/tetrad proportions, and cells were even seen to continue dividing without separation, thus forming multimers of 16 or 32 cells (Chou & Tan 1991). It was also reported that *D. radiodurans* grew as monomers in low nutrient concentration medium (TGY diluted 100 times) (Joshi & Toleti 2009). In this low nutrient medium, *D. radiodurans* might increase its survival by adapting its morphological forms to monomers, as it increases the cell surface to cell volume ratio of the cells, which might increase its nutrient uptake capabilities (Joshi & Toleti 2009). Interestingly, at this low nutrient concentration, a budding mode of reproduction of *D. radiodurans* was also reported (Joshi & Toleti 2009).

D. radiodurans cells divide sequentially in two perpendicular planes leading to tetrads (Murray et al. 1983; Thornley et al. 1965) (Figure 1.20 A). During division, two opposite division sites appear, from which septal growth will take place, growing towards each other. This septal growth has been reported to occur via a mechanism reminiscent of closing automatic doors, and not like a diaphragm (Murray et al. 1983). The newly forming septa are only composed of plasma membrane and PG layers (Figure 1.20 B). The other layers are only present when the cell wall is at the periphery of the cell. When the two growing septa meet, they form a double-layered cell wall that separates the mother cell into two daughter cells. It has also been hypothesized that the increase of *D. radiodurans* size during its cell cycle occurs both by an increase of the peripheral wall area and the thickening of the septal wall (Murray et al. 1983).

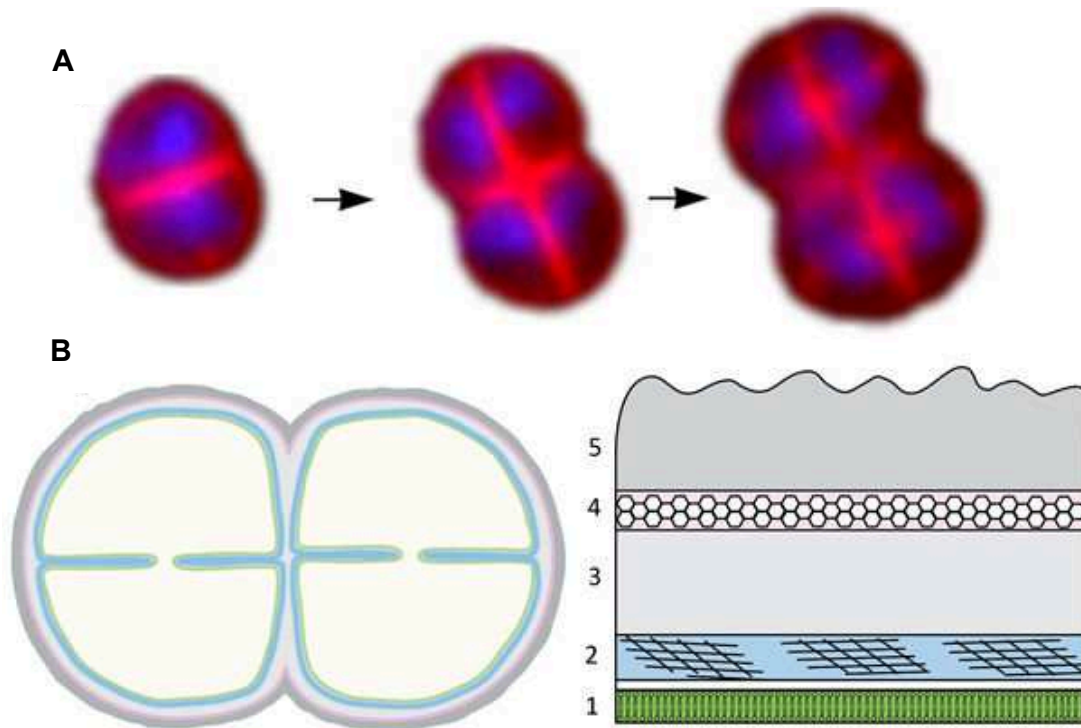


Figure 1.20: *D. radiodurans* cell growth and schematic representation of the cell wall structure of *D. radiodurans*. A) Cells grown in TGY at 30°C monitored by time-lapse fluorescent microscopy starting from a single diad. The DNA is stained with 4',6-diamidino-2-phenylindole (DAPI) and appears in blue, the lipid membrane is stained with FM-4-64 and appears in red. Adapted from (Slade & Radman 2011). B) The complex cell wall structure of *D. radiodurans* is composed of five distinct layers: 1, plasma membrane (green); 2, peptidoglycan layer (blue); 3, interstitial layer (light grey); 4, S-layer or backing (pink) composed of proteins, lipids and carotenoids; 5, carbohydrate layer (dark grey). The thickness of *D. radiodurans* cell wall is estimated to be between 75 and 150nm (Rothfuss et al. 2006; Slade & Radman 2011).

II

Overview of fluorescence microscopy

As revealed in the previous chapter, although research on (i) nucleoid organization, (ii) chromosome segregation and (iii) bacterial cell morphology during bacterial division were initiated several decades ago, the relatively small size of bacteria has represented a major bottleneck for their studies in optical microscopy. We showed in the previous section several contributions of super-resolution fluorescence microscopy on these three topics. As it is the major tool used during this PhD, this new field of fluorescence microscopy is described in the following section.

1. Optical microscopy

Optical microscopy relies on the use of visible light and a system of lenses to magnify objects. In biological applications, observation of several micron thick samples are possible with visible light. This technique is also able to examine a wide variety of entities (e.g. tissues, cells, molecules), as well as their dynamics (e.g. tissue development, cell cycle, molecular diffusion) (Figure 2.1), with relative ease. It is less invasive than electron-based microscopy and enables observing cells kept in culture (for the observation of events occurring on large time scale). Optical microscopy can be divided into bright-field and fluorescence microscopy. The extensive use in life science of fluorescence microscopy relies on the possibility to label targets with high specificity. However, optical microscopy is limited in resolution. This limitation was first described by Ernst Abbe in the 1870s. It is only recently that it has been bypassed by “super-resolution” microscopy, with “tricks” presented later on.

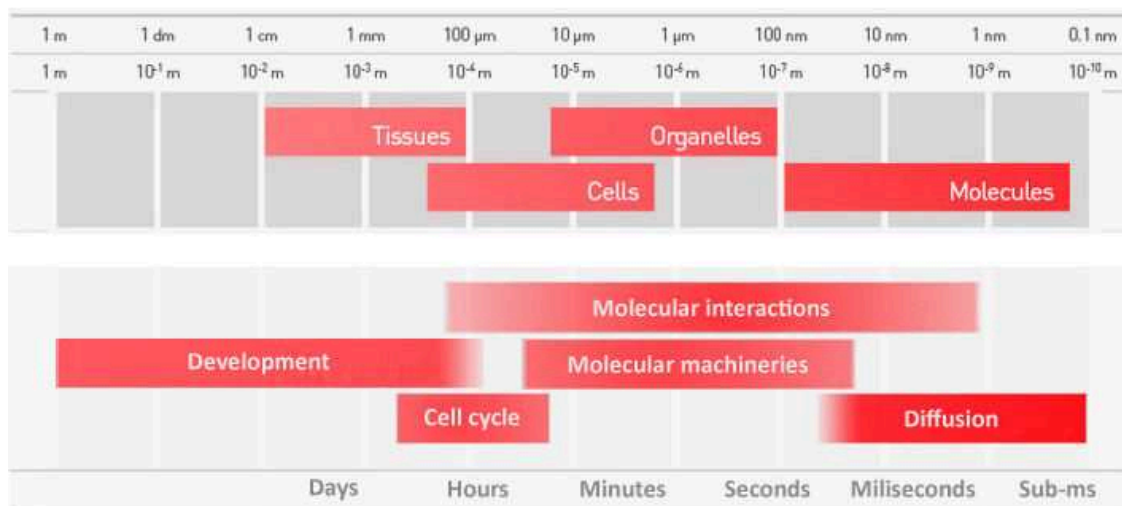


Figure 2.1: General scales of times and sizes in biology. To each range of sizes and times, corresponds specific biological materials with different dynamic behaviors, studied using different kinds of microscopes. Adapted from (Liu et al. 2015) and <https://www.thermofisher.com/fr/fr/home/life-science/cell-analysis/cell-analysis-learning-center/molecular-probes-school-of-fluorescence/fundamentals-of-fluorescence-microscopy/epifluorescence-microscope-basics.html>

2. History of fluorescence microscopy

In the 13th century, magnifying glasses were used to produce a magnified image of an object, but were relatively expensive and considered as a hobby for rich people. Most of the early uses of magnifying devices in science were focused on astronomy. It is not until the 1660-70s that Robert Hooke and Antonie Van Leeuwenhoek used microscopy for the first biological studies. Robert Hooke published “Micrographia” (1667). Using a 50x compound microscope (i.e. made of several lenses), he drew the first observations of a plant cell and coined the “cell” term. Van Leeuwenhoek used a simpler microscope made of a single lens with an achievable magnification of up to 250x. He was the first to observe bacteria in 1683. Fluorescence was first observed in 1845, by Sir John Frederik William Herschel, from a quinine solution under sunlight and the term “fluorescence” was coined in 1852 by Sir George Gabriel Stokes due to his studies on the fluorescence exhibited by fluorite/fluor spar. Ernst Abbe in 1873, for Zeiss, provided the scientific tools to foster mass production microscopes with reduced aberrations, thanks to calculation and not trial and error as it was the case before.

Unlike Van Leeuwenhoek single-lens microscopes, compound microscopes enable using advanced illumination set-ups. For example, Koehler introduced the “Koehler illumination” (1893) that is still largely used nowadays. In contrary to prior illumination scheme, the "critical illumination", it enables to observe objects without the perturbation of having the image of the light source in the field of view. Different techniques were developed to enhance the contrast of samples: phase contrast microscopy, by Zernike (1933) and differential interference contrast, DIC, by Nomarski (1952).

Another method to boost the contrast of biological samples is through the use of “tags”. The first ones used were stains, long before fluorescent tags. Different stains could be used to differentiate compartments of cells as they had different staining capabilities and light absorption properties. Otto Heimstaedt and Heinrich Lehmann (1911- 1913) used the first fluorescence microscope which relied on the autofluorescence of samples. They studied for example bacteria and animal tissues. Fluorescence microscopes were then used for a long time with chemical dyes. Stanislav Von Prowazek (1914) first used fluorescence microscopy to study dye binding to living cells and Albert Coons (1941) was the first to develop the immunofluorescence technique by labeling antibodies with fluorescein. Finally, the discovery of a green fluorescent protein, GFP, from the jellyfish *Aequorea Victoria* (1961) by Osamu Shimomura, paved the way to fluorescence microscopy based on the labeling of a target by a fluorescent protein, all expressed endogenously by the cells.

3. Fluorescence

Fluorescence like phosphorescence is a (photo-)luminescence phenomenon, generated by an exterior source of light. Other luminescence effects can occur, depending on the origin of the excitation, chemical (chemiluminescence) or thermal (thermo-luminescence) excitation. All of these emitting light materials have in common that their luminescence is due to a change of energy level of their excited electrons. This change can be described by the Perrin-Jablonski diagram, which represents the possible electronic states and their transitions between their ground states and their excited states, and the associated radiative and non-radiative transitions (Figure 2.2).

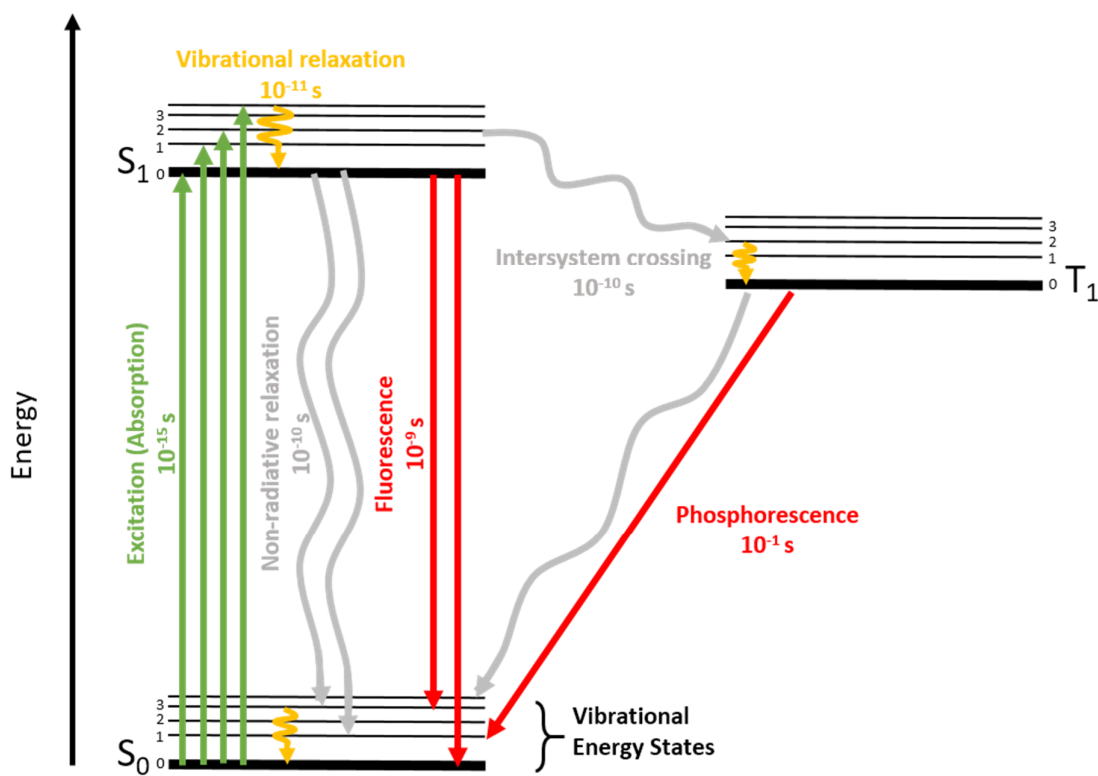


Figure 2.2: Simplified Perrin-Jablonski diagram. Horizontal lines represent energy levels. For each electronic states, bold lines are the vibrational ground states and thinner ones are possible vibrational levels. The horizontal lines are arranged vertically by energy and horizontally by total spin number (see later). Radiative transitions are indicated by straight arrows, gray for absorption, red for fluorescence or phosphorescence. Non-radiative relaxations are indicated as wiggling grey arrows and vibrational relaxation in yellow wiggling arrows.

In a Jablonski diagram, the different electronic states of a molecule are represented in vertical. S_0 being the ground state of the molecule, $S_{1...n}$ the different excited singlet states and $T_{1...n}$ the different excited triplet states. For each electronic state, the vibrational ground states are labeled by a 0 and higher vibrational states are labeled with 1, 2...n.

When a photon with a particular energy (corresponding to a possible energy difference between the ground and excited states) interacts with a molecule the photon may be absorbed, causing an electron to change its orbital and the molecule shifts to an excited state of the same total spin number (0), such as S_1 . Non-radiative relaxation of S_1 state can occur by internal conversion between electronic states of same total spin number (e.g. $S_1 \rightarrow S_0$) or by intersystem crossing between electronic states of different total spin number (e.g. $S_1 \rightarrow T_0$). The excited triplet states, $T_{1..n}$, have a total spin number of 1. The triplet states energy levels are degenerate in absence of magnetic field. Radiative relaxation of S_1 state is named fluorescence. The emitted photon has typically less energy than the absorbed photon, this energy difference being the Stokes shift. Radiative relaxation of T_1 state is named phosphorescence which is the slowest process of the different possible transitions.

4. Fluorophores

In fluorescence microscopy, fluorophores can be used to image biological objects. Depending on the application, fluorophores can be (i) inorganic such as quantum dots (ii) organic molecules, i.e. dyes, that can be conjugated to molecules (such as Alexa fluorophore bound to antibodies) or fluorescent stains, capable to bind specific regions of cells (such as Syto-9 and DNA), (iii) fluorescent proteins (FPs), such as the commonly used GFP, green fluorescent protein (Shimomura et al. 1962). These fluorescent proteins can be genetically encoded and used to label proteins of interest in order to localize them and follow their expressions.

Strong structural homology can be found among all the discovered fluorescent proteins, their structure being organized as a β barrel in 11 antiparallel β strands, measuring 2.4nm in diameter and 4.2nm in height, for a weight of 27kDa (Ormö et al. 1996; Yang et al. 1996). Shorter α helices form caps at the extremities of this barrel. The chromophore, made of three amino acids, is found covalently bound to an α helix that runs through the center of the β barrel. The interaction of the chromophore with the surrounding amino acids determines the photophysical properties of each FP.

Briefly, some of the properties of fluorophores are:

- Spectral properties:

Fluorophores possess specific absorption spectra that corresponds to the propensity for a molecule to be excited (e.g. $S_0 \rightarrow S_1$) as the function of the exciting wavelength. Fluorophores also possess specific emission spectra that corresponds to the propensity of emitting a photon at a given wavelength during the molecule relaxation.

- Molar extinction coefficient:

It measures the intrinsic capacity of a fluorophore to absorb light at a given wavelength, expressed in $M^{-1}.cm^{-1}$.

- Quantum yield:

It is the ratio between the number of fluorescence photons emitted and the number of excitation photons absorbed. As following an excitation, the molecule can be de-excited by radiative or non-radiative relaxations, the quantum yield can actually be understood as the competition between the radiative and non-radiative relaxations in a molecule. Thus, when no non-radiative relaxation happens, this ratio is equal to 1.

- Bleaching properties:

It corresponds to the permanent loss of fluorescence of a molecule due to its destruction upon prolonged exposure to excitation light. Each fluorophore will have its own

photobleaching characteristics, meaning it can emit fluorescence during multiple cycle of excitation/de-excitation before bleaching.

- Fluorescence intermittency, “Blinking”:

The blinking of a fluorophore corresponds to the random fluctuation between a fluorescent and a dark state upon continuously excitation. For example, some fluorescent proteins may alternate several times between an emitting “on” state and a dark “off” state, producing “blinkings” before bleaching.

5. Optical resolution principle

Despite numerous innovations in objectives and lens manufacturing, the electromagnetic properties of light limit the achievable optical resolution.

In microscopy, the emitted light from a point object (e.g. a fluorescent protein) passing through an objective will not be focused into an infinitely small point in the image plane. Indeed, the emitted light emerges from the microscope's objective into converging spherical waves, which will interfere in the whole image space. This emitting point object will thus have a peculiar pattern of light distribution near the image plane of the objective, called the point spread function (PSF). When viewed in the x-y plane, this PSF results in a bright central disk surrounded by series of concentric rings. This pattern is referred to as the Airy disk (Figure 2.3).

The resolving power of a microscope is commonly calculated from the Rayleigh criterion of the employed objective. This criterion gives the minimum distance needed between two neighboring points in order for them to be resolved in the image plane (i.e. to be identifiable as two points). This criterion corresponds to the distance between the center of the central spot of the Airy pattern and its first minimum (see Figure 2.3), which is given by:

$$d = 0.61 \frac{\lambda}{NA} \quad (1)$$

with λ being the wavelength of the emitted light and NA the numerical aperture of the objective.

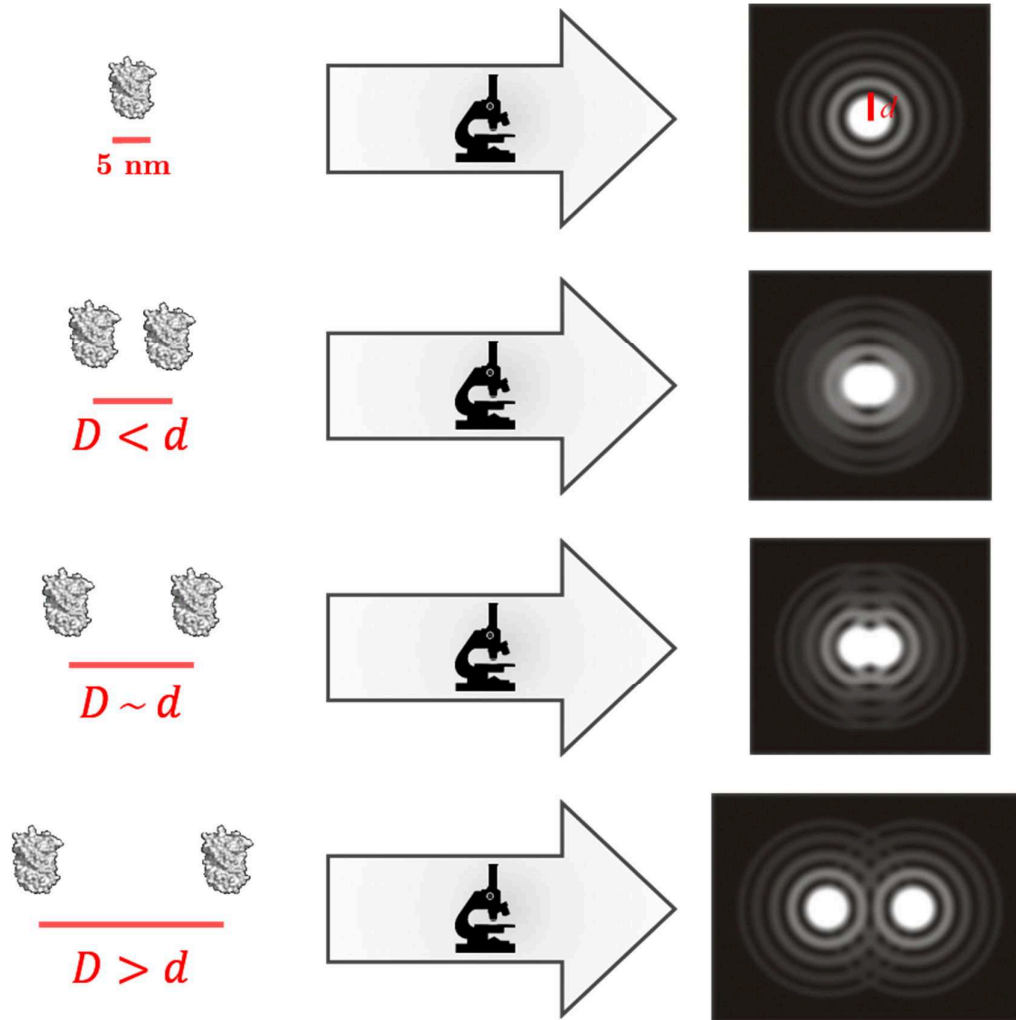


Figure 2.3: Optical resolution and Rayleigh criterion. The image of a point source is diffracted by the microscope into a 3D PSF, visible as an Airy disk in the x-y dimension of the image plane. The Rayleigh criterion (d), is the distance between the center of the central spot of the Airy pattern and its first minimum. Objects separated by a distance smaller than d will result in overlapping airy disks that will not be resolved in the final image. Objects separated by a distance close to d will result in one's airy disk maximum overlapping with one's airy disk first minimum. Objects separated by a distance greater than d will result in two distinct airy disks and a resolved final image. Source of the Airy disk: Wikipedia.

6. Conventional fluorescence microscopy

Fluorescence microscopy is one of the most spread imaging techniques. Its non-invasive nature and its ease of use makes it a suitable tool for studying the organization of biological tissues and cells. Moreover, the rather low illumination intensity required and its fast imaging capabilities proved to be important assets for the study of live cells and their dynamics, over a broad time range spanning sub-seconds to days (Figure 2.1).

Most fluorescence microscopes in use are widefield fluorescent microscopes (Jensen 2012). However, widefield fluorescence microscopy suffers from the broad and thick uniform illumination that is shed on the sample. All parts of the observed sample, in the optical path, are excited at the same time. Thus, a large amount of unfocused background signal is collected at the same time as the focused region of interest.

A solution to overcome this issue relies on the use of well-implemented confocal laser scanning microscopes (CLSM) that enable performing optical sectioning of the sample. Laser illumination in confocal microscopes is reduced to a point illumination instead of the broad illumination of widefield fluorescence microscopy. The emitted fluorescence is then filtered through a pinhole aperture that blocks the out-of-focus signal. The exciting beam is scanned across the sample in order to retrieve the image. Due to their point illuminations and their pinholes, confocal microscopes offer many advantages over widefield fluorescent microscopes. Theoretically, the possibility given by the pinhole to remove out-of-focus light can lead to a slight increase in lateral resolution (Wilson 2011). However, this requires to reduce the size of the pinhole to the point where it would decrease dramatically the signal to noise ratio. Practically, the pinhole only improves the effective axially achievable resolution, by increasing the contrast in the image, as the Z-sectioning removes the background noise arising from out-of-focus emitted light. The sectioning can also be used to reconstruct 3D images. However, confocal microscopy induces important phototoxic effects in live cells and requires several seconds to minutes to acquire the image of a sample.

An alternative to CLSM is spinning-disk (SD) microscopy. In CLSM, only one point at a time on the sample is illuminated and then scanned across the sample. In SD microscopy, instead of relying on a single pinhole, a rotating disk with a pattern of pinholes is used to scan the whole sample. A second rotating disk with microlenses can also be added before the previous one in the optical path (this configuration is named Yokogawa SD microscope). When both rotating disks are synchronized, every microlens enables focusing the light into each pinhole. SD microscopy can achieve faster imaging rates compared to CLSM, which makes it more suitable for imaging of live cells.

A strategy used both in widefield and confocal microscopy is the deconvolution of the acquired images in post-processing. An image acquired by a microscope can be seen as

the convolution of the sample with the PSF. Using a measured or a calculated PSF, deconvolution will attempt to reverse this process and try to reconstruct the sample from the acquired images. Typically, this method results in a slight increase in lateral resolution but in significant improvement in effective axial resolution. Indeed, out-of-focus signal will be shifted back to its initial focal plane by the deconvolution thus improving the image contrast. Despite the improvement brought by confocal microscopes or deconvolution, both widefield and confocal microscopes are limited in resolution by the diffraction of light. For example, an object emitting at 500nm wavelength, observed using a modern objective with a numerical aperture of $NA=1.49$, results in an achievable resolution of around 200nm. Several strategies have been developed to overcome this resolution limit in light microscopy, which are described below.

7. SR fluorescence microscopy

Throughout the years, various techniques have been developed to surpass or break the diffraction limit of light microscopes, and thus being able to distinguish objects separated by a distance below 200nm. These techniques conserve the advantages of labeling specificity and not requiring altered/sectioned cells but achieve a resolution which can reach up to 10nm.

Listing every imaging technique that has been developed in SR microscopy would be a daunting task. All of these imaging techniques (each having a cryptic name and their own specific applications/set-ups/data analysis) can be separated into two main approaches: deterministic/ensemble techniques or stochastic/single-molecule techniques.

It is noteworthy that all the techniques that have been developed until now and that will be described hereafter are based on far-field optical microscopy. Another type of optical microscopy exists, named near-field scanning optical microscopy (NSOM). It does not suffer from the diffraction limit imposed by light in far-field microscopy. Indeed, light is collected in the near-field (i.e. very close to the surface of the object), where it behaves as evanescent waves and thus is not subjected to diffraction. The illumination and the collection of the light emitted from the sample surface is achieved by an optical fiber positioned at a distance below 100nm, which scans the whole sample. Because the intensity of evanescent waves exponentially decays with distance from the object, this complex technique can only image the surface of cells. Moreover, the scanning of the sample by a fiber induces a relatively slow imaging process, preventing the study of fast dynamics. Due to these important pitfalls, the following paragraphs will only focus on far-field imaging.

7.1. Ensemble

All the deterministic/ensemble based techniques increase resolution by shaping the illuminating light.

Structured Illumination Microscopy (SIM) is an ensemble technique in which the entire field of view is illuminated, with a striped pattern of light (Gustafsson 2000). This striped pattern will interfere with the different spatial patterns of the sample (including the usually not resolvable pattern) and produce an interference pattern due to the Moiré effect. The illuminating pattern is translated and rotated several times on the field of view, which generates series of images with different Moiré fringes. Because the illumination patterns are precisely known, they can be “removed” from the Moiré fringes. Thus we can retrieve the patterns of the sample and access the conventionally non-resolvable sample features, leading to an increase in resolution. The resolution achievable with SIM is around $\sim 100\text{nm}$ in the x-y direction and $\sim 400\text{nm}$ axially

(Schermelleh et al. 2008), i.e. a gain by a factor of 2 compared to non SR fluorescence microscopy techniques.

SIM imaging has numerous advantages: the data are collected on a time scale of seconds so it is possible to rapidly acquire many field-of-views, the induced phototoxicity is close to the conventional microscopy one's, it can be used with all existing dyes and 3D is achievable. However, this technic is prone to artifacts as it requires a heavy load of post-acquisition work.

REversible Saturable Optical Linear Fluorescence Transitions, RESOLFT, is a category of deterministic SR microscopy where the PSF is engineered to be smaller than the diffraction limit by spatially controlling the non-linear response of fluorophores to a depletion laser. All methods that belong to this category (e.g. Stimulated emission depletion, STED or ground-state depletion, GSD) rely on the use of specially modified illumination lights and dyes that can switch between an emitting and a non-emitting state, with the transitions being optically induced. These techniques are also all based on confocal scanning of the sample.

The illuminating light is engineered as an excitation laser (Figure 2.4), of low power, surrounded by another high-intensity laser (Figure 2.4), the depletion beam, shaped as an annulus. In this annulus, the fluorescence of the dyes will be prevented, by forcing the dyes to transition to their ground states (for STED) (Hell & Wichmann 1994), to metastable dark state (GSD) (Bretschneider et al. 2007) or to switchable off state (RESOLFT) (Hofmann et al. 2005).

Practically, in the case of STED, the excitation laser is first shined on the sample to excite dyes. Before these dyes emit any fluorescence (time scale of nanoseconds), the depletion beam illuminates the sample, forcing the de-excitation of the dyes by stimulated emission. A key point in STED is the possibility to saturate the de-excitation of the excited fluorescent state of dyes due to their non-linear dependence on the depletion beam intensity. In other words, the fluorophores respond non-linearly to the local intensity of the depletion beam. If the depletion beam intensity exceeds a certain level of intensity called the saturation intensity, it becomes highly probable that incoming depletion beam photons will force the excited fluorophores to de-excite by stimulated emission.

During stimulated emission, a new photon is produced but unlike fluorescence, it possesses the exact same properties as the incoming exciting photon and in particular, the same wavelength. A bandpass filter then filters out the photons emitted by stimulated emission and thus, only those photons emitted by the normal fluorescence originating from the inside of the annulus are collected. Overlapping and synchronizing the two lasers result in an effective excitation beam that corresponds to the inside of the annulus of the depletion beam, with an effective diameter smaller than the diffraction

limit. Moreover, the effective PSF is tunable, it gets smaller as the intensity of the depletion beam increases. The photo-damage induced by the high power depletion beam (\sim MW.cm⁻²) is in fact limiting the possible usable intensities and therefore limits the achievable resolution for biological samples. Moreover, at such laser power the photobleaching of dyes is important. A super-resolved image, of around 20-30nm resolution (Westphal & Hell 2005) can be constructed by scanning the sample with the effective excitation laser.

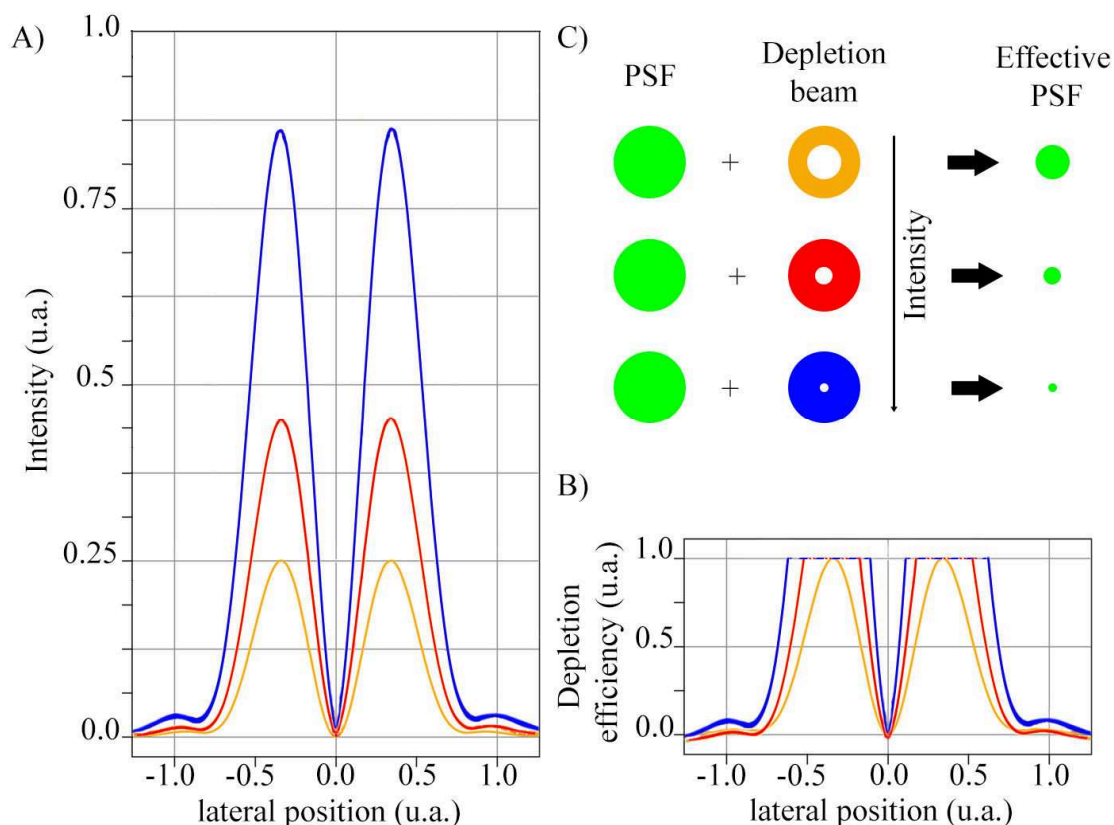


Figure 2.4: Effective PSF generation in STED. A) Intensity profile of three different depletion beam of increased intensity (blue>red>orange) B) Saturation of the depletion efficiency due to the non-linear response of the fluorescent proteins to the depletion beam of increased intensity (blue>red>orange). C) The illumination, first with an excitation beam (green) and then immediately after, with a depletion beam (these successive operations occur faster than fluorescence lifetime, i.e. below the nanosecond) results in an effective PSF. Increasing the intensity of the depletion beam results in smaller effective PSFs. Original depletion efficiency graph from (Otomo et al. 2015).

Thus the improvement in resolution achieved with STED requires the use of a strong depletion beam. In contrast, GSD relies on the use of fluorophores, capable of switching to metastable dark states by weaker laser power. Thus, in GSD the de-excitation beam has an intensity reduced by orders of magnitude compared to the depletion beam of STED.

RESOLFT-based techniques have numerous benefits and limitations. As they are operated in a similar manner as confocal microscopy, the learning curve for users might

be less steep than other SR techniques. However, compared to standard confocal microscopes, RESOLFT techniques require more time to scan the field of view (around 10 times slower is a good approximation), which is still much faster than single-molecule techniques. Another interesting point is that contrary to single-molecule techniques, in RESOLFT, during the acquisition, what-you-see-is-what-you-get, meaning that almost no post-treatment is required to exploit images, reducing the probability to introduce artifacts. The lateral improvement of the resolution achieved with these methods has also been extended to the axial dimension, enabling highly resolved 3D acquisition (Klar et al. 2000). However, RESOLFT techniques cannot work with every dye, thus rendering multicolor imaging challenging.

7.2. Single-molecule

7.2.1. Generalities

The most used single-molecule techniques were all presented in 2006: photoactivation localization microscopy (PALM)(Betzig et al. 2006), fluorescent PALM (fPALM) (Hess et al. 2006) and stochastic optical reconstruction microscopy (STORM) (Rust et al. 2006). All of these techniques enable to surpass the diffraction limit of classical microscopy down to ~ 20 nm. They are based on the same principle: exciting only a subset of a whole population of fluorescent markers at a given time, then acquire the corresponding images and repeat the whole process for a period of time long enough to collect enough molecules to resolve a given structure. The excitation of only a subset of a whole population relies on the use of special fluorophores, able to cycle between an emitting (“on” state) and a non-emitting state (“off” state). PALM and fPALM use genetically expressed phototransformable fluorescent proteins (PTFPs) to cycle between on and off states (Figure 2.5), whereas STORM originally used pairs of cyanine dyes, one acting as a reporter and the other as an activator. Today, STORM has been generalized to direct STORM, dSTORM, (Heilemann et al. 2008), which is based on the use of single synthetic dyes such as Alexa-Fluor dyes, typically linked to antibodies in an immunochemistry approach. These dyes usually possess long-lasting off-states, which can be further increased by employing special buffers (Dempsey et al. 2011).

PTFPs, unlike conventional fluorescent proteins, can change their fluorescence excitation and emission spectra after exposure to specific wavelength of light. PhotoActivable Fluorescent Proteins, PAFPs, can irreversibly change from a non-fluorescent state to a fluorescent state. PhotoConvertible Fluorescent Proteins, PCFPs, can irreversibly change from one fluorescent state to another fluorescent state. Reversibly Switchable Fluorescent Proteins, RSFPs, can be switched several times from a fluorescent to a non-fluorescent state.

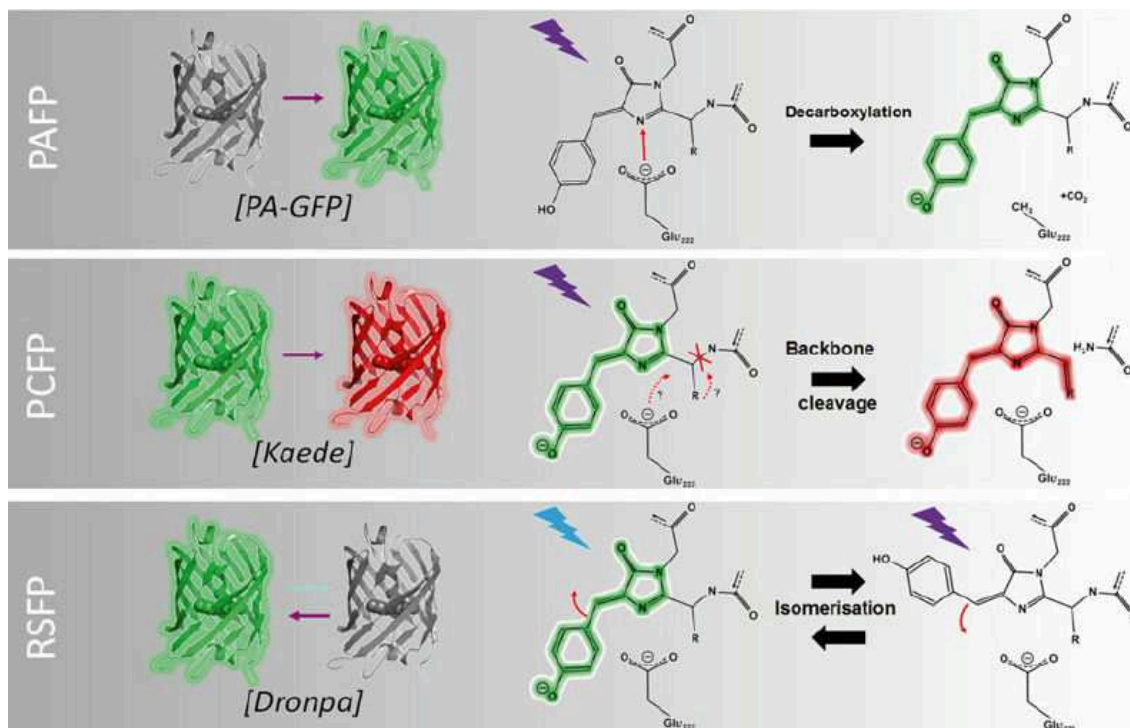


Figure 2.5: Illustration of the different type of PTFPs. The arrows represent the direction of the phototransformation and in each category in bracket is the name of a frequently used FP. Photoinduced reactions occurring at the chromophore level are represented for each case. Adapted from (Bourgeois et al. 2012).

- PALM/dSTORM

The acquisition of a PALM data set typically consists in alternate illuminations with a laser of low power (called “activation” laser) and a laser of higher power (called “excitation” laser). The low power enables activating stochastically a very small subset of the whole pool of fluorophores while the majority reside in a non-fluorescent state. The second laser is used to excite the activated fluorophores, which start to emit fluorescence. After a given period of time (typically 1 or a couple of frametimes), these fluorophores either switch back to a non-fluorescent state or irreversibly bleach and the whole process is repeated (Figure 2.6). The acquisition thus consists of a stack of numerous images acquired during the repeated sequence.

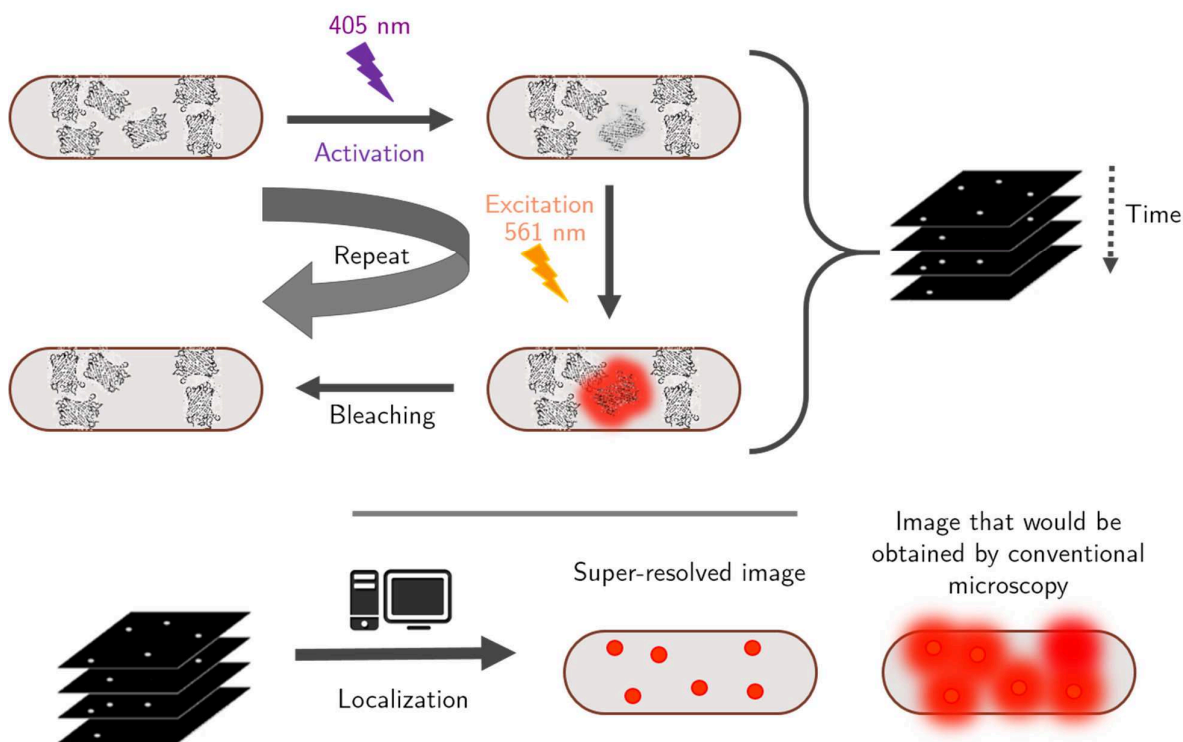


Figure 2.6: Scheme illustrating the PALM technique using PTFPs. A) Throughout-time, stacks of diffraction limited images are assembled, where subsets of PTFPs are activated and excited stochastically. On each image of the stack, the PSF of the different fluorophores are processed to retrieve their localizations. All the positions are then assembled into a single super-resolved image, in contrary to the conventional image that would be recorded if all the fluorophores were excited at the same time.

On each of the stack images, diffraction limited spots of the activated fluorophores appear. Then localization algorithms are used to determine the position of each single molecule with nanometric precision (Gelles et al. 1988; Yildiz et al. 2003). The final super-resolved image is constructed by assembling all the localized points from all images of the stack (Figure 2.6).

Due to the pointillist nature of PALM, the concepts of resolution, localization and labeling density must be carefully defined. The localization of a fluorophore, achieved by fitting a gaussian distribution over the measured PSF, is typically precise down to a few nanometers. This precision of positioning is called localization precision and mostly depend on the width of the PSF and on the inverse of the square root of the number of detected photons from each fluorophore. Practically, the achieved localization precision in the XY plane varies between 10nm (synthetic dyes) and 50nm (weak PTFPs). However, localization precision is not the same as resolution. Localizing fluorophores with high precision does not create a super-resolved image if there is not enough labeling of the desired structure (Figure 2.7).

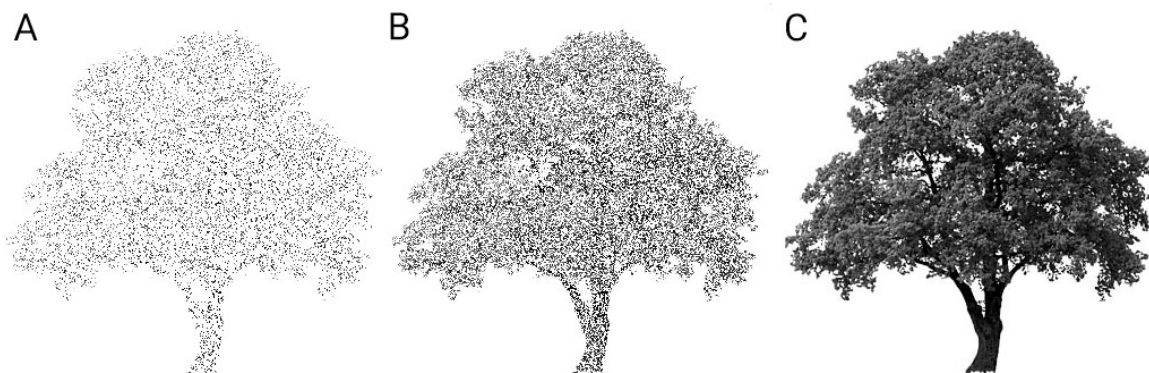


Figure 2.7: Effect of molecular density on super-resolved image. Random positioning of molecules on a tree, according to different labeling density (in percentage to full completion): A. 33%, B. 66% and C. 100%. Adapted from Nikon website: <https://www.microscopyu.com/tutorials/molecular-density-in-superresolution-microscopy>

Resolution of an image is in fact also related to labeling density, which must satisfy the Nyquist–Shannon criterion. According to this criterion, a feature can only be resolved when the distance between two of its labels is less than half the feature size. Thus in theory, in order to achieve a resolution of 40nm in 2D, it is necessary to have labels placed at least every 20nm on the sample, which means a density of 2500 label per μm^2 . In practice the required density is even higher. However, using too high density labeling can lead to too high activation density, which can also induce artifacts such as artificial sharpening (Marsh et al. 2018). The size of the PTFPs (4nm wide) or the antibodies (10nm wide, in dSTORM) used for the labeling is also a limiting factor for the resolution.

One of the main advantages of PALM is that it can be relatively easily implemented on any commercial inverse microscope, as it requires almost no optical engineering and essentially relies on the use of a few powerful lasers and a high-performance camera. Due to the pointillist nature of single-molecule imaging, the localizations of molecules can be used for cartography purposes but can also be used for different quantitative evaluations: counting of copy numbers of proteins or study of stoichiometry of complexes (Fürstenberg & Heilemann 2013). Different 3D implementation strategies exist. For example, the axial positions of a molecule can be determined by multiplane detection, where the axial position is determined by comparing images of the same molecule, but with different focus (Jüette et al. 2008). The PSF can also be modified in order to be z-dependent. The engineered PSF shape recorded in the 2D image can then be used to retrieve the axial position. The simplest example of this strategy is the astigmatism method (Huang et al. 2008).

A major pitfall of single-molecule based SR techniques is their slow speed of image acquisition. A single acquisition can require up to several minutes of continuous laser illumination. This makes imaging living cells quite challenging, due to potential artifacts (e.g. movement within a live cell leads to motion blur) and due to potential phototoxic effects. A possibility is to chemically fix cells. However, fixation may induce numerous artifacts that may seriously compromise the study (Schnell et al. 2012). Another issue

arising from long-lasting acquisitions is the drift occurring on the sample due to heat generated by the laser or mechanical vibrations. However, this can be easily compensated by post-treatment procedures. A typical method is to use fiducial markers, such as gold nanoparticles, on the field of view during the acquisition to be able to measure and thus compensate the drift of the sample.

7.2.2. Time-correlated detection counting with PALM (tcPALM)

TcPALM is a quantitative method that was developed to study the spatiotemporal organization and dynamics of RNA polymerase II as well as its clustering (Cisse et al. 2013). It consists in analyzing the temporal sequence of single-molecule detection. For example, if some monomeric proteins form a cluster of 20nm in size and are labeled by phototransformable proteins, it will be difficult to spatially distinguish them, based only on the PSFs. However, if the properties of the PTFPs used are known, the stoichiometry of the complex can be evaluated. The temporal sequence of the fluorescence of the complex will be the concatenation of the different PTFPs temporal sequences. An hypothetical case of such temporal analysis is presented in Figure 2.8, with an ideal PAFP, that can only emit fluorescence once. However, PTFPs can blink: it randomly fluctuates between an emitting “on” state and a dark “off” state upon continuously excitation. A single blinking PTFP may then be counted several times. If the blinking properties of PTFPs is not taken into account in the analysis of the temporal sequences of single-molecule detection, it may cause over-counting artifacts. To date, counting PTFPs is still quite unsolved. For an in depth review on this issue, see (Berardozzi 2016).

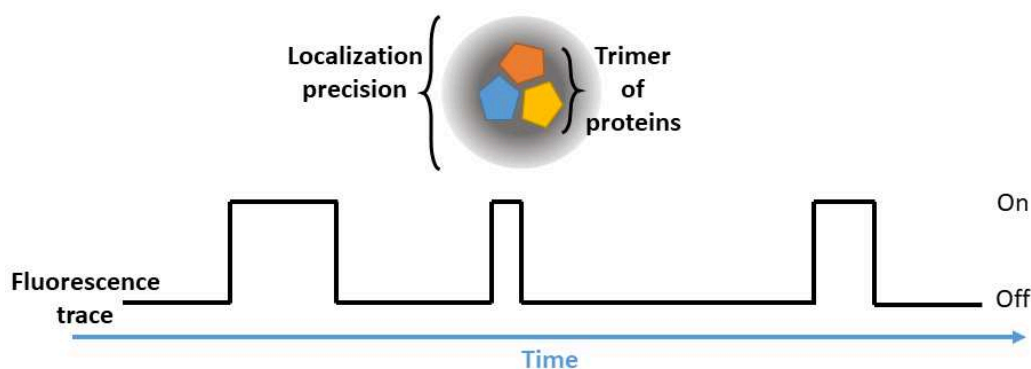


Figure 2.8: tcPALM analysis of a trimer of proteins labeled with an ideal PAFP. We suppose that the ideal PAFPs used will not blink. Moreover, using very small activation power laser, we can consider as close to zero, the chance of the three PAFPs to be activated simultaneously. The fluorescent signal emitted by the trimer of proteins will be spatially undistinguishable, but the temporal sequence of fluorescence will directly show the stoichiometry of the complex.

7.2.3. Single particle tracking (SPT)

A possibility to bypass the data acquisition speed issue is to decrease the laser power and switch to single particle tracking strategies (sptPALM), enabling to study the dynamics of different processes while decreasing the phototoxicity.

Studying the dynamics of specific proteins can lead to insights into the mechanisms of biological processes and be a crucial step for the functional study of cells. Using conventional fluorescent proteins as markers, there are different methods to extract the dynamics of proteins of interest. One of the most used methods is the Fluorescence recovery after photobleaching (FRAP). This technique relies on the use of a powerful laser, capable of photobleaching a specific area in a cell. Thus, right after the illumination, the area is deprived of its fluorescence signal. Then by visualizing the rise of the fluorescence in this area due to the non-bleached fluorophores diffusing back into the dark area, it is possible to extract diffusion coefficients corresponding to the ensemble of the population. A major drawback of this technique is the difficulty to distinguish for example two different diffusion regimes within the population of proteins of interest. Single particle tracking in contrast, enables to reconstruct the individual molecular trajectories and diffusion coefficient of individual molecule. The major drawback of this technique is to only enable the visualization of a protein of interest when it is present at a very low density. By combining single particle tracking with PTFPs (Manley et al. 2008), only a subset of the whole tagged population is stochastically activated, enabling to mimic this low labeling-density requirement. Fluorescence can be observed (Figure 2.9 A) and imaged at a frame rate that depends on the dynamics of the system studied and within the limits imposed by the instrumentation. This combination enables to reconstruct individual tracks by connecting the different successive positions of the labels in consecutive images (Figure 2.9 B).

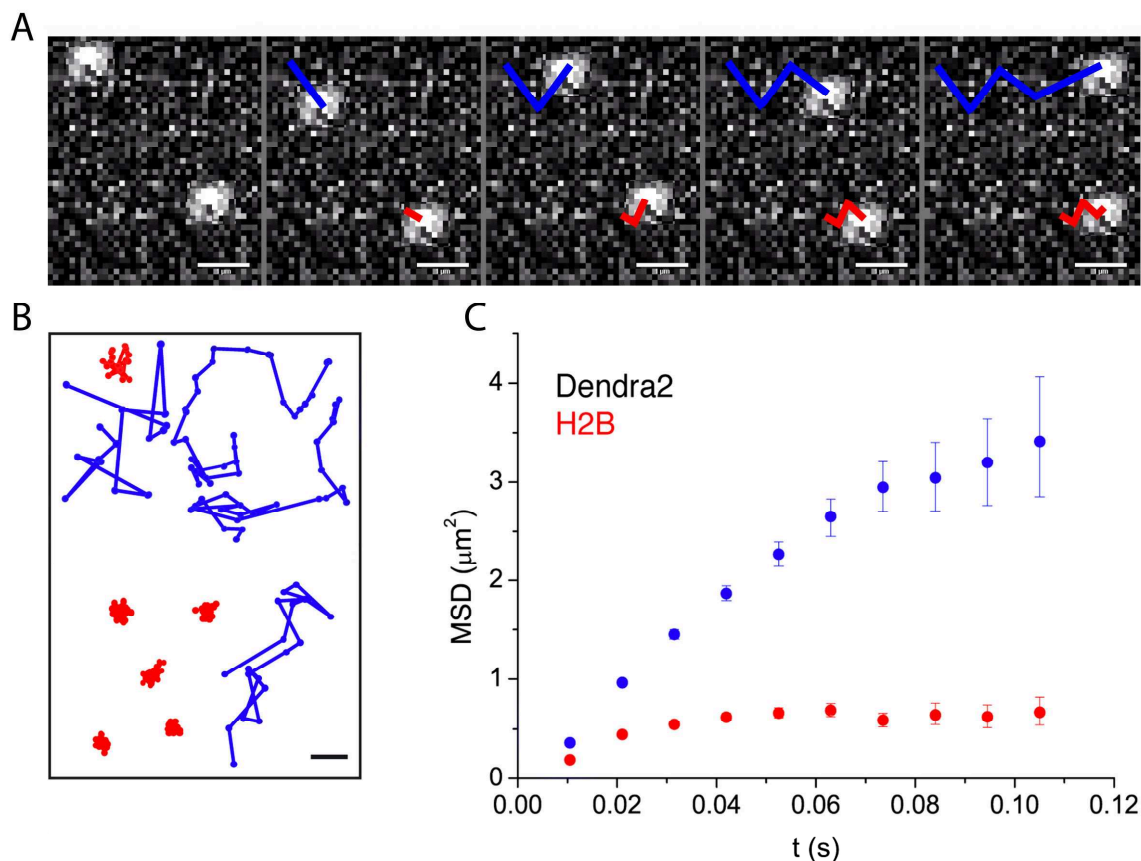


Figure 2.9: Study of molecular dynamics by sptPALM. (A) Localization and reconstruction of two tracks (one fast in blue and one slow in red) in consecutive frames during a sptPALM experiment. (B) Examples of reconstructed single molecule tracks of two diffusive populations (one fast in blue and one slow in red). (C) Example of average mean square displacements (MSD) computed from more than 10000 trajectories for the red and blue population. Scale bar: 1 μm . adapted from (Izeddin et al. 2014).

SptPALM enables statistical studies of the different trajectories retrieved. It is possible to compute the square displacement of a molecule, by measuring its deviation from a reference position over time. Then, by generalizing this calculation over the whole population of available trajectories and for different time-periods, we can compute the average mean square displacement (MSD) at different time-delays. It is then possible to extract diffusion coefficients or diffusion regimes (Figure 2.9 C).

7.2.4. PAINT

Numerous single-molecule based SR strategies have recently emerged, mostly due to their ease of implementation. PAINT imaging (Point Accumulation for Imaging in Nanoscale Topography), has been used as an easy-to-implement technique to precisely define the boundaries of cells (instead of using phase contrast images).

PAINT does not rely on the stochastic fluorescence emission of PTFPs to image a small subset of molecules once at a time like in PALM. Instead, it uses the fluorescence

emission of fluorophores that become fluorescent only when binding to the object of interest while remaining non-fluorescent in solution. For example, the Nile Red molecule is non-fluorescent in aqueous solution but emits fluorescence once in a hydrophobic environment such as that of the lipid bilayers of various vesicles (Sharonov & Hochstrasser 2006) (Figure 2.10). If the concentration of Nile Red is low enough to have a *sparse* density of emitting fluorophores once at a time, reconstructing a super-resolved image of the lipid bilayer is possible.

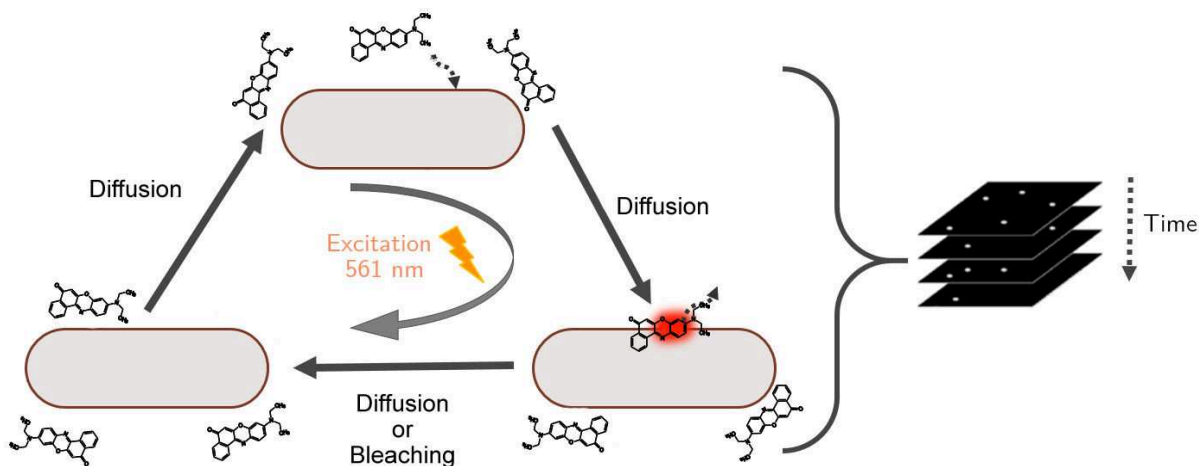


Figure 2.10: Principle of PAINt microscopy. Throughout-time, stacks of different diffraction limited images are assembled, where subsets of molecules, Nile Red here, are able to emit fluorescence only when they are excited and in a hydrophobic environment (such as the lipid membrane).

7.2.5. Spectral PALM

Recent advances in PALM microscopy also encompass more refined techniques, with specific advantages. One of the most promising is spectral PALM imaging (Mlodzianoski et al. 2016; Zhang et al. 2015). Briefly, the optical path of the emitted light by a fluorophore is divided in two paths. One going through a prism before detection on the camera and one going directly to the camera. It is then possible to correlate the spatial information of each fluorophore with its spectral information (Figure 2.11).

This technique enables to visualize changes in the emission spectra of the fluorophores in different parts of the sample, as well as changes of the spectra over time. These informations are particularly useful to achieve multi/“true-color” SR microscopy. Indeed, it enables to differentiate fluorophores that normally cannot be distinguished due to a too strong cross talk. An impressive 3D imaging of four dyes only 10 nm apart in their emission spectrum was realized with this spectral PALM method (Zhang et al. 2015).

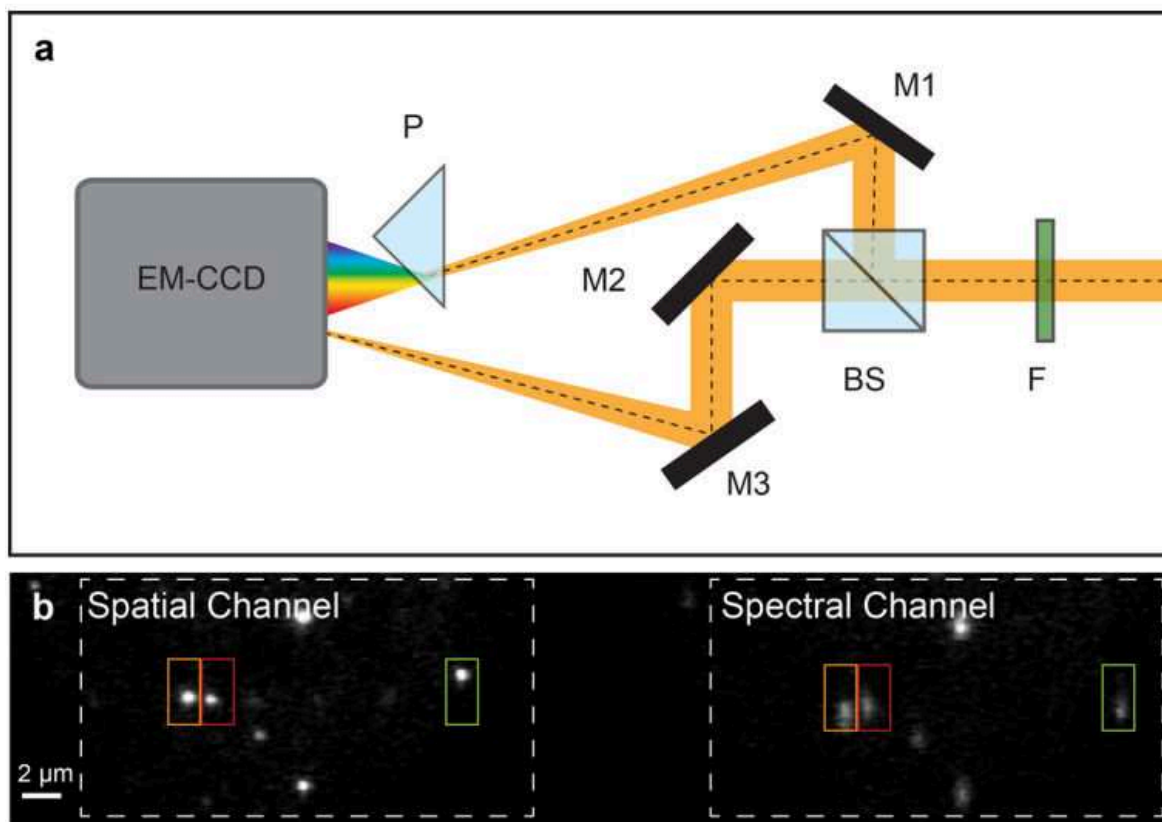


Figure 2.11: Spectral-PALM experimental setup. A) The Optical beam (in orange) passes through a first filter (F) in order to block the reflected laser light, then goes through a 50:50 beamsplitter (BS). The reflected path is then reflected by a mirror M1 and goes through a prism (P), before being collected on the camera as the spectral channel of (B.). The transmitted light from the BS is reflected on two mirrors, M2 and M3 in order to compensate for the path difference with the reflected light and thus assure that the same focal plane is imaged on the camera, in the spatial channel. Adapted from (Mlodzianoski et al. 2016)

III

Objectives of the PhD

The initial project of this PhD was to use for the first time the PALM SR microscopy on *D. radiodurans*, in order to investigate the distribution/localization and dynamics of DNA repair proteins (in particular Uvr proteins from the Nucleotide Excision Repair, NER, pathway) in response to DNA damage (UV irradiation).

To this end, PALM microscopy would have been used to unravel the mechanisms of different proteins expressed at low levels. However, during this PhD it appeared that before envisioning to study the NER by SR microscopy, two obstacles would have to be overcome (i) the autoblinking, making the visualization of low-level proteins challenging and (ii) the lack of knowledge regarding the organization and distribution of the DNA/nucleoid in *D. radiodurans*.

Therefore, the aim of the PhD project shifted toward (i) the characterization and the taming of the autoblinking and (ii) the characterization of the nucleoid organization and dynamics as a function of *D. radiodurans* cell cycle. This work constitutes the basis for the future study of DNA repair processes.

1. Autoblinking: a SR artifact

Nowadays, the trend in microscopy is shifting from purely qualitative imaging towards quantitative imaging. Retrieving quantitative information is a complex process in fluorescence microscopy and can be hindered by various artifacts. These can come from various sources that are sometimes difficult to control: the fusion of fluorescent proteins to proteins of interest may change the characteristics of the targeted protein, immunolabeling and in particular fixation procedures may alter the biological sample itself.

Not so surprisingly, SR fluorescence microscopy also faces several challenges, some of which are common with those encountered in conventional microscopy (e.g. photobleaching), but also new/specific challenges, reviewed in (Shivanandan et al. 2014). For examples, PTFPs may alternate several times between an emitting on state and a dark off state, producing “blinking” before bleaching. This may heavily disturb the quantitative analysis of samples.

In this PhD work, we have shed light on a poorly characterized phenomenon observed in SR microscopy imaging of bacterial samples, which we have coined “autoblinking”, which could potentially introduce severe artifacts into SMLM analyses. While observing unlabeled samples of wild type *D. radiodurans* we observed the presence of spurious blinking events of unknown origin, very similar to the blinking events of PTFPs. Thus its signal might be considered as a signal originating from PTFPs during the data processing. Therefore, autoblinking may be localized at the same time as the PTFPs and depending on the number of autoblinking events (and their cartography), the information deduced regarding the labeled structure may be incorrect. Thus, we decided to investigate this phenomenon and to try to determine its origin, a procedure to decrease the number of autoblinking events and its photophysical properties.

2. D. radiodurans cell and nucleoid dynamics

As presented in the introduction, most of our knowledge of bacteria morphology during growth and division and of nucleoid organization/segregation arises from the study of a small number of “model bacteria”, that are mainly rod-shaped or ovoid. In contrast, little is known on the nucleoid organization/segregation of cocci. Their morphology during their cell cycle is better understood.

Most studies on *D. radiodurans* have mainly focused on its tremendous radioresistance. 52 years after its discovery, its nucleoid organization/segregation as well as its cell morphology during its cell cycle still remain elusive.

Thus, one of the aims of this PhD project is to contribute to a better understanding of the cell morphology and the nucleoid organization/segregation in cocci. This will lead to a better understanding of the mesh that connects nucleoid structure, cell shape and DNA-based mechanisms.

3. Dissemination

The accomplishments of this PhD project presented in this manuscript have also been the subject of two publications and different presentations & posters.

Publications:

- Floc'h, K., Lacroix F., Barbieri L., Servant P., Galland R., Butler C., Sibarita J.B., Bourgeois D., Timmins J. Bacterial cell wall nanoimaging by autoblanking microscopy. *Sci Rep.* 2018 Sep 19;8(1):14038, DOI: 10.1038/s41598-018-32335-z
- Floc'h, K., Lacroix F., Servant P., Wong, Y.S., Kleman J.P., Bourgeois D., Timmins J. Cell morphology and nucleoid dynamics in dividing *D. radiodurans*. (in preparation).

Presentations & posters:

- France BioImaging Advanced Training (poster), Montpellier, 2016.
- Single Molecule Localization Microscopy Symposium (poster), Lausanne, 2016.
- Journée Annuelle des Doctorants EDCSV (poster), Grenoble, 2017.
- IBS scientific day (Flash talk + poster. Best poster award), Grenoble, 2018.
- Single Molecule Localization Microscopy Symposium (poster), Berlin, 2018.

IV

Autoblinking

In organisms, autofluorescence can arise as a result of the excitation of naturally occurring fluorescent molecules, such as chlorophyll or flavoproteins. Autofluorescence can severely impair conventional fluorescence microscopy (by affecting the signal-to-noise ratio), but also single-molecule microscopy. It can render the localization of fluorophores almost impossible: if the autofluorescence intensity is comparable to that of fluorophores, the blinking events will be “drowned” in the background autofluorescence.

By analogy to autofluorescence, we coined “autoblinking”, a phenomenon that arises only in SR microscopy. While observing unlabeled samples of wild type *D. radiodurans*, we observed the presence of spurious blinking events of unknown origin, very similar to the blinking events of PTFPs. Like autofluorescence, autoblinking might greatly disturb the acquisition of super-resolved images. Indeed, even if it does not decrease the signal to noise ratio per se, autoblinking might be identified as PTFPs. This autoblinking has been reported to our knowledge in *B. subtilis* and *E. coli* (Leon et al. 2017; Tuson et al. 2016). In these papers, the authors proposed different strategies to reduce it, they also assessed some of its photophysical properties, but did not advance any proof concerning its origin. The autoblinking that we are facing in *D. radiodurans* reaches a level never reported before. The amount of autoblinking is such that it might totally prevent us from studying endogenous proteins. Thus, a thorough investigation was conducted on this phenomenon and reported in the following article published in *Scientific Reports* in September 2018.

SCIENTIFIC REPORTS

OPEN

Bacterial cell wall nanoimaging by autoblanking microscopy

Kevin Floc'h¹, Françoise Lacroix¹, Liliana Barbieri¹, Pascale Servant², Remi Galland^{3,4}, Corey Butler^{3,4}, Jean-Baptiste Sibarita^{3,4}, Dominique Bourgeois¹ & Joanna Timmins¹

Spurious blinking fluorescent spots are often seen in bacteria during single-molecule localization microscopy experiments. Although this 'autoblanking' phenomenon is widespread, its origin remains unclear. In *Deinococcus* strains, we observed particularly strong autoblanking at the periphery of the bacteria, facilitating its comprehensive characterization. A systematic evaluation of the contributions of different components of the sample environment to autoblanking levels and the in-depth analysis of the photophysical properties of autoblanking molecules indicate that the phenomenon results from transient binding of fluorophores originating mostly from the growth medium to the bacterial cell wall, which produces single-molecule fluorescence through a Point Accumulation for Imaging in Nanoscale Topography (PAINT) mechanism. Our data suggest that the autoblanking molecules preferentially bind to the plasma membrane of bacterial cells. Autoblanking microscopy was used to acquire nanoscale images of live, unlabeled *D. radiodurans* and could be combined with PALM imaging of PAMCherry-labeled bacteria in two-color experiments. Autoblanking-based super-resolved images provided insight into the formation of septa in dividing bacteria and revealed heterogeneities in the distribution and dynamics of autoblanking molecules within the cell wall.

The advent of super-resolution fluorescence imaging has opened considerable opportunities for the investigation of bacteria, notably because the small size of these microorganisms largely prevents their detailed visualization by conventional optical microscopy^{1,2}. Practically all nanoscopy schemes, including point-scanning, structured-illumination and single-molecule localization methods have thus been used to provide fundamental insight into complex mechanisms in bacteria such as DNA repair^{3,4}, cell division⁵, gene expression⁶ or cell wall synthesis⁷. Localization methods such as PhotoActivated Localization Microscopy (PALM) and direct Stochastic Optical Reconstruction Microscopy (dSTORM) offer the advantages that they typically achieve the highest spatial resolution^{8–10}, are able to generate 3-D multicolor images with relatively simple instrumentation¹¹, and can deliver both a quantitative¹² and a dynamic¹³ view of processes under study.

Yet, a potential caveat when these techniques are used for bacterial imaging has recently been reported: several localization microscopy studies of unlabeled bacteria have indeed reported punctate fluorescent spots that were found to be indistinguishable from those originating from single PAMCherry molecules^{3,14,15}. These studies revealed that some bacteria, such as *Bacillus subtilis* exhibited higher levels of such fluorescent spots than others such as *Escherichia coli* or *Enterococcus faecalis*. It was proposed that the spurious localization events in *B. subtilis* were associated with membrane localized fluorophores, but only limited details were given concerning the properties of these fluorophores as well as their possible origin³.

In the present study, we show that this phenomenon, which we have named 'autoblanking', is widespread in bacteria and is observed to varying extents in both Gram-negative and Gram-positive species. Interestingly, two radiation-resistant *Deinococcus* strains, *D. radiodurans* and *D. deserti*, were found to exhibit particularly strong autoblanking located at the periphery of *Deinococcus* cells, as in *B. subtilis*, but at a much higher level. The density of autoblanking was such that it provided nanoscale imaging of the *D. radiodurans* cell wall 'for free' in both live and fixed cells. Intrigued by these observations, we investigated the possible origin of the autoblanking molecules, characterized their photophysical properties and demonstrated their potential relevance in deciphering *D. radiodurans* cell wall structure and dynamics.

¹Univ. Grenoble Alpes, CEA, CNRS, IBS, F-38000, Grenoble, France. ²Institute for Integrative Biology of the Cell (I2BC), CEA, CNRS, Univ. Paris-Sud, Université Paris-Saclay, 91198 Gif-sur-Yvette, France. ³Institut Interdisciplinaire de Neurosciences, University of Bordeaux, Bordeaux, France. ⁴Centre National de la Recherche Scientifique, UMR5297, Bordeaux, France. Correspondence and requests for materials should be addressed to D.B. (email: dominique.bourgeois@ibs.fr) or J.T. (email: Joanna.timmins@ibs.fr)

Received: 8 February 2018

Accepted: 6 September 2018

Published online: 19 September 2018

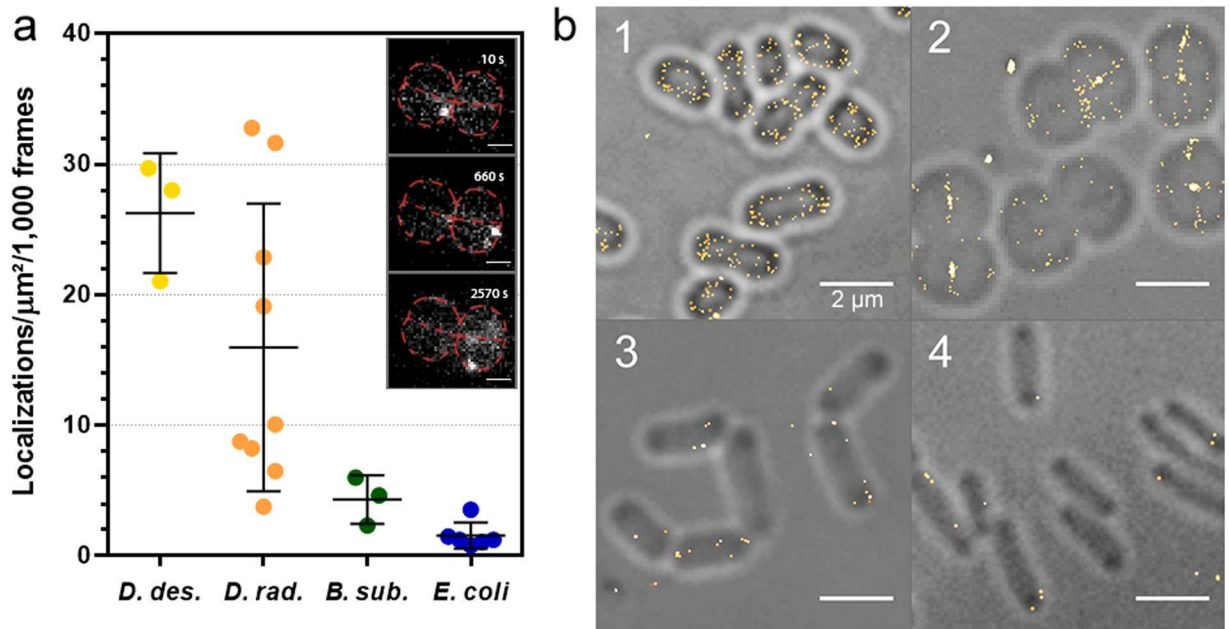


Figure 1. Autoblinking levels in *D. deserti*, *D. radiodurans*, *B. subtilis* and *E. coli*. **(a)** Number of localizations per μm^2 per 1000 frames extracted from images acquired with 50 ms exposure under continuous 0.8 kW/cm² 561 nm laser. Individual data points correspond to the autoblinking levels derived from a given stack of images. Means and standard deviations are plotted in the graph. Inset: examples of raw autoblinking signal (bright white spots) observed in the cell periphery of a *D. radiodurans* tetrad (outlined in red and presented in Fig. 2) at different timepoints during image acquisition (see also Supplementary Movie S1). Scale bar: 1 μm . **(b)** Representative reconstructions of live, unlabeled *D. deserti* (1), *D. radiodurans* (2), *B. subtilis* (3) and *E. coli* (4) superimposed on their respective brightfield images. In each case, the reconstructed images are derived from a stack of 1000 frames of 50 ms exposure acquired under continuous 0.8 kW/cm² 561 nm laser. Scale bar: 2 μm .

Results

Autoblinking: a widespread phenomenon in bacteria. In order to test whether *D. radiodurans* bacterial cells would be suitable for single-molecule localization microscopy (SMLM) despite their high carotenoid content and associated pink color, we submitted unlabeled bacteria to PALM imaging. Illumination with a 561 nm laser (0.8 kW/cm²), in the absence of additional 405 nm light, resulted in rapid fading of the autofluorescence of the bacterial cell wall and progressive appearance of sparse single-molecule blinking events (Fig. 1a and Supplementary Movie S1), which were reminiscent of those described in *B. subtilis* and in *E. coli*^{14,15}. We studied this ‘autoblinking’ phenomenon in several bacterial species (*B. subtilis*, *E. coli*, *D. radiodurans* and *D. deserti*) grown in their respective media, and observed that, although always present, its level was clearly species-dependent (Fig. 1). We noticed that the levels of autoblinking were much higher in *Deinococcus* strains than in the model bacteria *B. subtilis* and *E. coli*. While *D. deserti* exhibited the highest levels of autoblinking, *E. coli* showed the lowest level, although both of these bacteria are rod-shaped Gram-negative bacteria. This suggests that the extent of autoblinking is unrelated to the shape and Gram staining of bacteria. Likewise, *D. deserti* and *D. radiodurans* both displayed high levels of autoblinking, although they differ greatly in terms of cell morphology. To further characterize the autoblinking phenomenon, we focused our work on the well-studied *D. radiodurans* bacterium.

Autoblinking in *D. radiodurans*. *D. radiodurans* is a pink-colored, Gram-positive, spherical bacterium able to withstand the normally lethal effects of DNA-damaging agents, notably ionizing radiation, UV light and desiccation^{16–18}. As such, specific properties of this microorganism related to this outstanding phenotype, including its morphology, DNA repair repertoire, nucleoid organization, carotenoid content and cell wall structure have been the subject of intense research over the past decades^{19–25}. SMLM of live, unlabeled *D. radiodurans* bacteria provided unambiguous, super-resolved images of the bacterial cell wall (Fig. 2), similar to those obtained using the membrane dye Nile Red (Supplementary Fig. S1). Practically no autoblinking (<0.2 localizations per $\mu\text{m}^2/1000$ frames) was observed within the cytoplasm or in the extracellular medium. Autoblinking molecules were localized with a mean precision of ~22 nm and the Fourier Ring Correlation (FRC) method^{26,27} suggested an overall resolution of 110 nm. Simulations indicated that the achieved resolution, however, was significantly affected in the 2-D images by 3-D projection of the curved cell wall through the objective’s depth of field, notably on the cytoplasmic side of the external cell border (Fig. 2e, Supplementary Discussion and Fig. S2).

Source of autoblinking. The finding that autoblinking is particularly strong and localized to the cell wall in *Deinococcus* strains led us to hypothesize that this phenomenon could be associated with the high content in carotenoid molecules of these bacteria, which are responsible for their pink/orange color and in the case of *D.*

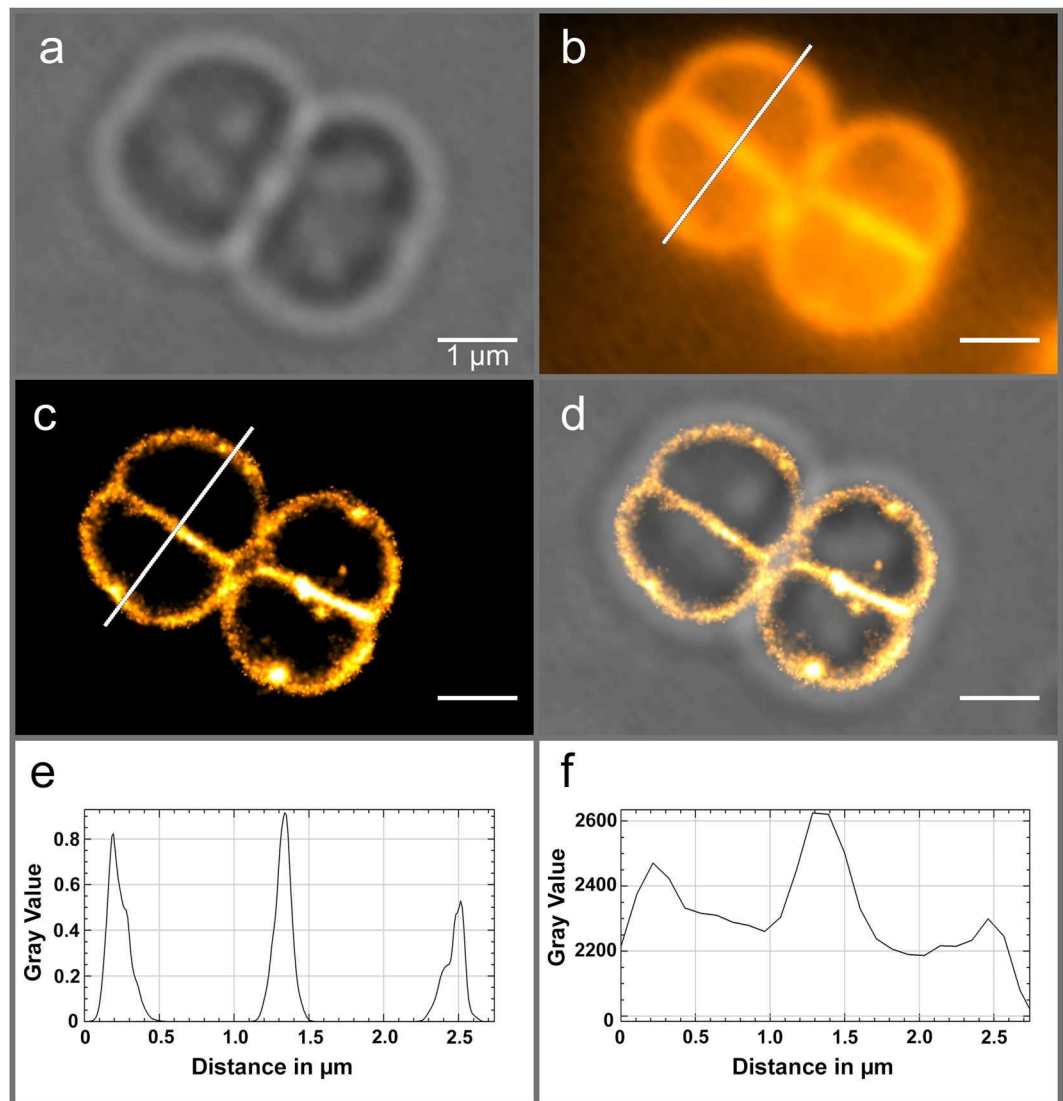


Figure 2. Autoblinking nanoscopy of live, unlabeled *D. radiodurans* bacterial cell walls. (a) Brightfield image. (b) Z-projection of 1000 frames of the original stack. (c) Super-resolved image rendered from a stack of 50,000 frames acquired under continuous 0.8 kW/cm² 561 nm laser (Supplementary Movie S1 provides an example of 500 frames of this stack). (d) Superimposed image of (a,c). (e,f) Profiles along the white line of (c,b) respectively. Scale bar: 1 μ m.

radiodurans are known to associate with its unusual cell wall²⁸. Although *D. radiodurans* is classified as a Gram positive bacterium, it possesses a complex, multilayered cell wall including an inner plasma membrane, a peptidoglycan layer, an interstitial layer, a highly structured 'S-layer', and finally a thick layer of carbohydrates^{21,29} (Supplementary Fig. S3). Earlier studies have reported that *D. radiodurans* produces a specific carotenoid, deinoxanthin, and the biosynthesis pathway for this carotenoid has been well characterized³⁰ (Supplementary Fig. S4).

To test our hypothesis, we evaluated the levels of autoblinking in two mutant strains of *D. radiodurans* ($\Delta crtB$ and $\Delta crtI$), which are colorless and no longer produce complex carotenoids²³. $\Delta crtB$ mutant accumulates a carotenoid precursor, geranylgeranyl-pyrophosphate (GGPP), while $\Delta crtI$ accumulates phytoene. Moreover, we also investigated the autoblinking levels in an engineered *E. coli* K12 strain, BW-LYCO, able to produce high levels of a common carotenoid, lycopene, the pigment that gives the red color to tomatoes³¹. No significant difference was observed between the levels of autoblinking in wild-type (WT), $\Delta crtI$ and $\Delta crtB$ *D. radiodurans*, on the one hand, and between WT and lycopene-producing *E. coli*, on the other hand (Fig. 3). These results strongly suggest that carotenoids are not implicated in the autoblinking phenomenon, also in agreement with the notion that carotenoids in their ground state typically do not absorb 561 nm light strongly³².

To determine whether the source of autoblinking is endogenous or exogenous, we evaluated autoblinking levels in exponential or stationary growing live bacteria and in fixed bacteria (Supplementary Fig. S5). Although the cell wall labelling was partly deteriorated in fixed cells, we did not observe any significant difference in the autoblinking levels in live vs. fixed cells. Moreover, autoblinking was found to be very long-lasting (see photophysics

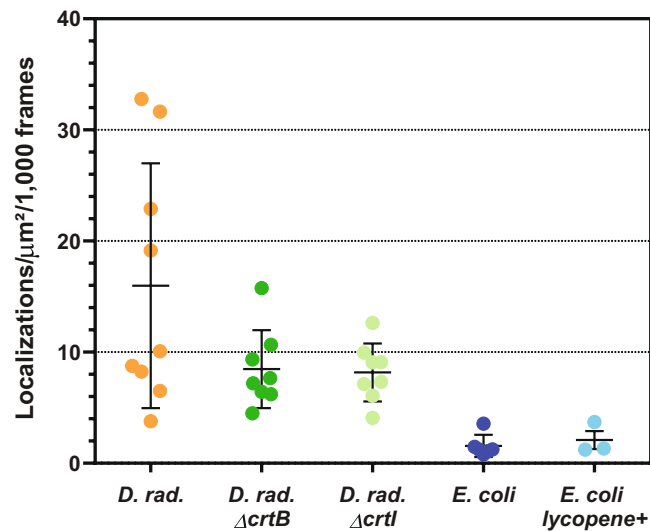


Figure 3. Autoblanking levels (localizations/ $\mu\text{m}^2/1000$ frames) in wild-type and carotenoid biosynthesis mutants (ΔcrtB and ΔcrtI) of *D. radiodurans*, and in wild-type and lycopene producing *E. coli* strains. Images were acquired with a 50 ms framerate under continuous 0.8 kW/cm^2 561 nm laser. Individual data points correspond to the autoblanking levels derived from a given stack of images. Means and standard deviations are plotted in the graph.

analysis below) even in fixed cells, suggesting that the source is likely not endogenous. We, thus, set out to investigate whether exogenous fluorophores could be responsible for autoblanking.

Under PALM illumination conditions, sparse blinking events can always be seen at the surface of glass coverslips or agarose pads, despite thorough cleaning of the glassware and even in the absence of any deposited biological sample. To investigate whether the molecules at the origin of these blinking events could be the same as those decorating the periphery of *D. radiodurans* cells, we performed a comparative study using single-molecule spectral imaging³³. We observed that, under illumination with 561-nm light, the average spectral signature of localization events at the *D. radiodurans* cell wall resulting from autoblanking closely matched that derived from localization events detected at the surface of the agarose pad (Fig. 4). This was in sharp contrast with the spectral signature produced by nanodiamonds that were used for drift correction and spectral calibration, which showed a strongly red-shifted spectrum (Fig. 4). These results thus strongly suggest that blinking molecules originating from the sample environment could be the same as those responsible for autoblanking in *D. radiodurans*. Spectral imaging was also performed on sparse molecules seen directly at the surface of untreated glass coverslips (Supplementary Fig. S6). The spectrum of such molecules displayed a peak centered around 600 nm, similar to the spectra of autoblanking molecules, but also exhibited a second red-shifted peak (around 675 nm), indicating that the nature of these molecules may differ from those found in the cell walls of the bacteria and on the agarose pad surface.

We then systematically investigated possible effects of the different components used for sample preparation on autoblanking levels in *D. radiodurans* (Fig. 5 and Supplementary Figs S6 and S7). In all these experiments, we noticed that the autoblanking levels displayed a relatively high variation from sample to sample and even from one field of view to another within a given sample.

We first studied the influence of the glass coverslips on which the samples are deposited. In the absence of preliminary treatment in an ozone oven, we observed numerous blinking events at the surface of the coverslips that rapidly bleached under excitation by the laser beam. These blinking events could be efficiently removed by ozone treatment (Supplementary Fig. S6). Although blinking on glass was generally accompanied by the sparse detection of rapidly diffusing fluorescent molecules in the medium around the imaged bacteria, it did not lead to a significant increase in autoblanking levels within the cells (Fig. 5a). This finding is in line with the observation by spectral imaging that sparse blinking molecules on the glass surface may differ from those binding to *D. radiodurans* cell walls. Nevertheless, as it is generally recommended for SMLM experiments, all our experiments made use of ozone-treated glass coverslips. Next, we studied the influence of the growth medium on autoblanking levels. These experiments clearly revealed that growing and/or resuspending cells in rich TGY medium resulted in the highest levels of autoblanking, whereas washing TGY-grown cells with highly pure PBS solution significantly reduced autoblanking to a minimal level (Fig. 5b). The main source of autoblanking is thus likely to be the cell culture medium. Growing cells in minimal medium (MM) resulted in relatively low levels of autoblanking, similar to those obtained with washed cells. A comparison of the levels of autoblanking in TGY and MM measured at the surface of agarose pads in the absence of bacterial cells confirmed that TGY is indeed the major source of exogenous fluorophores (Supplementary Fig. S7). Finally, we compared autoblanking levels in cells mounted either directly between glass coverslips or deposited on agarose pads (Fig. 5c). The agarose pad led to slightly increased autoblanking levels, suggesting that the agarose itself may also be a source of autoblanking fluorophores. It is

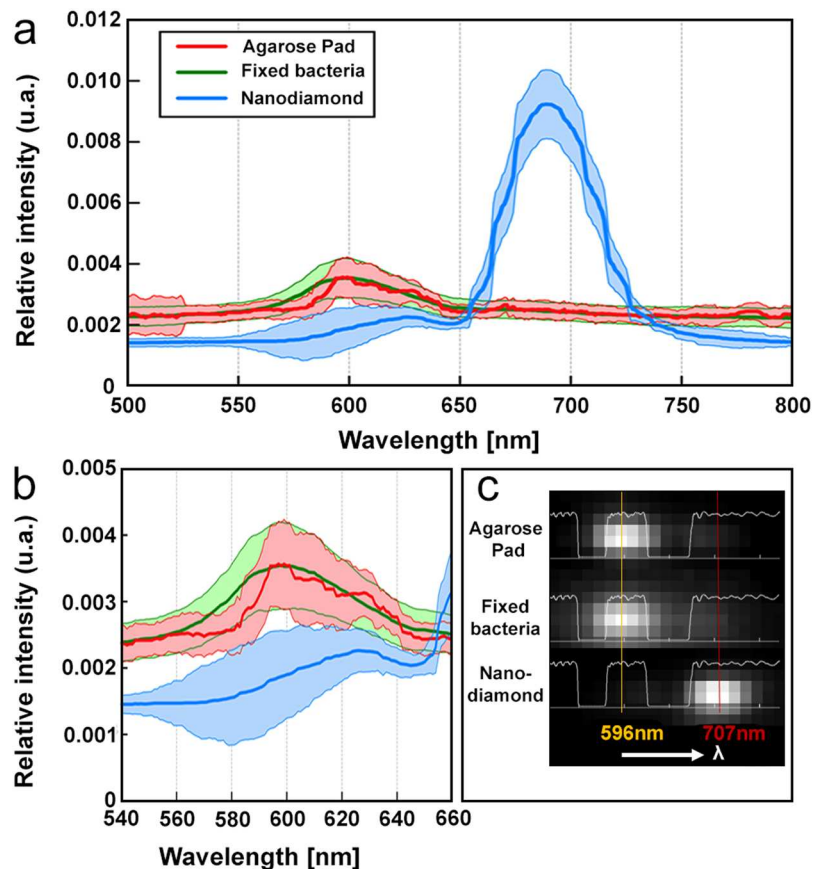


Figure 4. Single-molecule spectral imaging of molecules on the surface of the agarose pads (red), of autoblanking molecules in fixed *D. radiodurans* cells (green), and of nanodiamonds (blue). (a) Average emission spectra (500 nm to 825 nm) derived from 34, 1221 and 1013 individual spectra respectively. (b) Inset of (a) focusing on the 540 nm to 660 nm wavelength range. (c) Examples of raw spectra produced by molecules on the agarose pad, within fixed bacterial samples and by nanodiamonds. In light white is represented the Quad band notch spectrum used for the acquisition on the spectral channel.

noteworthy that throughout our study, we noticed that conditioning (in glass vs. plastic) and/or age of chemicals used for sample preparation also influenced the autoblanking levels (Supplementary Fig. S7).

Having determined that the growth medium is the principal source of autoblanking molecules, we set out to determine which part of the bacterial cell wall preferentially traps these fluorophores. As illustrated in Supplementary Fig. S3, *D. radiodurans* possesses a complex cell wall composed of multiple layers. The S-layer and carbohydrate layer are only present in the external cell periphery and not in the internal cell septa^{21,34}. As we can see in Fig. 2 and Supplementary Fig. S1, autoblanking molecules efficiently label both the external and internal cell walls, indicating that it must be associated with either the peptidoglycan layer and/or the plasma membrane. We thus examined the levels and distribution of autoblanking in *D. radiodurans* cells treated with either lysozyme, an enzyme known to digest both the carbohydrate and the peptidoglycan layers of bacterial cell walls, or with Triton X-100, a common detergent used to disrupt membrane bilayers (Supplementary Fig. S8). The autoblanking distribution was essentially unaffected by lysozyme treatment, while in contrast, Triton X-100 led to a complete loss of cell wall labelling. These findings strongly suggest that autoblanking molecules bind to the plasma membrane, in line with the very similar images obtained when using the lipid binding dye, Nile Red (Supplementary Fig. S1). Although all bacteria possess such a lipidic membrane, the species-dependent levels of autoblanking observed in different bacteria may nonetheless be explained by the particular structure and chemical nature of their cell walls, which may differentially affect accessibility to the plasma membrane.

Autoblanking mechanism and photophysics. We next set out to characterize the properties of the autoblanking molecules and compare them with those of PAmCherry, a classical photoactivatable red fluorescent protein (PAFP) routinely used in PALM experiments, which we expressed in *D. radiodurans*. Photophysical parameters extracted from the analysis of single-molecule fluorescence traces³⁵ are listed in Supplementary Tables S1 and S2 and histograms of the distribution of single-molecule photon counts are provided in Supplementary Fig. S9. Under 561 nm illumination (0.8 kW/cm²), autoblanking fluorophores delivered a mean number of photons per localization event approx. equal to that of PAmCherry, while the total photon count was about half that of PAmCherry (Supplementary Table S1). Interestingly, autoblanking fluorophores could be

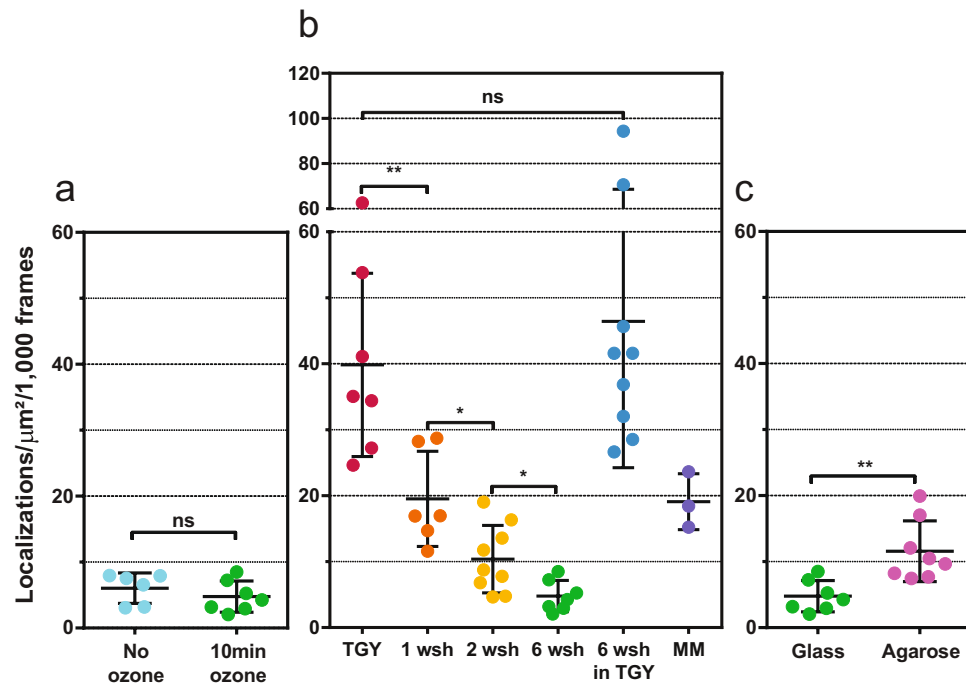


Figure 5. Comparative study of the autoblinking levels in fixed, unlabeled *D. radiodurans* cells. (a) Effect of ozone treatment of glass coverslides on the number of localizations in cells per μm^2 per 1000 frames. (b) Effect of TGY growth medium and washes with highly pure PBS prior to sample mounting on the number of localizations in cells per μm^2 per 1000 frames. TGY grown cells were either deposited directly between coverslides (TGY) or were washed once (1 wsh), twice (2 wsh) or 6 times (6 wsh) prior to imaging. A sample of cells washed 6 times with PBS was also resuspended again in TGY medium (6 wsh in TGY) before imaging. Cells initially grown in TGY and then transferred to minimal medium (MM) for 24 hours were also imaged. (c) Effect of the agarose pad on the number of localizations in cells per μm^2 per 1000 frames. All images were acquired with a 50 ms framerate under continuous 0.8 kW/cm^2 561 nm laser. Individual data points correspond to the autoblinking levels derived from a given stack of images. Means and standard deviations are plotted in the graph.

successfully observed upon excitation with 488 nm, 561 nm, and to a lesser extent 643 nm lasers and thus exhibit a wide excitation spectrum (Supplementary Table S2 and Fig. S9).

In contrast to PAmCherry, the apparent rate of activation of autoblinking molecules was found to be (i) constant overtime, (ii) insensitive to the use of additional 405 nm light, and (iii) independent of the readout laser power (Fig. 6). These observations demonstrate that autoblinking molecules decorate *D. radiodurans* cell walls by transient binding, thus allowing super-resolution imaging through Point Accumulation for Imaging in Nanoscale Topography (PAINT)³⁶. This finding was corroborated by the observation that the apparent bleaching rate of autoblinking molecules ($\sim 18\text{ s}^{-1}$) was essentially independent of the applied readout laser power (Supplementary Table S3), thus being driven by fluorophore unbinding rather than bleaching or reversible dark state formation.

As the membrane dye Nile Red is also classically used for PAINT imaging, we compared its photophysical properties to those of autoblinking molecules (Supplementary Table S3). To this aim, the concentration of Nile Red was adjusted so that 90% of localizations originated from this dye, and only 10% from autoblinking molecules. Two interesting differences between the two dyes were noticed. Firstly, the average unbinding rate of Nile Red molecules was 15% higher than that of autoblinking molecules. Secondly, contrary to autoblinking molecules, the apparent activation rate of Nile Red molecules progressively decayed along data acquisition (Fig. 6a), suggesting a depletion of the pool of available molecules for binding, possibly associated to a higher susceptibility to photobleaching. Thus the properties of autoblinking molecules make them more favorable for single particle tracking (spt) than Nile Red (see Supplementary Methods).

PALM imaging in the presence of autoblinking. To test whether PALM imaging of a specific molecular target labeled with a photo-transformable fluorescent protein (PTFP) can nonetheless be achieved in the presence of autoblinking, we attempted to overrun the phenomenon by taking advantage of the relatively low binding rate of autoblinking molecules and of their lack of response to a 405 nm laser. We imaged wild-type *D. radiodurans* cells either transformed with a plasmid expressing low levels of PAmCherry or genetically-modified to express the highly abundant nucleoid-associated HU protein³⁷ fused to PAmCherry. In the first case, illumination at both 405 nm (0.4 W/cm^2) and 561 nm (0.8 kW/cm^2) combined with the use of short frametimes ($\sim 5\text{ ms}$, also serving to freeze the movement of the rapidly diffusing PAmCherry molecules) allowed acquiring high-quality PAmCherry images in less than a minute, at the expense of a reduced field of view but keeping the amount of autoblinking

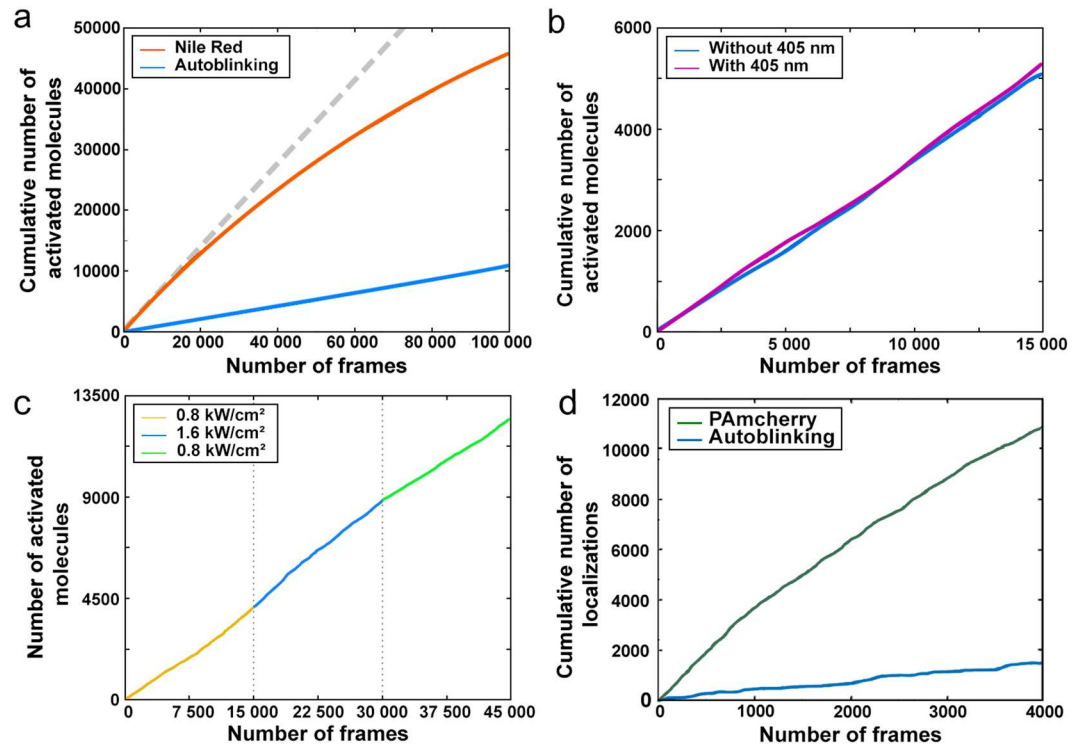


Figure 6. Photophysical properties of autoblinding molecules. (a) Cumulative number of autoblinding molecules (blue) under constant 561 nm laser illumination (0.8 kW/cm^2), compared to Nile Red (orange). Accumulation of autoblinding molecules follows a linear regression, while that of Nile Red progressively slows down during the data acquisition. (b) Cumulative number of activated autoblinding molecules under constant 561 nm laser illumination (0.8 kW/cm^2) in the presence (violet) and absence (blue) of constant 405 nm illumination. (c) Cumulative number of activated autoblinding molecules under varying 561 nm laser illumination (0.8 kW/cm^2 , yellow; 1.6 kW/cm^2 , blue; 0.8 kW/cm^2 , green). Accumulation of autoblinding molecules follows a linear progression and is only marginally affected by the increased laser power. (a–c) Images were acquired with a 50 ms timeframe. (d) Cumulative number of localizations of cytoplasmic PAmCherry (green) expressed in *D. radiodurans* and of autoblinding molecules (blue). PAmCherry localizations were acquired first using a 5 ms timeframe, constant 561 nm illumination (0.8 kW/cm^2) and varying 405 nm laser, and once all the PAmCherry molecules had been bleached, the autoblinding molecules were imaged under constant 561 nm illumination (0.8 kW/cm^2) and with 50 ms timeframes.

signal sufficiently low (Supplementary Fig. S10). In the second case, “readout activation” by the 561 nm laser alone³⁸ was sufficient to rapidly collect a PAmCherry image and outrun autoblinding (Fig. 7).

Next, we set out to investigate whether two-color PALM/PAINT images could be acquired by using both the signals of PAmCherry and that of autoblinding, as reported previously using PAmCherry-labelled proteins and the membrane dye Nile Red in fixed *E. coli* cells³⁹. In the case of low PAmCherry expression (Fig. 7a–c), an autoblinding-based image of the bacterial cell wall could be collected before the PAmCherry image by first exciting the sample at 561 nm (0.5 kW/cm^2), in the absence of 405 nm illumination, and with a standard 50 ms timeframe. The PAmCherry image was then collected as described above, using 405 nm illumination and a reduced timeframe (~ 5 ms) compensated by a stronger 561 nm laser power density (2 kW/cm^2), so as to outrun the binding rate of autoblinding molecules. This data collection strategy shows similarities to that recently proposed for two-color experiments based on primed photoconversion⁴⁰. The resulting two-color image (Fig. 7c), free of chromatic aberrations, suggests that PAmCherry molecules are not uniformly distributed throughout the cytoplasm, but rather tend to accumulate close to the periphery of the cell, possibly as a result of exclusion by the highly condensed nucleoid of *D. radiodurans* cells²⁰.

In the case of the highly abundant HU-PAmCherry fusion protein (Fig. 7d–f), strong readout activation by the 561-nm light prevented imaging of autoblinding molecules without significant cross talk with PAmCherry signals. However, we relied on the spectral differences between the autoblinding molecules and PAmCherry to image autoblinding using a 643 nm laser (Fig. 7d). Although not ideal, since autoblinding molecules are rather weakly excited at this wavelength, this strategy provided a two-color image in which the *D. radiodurans* nucleoids could clearly be positioned relative to the surrounding cell wall (Fig. 7f).

Overall, our experiments demonstrate that PALM imaging of a specific target labeled with a PTFP is possible in *D. radiodurans* despite the autoblinding phenomenon, and that under suitable conditions, autoblinding could in fact be used for complementary cell wall imaging in single- or two-color PALM/PAINT experiments.

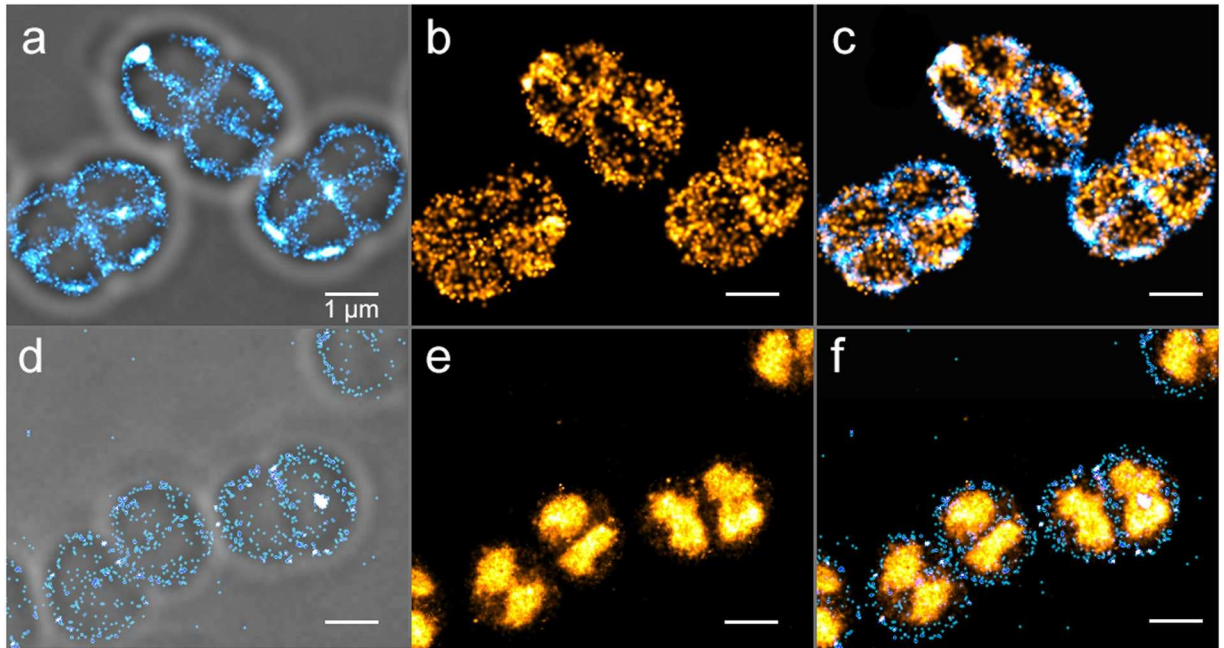


Figure 7. Two-color PALM/PAINT imaging of *D. radiodurans*. (a–c) PALM/PAINT imaging of *D. radiodurans* cells expressing cytoplasmic PAmCherry. (a) Autoblinking-based PAINT image (50 ms framerate; 561 nm laser only), superimposed on the brightfield image. (b) PAmCherry-based PALM image (4.8 ms framerate; 561 nm plus 405 nm lasers). (c) Superimposed image of (a) and (b). (d–f) PALM/PAINT imaging of *D. radiodurans* cells expressing PAmCherry fused to HU. (d) Autoblinking-based PAINT image (50 ms framerate; 643 nm laser), superimposed on the brightfield image. (e) PAmCherry-based PALM image (50 ms framerate; 561 nm laser). (f) Superimposed image of (d) and (e). Scale bar: 1 μm .

Interestingly, by deliberately choosing sample preparation conditions favoring high levels of autoblinking, we could acquire remarkably well-defined images of *D. radiodurans* cell walls in which the double-layered internal septa can clearly be visualized (Fig. 8a). We hypothesize that the improved resolution and quality of these images result from the high density of autoblinking molecules allowing to acquire an image stack rapidly, thereby minimizing image blurring due to residual motion of the live cells.

Insight into septum formation and cell wall structure in *D. radiodurans*. *D. radiodurans* is a spherical bacterium that divides in alternating perpendicular planes⁴¹. Our autoblinking-based SMLM images of the cell wall of live *D. radiodurans* provide unprecedented views of the morphology of these bacteria along their cell cycle (Fig. 8a and Supplementary Fig. S1). Four different stages can be distinguished, that provide snapshots of growing internal septa. In stage 1, *D. radiodurans* cells are in the form of diads with a single internal septum separating the two cells; in stage 2, foci at the positions of future septa become visible, perpendicular to the previous cell division plane; in stage 3, newly forming septa are closing; and in stage 4, these new septa are closed and *D. radiodurans* cells form tetrads that will rapidly separate into two diads for a new cell cycle.

Figure 8a clearly shows that the density of autoblinking molecules is not homogeneous throughout the cell wall. To further explore these heterogeneities, we performed a cluster analysis using the SR-Tesseler software⁴². We computed potential clusters using a threshold $\delta > 2\delta_N$, where δ_N is the average autoblinking molecular density in the analyzed fields of view. Identified ‘clusters’ located preferentially within the internal septa of the bacteria and at sites of new septa formation (Fig. 8b). Their broad size distribution and constant molecular density (Fig. 8c) suggest that autoblinking molecules do not form clusters with a preferential radius in *D. radiodurans*, but instead bind to septal regions at a faster apparent rate, likely as a result of a higher concentration of binding sites in the double-layered structure of the cell wall in these regions. In addition, as shown in Supplementary Fig. S2, the lower curvature of the cell wall at the septum also contributes to the increased apparent molecular density.

Interestingly, visual inspection of the fluorescent traces of the autoblinking molecules revealed that some of them appeared to be largely immobile, while others seemed to diffuse around the periphery of the cells. A few immobile molecules remained visible for more than 1 s (number of localizations >20 ; Supplementary Fig. S11), producing autoblinking ‘hotspots’. These observations hinted that autoblinking molecules may display several diffusion regimes depending on their localization within the cell wall, and potentially in relation with the different observed stages of cell division. To investigate this, several sptPAINT data sets were acquired and analyzed, in which the trajectories of individual autoblinking molecules were reconstituted (Fig. 8d). Cumulative probability distribution (CPD) analysis⁴³ of more than 1000 individual tracks extracted from multiple datasets revealed that two distinct populations of molecules could be distinguished. No specific distribution of these two populations throughout the cell wall could be observed (Fig. 8d). Approx. half of the molecules displayed an average apparent diffusion coefficient of $\sim 0.065 \mu\text{m}^2/\text{s}$ and were clearly seen to move along the cell wall with a confinement

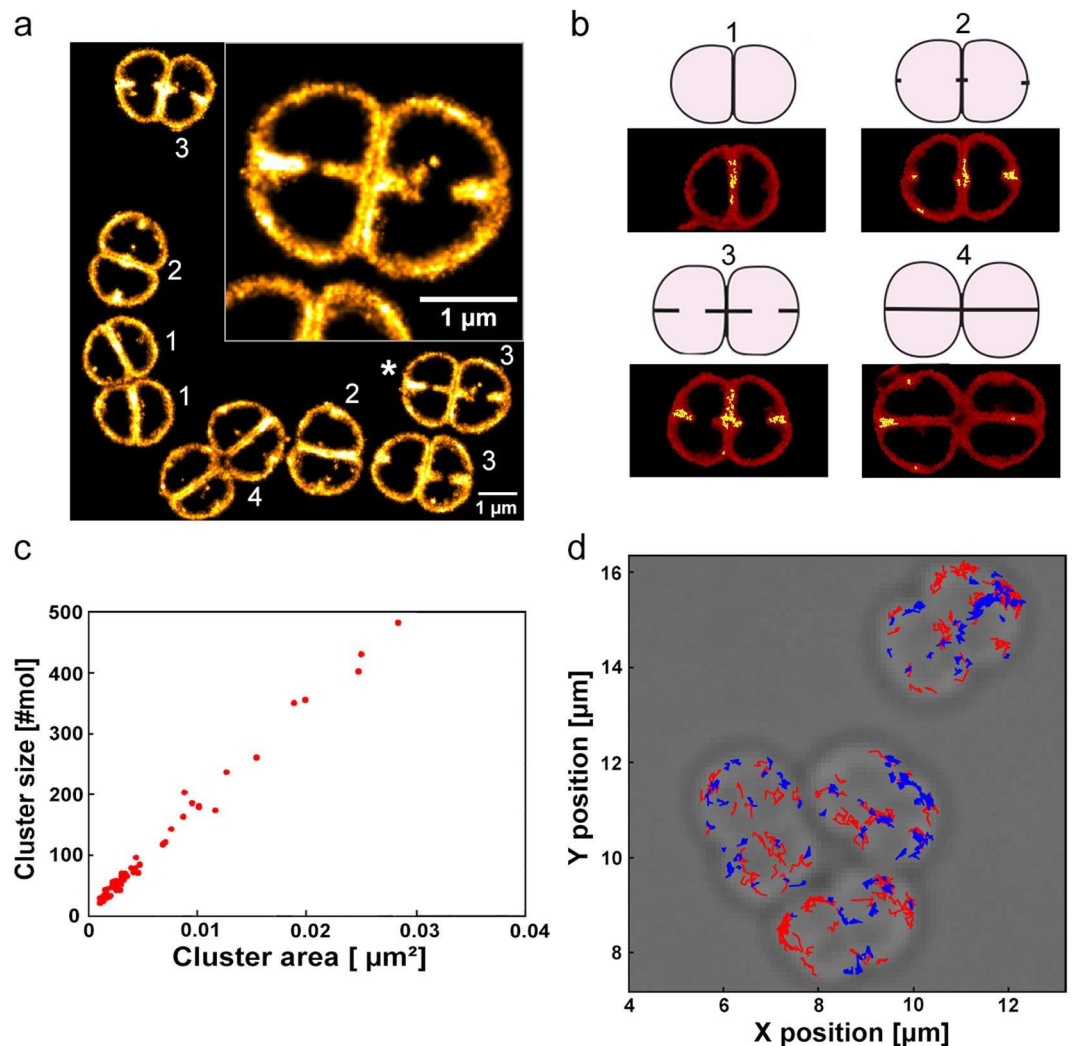


Figure 8. Cell division and septa formation in *D. radiodurans*. (a) Autoblinking-based PAINt image (15 ms framerate; 561 nm laser) of exponentially growing, live, unlabeled *D. radiodurans* cells. Bacteria are seen at different stages of their division cycle shown schematically in (b). Scale bar: 1 μm. Inset: close-up view of a *D. radiodurans* diad (indicated with a *) in which the double-layered cell wall separating the two bacteria can clearly be seen. (b) Schematic representations of *D. radiodurans* morphology along its cell cycle. Representative bacteria in each stage are shown in red as Voronoi diagrams following cluster analysis of the image shown in (a). Identified clusters are highlighted in yellow. (c) Number of autoblinking molecules per cluster as a function of cluster area. (d) Individual tracks of autoblinking molecules superimposed on the corresponding brightfield image. The faster and slower diffusing molecules are shown in red and blue respectively.

radius of ~250 nm, whereas another half were nearly immobile, exhibiting an apparent diffusion coefficient of ~0.014 μm²/s that can be accounted for solely by their localization uncertainty (Supplementary Figs S12, S13 and Table S4).

Together, these data demonstrate that autoblinking is a powerful tool for imaging *D. radiodurans* cell walls and for following septa formation, but also for probing the structural and chemical complexity of the multiple layers composing these unusual cell walls.

Discussion

In this work, we have confirmed that many bacteria show a tendency for autoblinking, which should be carefully taken into consideration when analyzing SMLM data. We have discovered that *D. radiodurans* and *D. deserti* stand out amongst the tested bacteria, by exhibiting particularly strong autoblinking. Our data demonstrate that the autoblinking phenomenon is caused by transient binding of fluorescent molecules originating mostly from the growth medium to bacterial cell walls in a PAINt-based regime. Agarose was also found to be a source of autoblinking molecules to a lesser extent, in contrast to the impurities commonly observed on uncleaned coverslips, which did not contribute to autoblinking levels. We hypothesize that autoblinking molecules might have a common origin linked to contact with plastic materials. This could explain why older stocks of chemicals result in increased levels of autoblinking. Until the exact nature of the autoblinking molecules is revealed, it cannot be

excluded that they are composed from a heterogenous pool of molecules with different spectral and photophysical properties. Finally, we almost never detected such molecules as single emitters in the extracellular medium. This could be explained by their fast diffusion in the liquid phase and/or by their possible fluorogenicity whereby their fluorescence would be enhanced upon binding to specific environments such as lipid bilayers or agarose.

The strong binding in the case of *D. radiodurans* and *D. deserti* probably results from the unusual cell wall composition of these microorganisms. *D. radiodurans* stains Gram-positive, but its cell wall does not resemble that of classical Gram-positive bacteria, as it is composed of five different layers^{21,29} (Supplementary Fig. S3). Although our reconstructed images of *D. radiodurans* cell walls do not permit us to directly identify which layer of the cell wall is preferentially bound by autoblinding molecules, several observations indicate that it is likely to be the plasma membrane: (i) autoblinding molecules are found in both the external cell wall and the internal septa of *D. radiodurans* cells, suggesting that they are most likely not binding to the carbohydrate and pink envelope layers that are only found on the external periphery of the bacterial diads or tetrads, (ii) the density of autoblinding molecules is increased in the internal septa in agreement with the peptidoglycan and plasma membrane layers being doubled in these regions, and (iii) treatment of cells with the detergent, Triton X-100, but not with lysozyme, which degrades the peptidoglycan layer, disrupts the localization of the autoblinding molecules to the cell wall. Although *D. deserti*'s cell wall has not been as thoroughly characterized as *D. radiodurans*'s, it has also been shown to possess a similarly dense cell wall, which may also favor the binding and trapping of autoblinding molecules within a lipid-containing layer.

Autoblinding in bacteria in general, and in *D. radiodurans* in particular, offers both advantages and disadvantages. The possibility to achieve label free nanoscale imaging of the bacterial cell wall is of definite potential interest. Precisely delineating the boundaries of bacterial cells being imaged using super-resolution techniques is critical for image analysis and data interpretation. Differential interference contrast or brightfield images superimposed onto fluorescence nanoscopy images typically provide inaccurate cell boundaries (see Fig. 2d), in particular due to high sensitivity of such images to the axial position of the sample relative to the focal plane. In addition, such images do not allow distinguishing changes in cell wall structure or newly forming septa during cell division. Observing such morphological features typically requires extra manipulation of the sample such as addition of a lipid targeting dye that is suitable for single-molecule localization imaging. Autoblinding, in contrast allows achieving label-free imaging of the cell wall of live *D. radiodurans* cells at sub-diffraction resolution. In this way, unprecedented images of *D. radiodurans* could be obtained, providing snapshots of internal septa formation at various stages of the cell cycle. Moreover, analysis of autoblinding data allowed us to observe clear heterogeneities in the distribution and dynamics of autoblinding molecules within the cell wall that reflect the complex nature of this essential cell barrier.

Autoblinding molecules may advantageously be used for sptPAINT, notably because they sparsely decorate the cell wall of bacteria in a seemingly endless manner. In *D. radiodurans*, the high-level of autoblinding in fact prevents the use of another exogenous dye to perform single-particle tracking experiments, because a too high density of labeling would be required to hide the contribution of autoblinding. In this bacterium, we observed two approximately equal populations of autoblinding molecules, one nearly immobile and one diffusing along the cell wall periphery with an apparent diffusion coefficient of $0.06 \mu\text{m}^2/\text{s}$. In *E. coli*, it was shown that different lipid binding dyes may exhibit different diffusion behaviors, and that the dye DiI-C12 displays two diffusion regimes, pointing at heterogeneities in the bacterial membrane⁴⁴. Moreover, autoblinding molecules in *E. coli* were also recently found to diffuse with a diffusion coefficient close to $0.06 \mu\text{m}^2/\text{s}$ ⁴⁴. Our results in *D. radiodurans* possibly suggest that heterogeneities in the plasma membrane of this bacterium also exist. However, we cannot exclude that this could also result from the possible inherent heterogeneity in the autoblinding molecules themselves. In addition, the absolute values of our diffusion coefficients should be taken with care, due to the relatively long frametimes that we used (30 ms)⁴⁵, effects of diffusion in 3D⁴⁴, and the difficulty to accurately extract several populations of molecules experiencing confined diffusion regimes by currently available software. Further work will be required to establish the full potential of the autoblinding phenomenon for sptPAINT.

In this study, we never totally silenced autoblinding, but we succeeded in minimizing it using well-defined sample preparation routines and carefully planned imaging schemes, taking into account the unusual photophysical characteristics of autoblinding molecules, in order to successfully image PTFP-labelled targets expressed in *D. radiodurans*. The thorough characterization of the autoblinding molecules, nonetheless, clearly reveals a single-molecule behavior that significantly overlaps with those of PTFPs typically used in PALM bacterial imaging such as PAmCherry. This makes the strict discrimination between them and PTFP-labeled targets challenging, particularly in the case of colocalization with cell wall associated low abundance target proteins. In such cases, it would be recommended to use alternative imaging protocols such as dSTORM, with bright organic fluorophores emitting light in the far-red region of the spectrum. However, in the future, resonant out-of-phase fluorescence microscopy⁴⁶ or improvements in spectroscopic SMLM could enable differentiating autoblinding molecules and fluorescent proteins at the single molecule level. In general, the autoblinding phenomenon offers exciting prospects for multicolor semi-label free nanoscopy of bacteria.

Methods

Detailed methods are provided in Supplementary Methods. **Bacterial cultures:** *Deinococcus radiodurans* strains were grown at 30 °C in either TGY2X or in minimal medium as described previously⁴⁷. *Deinococcus deserti* VCD115 strain was grown as described earlier⁴⁸. *Bacillus subtilis* and *Escherichia coli* strains were grown at 37 °C in respectively TGY and LB medium. **Single-molecule imaging:** State-of-the-art cleaning protocols were used for sample preparation^{3,49}. Images were acquired at 20 °C with a home-built PALM setup based on an Olympus IX81 microscope (Olympus) and equipped with diode-pumped solid-state lasers at 405 nm (CrystaLaser), 488 nm (Spectra-Physics), 561 nm (Cobolt) and 643 nm (Toptica Photonics). Fluorescence images were acquired with an Evolve 512 back-illuminated EMCCD camera (Photometrics) controlled by the

Metamorph software (Molecular Devices). Sample drift was corrected in ImageJ using gold nanobeads (Sigma) deposited on the agarose pads. Autoblanking events were analyzed with the ThunderStorm analysis plugin⁵⁰ in Fiji⁵¹. Single-molecule data were processed as described previously³⁵. For spectral imaging, the optical set-up was built similarly to the set-up described by Zhang *et al.*³³. Localization and evaluation of the spectral properties of the detected single molecules was done on a home-made software and compiled as a plugin of the MetaMorph software (Molecular Device).

Data Availability

All data generated and analyzed in this study are either included in this published article (and its Supplementary Information files) or available from the corresponding authors on reasonable request.

References

- Coltharp, C. & Xiao, J. Superresolution microscopy for microbiology. *Cellular microbiology* **14**, 1808–1818 (2012).
- Gahlmann, A. & Moerner, W. Exploring bacterial cell biology with single-molecule tracking and super-resolution imaging. *Nature Reviews. Microbiology* **12**, 9 (2014).
- Liao, Y., Schroeder, J. W., Gao, B., Simmons, L. A. & Biteen, J. S. Single-molecule motions and interactions in live cells reveal target search dynamics in mismatch repair. *Proceedings of the National Academy of Sciences* **112**, E6898–E6906 (2015).
- Stracy, M. *et al.* Single-molecule imaging of UvrA and UvrB recruitment to DNA lesions in living *Escherichia coli*. *Nature communications* **7** (2016).
- Fu, G. *et al.* In vivo structure of the *E. coli* FtsZ-ring revealed by photoactivated localization microscopy (PALM). *Plos one* **5**, e12680 (2010).
- Stracy, M. *et al.* Live-cell superresolution microscopy reveals the organization of RNA polymerase in the bacterial nucleoid. *Proceedings of the National Academy of Sciences* **112**, E4390–E4399 (2015).
- Kim, S. Y., Gitai, Z., Kinkhabwala, A., Shapiro, L. & Moerner, W. Single molecules of the bacterial actin MreB undergo directed treadmilling motion in *Caulobacter crescentus*. *Proceedings of the National Academy of Sciences* **103**, 10929–10934 (2006).
- Betzig, E. *et al.* Imaging intracellular fluorescent proteins at nanometer resolution. *Science* **313**, 1642–1645 (2006).
- Hess, S. T., Girirajan, T. P. & Mason, M. D. Ultra-high resolution imaging by fluorescence photoactivation localization microscopy. *Biophysical journal* **91**, 4258–4272 (2006).
- Rust, M. J., Bates, M. & Zhuang, X. Sub-diffraction-limit imaging by stochastic optical reconstruction microscopy (STORM). *Nature methods* **3**, 793–795 (2006).
- Huang, B., Wang, W., Bates, M. & Zhuang, X. Three-dimensional super-resolution imaging by stochastic optical reconstruction microscopy. *Science* **319**, 810–813 (2008).
- Endesfelder, U. *et al.* Multiscale spatial organization of RNA polymerase in *Escherichia coli*. *Biophysical journal* **105**, 172–181 (2013).
- Manley, S. *et al.* High-density mapping of single-molecule trajectories with photoactivated localization microscopy. *Nature methods* **5**, 155–157 (2008).
- Leon, F. G., de, Sellars, L., Stracy, M., Busby, S. J. & Kapanidis, A. N. Tracking low-copy transcription factors in living bacteria: the case of the lac repressor. *Biophysical journal* **112**, 1316–1327 (2017).
- Tuson, H. H., Aliaj, A., Brandes, E. R., Simmons, L. A. & Biteen, J. S. Addressing the Requirements of High-Sensitivity Single-Molecule Imaging of Low-Copy-Number Proteins in Bacteria. *Chem Phys Chem* **17**, 1435–1440 (2016).
- Battista, J. R. Against all odds: the survival strategies of *Deinococcus radiodurans*. *Annual Reviews in Microbiology* **51**, 203–224 (1997).
- Blasius, M., Hübscher, U. & Sommer, S. *Deinococcus radiodurans*: what belongs to the survival kit? *Critical reviews in biochemistry and molecular biology* **43**, 221–238 (2008).
- Makarova, K. S. *et al.* Genome of the extremely radiation-resistant bacterium *Deinococcus radiodurans* viewed from the perspective of comparative genomics. *Microbiology and Molecular Biology Reviews* **65**, 44–79 (2001).
- Cox, M. M., Keck, J. L. & Battista, J. R. Rising from the ashes: DNA repair in *Deinococcus radiodurans*. *Plos genetics* **6**, e1000815 (2010).
- Levin-Zaidman, S. *et al.* Ringlike structure of the *Deinococcus radiodurans* genome: a key to radioresistance? *Science* **299**, 254–256 (2003).
- Rothfuss, H., Lara, J. C., Schmid, A. K. & Lidstrom, M. E. Involvement of the S-layer proteins Hpi and SlpA in the maintenance of cell envelope integrity in *Deinococcus radiodurans* R1. *Microbiology* **152**, 2779–2787 (2006).
- Slade, D. & Radman, M. Oxidative stress resistance in *Deinococcus radiodurans*. *Microbiology and molecular biology reviews* **75**, 133–191 (2011).
- Tian, B. & Hua, Y. Carotenoid biosynthesis in extremophilic *Deinococcus-Thermus* bacteria. *Trends in microbiology* **18**, 512–520 (2010).
- Timmins, J. & Moe, E. A Decade of Biochemical and Structural Studies of the DNA Repair Machinery of *Deinococcus radiodurans*: Major Findings, Functional and Mechanistic Insight and Challenges. *Computational and structural biotechnology journal* **14**, 168–176 (2016).
- Work, E. & Griffiths, H. Morphology and chemistry of cell walls of *Micrococcus radiodurans*. *Journal of bacteriology* **95**, 641–657 (1968).
- Banterle, N., Bui, K. H., Lemke, E. A. & Beck, M. Fourier ring correlation as a resolution criterion for superresolution microscopy. *Journal of structural biology* **183**, 363–367 (2013).
- Nieuwenhuizen, R. P. *et al.* Measuring image resolution in optical nanoscopy. *Nature methods* **10**, 557–562 (2013).
- Farci, D., Slavov, C., Tramontano, E. & Piano, D. The S-layer protein DR_2577 binds deinoxanthin and under desiccation conditions protects against UV-radiation in *Deinococcus radiodurans*. *Frontiers in microbiology* **7** (2016).
- Farci, D. *et al.* New features of the cell wall of the radio-resistant bacterium *Deinococcus radiodurans*. *Biochimica et Biophysica Acta (BBA)-Biomembranes* **1838**, 1978–1984 (2014).
- Zhang, L. *et al.* Knockout of crtB or crtI gene blocks the carotenoid biosynthetic pathway in *Deinococcus radiodurans* R1 and influences its resistance to oxidative DNA-damaging agents due to change of free radicals scavenging ability. *Archives of microbiology* **188**, 411–419 (2007).
- Albermann, C. High versus low level expression of the lycopene biosynthesis genes from *Pantoea ananatis* in *Escherichia coli*. *Biotechnology letters* **33**, 313–319 (2011).
- Gillbro, T. & Cogdell, R. J. Carotenoid fluorescence. *Chemical Physics Letters* **158**, 312–316 (1989).
- Zhang, Z., Kenny, S. J., Hauser, M., Li, W. & Xu, K. Ultrahigh-throughput single-molecule spectroscopy and spectrally resolved super-resolution microscopy. *Nature methods* **12**, 935–938 (2015).
- Thornley, M. J., Horne, R. & Glauert, A. M. The fine structure of *Micrococcus radiodurans*. *Archiv für Mikrobiologie* **51**, 267–289 (1965).
- Avilov, S. *et al.* In cellulo evaluation of phototransformation quantum yields in fluorescent proteins used as markers for single-molecule localization microscopy. *Plos one* **9**, e98362 (2014).

36. Sharonov, A. & Hochstrasser, R. M. Wide-field subdiffraction imaging by accumulated binding of diffusing probes. *Proceedings of the National Academy of Sciences* **103**, 18911–18916 (2006).
37. Bouthier de la Tour, C. *et al.* The abundant and essential HU proteins in *Deinococcus deserti* and *Deinococcus radiodurans* are translated from leaderless mRNA. *Microbiology* **161**, 2410–2422 (2015).
38. Thédié, D., Berardozi, R., Adam, V. & Bourgeois, D. Photoswitching of Green mEos2 by Intense 561 nm Light Perturbs Efficient Green-to-Red Photoconversion in Localization Microscopy. *The Journal of physical chemistry letters* **8**, 4424–4430 (2017).
39. Spahn, C., Cella-Zannacchi, F., Endesfelder, U. & Heilemann, M. Correlative super-resolution imaging of RNA polymerase distribution and dynamics, bacterial membrane and chromosomal structure in *Escherichia coli*. *Methods and Applications in Fluorescence* **3**, 014005 (2015).
40. Mohr, M. A. *et al.* Rational Engineering of Photoconvertible Fluorescent Proteins for Dual-Color Fluorescence Nanoscopy Enabled by a Triplet-State Mechanism of Primed Conversion. *Angewandte Chemie (International ed. in English)* **56**, 11628–11633 (2017).
41. Murray, R., Hall, M. & Thompson, B. Cell division in *Deinococcus radiodurans* and a method for displaying septa. *Canadian journal of microbiology* **29**, 1412–1423 (1983).
42. Levet, F. *et al.* SR-Tesseler: a method to segment and quantify localization-based super-resolution microscopy data. *Nature methods* **12**, 1065–1071 (2015).
43. Matysik, A. & Kraut, R. S. TrackArt: the user friendly interface for single molecule tracking data analysis and simulation applied to complex diffusion in mica supported lipid bilayers. *BMC research notes* **7**, 274 (2014).
44. Oswald, F., Varadarajan, A., Lill, H., Peterman, E. J. & Bollen, Y. J. MreB-dependent organization of the *E. coli* cytoplasmic membrane controls membrane protein diffusion. *Biophysical journal* **110**, 1139–1149 (2016).
45. Lill, Y. *et al.* Single-molecule study of molecular mobility in the cytoplasm of *Escherichia coli*. *Physical Review E* **86**, 021907 (2012).
46. Quérard, J. *et al.* Resonant out-of-phase fluorescence microscopy and remote imaging overcome spectral limitations. *Nature communications* **8**, 969 (2017).
47. Venkateswaran, A. *et al.* Physiologic Determinants of Radiation Resistance in *Deinococcus radiodurans*. *Applied and environmental microbiology* **66**, 2620–2626 (2000).
48. De Groot, A. *et al.* *Deinococcus deserti* sp. nov., a gamma-radiation-tolerant bacterium isolated from the Sahara Desert. *International journal of systematic and evolutionary microbiology* **55**, 2441–2446 (2005).
49. Haas, B. L., Matson, J. S., DiRita, V. J. & Biteen, J. S. Imaging live cells at the nanometer-scale with single-molecule microscopy: obstacles and achievements in experiment optimization for microbiology. *Molecules* **19**, 12116–12149 (2014).
50. Ovesn, M., Krížek, P., Borkovec, J., Švindrych, Z. & Hagen, G. M. ThunderSTORM: a comprehensive ImageJ plug-in for PALM and STORM data analysis and super-resolution imaging. *Bioinformatics* **30**, 2389–2390 (2014).
51. Schindelin, J. *et al.* Fiji: an open-source platform for biological-image analysis. *Nature methods* **9**, 676–682 (2012).

Acknowledgements

We thank Geneviève Coste for technical assistance in the preparation of genetically engineered strains ($\Delta crtI$ and HU::PamCherry) of *D. radiodurans*. We are very grateful to Prof. Bing Tian from Zhejiang University, China, for providing us with the $\Delta crtB$ strain of *D. radiodurans*. We also wish to thank Dr. Laurence Blanchard and Dr. Arjan De Groot from CEA Cadarache for providing us with the *D. deserti* strain VCD115, Prof. Georg Sprenger from Stuttgart University, Germany, for providing us with the BW-Lyco strain of *E. coli* K12, and Dr. Cécile Morlot from IBS, Grenoble for providing us with *B. subtilis*. This work was supported by FranceBioImaging infrastructure ANR-10-INBS-04, CEA Radiobiology grant (A-IRBIO-01-19), EuroBioImaging, the LabEx BRAIN to J.-B.S. This work used the M4D imaging platform of the Grenoble Instruct-ERIC Center (ISBG: UMS 3518 CNRS-CEA-UGA-EMBL) with support from FRISBI (ANR-10-INBS-05-02) and GRAL (ANR-10-LABX-49-01) within the Grenoble Partnership for Structural Biology (PSB).

Author Contributions

K.F., D.B. and J.T. designed the research and analyzed the data. K.F., F.L., L.B., P.S. and R.G. performed the experiments. C.B., R.G. and J.B.S. designed the single-molecule spectral imaging microscopy set-up and analyzed the spectral imaging data. K.F., D.B. and J.T. wrote the manuscript with contributions from R.G. and J.B.S. All authors discussed the results and approved the manuscript.

Additional Information

Supplementary information accompanies this paper at <https://doi.org/10.1038/s41598-018-32335-z>.

Competing Interests: The authors declare no competing interests.

Publisher's note: Springer Nature remains neutral with regard to jurisdictional claims in published maps and institutional affiliations.



Open Access This article is licensed under a Creative Commons Attribution 4.0 International License, which permits use, sharing, adaptation, distribution and reproduction in any medium or format, as long as you give appropriate credit to the original author(s) and the source, provide a link to the Creative Commons license, and indicate if changes were made. The images or other third party material in this article are included in the article's Creative Commons license, unless indicated otherwise in a credit line to the material. If material is not included in the article's Creative Commons license and your intended use is not permitted by statutory regulation or exceeds the permitted use, you will need to obtain permission directly from the copyright holder. To view a copy of this license, visit <http://creativecommons.org/licenses/by/4.0/>.

© The Author(s) 2018

Bacterial cell wall nanoimaging by autoblinking microscopy

Kevin Floc'h¹, Françoise Lacroix¹, Liliana Barbieri¹, Pascale Servant², Remi Galland^{3,4}, Corey Butler^{3,4}, Jean-Baptiste Sibarita^{3,4}, Dominique Bourgeois^{1*}, Joanna Timmins^{1*}

Supplementary Information

Supplementary Discussion

Supplementary Methods

Supplementary Tables S1-S4

Supplementary Movie S1

Supplementary Figures S1-S13

Supplementary References

Supplementary Discussion

Effect of the objective's depth of field on the observed width of the bacterial cell wall in 2-D super resolution images.

A careful observation of the *D. radiodurans* autoblinking images (Fig. 2c and e) suggests that the apparent resolution of these images is significantly affected by a projection effect of the curved 3-D cell wall onto the 2-D imaging plane. Such projection effect is not specific to *D. radiodurans* nor to the autoblinking process, but occurs for any 2-D super-resolution image of samples displaying a curvature along the optical axis that is significant within the objective depth of field. Thus, the effect is likely present in many super-resolved images of bacterial cell walls shown in the literature. Hence, we set out to perform simulations demonstrating the issue (Supplementary Fig. S2) and highlighting that our data are consistent with autoblinking molecules binding to very thin lipid-containing layers of the cell wall.

Using Matlab, we generated two different 3-D cylinders each decorated with 5000 randomly positioned fluorophores: one with a radius of curvature of 1.25 μm , close to the average radius of curvature of *D. radiodurans*, and one with a much larger radius of curvature of 5 μm . Both of these cylinders possessed a 10 nm thick wall. To perform the simulations, a homemade Matlab package was used¹ that allows generating localization microscopy data based on a comprehensive description of the microscope setup as well as the employed fluorophore's photophysics. The signal of each blinking fluorophore was thus

deformed according to the objective point spread function at its Z position, assuming a 1.49 NA objective exhibiting a depth of field of 500 nm. The outputs consisted of stacks of 10,000 images, similar to classical PALM stacks, which were subsequently processed in the same way as the other experimental data sets presented in this paper. The results presented in Supplementary Fig. S2 clearly show the expected effect, with the curved cylinder showing an effective thickness of ~80 nm and the straight cylinder showing a thickness of only ~40 nm. In Fig. S2e, the shape of the 1-D profile is clearly asymmetric on each side as a result of Z-projection. A similar shape can be observed in Fig. 2e, demonstrating the impact of the described effect.

Supplementary Methods

***Deinococcus radiodurans* strains**

A codon-optimized gene encoding PAmCherry was gene-synthesized (MWG Eurofins) and cloned into the plasmid p11559 for expression in *D. radiodurans* under the control of an IPTG-inducible *pSpac* promoter. Wild-type *D. radiodurans* cells (ATCC13939) were transformed with p11559-PAmCherry as described previously² and transformants were selected on TGY (Tryptone, Glucose, Yeast extract) agar plates containing 75 $\mu\text{g}\cdot\text{ml}^{-1}$ spectinomycin. The ΔcrtI strain (GY15501) and the genetically engineered strain of *D. radiodurans* expressing HU fused to PAmCherry (GY17031) were obtained by the tripartite ligation method³. Briefly, the gene encoding PAmCherry and the regions flanking the insertion site (3' end of *hu* gene, DR_A0065) were PCR amplified, and the three fragments were ligated together. *D. radiodurans* cells were then transformed by the ligation product and plated on selective medium containing 6 $\mu\text{g}\cdot\text{ml}^{-1}$ kanamycin, leading to allelic replacement on one genome copy. Because *D. radiodurans* is multigenomic, the transformant colonies were further streaked three times successively on selective medium to ensure that all copies of the genome had incorporated the foreign DNA.

Bacterial cultures

All *Deinococcus radiodurans* strains were grown at 30°C with shaking in either TGY2X or in minimal medium (MM) as described previously⁴. PAmCherry expression from the p11559 plasmid was induced by addition of 1mM IPTG to the cultures. For growth in MM, cells were initially grown in TGY2X and were transferred to MM at an optical density at 650nm (OD_{650}) of 0.2-0.4 and were incubated at 30°C for a further 24h to reach OD_{650} ~0.6-0.8. This procedure was repeated several times to allow the cells to adapt to growth in MM. *Deinococcus deserti* VCD115 strain was grown in diluted TSB (tryptic soy broth) medium supplemented with trace elements at 30°C with shaking as described previously⁵. *Bacillus*

subtilis and *Escherichia coli* strains (BL21 and lycopene producing strain, BW-Lyco) were grown at 37°C with shaking in respectively TGY and LB medium.

Sample preparation for microscopy

Glass coverslides used for *D. radiodurans* imaging were treated in an ozone oven for at least 10 minutes. 1.75% low-melting agarose (Biorad) pads dissolved in MM were poured on a cover slide inside a frame made from double-faced tape. A glass coverslip was placed on top of the agarose pad in order to flatten the surface of the agarose while hardening. This coverslip was removed once the agarose had solidified. For imaging, bacterial cultures in exponential ($OD_{650} \sim 0.3$) or stationary phase ($OD_{650} > 2$) were centrifuged 5 min at 3000 x g and were resuspended in 10 μ l of medium or washed in high purity PBS (GIBCO). For live cell imaging, 1 μ l of this cell suspension was deposited on the pads. The drop was spread over the surface of the pad by rotating the coverslip. A second coverslip was placed over the agarose pad containing the sample, thereby immobilizing the bacteria on the pad. For fixed-cell imaging, cells were fixed for 10 min at room temperature in the culture medium containing 3.7% formaldehyde and resuspended in high purity PBS (GIBCO) prior to deposition on the agarose pads or directly on coverslips. Minimal autoblinking levels were obtained when the cells were rinsed several times in high purity PBS (GIBCO). When desired, higher autoblinking levels could be obtained by depositing live cells in rich TGY medium directly on the agarose pads. To assess the levels of autoblinking in the growth media, 1 μ l of medium (TGY and MM) was deposited on the agarose pads along with gold nanobeads that were used to define the focus. The levels of autoblinking of our different samples were determined by evaluating the number of blinking events per μm^2 per 1000 frames. For samples with bacteria, only the surface covered by cells was taken into account for these calculations, while for the growth media control samples, the full imaged area was used. Cell wall staining with Nile Red (Sigma) was achieved by incubating the bacteria with 15 nM Nile Red for 5 min prior to depositing the cells on agarose pads. Digestion of the carbohydrate and peptidoglycan layers of *D. radiodurans* was achieved by incubating exponentially growing bacteria in 4 mg/ml lysozyme for 30 min at 37°C. Disruption of the lipid containing layers of the cell wall was achieved by incubating cells in 0.1% Triton X-100 at 20°C for 4 min. The cells were then rinsed and deposited on agarose pads for imaging.

Image acquisition and analysis

Wide-field illumination was achieved by focusing the laser beams to the back focal plane of a 100 \times 1.49-numerical-aperture (NA) oil immersion apochromatic objective lens (Olympus). The intensity and time sequence of laser illumination at the sample were tuned by an acousto-optical tunable filter (AOTF;

Quanta Tech). Laser beam profiles were recorded before each experiment using a coverslip uniformly marked with a fluorescent dye so as to retrieve the power densities along the laser profile. Near circular polarization of the laser beams was ensured by inserting a polychromatic quarter-wave plate downstream the AOTF. All PALM/PAINT data were collected with continuous 561-nm light illumination using a framerate of 50 ms, except for two-color acquisitions where the PAmCherry channel was acquired with frametimes of ~5 ms. High-resolution images of *D. radiodurans* cell walls (Fig. 8a) were acquired on cells exhibiting particularly high levels of autoblinking. In this case, the framerate used was 15 ms, allowing to collect a stack of images in a short time, thereby minimizing image blurring due to moving or growth of the cells. 5 to 20 cells were imaged per field of view. Typically, for each sample 2 or 3 fields of view on the same agarose pad were imaged and at least three independent experiments were performed on different days. Sample drift was corrected in ImageJ using gold nanobeads (Sigma) deposited on the agarose pads nearby the bacteria.

SptPAINT data were acquired with continuous 561 nm light illumination, at low power (130 W/cm²) using a framerate of 30 ms. Importantly sptPAINT experiments could not be performed with Nile Red on *D. radiodurans* as the relatively high concentration needed to 'mask' autoblinking was incompatible with the sparsity of events required by this method to follow single-molecule tracks unambiguously. The Trackmate plugin for ImageJ was used to localize the particles in each frame and to connect the coordinates into trajectories⁶. Simple LAP (Linear Assignment Problem) Tracker generated the tracks, with a maximal allowed linking distance set to 200 nm and a maximal frame interval between two spots to be bridged set to 2. Only tracks that contained more than four points were exported into MATLAB for further processing. The TrackArt MATLAB software⁷ was used to analyze trajectories and determine cumulative probability distributions and apparent diffusion coefficients. Trajectories shorter than 10 frames or with a minimal individual mean square displacement (MSD) fit "R²" values below 0.9 were filtered out. TrackArt estimated the relative error on the diffusion coefficients by calculating the diffusion coefficients of 10 randomly chosen sets of trajectories containing 50% of all trajectories. The standard deviation for these 10 diffusion coefficients was calculated and the relative error was estimated by extrapolating the standard deviation to the full dataset. Imposing only one population of diffusing molecules resulted in a deviation of the fit of the CPDs exceeding the uncertainty of the data. Cluster analysis was performed with SR-Tesseler⁸ using the coordinates of autoblinking molecules as input data (*i.e.*, after merging of localizations). Potential clusters were computed using a threshold $\delta > 2\delta_N$, where δ_N was the average localization density inside the bacterial contour.

Photophysical analysis

Localizations were clustered using defined space and time limits enabling, for each cluster, to calculate a fluorescence time trace. The time traces were analyzed based on the iterative method of Li *et al*⁹, which allows extracting the single molecules possibly belonging to a single cluster. Analysis of on-time, off-time and apparent bleach-time histograms was then performed to extract the corresponding rates. The absence of significant change in these rates when the applied laser power was increased led us to conclude that the overall apparent blinking behavior of autoblanking molecules was essentially driven by light-independent transient binding to the *D. radiodurans* cell wall. Thus final fluorescence time traces were obtained by applying an arbitrary small cut-off value of 0.1 s to rescue artifactual short blinks due to missed detections. Values reported in Supplementary Table S1, S2 and S3 were extracted from these traces.

Spectral single-molecule imaging and analysis

Two infinity-corrected microscope objectives, 1 (Nikon, 100x OI – NA 1.49) and 2 (Nikon, 60x WI – NA 1.27), were placed on each side of the sample and aligned to focus on the same plane. Illumination lasers (405 nm; 488 nm; 561 nm; 646 nm) were combined into a single mode optical fiber after passing through an acousto-optic tunable filter (AOTF) and sent into an azimuthal TIRF illumination system (Roper, iLas²). The laser beam was then sent into the sample via objective 1 (Nikon, 100x – NA 1.49) and a Quad Band filter cube (AHF, F66-04TN). Fluorescence signal was collected on one side by objective 1 and directed to a EMCCD camera (Photometrics, Evolve™ 512) through the Quad Band filter on path 1. On the other side, objective 2 (Nikon, 60x – NA 1.27) collected the fluorescence signal, which was filtered by a long pass filter (AHF, F76-567 – 568 long pass filter) and a Quad Band Notch filter (AHF, F57-406) and directed to a second EMCCD camera through path 2. Path 2 was composed of a 4f system providing 1.5x magnification in which a 10° wedge prism (Thorlabs, PS814-A) was inserted at the Fourier plane to transform the spectral property of the detected fluorescence into a spatial shift onto the EMCCD camera. Calibration of the spectral dispersion and resolution of path 2 was achieved by imaging Tetraspeck beads (0.1 μm in diameter, Invitrogen) coated with 4 different dyes with well-separated spectra (excitation and emission peaks: 360/430 nm; 505/515 nm; 560/580 nm; 660/680 nm). Tetraspeck beads were absorbed on a glass coverslip at low density and mounted in PBS between two coverslips using a custom sample holder and excited successively with a 488 nm laser, a 561 nm, and a 642 nm laser. For each excitation wavelength, the beads were localized on both cameras and the

displacement induced by the prism in path 2 was measured. This enabled us to determine that the spectral shift induced by the 10° wedge prism inserted in path 2 was of 11.2 nm/pixels.

For analysis, a first calibration step was performed to superimpose the fields acquired in the two channels. Mono-color beads (Nano-diamond – Adámas Nanotechnologies, NDNV100nmMd10ml) were displaced along an 8x8 grid covering the whole acquisition field of view and an image was acquired on both channels for each grid position. The bead positions were then determined by Gaussian fitting separately on each channel and the field transformation from path 2 to path 1 was determined by fitting a second order polynomial function. The error of superposition of the two channels was less than 30 nm after field transformation. The spectral properties of the detected autoblanking single molecules were then determined: the localization of each single molecule was done on path 1 by 2D Gaussian fitting and then reported to the Channel 2. This defines for each detected single molecule a region of interest on channel 2 where the single molecule spectrum has been acquired. Averaging those spectra for hundreds of localizations enables to eventually reconstruct the spectrum of the detected autoblanking molecules. It must be noted that, because each single-molecule spectrum is convolved with the point spread function (PSF) of the spectral detection path, reconstructed spectra are broadened by ~30 nm. Other factors such as low photon counts, pixilation noise, spatially varying local background and precision of the calibration also affect the spectral resolution, especially when a low number of single molecules are detected, as for example is the case for the agarose pad spectrum in Fig. 4.

Supplementary Tables

Table S1: Photophysical properties of autoblinding molecules and PAmCherry fluorescent proteins in fixed *D. radiodurans* under constant 0.8kW/cm² 561nm laser .

	Autoblinding	PAmCherry
Mean number of emitted photons per localization	335±63	352±19
Photon Counts per molecule*	563±31	1150±70
Dissociation Rate [s ⁻¹]	17.1±0.9	
Bleaching Rate [s ⁻¹]		8.8±0.9
Blinking ON-OFF Rate [s ⁻¹]		6.8±0.7
Blinking OFF-ON Rate 1 [s ⁻¹]		16.4±0.8
Blinking OFF-ON Rate 2 [s ⁻¹]		2.0±0.3
Fraction of molecules with Rate 1		0.4±0.0

* In the case of autoblinding, the “photon counts” relates to the integrated number of recorded photons during the binding time and in the case of PAmCherry relates to that number until photobleaching.

Table S2. Photophysical properties of autoblinding molecules in response to illumination with 488nm, 561nm and 647nm lasers at a constant laser power of 0.8kW/cm².

	Autoblinding		
	488nm	561nm	647nm
Relative density of localizations	0.71	1	0.09
Mean Photon Counts per molecule	381±46	563±31	329±85
Dissociation Rate [s ⁻¹]	23.8±2.8	17.1±0.9	18.9±2.9

Table S3. Photophysical properties of autoblanking and Nile Red molecules under increasing 561nm laser illumination power.

	0.2 kW/cm ²		0.8 kW/cm ²		1.6 kW/cm ²	
	Autoblanking	Nile Red	Autoblanking	Nile Red	Autoblanking	Nile Red
Mean Photon Counts per molecule	330	290	560	470	600	610
Apparent Dissociation Rate [s ⁻¹]	19	21	17	22	18	19

Table S4: Diffusion coefficients and confinement radii of the two populations of autoblanking molecules.

	Population 1	Population 2
D _{app} diffusion coefficient (μm ² /s)	(6.35±0.39)×10 ⁻²	(1.42±0.09)×10 ⁻²
Confinement radius (nm)	249	86
Fraction of the whole populations	0.48±0.01	0.52±0.01

Supplementary Movie

Movie S1: Extract (500 out of 50,000 images) of the stack used for autoblanking-based imaging of the *D. radiodurans* cell presented in Fig. 2. Images were acquired with 50 ms frametimes under continuous 0.8kW/cm² 561nm laser.

Supplementary Figures

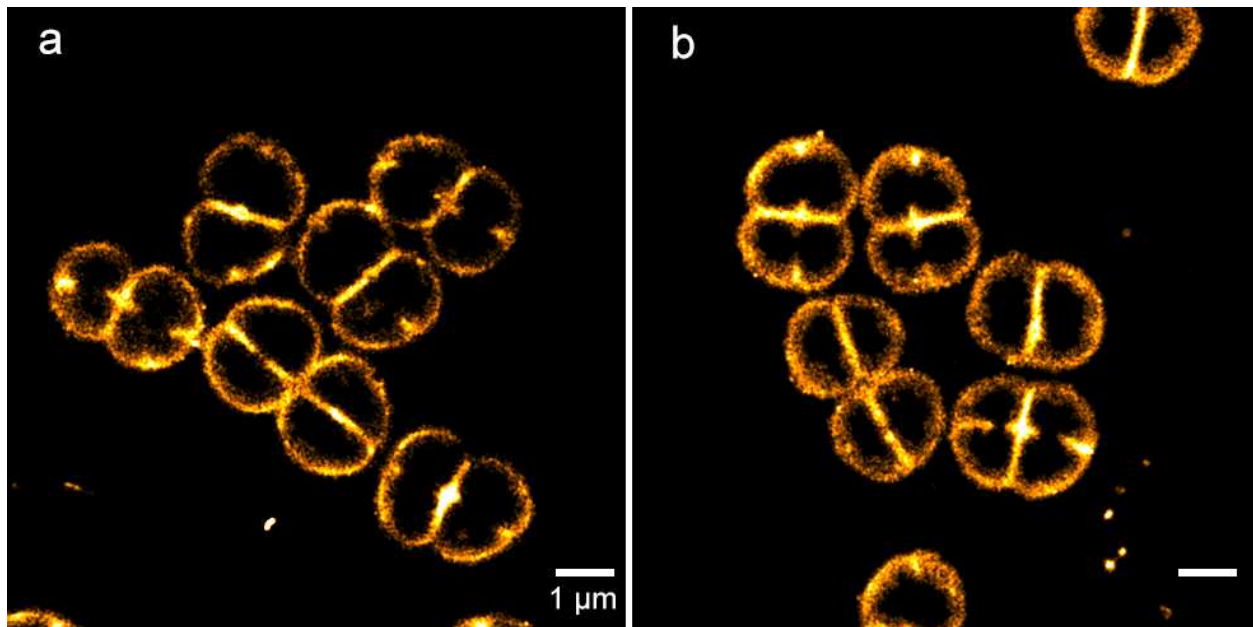


Figure S1. Examples of super-resolved images of live *D. radiodurans* acquired using either (a) autoblinking or (b) Nile Red labeling. Scale bar: 1 μ m. Images were acquired with a 50 ms frametime under continuous 0.8kW/cm² 561nm laser. The autoblinking reconstruction (a) was prepared using 30,000 frames, whereas the Nile Red reconstruction (b) was prepared using 15,000 frames.

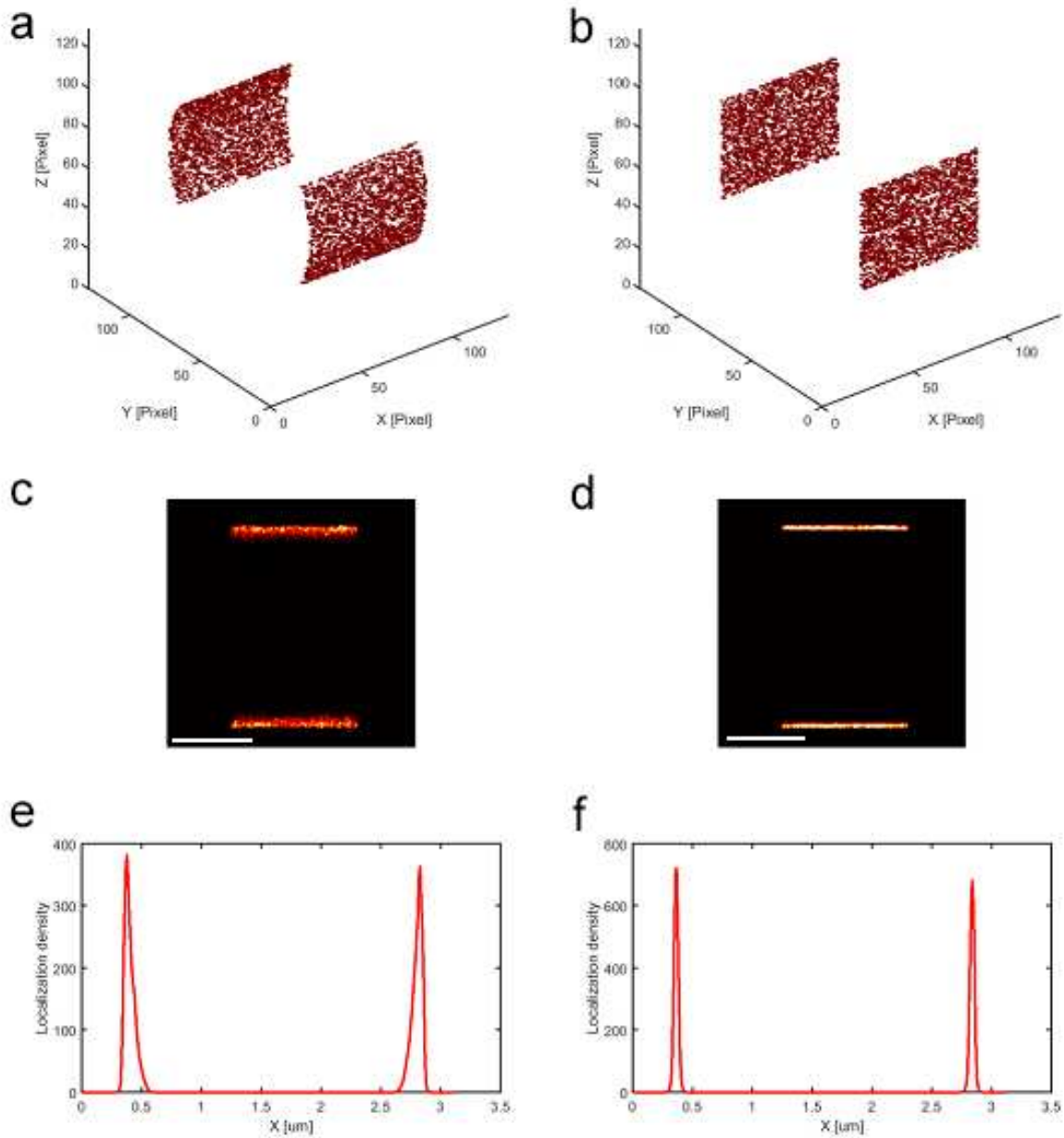


Figure S2. Effect of cell wall curvature on apparent image resolution. (a,b) 3-D views of 5,000 fluorophores decorating Z-sections (1.25 μm overall height) of 10-nm thick cylinders of high (1.25 μm) and low (5 μm) radius of curvature. (c-d) PALM images reconstituted from data sets simulated with Matlab, using the samples shown in (a-b), and an objective depth of field of 500 nm. Photophysical parameters of typical blinking fluorophores were used in the simulations, achieving a mean localization precision of 20 nm. Scale bar: 1 μm. (e-f) 1-D projection profiles from (c-d) along the vertical dimension, highlighting the loss of resolution resulting from sample curvature along the optical axis.

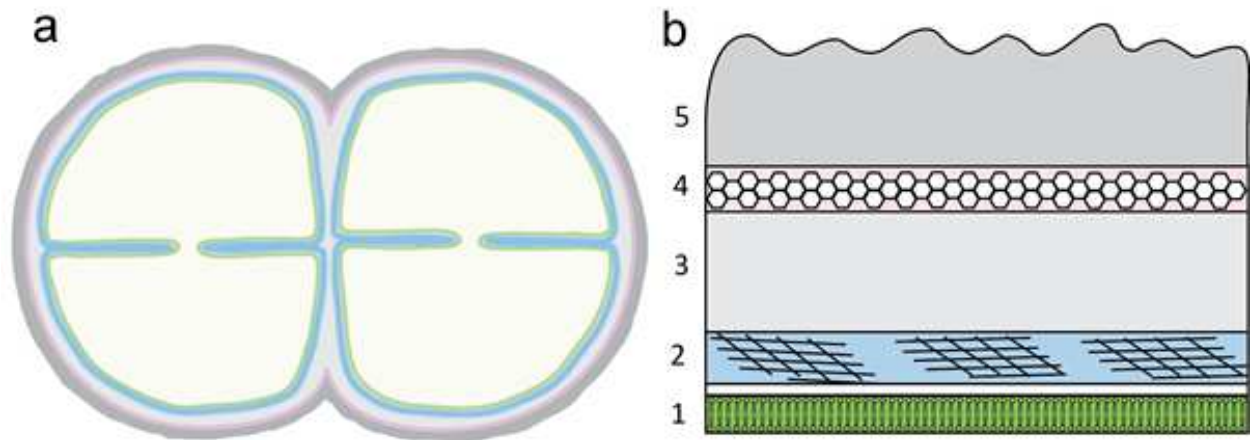


Figure S3. Schematic representation of the complex cell wall structure of *D. radiodurans* (a), composed of five distinct layers (b): 1, plasma membrane (green); 2, peptidoglycan layer (blue); 3, interstitial layer (light grey); 4, S-layer or backing (pink) composed of proteins, lipids and carotenoids; 5, carbohydrate layer (dark grey). The thickness of *D. radiodurans* cell wall is estimated to be between 75 and 150nm^{10,11}.

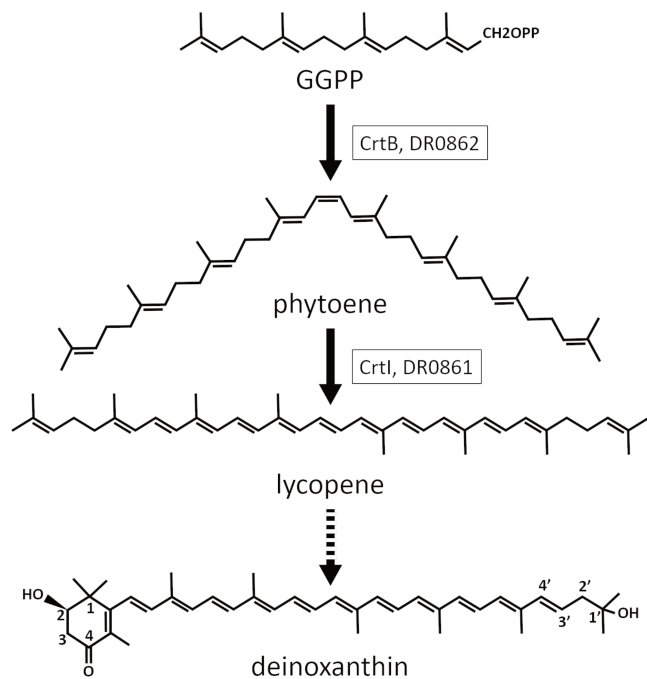


Figure S4. Schematic representation of the deinoxanthin carotenoid biosynthetic pathway of *D. radiodurans*. Bold arrows indicate a single step; discontinuous arrows refer to multiple steps. Abbreviations: GGPP, geranylgeranyl-pyrophosphate. A $\Delta crtB$ strain of *D. radiodurans* accumulates GGPP precursor, while a $\Delta crtI$ mutant accumulates phytoene by-product.

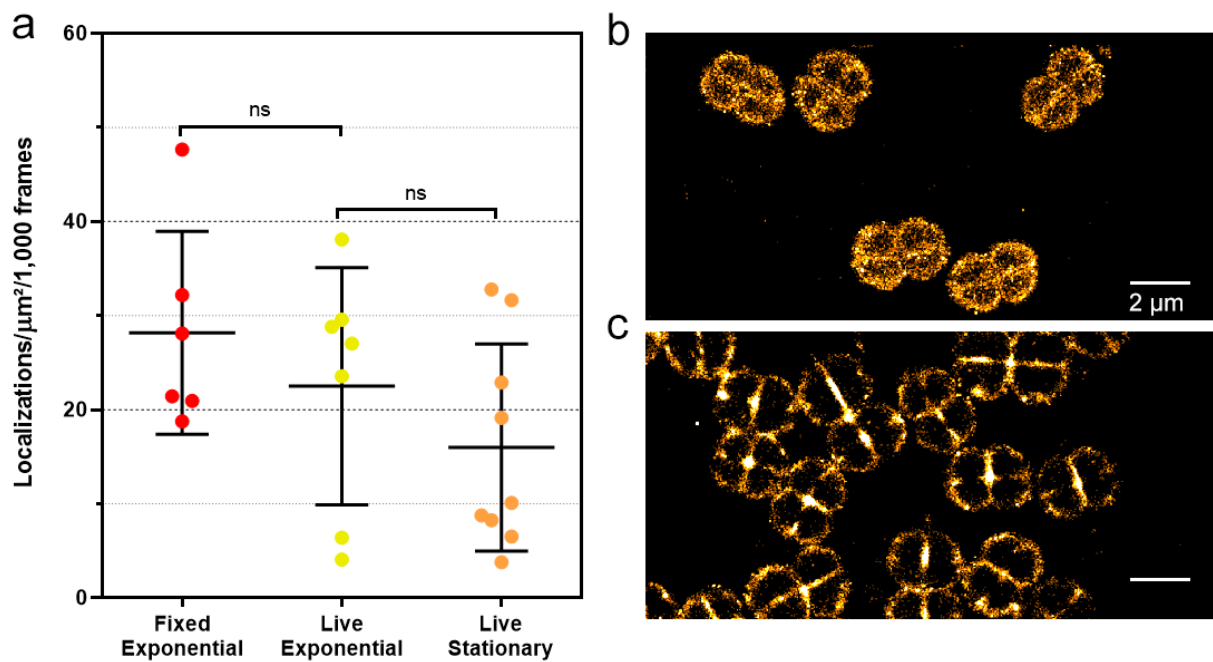


Figure S5. (a) Autoblanking levels (localizations/ $\mu\text{m}^2/1000$ frames) in fixed or live wild-type *D. radiodurans* cells, in exponential (OD=0.3) or stationary (OD>4) growth phases and grown in rich TGY medium. Images were acquired with a 50 ms framerate under continuous $0.8\text{kW}/\text{cm}^2$ 561nm laser. Individual data points correspond to the autoblanking levels derived from a given stack of images. Means and standard deviations are plotted in the graph. (b)-(c) Examples of super-resolved images of fixed *D. radiodurans* (b) and live, stationary phase cells (c). Cell fixation leads to a reduction in the size of the bacteria and deteriorates the quality of the cell wall labeling. In both cases, reconstructions were prepared using 15,000 frames acquired with a 50 ms framerate and under continuous $0.8\text{kW}/\text{cm}^2$ 561nm. Scale bar: $2\ \mu\text{m}$.

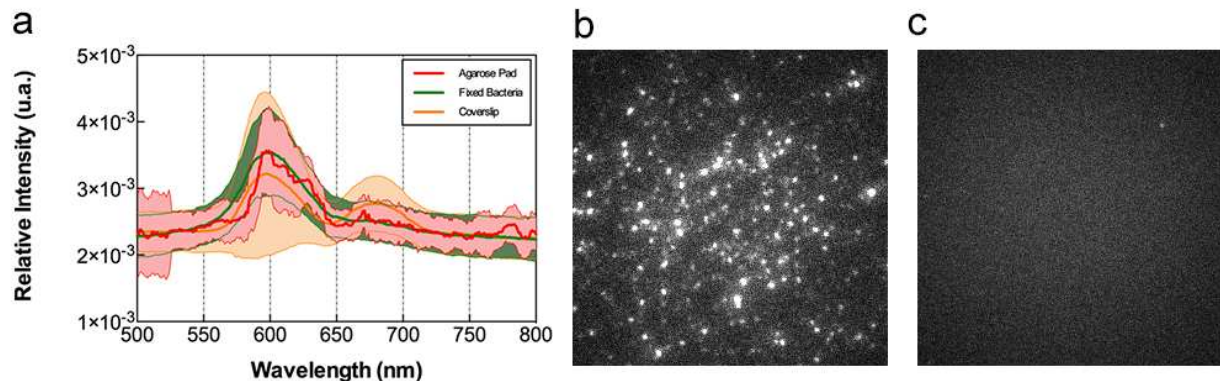


Figure S6. Effect of ozone-treatment of the glass coverslides. (a) Spectral imaging of single molecules found at the surface of the glass coverslides (no ozone treatment; orange), of the agarose pad (red) or at the periphery of fixed *D. radiodurans* cells (green). An additional peak centered around 675 nm is seen for blinking molecules at the surface of glass coverslides. (b) Numerous blinking molecules are seen at the surface of untreated coverslides. (c) Incubation of the glass coverslides for 10 min in an ozone oven is sufficient to remove most of these blinking molecules.

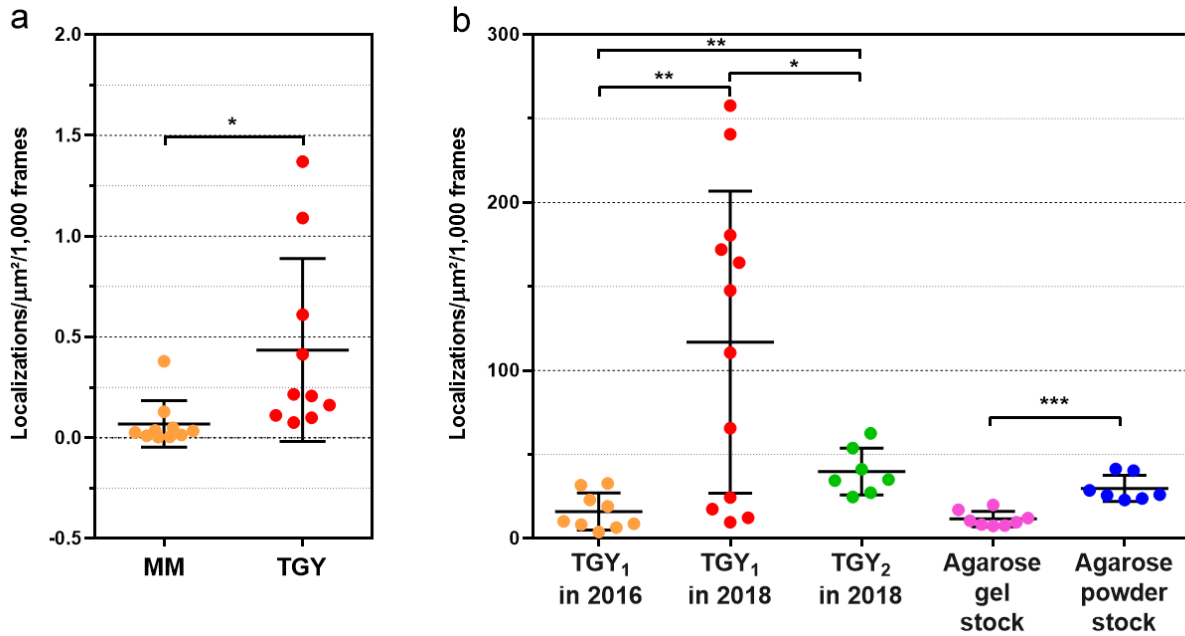


Figure S7. Autoblanking levels in growth medium and effect of conditioning and storage time of chemicals on autoblanking levels in *D. radiodurans*. (a) Autoblanking levels (localizations/ $\mu\text{m}^2/1000$ frames) in minimal medium (MM) and in TGY medium deposited directly on agarose pads in the absence of bacterial cells. The number of localizations are extracted from the entire field of view and not exclusively from the areas covered by cells as is the case in Figures 3, 5, S5a and S7b. (b) Autoblanking levels (localizations/ $\mu\text{m}^2/1000$ frames) in live *D. radiodurans* cells grown in different sources of TGY medium. TGY₁ in 2016: experiments performed in 2016 on cells grown in TGY medium purchased in 2016 (stock 1). TGY₁ in 2018: experiments performed in 2018 on cells grown in TGY medium purchased in 2016 (stock 1). TGY₂ in 2018: experiments performed in 2018 on cells grown in TGY medium purchased in 2018 (stock 2). Autoblanking levels (localizations/ $\mu\text{m}^2/1000$ frames) in live *D. radiodurans* cells deposited on agarose pads prepared either from agarose stored as a gel in a glass container (Agarose gel) or from agarose powder stored in a plastic container (Agarose powder). (a)-(b) Images were acquired with a 50 ms framerate under continuous $0.8\text{kW}/\text{cm}^2$ 561nm laser. Individual data points correspond to the autoblanking levels derived from a given stack of images. Means and standard deviations are plotted in the graph.

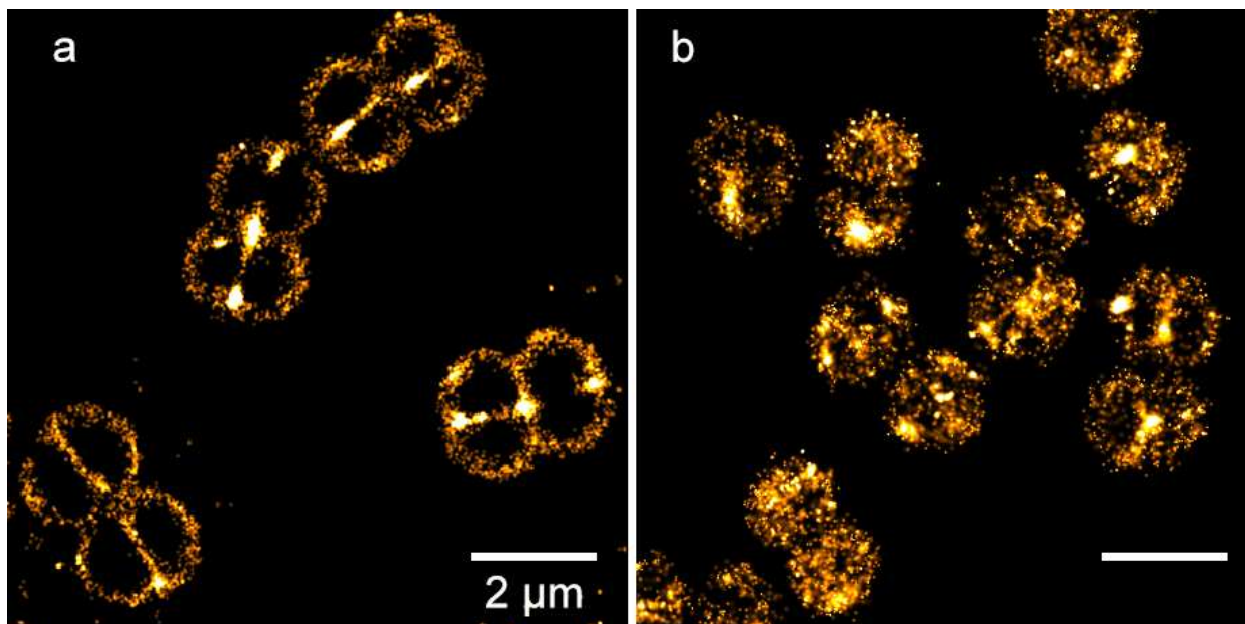


Figure S8. Effect of lysozyme and Triton X-100 treatments on autofluorescence distribution in live, unlabelled *D. radiodurans*. (a) Images of cells treated for 30 minutes at 37°C with 4mg/ml lysozyme, (b) images of cells treated with 0.1% Triton X-100 for 4 minutes at 20°C. In both cases, reconstructions were prepared using 5,000 frames acquired with a 50 ms frametime and under continuous 0.8kW/cm² 561nm. Scale bar: 2 µm.

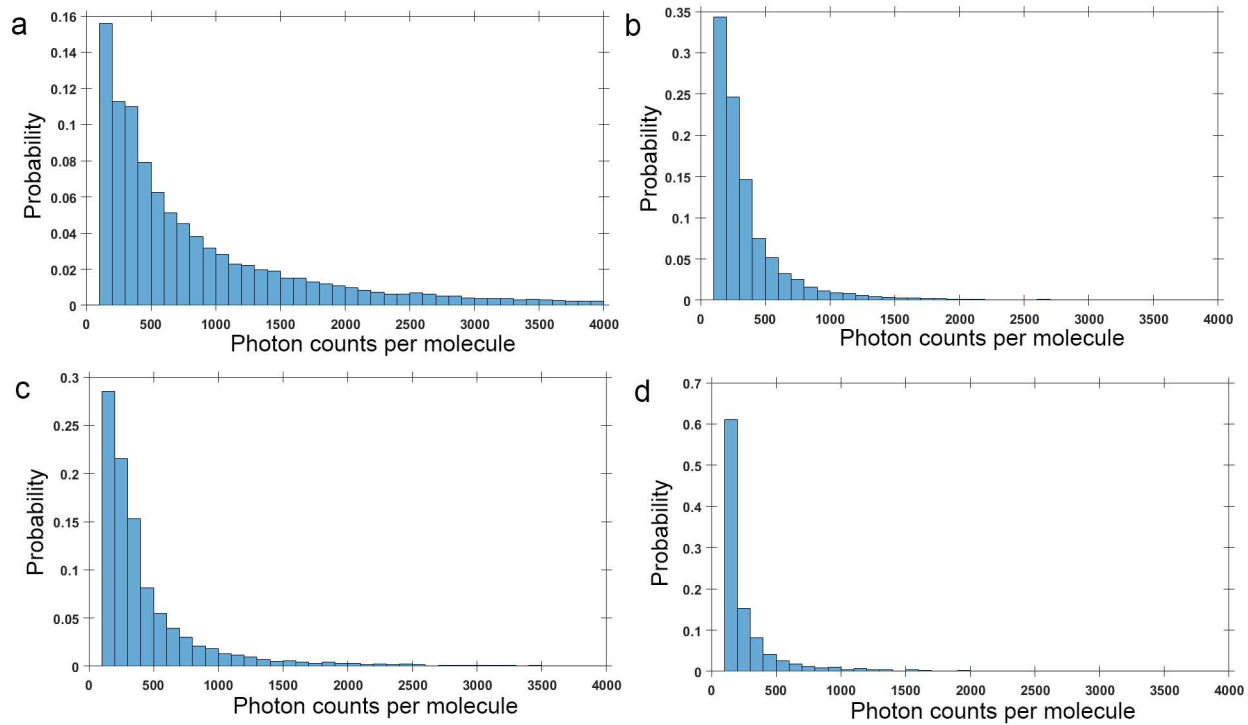


Figure S9. Histogram distributions of the photon counts per molecules for PAmCherry molecules (a) under 561 nm illumination and for autoblanking molecules (b)-(d) under 488 nm (b), 561 nm (c) or 643 nm (d) illumination. All data were acquired with a constant laser power of 0.8kW/cm².

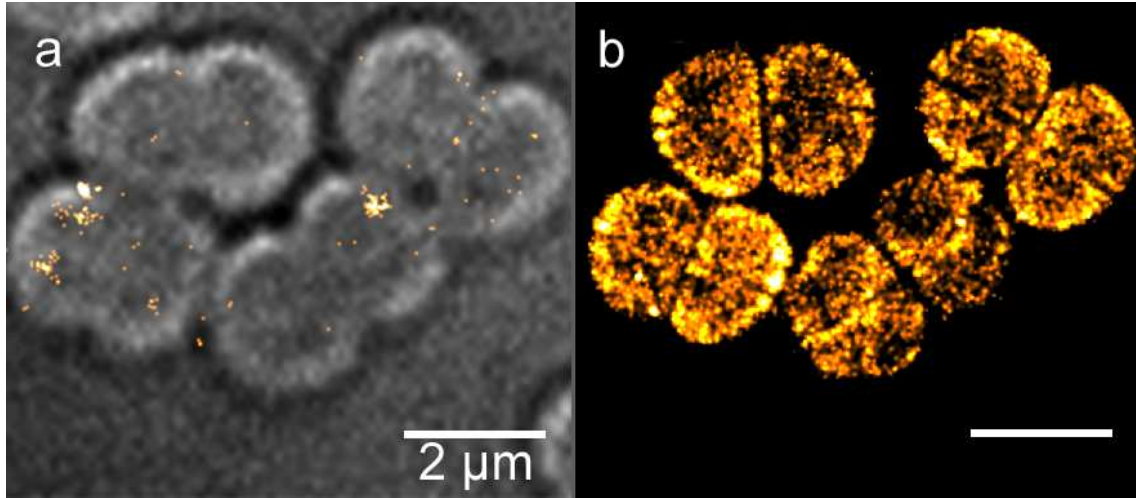


Figure S10. PALM imaging of photo-activated fluorescent proteins in autoblinking bacteria. (a)-(b) 4000 image stacks of autoblinking (a) and PAmCherry (b) in *D. radiodurans* expressing free PAmCherry, acquired with ~ 5 ms frametimes, under continuous $0.8\text{kW}/\text{cm}^2$ 561nm laser, and either without (a) or with (b) $0.4\text{ W}/\text{cm}^2$ 405nm laser. Scale bar: $2\ \mu\text{m}$.

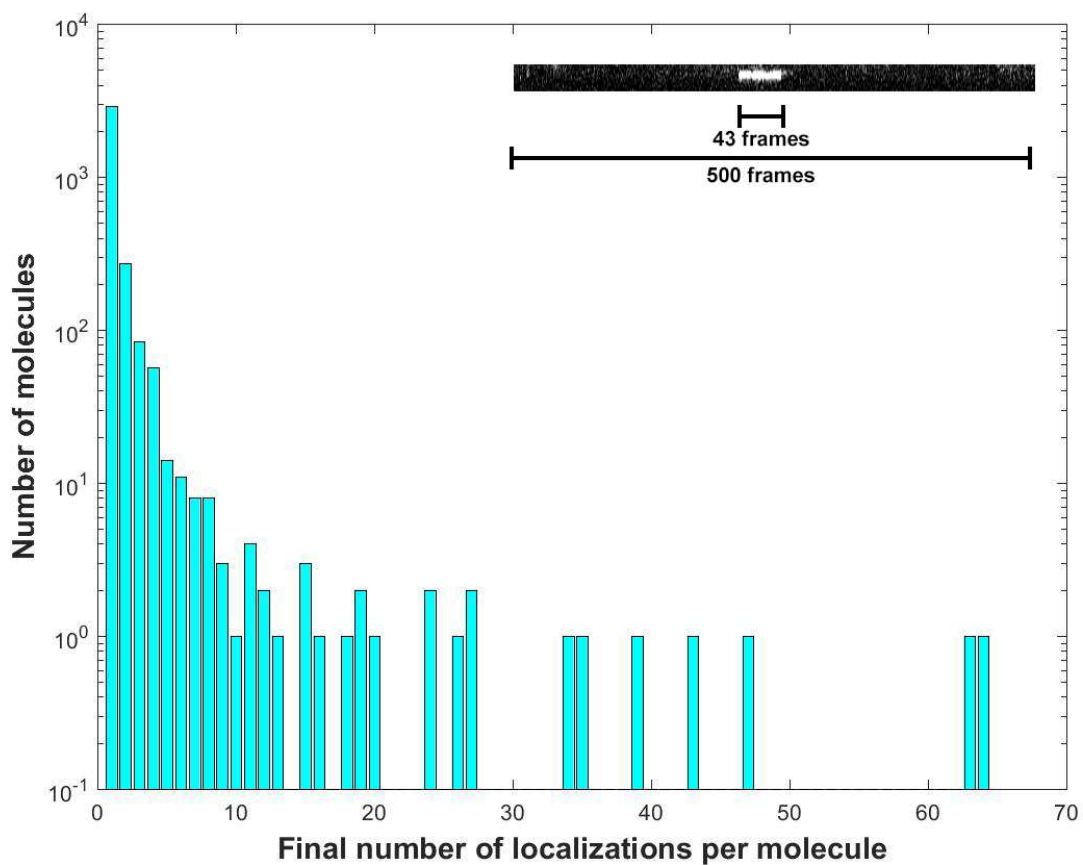


Figure S11: Number of localizations per autoblanking molecules during a 10,000 frame acquisition. Inset: example of a kymograph showing the localization of a given molecule in 43 consecutive frames.

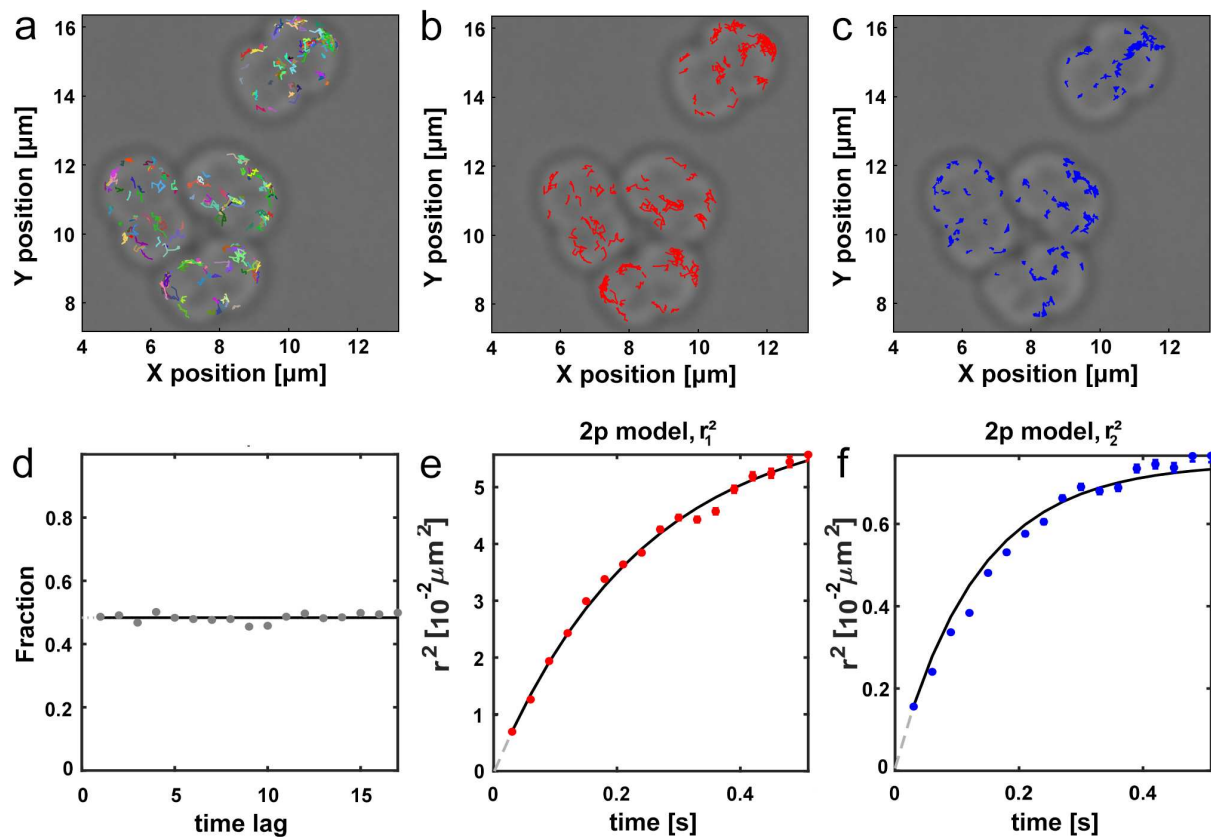


Figure S12. Single-particle tracking analysis of autoblanking molecules. (a)-(c) Individual trajectories of autoblanking molecules superimposed on the corresponding brightfield image. Faster and slower diffusing molecules are colored respectively red (b) and blue (c). (d) Fraction of the slower population over the faster diffusing population. (e)-(f) Mean square deviation (MSD) plots of the faster population (e) and the slower population (f). ($\Delta t = 30$ ms). Both populations are confined.

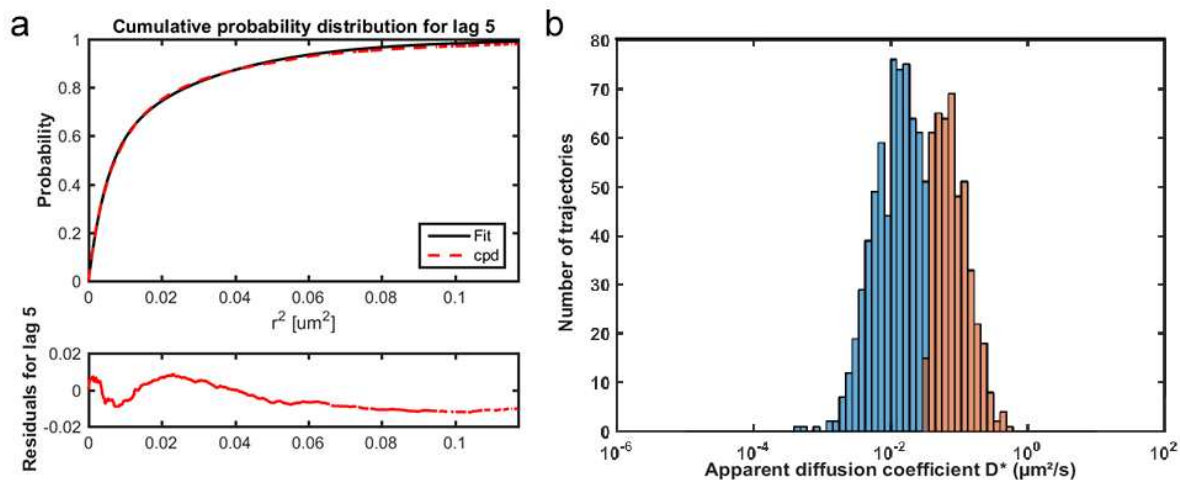


Figure S13. (a) Cumulative probability distribution (CPD) of mean square displacements and residuals for the fit of the two-population model of autoblanking molecules. Distributions and fits are presented only for the fifth time-lag ($\Delta t = 30$ ms). The two-species model described in this manuscript is retrieved from the fit of the CPD. (b) Distribution of apparent diffusion coefficients. As an alternative analysis of the single particle tracks, the distribution of the apparent coefficients was fitted with a simple Gaussian mixture model. The results are consistent with the two-population model obtained from CPD analysis, with a slower population (blue, 61% of the whole population, with $D=0.015 \mu\text{m}^2/\text{s}$) and a faster one (orange, 39% of population with $D=0.065 \mu\text{m}^2/\text{s}$).

Supplementary References

1. Avilov, S. *et al.* In cellulo evaluation of phototransformation quantum yields in fluorescent proteins used as markers for single-molecule localization microscopy. *PloS one* **9**, e98362 (2014).
2. De Almeida, C. B., Coste, G., Sommer, S. & Bailone, A. Quantification of RecA protein in *Deinococcus radiodurans* reveals involvement of RecA, but not LexA, in its regulation. *Molecular Genetics and Genomics* **268**, 28–41 (2002).
3. Mennequier, S., Coste, G., Servant, P., Bailone, A. & Sommer, S. Mismatch repair ensures fidelity of replication and recombination in the radioresistant organism *Deinococcus radiodurans*. *Molecular genetics and genomics* **272**, 460–469 (2004).
4. Venkateswaran, A. *et al.* Physiologic Determinants of Radiation Resistance in *Deinococcus radiodurans*. *Applied and environmental microbiology* **66**, 2620–2626 (2000).
5. De Groot, A. *et al.* *Deinococcus deserti* sp. nov., a gamma-radiation-tolerant bacterium isolated from the Sahara Desert. *International journal of systematic and evolutionary microbiology* **55**, 2441–2446 (2005).
6. Tinevez, J.-Y. *et al.* TrackMate: An open and extensible platform for single-particle tracking. *Methods* **115**, 80–90 (2017).
7. Matysik, A. & Kraut, R. S. TrackArt: the user friendly interface for single molecule tracking data analysis and simulation applied to complex diffusion in mica supported lipid bilayers. *BMC research notes* **7**, 274 (2014).
8. Levet, F. *et al.* SR-Tesseler: a method to segment and quantify localization-based super-resolution microscopy data. *Nature methods* **12**, 1065–1071 (2015).
9. Lee, S.-H., Shin, J. Y., Lee, A. & Bustamante, C. Counting single photoactivatable fluorescent molecules by photoactivated localization microscopy (PALM). *Proceedings of the National Academy of Sciences* **109**, 17436–17441 (2012).
10. Rothfuss, H., Lara, J. C., Schmid, A. K. & Lidstrom, M. E. Involvement of the S-layer proteins Hpi and SlpA in the maintenance of cell envelope integrity in *Deinococcus radiodurans* R1. *Microbiology* **152**, 2779–2787 (2006).
11. Slade, D. & Radman, M. Oxidative stress resistance in *Deinococcus radiodurans*. *Microbiology and molecular biology reviews* **75**, 133–191 (2011).

V***D. radiodurans* cell and nucleoid dynamics**

D. radiodurans is a relatively large coccoid bacterium with exceptional resistance to genotoxic stress. It possesses a toroidal and highly compact nucleoid, which may play a role in its outstanding phenotype. In addition, *D. radiodurans* has a complex genome composed of four replicons, each of which are present in multiple copies. Most studies of *D. radiodurans* have so far focused on its radioresistance, and little is known regarding the morphological changes and nucleoid dynamics occurring during its cell cycle. Moreover, most of our knowledge of nucleoid organization, chromosome segregation and bacterial cell morphology arises from studies of rod- or crescent-shaped bacteria. Little is known on the nucleoid organization of spherical bacteria such as *D. radiodurans*.

The small size of bacteria, close to the diffraction limit, have limited the studies of their morphologies and their nucleoids. For example, it was not until recently, thanks to 3D-SIM, that *S. aureus* was seen as possessing different phases of enlargement, including one prior to the formation of the dividing septum (Monteiro et al. 2015).

Thus, using advanced fluorescence microscopy, we characterized the cell cycle of *D. radiodurans* in exponentially growing cells and studied the changes in *D. radiodurans* cell shape, as well as the organization of its complex nucleoid all along its cell cycle. The results of this work are presented in the following manuscript, which we expect to submit shortly.

Cell morphology and nucleoid dynamics in dividing *D. radiodurans*

Kevin Floc'h[†], Françoise Lacroix[†], Pascale Servant², Yung-Sing Wong³, Jean-Philippe Kleman¹, Dominique Bourgeois¹, Joanna Timmins^{1*}

1 Univ. Grenoble Alpes, CEA, CNRS, IBS, F-38000 Grenoble, France.

2 Institute for Integrative Biology of the Cell (I2BC), CEA, CNRS, Univ. Paris-Sud, Université Paris-Saclay, Gif-sur-Yvette, France.

3 Département de Pharmacochimie Moléculaire, Univ. Grenoble Alpes, UMR 5063 CNRS, ICMG FR 2607 , 470 rue de la Chimie , 38041 Grenoble , France.

[†]These authors contributed equally to this work.

*Corresponding authors: Joanna Timmins (Joanna.timmins@ibs.fr)

1. Abstract

Most of our knowledge of the spatial organization and dynamics of nucleoids originates from studies of rod- or crescent-shaped bacteria. Here, we reveal that *Deinococcus radiodurans*, a relatively large, spherical bacterium, well-known for its exceptional radioresistance, constitutes a valuable system for the study of nucleoid structure and dynamics in cocci. Using advanced microscopy approaches, we have determined that *D. radiodurans* increases in size throughout its cell cycle through growth of both septal and peripheral cell walls, and have revealed that its nucleoid is highly compact at all times, but also surprisingly dynamic, adopting six distinct configurations, including the previously described toroid, as it progresses through its cell cycle. This remarkable plasticity is permitted by the loose binding of the highly abundant histone-like HU protein to the genomic DNA, as revealed by single-molecule and ensemble measurements of HU dynamics. Moreover, by mapping specific chromosome loci, we show that *D. radiodurans* chromosome 1 presents a radial organization in which *ori* loci are distributed evenly around *ter* sites that are largely clustered at the centre of cells for most of the cell cycle. Taken together, these results demonstrate that nucleoids are highly organized and dynamic structures, which are tightly regulated by cell shape and cell cycle progression.

2. Introduction

In all organisms, genomic DNA is compacted several orders of magnitude and yet must remain accessible for essential DNA-related processes including DNA replication, repair and transcription. In bacteria, packaging of genomic DNA is achieved by several mechanisms, including DNA supercoiling (Luijsterburg et al. 2006) and DNA compaction by nucleoid-associated proteins (NAPs), such as HU (Badrinarayanan et al. 2015; Dillon & Dorman 2010; Wang et al. 2013). However, recent studies now indicate that additional factors, such as molecular crowding and depletion forces, also play important roles in determining the volume of the cell occupied by the nucleoid (Jun 2015; Pelletier et al. 2012; Shendruk et al. 2015), and suggest that cell shape and size may critically influence nucleoid organization (Shendruk et al. 2015; Wu et al. 2018).

So far a vast majority of the studies of bacterial nucleoids have focused on three model bacteria, *E. coli*, *B. subtilis* and *C. crescentus*, all of which are either rod- or crescent-shaped bacteria. Recent developments in single-molecule and genome-wide analytical techniques have started to shed light on how these model bacteria organize, compact and segregate their chromosomes, three processes that are intimately connected. Microscopy and chromosome conformation capture studies have revealed that nucleoids are organized into micro- and macrodomains, the origins of which are still unclear (review (Dame & Tark-Dame 2016)) and have been shown to adopt an overall helical arrangement (Fisher et al. 2013; Le et al. 2013; Marbouty et al. 2015), which is distributed along the longitudinal axis filling a large fraction of the cell volume (~70% in *E. coli*). Mapping of specific chromosome loci such as the origin (*ori*) or the termination sites (*ter*) have also revealed that chromosomes in model bacteria can be seen to adopt two stereotypical configurations. Under certain conditions, they may arrange longitudinally, along an *ori-ter* axis with the *ori* and *ter* regions located at opposite poles of the cell, or transversally in which both the *ori* and *ter* are localized at mid-cell and the left and right arms are located on either sides (Badrinarayanan et al. 2015; Marbouty et al. 2015; Umbarger et al. 2011; Wang et al. 2006).

Although in all bacteria irrespective of their shapes, chromosome organization and segregation are tightly coupled to the division process, in cocci, the directionality of chromosome segregation has additionally been proposed to play a key role in determining the division site (Veiga et al. 2011). The two most studied cocci are the ovoid *Streptococcus pneumoniae* and the spherical *Staphylococcus aureus*, two major human pathogens. So far, however, the small size of these cocci has largely restricted the study of nucleoid rearrangements and concomitant morphological changes occurring during their cell cycle. In contrast, *Deinococcus radiodurans* is a non-pathogenic, relatively large (~2 μm in diameter) coccus, displaying an outstanding resistance to DNA-damaging agents including ionizing radiation, UV light and desiccation (Blasius et al.

2008; Makarova et al. 2001; Slade & Radman 2011). Several factors have been proposed to contribute to this outstanding phenotype: (i) a highly efficient and redundant DNA repair machinery, (ii) the presence of numerous antioxidant metabolites (Daly 2009; Makarova et al. 2001; Tian et al. 2007; Wang & Schellhorn 1995) that contributes to an increased protection of the proteome, and (iii) the unusual properties of its genome. *D. radiodurans* has indeed been shown to possess a complex, multipartite genome composed of four replicons each of which are present in multiple copies ranging from 4 to 10 copies, as a function of its cell cycle and growth Phase (Battista 1997). Moreover, *D. radiodurans* genome has also been reported to be more condensed (Zimmerman & Battista 2005) compared to that of radio-sensitive bacteria, such as *E. coli*, and to adopt an unusual ring-like structure (Englander et al. 2004; Levin-Zaidman et al. 2003). These unusual features have been suggested to facilitate genome maintenance and repair (Minsky et al. 2006; Minton & Daly 1995).

Using both spinning-disk time-lapse microscopy and super-resolution imaging, we have performed a detailed analysis of the morphological changes that occur at the cellular and nucleoid level as *D. radiodurans* grows and divides in alternating perpendicular planes. These data reveal that its nucleoid is indeed highly compact, while remaining surprisingly dynamic, adopting multiple distinct configurations as the bacterium progresses through its cell cycle. Studies of the dynamics of the highly abundant histone-like HU protein, which is the major NAP that coats the genomic DNA in *D. radiodurans*, reveal that it only associates loosely with DNA, thereby facilitating the structural rearrangements of the nucleoid. Finally, we followed the choreography of the *ori* and *ter* loci of chromosome 1 during the various stages of the cell cycle and show that they exhibit very different distributions within the cell with the *ori* loci being radially distributed around the centrally located *ter* sites. Taken together, these findings demonstrate that the properties of *D. radiodurans* make it particularly well suited for the study of nucleoid organization in cocci, and provide new, compelling evidence indicating that bacterial nucleoids are complex and dynamic entities that are tightly regulated by cell shape, cell cycle progression and septal growth.

3. Results

Growth and division of *D. radiodurans* cells

To follow the morphological changes occurring during the growth of *D. radiodurans*, cells were labelled with the membrane dye Nile Red and deposited on an agarose pad for either time-lapse imaging on a spinning-disk confocal microscope or super-resolution imaging using Point Accumulation for Imaging in Nanoscale Topography (PAINT) microscopy (see Methods and Supplementary Fig. S1 for comparison of two imaging systems). All cell measurements presented below were extracted from super-resolution images (Fig. 1A), while durations of the various stages of the cell cycle were derived from time-lapse imaging.

Exponentially growing *D. radiodurans* cells cultured in rich medium form diads (Daly et al. 2004) that transiently form tetrads before the start of a new cell cycle (Fig. 1B). Single cells were scarcely seen in our experiments. *D. radiodurans* cells divide sequentially in two perpendicular planes (Murray et al. 1983; Thornley et al. 1965). Starting from an elliptical and largely symmetric diad (Phase 1), the cells initiate their cell cycle by a phase of cell growth (Phase 2) leading to a slight invagination at the junctions between the central septum and the cell periphery (Fig. 1B and Supplementary Fig. S2). This phase ends with the appearance of bright foci corresponding to the start of the growth of the new septa (Phase 3). These foci appear in the centre of the central septum and in the middle of the opposite peripheral cell wall. We observed that one foci may appear before the other in a given phase 3 cell and septal growth in the two cells forming the diad were also seen to be sometimes asynchronous (eg. cells bottom left in Fig. 1A). Phase 4 corresponds to cells in which the growth of the new septa is partial and in Phase 5, the newly formed septum is about to close. Finally, in Phase 6 septal growth is complete and tetrads are formed (Fig. 1B). As the cells progress through Phases 3 to 6, the invagination at the diad junction becomes more pronounced and the length of the central septum progressively decreases (Supplementary Fig. S2) until disappearing completely as the tetrads fall apart to form two diads. In stationary phase cells, the tetrads no longer separate into diads and the number of Phase 6 cells increases markedly (Supplementary Fig. S3). Moreover, a substantial fraction of these tetrads engage in a new division cycle, but cell cycle progression is very slow and only a small number of octads are seen (Supplementary Fig. S3).

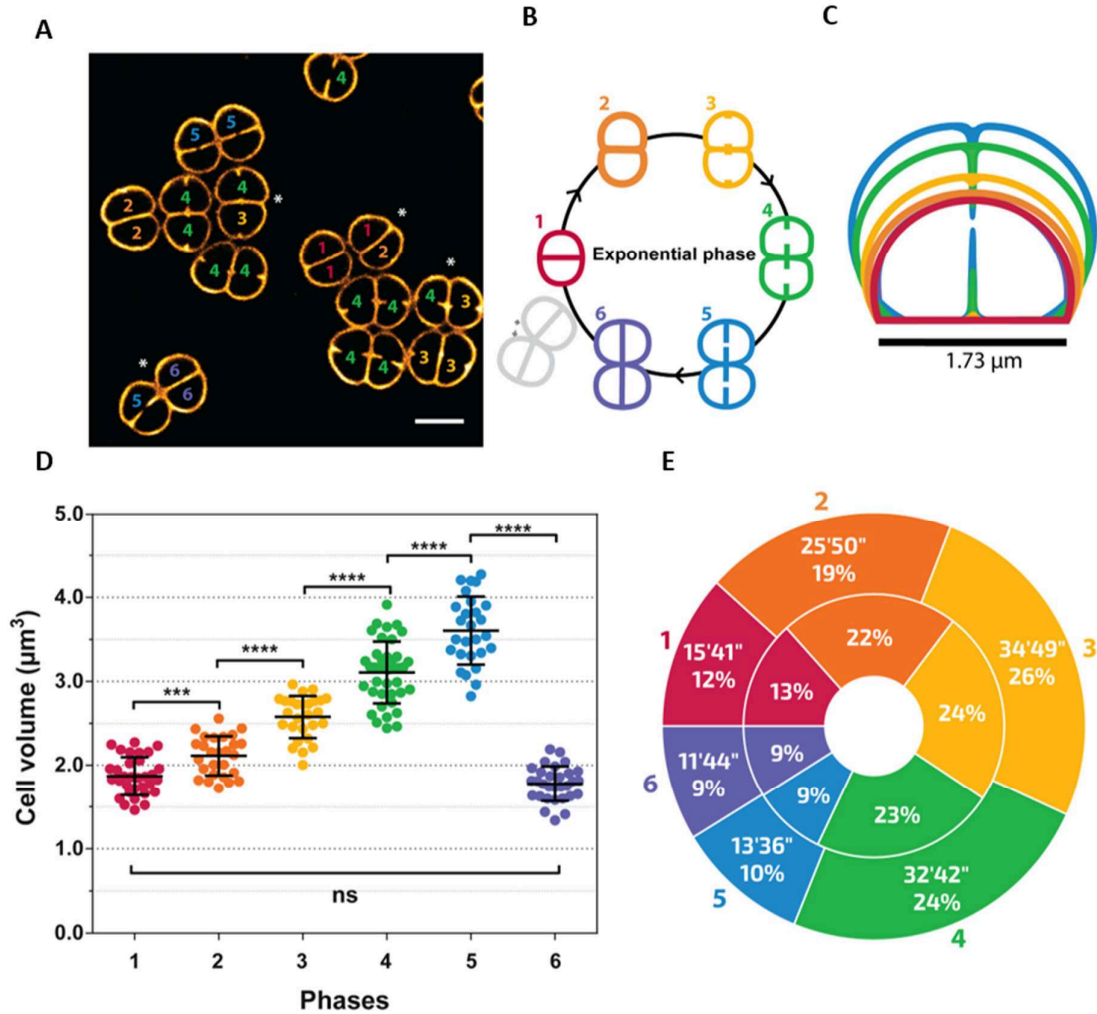


Figure 1: Morphological changes occurring during the growth of *D. radiodurans*. (A) PAINT imaging of live *D. radiodurans* cells stained with the membrane dye Nile Red. Numbers inside each cell correspond to their growth phase shown schematically in (B). Cells in diads marked with an asterisk are asynchronous. Scale bar: 2 μm . (B) Schematic representation of the different phases of the *D. radiodurans* cell cycle in exponentially growing bacteria. (C) On-scale representation of the average cell sizes and morphologies at the different phases of the cell cycle colored as in (B). Phase 6 cells are very similar to Phase 1 cells. (D) Changes in cell volume during the cell cycle (N=180 cells, N>27 for each phase). Cell volumes were calculated by measuring the cell parameters presented in Fig. S4 on PAINT images of exponentially growing wild-type *D. radiodurans* stained with Nile Red. The mean cell volume progressively increases from a volume of $1.87 \pm 0.23 \mu\text{m}^3$ in Phase 1 to a volume of $3.60 \pm 0.40 \mu\text{m}^3$ in Phase 5 just before cytokinesis. (***: $P < 0.001$, ****: $P < 0.0001$, ns: not significant). (E) Duration of each growth phase in exponentially growing *D. radiodurans* cells. Interior annulus: Distribution of exponentially growing cells in the different phases of the cell cycle when observed at a single time point (N>600). Exterior annulus: Duration of phases measured on exponentially growing cells observed by time-lapse imaging (N>30). Data were collected from 2 independent experiments.

Various cell parameters were extracted from our images (Supplementary Fig. S2 and S4) and were used to determine the average shape and volume of cells at each phase of the cell cycle (Fig. 1C and D). *D. radiodurans* cells were found to grow linearly throughout their cell cycle (Supplementary Fig. S5), as seen by the progressive increase in cell volume starting from a mean volume of $1.87 \pm 0.18 \mu\text{m}^3$ in Phase 1 until a volume of $3.60 \pm 0.34 \mu\text{m}^3$ in Phase 5 just before cytokinesis (Fig. 1D). The change in cell volume was also accompanied by a change in ellipticity of the cells as they progress through the cell cycle (Supplementary Fig. S2). Starting from hemispheres in Phase 1, individual cells become quasi ellipsoids by the end of Phase 5. In stationary phase, cell growth arrests and the mean volume of cells in tetrads decreases to $1.65 \pm 0.34 \mu\text{m}^3$ (Supplementary Fig. S3).

To assess the duration of each growth phase in exponential cells, two approaches were used. Durations were either deduced from the distribution of phases in the population of exponentially growing cells when deposited on an agarose pad and directly observed under the microscope (the fraction of cells in each phase reflects the relative duration of these phases, Fig. 1E interior annulus), or by time-lapse imaging of cells (Fig. 1E exterior annulus and Supplementary Movie S1). Very similar results were obtained for the two approaches and the total cell cycle duration measured in our time-lapse experiments (134 ± 11 min) was close to that extracted from our growth curves performed on *D. radiodurans* cells grown in liquid medium in a shaking incubator (122 min; Supplementary Fig. S5). Cells spend 91% of their time as diads and 9% as tetrads, and septal growth (Phases 3, 4 and 5) occurs during more than half of the cell cycle. Phases 1, 5 and 6 are the shortest, lasting between 11 and 15 min, while Phases 2, 3 and 4 are longer and last 25 to 35 min (Fig. 1E).

Next, we evaluated the position and angle of the newly growing septa relative to the central septum in exponentially growing cells. In all cells, septal growth was found to occur precisely in the middle ($50\% \pm 1.5\%$) at a $90^\circ (\pm 7^\circ)$ angle to the central septum (Supplementary Fig. S6). Early electron micrographs of *D. radiodurans* cells suggested that septal closure occurs through a closing door mechanism and not as a diaphragm (Murray et al. 1983). Three-dimensional imaging of Nile Red stained cells confirmed this. The closing septum grows from both sides of the cells leaving a gap that stretches across the whole cell (Supplementary Fig. S6).

In bacteria, cell growth is associated with peptidoglycan (PG) synthesis within the cell wall. We thus investigated whether PG synthesis occurs (i) in the septal regions only, (ii) throughout the septal and peripheral cell walls, or (iii) only in the peripheral cell walls of *D. radiodurans* (Fig. 2A). For this, cells were pulse labelled with two dyes: BODIPY-FL 3-amino-d-alanine (BADA), a green dye that is stably incorporated into the pentapeptide chain of PG during its synthesis and does not reorganize during the cell cycle, and Nile Red that diffuses into lipid membranes and thus labels the whole cell wall, including newly synthesized cell wall during the cell cycle. The samples were then

washed to remove any unbound dye prior to imaging. The use of two lasers prevented *D. radiodurans* from growing under the microscope. Instead, cells were therefore observed shortly after the labelling procedure ($T=0$) and then again after a complete cell cycle ($T=130$ min). The mode of PG synthesis could be deduced from such images by comparing the lengths of green- and red only-labelled cell walls per cell (Fig. 2A) at $T=0$ with that observed after a complete cell cycle ($T=130$ min). If growth is restricted to the septal region (model i), which is not labelled with the BADA dye at $T=0$, the length of the green-labelled cell wall should remain constant after one cell cycle; if growth occurs throughout all cell walls (model ii), the lengths of both the green- and red-labelled cell walls should increase, and if growth is restricted to the outer periphery of the cells (model iii), then the red only-labelled cell wall should remain constant (Fig. 2A). For ease of analysis, we performed our measurements on Phase 1 cells that displayed complete BADA (green) labelling of their peripheral cell wall, but only Nile Red staining of their central septum at $T=0$ (Fig. 2B) and could thus be compared to our proposed models presented in Fig. 2A. After a complete cell cycle, Phase 1 cells clearly displayed an altered labelling pattern (Fig. 2B and 2C). Measurements revealed that the lengths of both green- and red-labelled regions had significantly increased (Fig. 2D), thus indicating that PG synthesis and cell wall growth occur throughout the entire cell surface of *D. radiodurans* cells including septal regions (Fig. 2A), as reported for *S. aureus* (Monteiro et al, 2015).

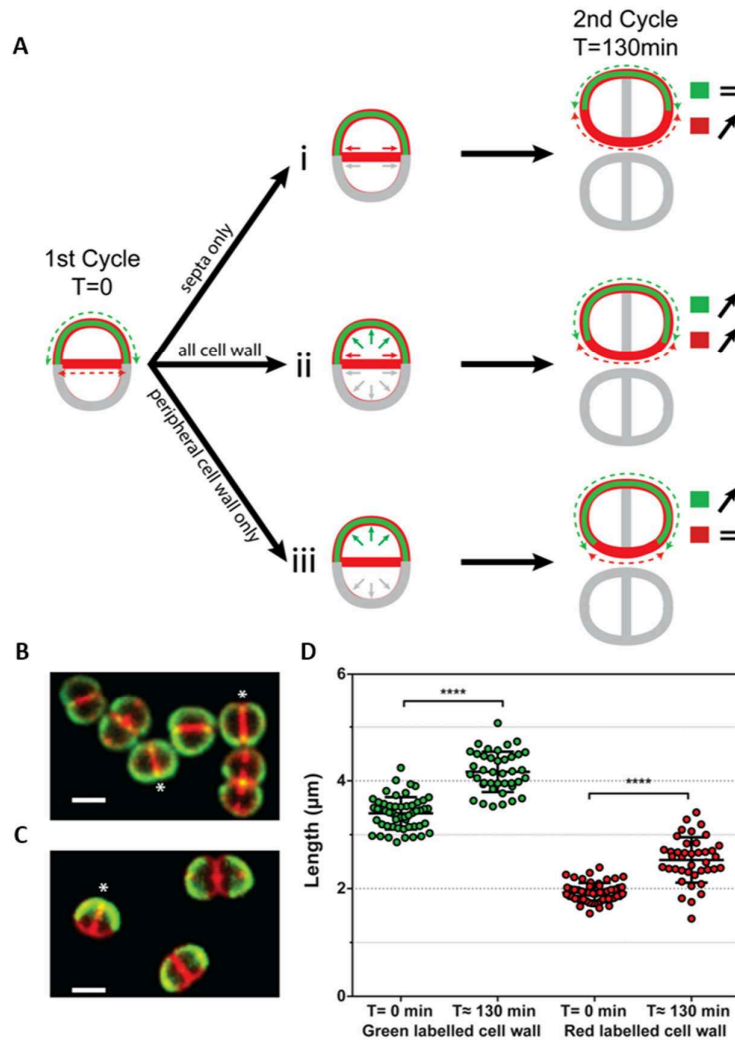


Figure 2: Mode of growth and division of *D. radiodurans*. (A) Schematic representation of three possible models of cell wall growth for a cell initially in Phase 1 and undergoing a complete cell cycle. At T=0 min, only the peripheral cell wall of the mother cell is labelled with BADA, represented in green; the whole cell wall (peripheral and septal) is labelled with Nile Red, represented in red. Nile Red signal suffers from a poorer signal/noise ratio than BADA, thus the Nile Red intensity was not adjusted to the level of BADA and the superposition of both colors does not appear yellow. Considering the periphery of the new diad after a complete cell cycle (T=130 min), if the growth occurred by peptidoglycan synthesis (i) in the septal regions only, the length of the BADA labelled cell wall would remain the same while the length of the cell wall labelled only with Nile Red would increase; (ii) throughout the bacterial cell walls, both the length of the BADA labelled cell wall and the cell wall labelled only with Nile Red would increase; (iii) only in peripheral cell walls, the length of the BADA labelled cell wall would increase while the length of the cell wall labelled only with Nile Red would remain the same. (B)-(C) Examples of *D. radiodurans* cells at T=0 (B) and T=130min (C). Cells marked by an asterisk are cells in Phase 1 that were used for the perimeter measurements and cell wall growth analyses (D). Scale bar: 2 μm. (D) Lengths of the green- and red only-labelled cell walls at T=0 min and T=130 min for Phase 1 cells (N>50). Both significantly increase after a complete cell cycle. (****: P<0.0001). Data were collected from 3 independent experiments.

Nucleoid organization during the cell cycle

Next, we used spinning-disk microscopy on live cells to follow the morphology of *D. radiodurans* nucleoids as a function of their cell cycle in exponentially growing and stationary phase bacteria. The nucleoids were visualized either by using a genetically modified strain of *D. radiodurans* in which the gene encoding the highly abundant HU protein was endogenously fused to mCherry, or by staining the DNA with the Syto9 dye (Fig. 3). The high extent of colocalization observed when double staining *D. radiodurans* nucleoids with both HU-mCherry and Syto9 (Supplementary Fig. S7) confirmed that HU largely coats the genomic DNA and that the same structures could be seen in both cases, including the previously described ring-like or toroid structure. This was in marked contrast with observations made in fixed and in DAPI or Hoechst labelled cells in which the nucleoids were found to be largely decondensed and to occupy a wide fraction of the cell. When using Syto9, cell membranes could additionally be stained with Nile Red in order to distinguish the different phases of the cell cycle (Fig. 3).

Nucleoid conformations were assessed in a large number ($N > 200$) of Syto9 and Nile Red stained wild-type *D. radiodurans* cells and representative three-dimensional shapes of nucleoids were retrieved for each phase of the cell cycle (Fig. 3). In addition, time-lapse imaging of either Syto9 stained nucleoids (Supplementary Movies S2) or HU-mCherry expressing *D. radiodurans* (Supplementary Movies S3) performed during a complete cell cycle enabled us to determine the chronological order in which these different conformations appeared. In Phases 1 and 2, a majority of nucleoids (respectively 52% and 42%) adopted toroidal shapes with an average diameter of $0.95 \pm 0.10 \mu\text{m}$. Additionally, in Phase 1, a substantial fraction (28%) of nucleoids were found to form condensed, undefined structures, which were seen to be short-lived (minutes) in our time-lapses and rapidly became toroids, which appeared to be more stable and long-lasting. Due to the reduced resolution of the spinning-disk images in the Z axis, we cannot rule out that these undefined structures may correspond to top views of toroids with an interior ring size below the resolution limit of the images. In Phase 2, 16% of nucleoids presented a square configuration with bright vertices, and a significant fraction (21%) also adopted a more open configuration (open ring or crescent). In Phase 3, these two nucleoid configurations were found to be the most prevalent (respectively 25 and 30%) and the crescent-shaped nucleoids were positioned with their convex sides facing the central septum of the diad (Fig. 3A). The fraction of toroidal-shaped nucleoids decreased significantly in Phase 3 and instead they were seen to open up to form crescents. In some cases, an intermediary step was observed in which the toroids became squares with 3 or 4 of their vertices exhibiting strong fluorescent foci before opening up to adopt a crescent shape. In Phase 4 cells, most of these configurations had disappeared and instead a large proportion of nucleoids were now elongated rods (54%) with an average length of $1.48 \pm 0.25 \mu\text{m}$ and an apparent full width at half maximum of $0.52 \pm 0.08 \mu\text{m}$. More complex branched structures (35%) were also observed in Phase 4. Remarkably, these structures

were all positioned with their long axis perpendicular to the future division axis (Fig. 3A). Time-lapse imaging revealed that these elongated structures resulted from the opening and stretching of the crescent-shaped nucleoids seen in Phase 3. In Phase 5 cells, in which the formation of the newly dividing septa was nearly complete, nucleoids appeared mostly as branched, elongated structures (35%), as seen in Phase 4, or as double rings connected by a thin thread (42%), in which each ring was positioned in one of the two future daughter cells. A clear constriction was observed around the center of these nucleoids resulting from the two closing septal segments (Fig. 3A). Time-lapse imaging revealed that the rod-like structures predominantly found in Phase 4 progressively formed more complex, branched structures that eventually formed double crescents or rings connected by short stretches of DNA. Finally, in Phase 6 cells, chromosome segregation was complete and the newly formed nucleoids presented similar configurations as those seen in Phase 1 cells, i.e. condensed, undefined structures (45%) or toroids (45%). These findings are summarized in a simulated movie that illustrates the principal morphological changes of the nucleoids observed in exponentially growing *D. radiodurans* cells as they progress through their cell cycle (Fig. 3B and Supplementary Movie S4). Interestingly, as observed previously when characterizing the different phases of the cell cycle, the two cells composing a diad were not necessarily synchronized in terms of nucleoid morphology. However, it was clear that the morphological changes at the nucleoid level were highly coordinated with cell cycle progression and septal growth (Fig. 3B).

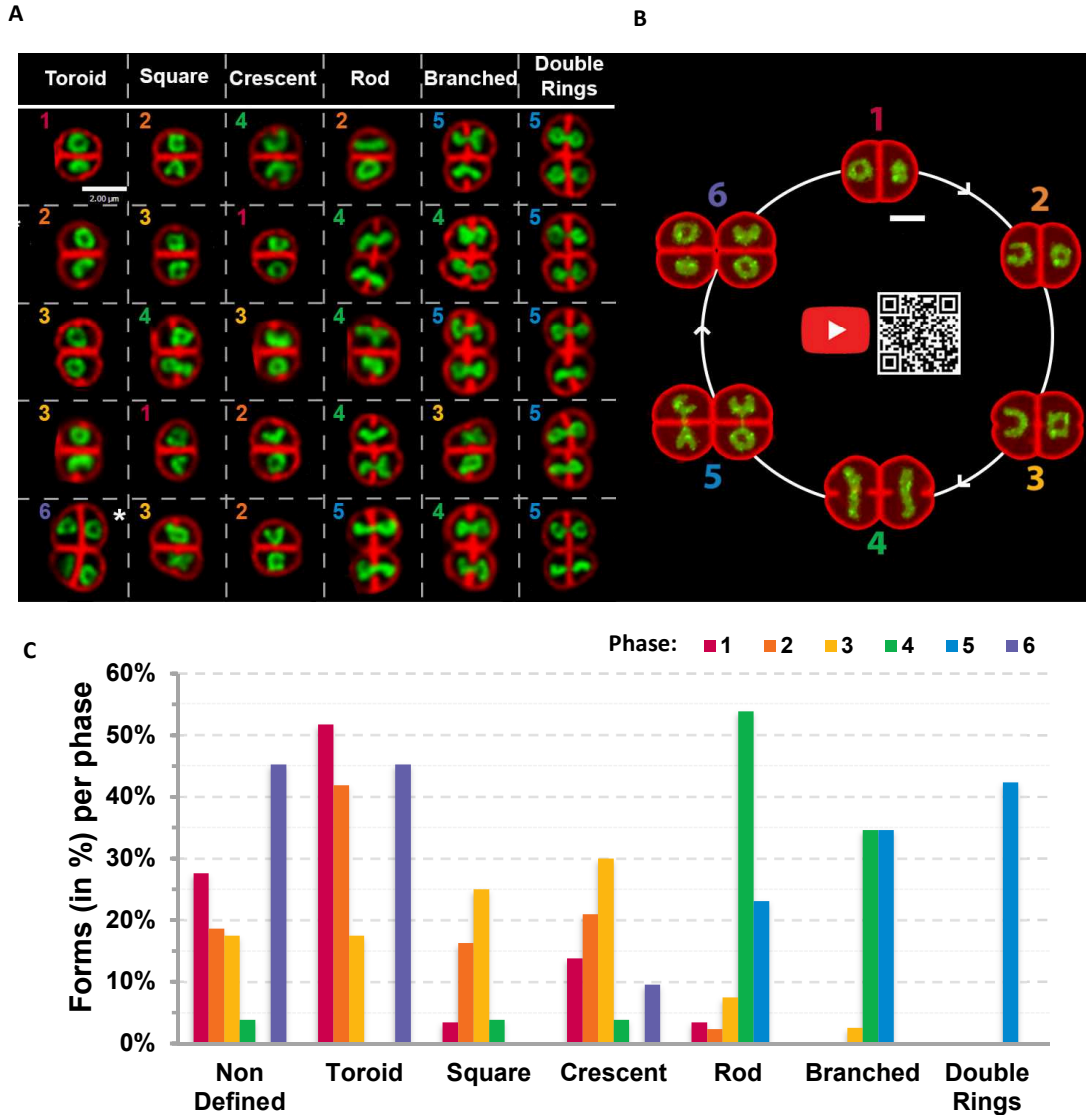


Figure 3: Nucleoid structures observed in exponentially growing *D. radiodurans*. (A) Array of the representative shapes of *D. radiodurans* nucleoids stained with the DNA dye Syto9. Cell membranes were stained with Nile Red. In each box, the representative shape is seen in the upper cell of the diad. In the case of tetrads, the representative shape is the cell marked with an asterisk. Numbers in each box represent the cell cycle phase of the upper cell. Scale: 2 μm . (B) Snapshot and link to an on-scale simulated reconstitution of the changes in cell shape and nucleoid structure occurring during the *D. radiodurans* cell cycle, illustrating the tight coordination of nucleoid rearrangements with septal growth (Supplementary Movie S4). This movie was created based on the cell and nucleoid measurements presented in Fig. 1D, Fig. 4A and Fig. S2 and on the cell cycle duration presented in Fig. 1E. Scale bar: 1 μm . (C) Distribution of the various nucleoid morphologies observed as a function of the phases of the cell cycle ($N > 200$ nucleoids).

Images of Syto9- and Nile Red-stained *D. radiodurans* were also used to determine the volume occupied by the nucleoid in *D. radiodurans* as a function of its cell cycle (Fig. 4A). Volumes were determined using the Imaris software and for comparison, the

same procedure was used for analysis of *E. coli* cells (Supplementary Fig. S7). Unlike the cell volume (Fig. 1C), the nucleoid volume did not increase linearly throughout the cell cycle (Fig. 4A). Instead it was found to remain constant ($\sim 0.7 \mu\text{m}^3$) during Phases 1 to 3 and then to increase in Phases 4 and 5 to reach a maximum volume of $\sim 1.2 \mu\text{m}^3$ just before cytokinesis. The newly formed nucleoids in Phase 6 exhibited the smallest volumes ($\sim 0.6 \mu\text{m}^3$). As a result, the fraction of the cell occupied by the nucleoid varied as a function of the cell cycle from a minimal value of $29.7 \pm 6.2 \%$ observed in Phase 4 to a maximal value of $35.6 \pm 5.6 \%$ detected in Phase 1 cells (Fig. 4B). In comparison, the mean cell and nucleoid volumes of *E. coli* cells were found to be $1.33 \mu\text{m}^3$ and $0.83 \mu\text{m}^3$ respectively, corresponding to a cell fraction occupied by the nucleoid of $65.2 \pm 14.9\%$ (Supplementary Fig. S7), in agreement with previously reported values (Fisher et al. 2013). These quantitative measurements thus confirm that *D. radiodurans* possesses a highly condensed nucleoid, but also reveal that its level of condensation varies during its cell cycle. We also determined the mean volume of Syto9-stained nucleoids in *D. radiodurans* expressing HU-mCherry, and found that these were slightly higher than that of wild-type cells (Supplementary Fig. S7), perhaps as a consequence of steric hindrance caused by the mCherry fusion protein. Exponentially growing *D. radiodurans* cells have been reported to possess 4 to 10 copies of their 3.2Mbp genome (Passot et al. 2015), so the DNA density in an average *D. radiodurans* nucleoid ($\sim 0.7 \mu\text{m}^3$) would be expected to be in the range of 18 to 46Mbp/ μm^3 . In *E. coli*, which possesses a single copy of a 4.6Mbp genome, the DNA density in its nucleoid is $\sim 6 \text{Mbp}/\mu\text{m}^3$, corresponding to a density 3 to 8 times lower than that observed in *D. radiodurans* cells.

Finally, Syto9- and Nile Red-stained stationary phase *D. radiodurans* tetrads were also analyzed to determine the level of nucleoid compaction in such cells (Supplementary Fig. S3). The average volume occupied by the nucleoid was found to be $18.6 \pm 4.7\%$, which is significantly lower than the highest level of DNA compaction measured in exponentially growing Phase 4 cells (Fig. 4B).

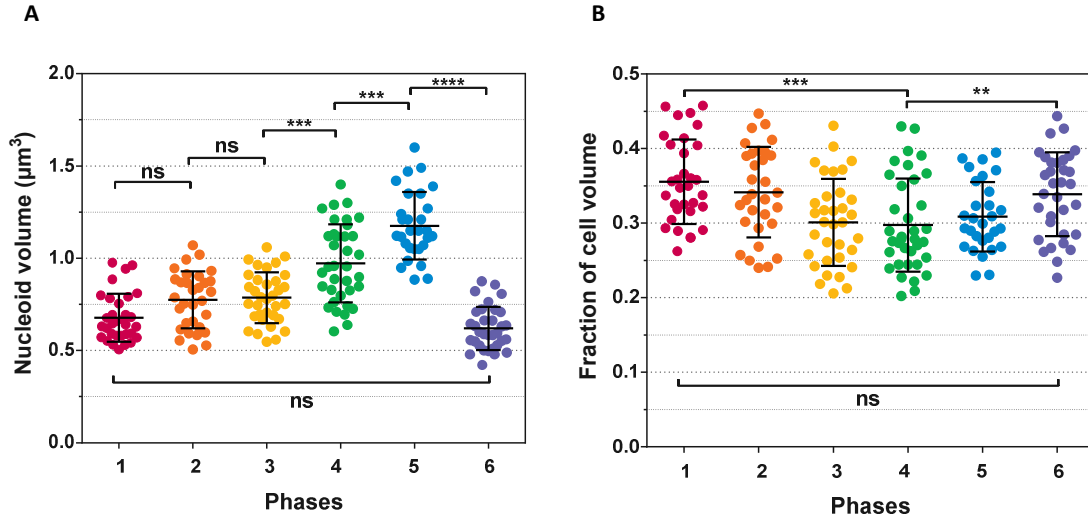


Figure 4: Nucleoid compaction as a function of *D. radiodurans* cell cycle. (A) Changes in nucleoid volume as cells progress through their cell cycle. Nucleoid volumes were retrieved from the three-dimensional signal of Syto9-labelled nucleoids of live, exponentially growing *D. radiodurans* cells. The nucleoid volume is relatively constant during the first three phases ($\sim 0.7 \mu\text{m}^3$) and then progressively increases to reach a maximal volume of $\sim 1.2 \mu\text{m}^3$ in Phase 5 cells just before cytokinesis. (B) The fraction of the cell volume occupied by the nucleoid was retrieved by dividing the nucleoid volume of individual cells by their matched cell volume, derived from spinning-disk images of dual labelled Syto9 and Nile Red stained cells, using the cell measurements presented in Fig. S4. The fraction of the cell occupied by the nucleoid significantly decreases during the first three phases (from 35.6% to 29.7%), and then remains around 30% until cytokinesis. After septal closure, the fraction increases again to $\sim 34\%$. (*: $P < 0.05$, **: $P < 0.01$, ***: $P < 0.001$, ****: $P < 0.0001$, ns: not significant, $N > 190$, $N > 29$ for each phase).

HU and nucleoid dynamics

To further characterize *D. radiodurans* nucleoids in exponentially growing bacteria, we used super-resolution photoactivated localization microscopy (PALM) to image a *D. radiodurans* strain in which the most abundant NAP, HU, was fused to PAmCherry. PALM experiments were performed exclusively on live bacteria because fixing protocols strongly affected the nucleoid organization (loss of diverse shapes and decondensation of the DNA). Several of the nucleoid morphologies described above (*eg.* crescent- and rod-shaped nucleoids) could be seen in the reconstructed PALM images, but most of the distinguishing features and details were lost (Fig. 5A). Although, PALM provides higher spatial resolution, acquiring a complete dataset in PALM microscopy can take several minutes. The loss of details in our PALM images thus most likely reflects the dynamic nature of the nucleoids in the second to minute timescale, as confirmed by a spinning-disk microscopy time-lapse experiment in which images of HU-mCherry were acquired in live *D. radiodurans* with short interval times (Supplementary Fig. S8).

HU has been shown to play a major role in the compaction and organization of the nucleoid in *D. radiodurans* (Passot et al. 2015; Toueille et al. 2012) and to be essential for viability. We therefore wondered whether HU was responsible for the remarkable plasticity of *D. radiodurans* nucleoids. Both single-molecule and ensemble measurements were carried out to probe the dynamics of HU proteins in live, exponentially growing *D. radiodurans*. Single-particle tracking PALM (sptPALM) experiments were performed on the HU-PAmCherry expressing *D. radiodurans* strain in which the trajectories of individual HU-PAmCherry molecules were reconstituted (Fig. 5B). Cumulative probability distribution (CPD) analysis (Matysik & Kraut 2014) of 1000 individual tracks extracted from several datasets revealed that only a single population of molecules could be distinguished, which displayed a confined diffusion (with a confinement radius of ~ 400 nm; Supplementary Fig. S8) with an average apparent diffusion coefficient of $\sim 0.32 \mu\text{m}^2.\text{s}^{-1}$. This value, which is significantly lower than that obtained for freely diffusing fluorescent proteins in bacteria ($6-9 \mu\text{m}^2.\text{s}^{-1}$; (Kumar et al. 2010)), but also higher than that of immobile, DNA-binding proteins ($D^* < 0.2 \mu\text{m}^2.\text{s}^{-1}$ (Gao et al. 2017; Stracy et al. 2015)), clearly indicates that HU is not tightly associated with the genomic DNA. Ensemble measurements of HU mobility probed by fluorescence recovery after photobleaching (FRAP) on HU-mCherry expressing *D. radiodurans* cells confirmed these findings and revealed that 95% of HU molecules were mobile exhibiting a half-life of 0.75 s (Fig. 5C). These data are consistent with a FRAP study of the *E. coli* NAP, H-NS (Kumar et al. 2010) and suggest that even though HU coats the DNA, it most likely only associates transiently with DNA, thereby allowing the nucleoid to rapidly reorganize as the cells progress through their cell cycle.

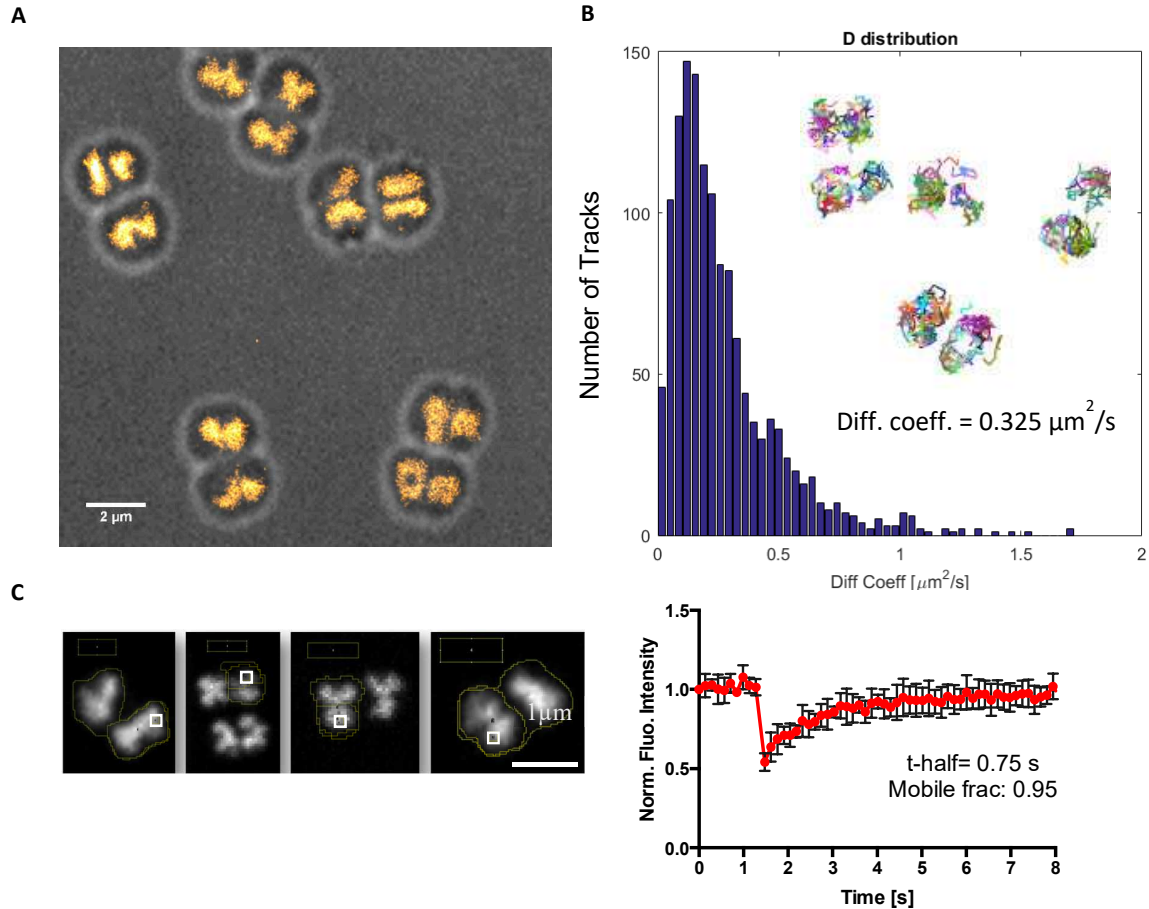


Figure 5: Dynamics of the abundant, histone-like protein HU in live *D. radiodurans*. (A) Reconstructed PALM image of HU-PAmCherry expressing cells (stack of 15,000 frames with 50ms framerate and acquired with constant 1 kW/cm² 561nm laser and increasing 405nm laser power). Several of the nucleoid morphologies illustrated in Fig. 3 can be seen in this image, but without a significant improvement in spatial resolution, due to the dynamics of nucleoids in live cells that change conformation in the minute timescale (Supplementary Fig. S8). (B) Distribution of the apparent diffusion coefficients of single tracks of HU-PAmCherry measured by single-particle tracking PALM in live, exponentially growing HU-PAmCherry expressing *D. radiodurans*. Inset: example of individual trajectories of HU-PAmCherry molecules and mean diffusion coefficient derived from 1,000 tracks. (C) Ensemble measurements of HU-mCherry mobility probed by fluorescence recovery after photobleaching (FRAP) on HU-mCherry expressing live *D. radiodurans* cells. Left: examples of HU-mCherry labelled nucleoids used for FRAP experiments. The photobleached region is indicated with a white box. Scale bar: 1 μm. Right: Analysis of the recovery of the fluorescence signal of HU-mCherry after photobleaching ~50% of the fluorescence signal. These data reveal that 95% of HU-mCherry molecules are mobile exhibiting a half-life of 0.75 s. Presented data are the mean values (with standard deviation) derived from 3 independent experiments.

Choreography of *ori* and *ter* sites during the cell cycle

To follow the choreography of the *ori* and *ter* loci during the cell cycle of exponentially growing *D. radiodurans*, we used engineered *D. radiodurans* strains, GY15787 and GY15800, in which a heterologous ParABS system is used to fluorescently label respectively the *ori* and *ter* loci of chromosome 1, allowing them to be detected as bright foci within the cells (Passot et al. 2015). Three colour spinning-disk microscopy images were recorded on such cells in order to visualize GFP-labelled *ori* or *ter* loci, hydroxycoumarin-amino-D-alanine (HADA)-stained cell walls and HU-mCherry labelled nucleoids (Supplementary Fig. S9). When analysing these images, we chose to restrict our analysis to the bright ParB-labelled foci that could unambiguously be discriminated from the background fluorescence. This most likely explains why a reduced number of foci were counted per cell compared to the original study (Passot et al. 2015).

Throughout the cell cycle, the number of *ter* foci in cells was systematically lower than that of *ori* foci (Fig. 6A), as reported previously (Passot et al. 2015). The number of *ori* foci was found to double as the cells progress from Phase 1 to Phase 5, going from a mean number of 2.25 foci/cell to 4.44 foci/cell in Phase 5 (Fig. 6B). After septal closure, in Phase 6, the number of *ori* foci was almost divided by 2, reaching 2.38 foci/cell. This suggests that DNA replication occurs all along the cell cycle until all copies of *ori* from chromosome 1 have been duplicated. In contrast, the number of *ter* foci remains much lower around 1.15 foci/cell and constant for most of the cell cycle until Phase 5 where it increases to reach 1.5 foci/cell.

We also investigated the localization and distribution of the two loci within the cells (Fig. 6C-D). The *ter* foci were found to be specifically located to the central region of cells during most of the cell cycle with a majority of foci being located along the new division axis (Fig. 6C and Supplementary Fig. S19). 47% of them were still localized in the region of septal closure in Phase 5, just before cytokinesis, indicating a very late segregation of *ter*. Interestingly, it was in Phase 2 that the highest proportion of *ter* foci were localized along the new division axis (65%). In contrast, the *ori* foci displayed a very different cellular distribution and could be seen throughout the cell (Fig. 6D) with only a minor fraction localized along the new division axis (Supplementary Fig. S9). Interestingly, both *ter* and *ori* seemed to be excluded from the peripheral region of the cell bordering the cell wall.

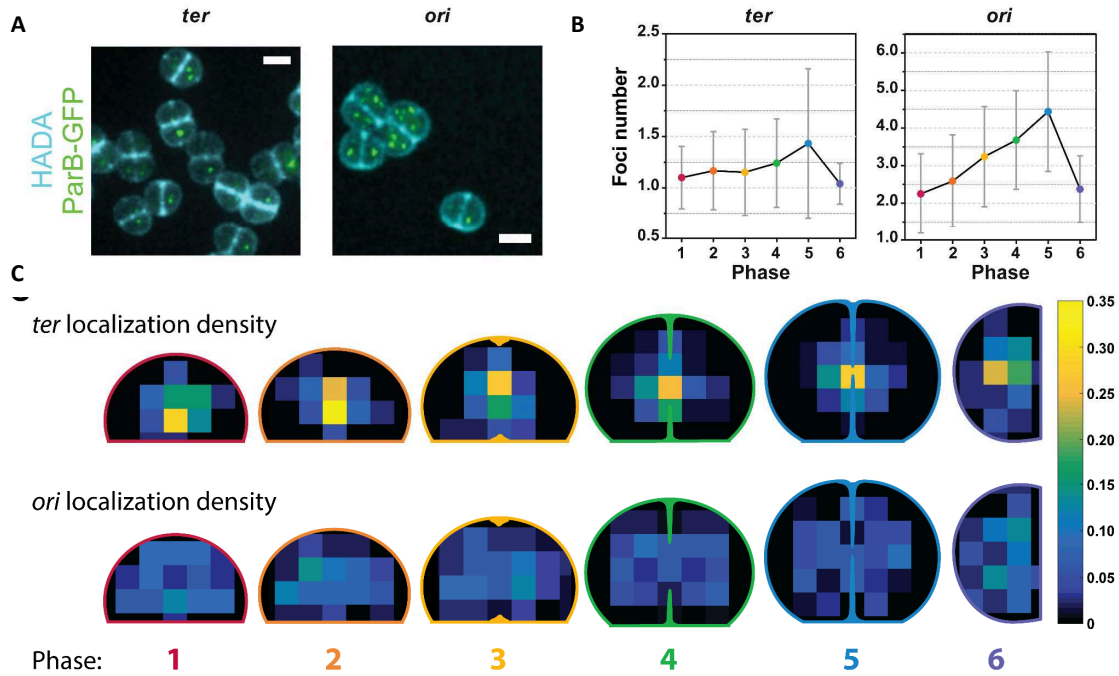


Figure 6: Number and distribution of *ter* and *ori* loci of *D. radiodurans* chromosome 1 in exponential growing cells. (A) Images of *D. radiodurans* strains GY15787 and GY15800 expressing HU-mCherry and a heterologous ParB fused to GFP (green foci), with multiple copies of its cognate *parS* sequence inserted nearby chromosome 1 *ter* (left) or *ori* (right) loci respectively, and stained with the cell wall HADA dye (blue). For clarity, the HU-mCherry signal is not included in these images. Scale bar: 2 μ m. (B) Average number of *ter* and *ori* foci detected per cell at the different phases of the cell cycle. (C) Weighted distribution density of *ter* (top) and *ori* (bottom) foci at the different phases of the cell cycle. In (B)-(C) >300 foci of either *ter* or *ori* were analyzed and data were retrieved from 2 independent experiments.

No clear correlation could be established between foci localization and nucleoid morphology. However, particular configurations could be seen (Supplementary Fig. S9). *ter* foci could for example be observed occasionally in the centre of the toroid- and square-shaped nucleoids, i.e. in regions devoid of HU-mCherry labelling. In the late stage of nucleoid segregation (Phase 5), *ter* foci were also seen to localize on the thin thread connecting the partially segregated nucleoids (double rings), close to the new division axis and the closing septum. *ori*, in contrast, was often seen at the periphery of the nucleoids, and occasionally at the outer tips of the branched nucleoids observed in Phase 4 cells.

4. Discussion

In this work, we have characterized the cell cycle of exponentially growing *D. radiodurans*, enabling us to define 6 distinct phases, and have followed the changes in the cell and nucleoid morphology occurring during this process. We determined that *D. radiodurans* diads grow throughout their cell cycle via remodelling of their entire cell surface (peripheral and septal cell walls) and divide in alternate orthogonal planes. As proposed in an early study of *D. radiodurans*, our 3D images confirmed that growth of the dividing septum occurs through a closing door mechanism and not as a diaphragm as has been reported for other cocci bacteria (Murray et al. 1983): one side originating precisely from the middle of the central septum, the other from the middle of the opposite peripheral cell wall, both growing at a 90° angle to the central septum. Septal growth lasts for two-thirds of the cell cycle (Phases 3-6). Asynchronization of the division process was occasionally observed: (i) between two cells that form a diad, resulting in cells of the same diad being in different phases of the cell cycle, or (ii) within a given cell, in which one side of the closing septum started growing earlier or faster than the other side, although overall, no difference in growth speed was observed between the two sides of the closing septum (Supplementary Fig. S2). In exponentially growing *D. radiodurans*, once the dividing septum closes (Phase 6), the newly formed tetrads are relatively short-lived, lasting for a dozens of minutes before splitting into two diads to initiate a new cell cycle (Phase 1). Cytokinesis results from the progressive increase in the curvature of the central septum (and reduction in its length) until the two diads eventually separate, creating a small gap between the two adjacent diads. It was recently shown in *S. aureus*, that the splitting of the diads into single cells occurs on the millisecond timescale driven by the turgor pressure (Monteiro et al. 2015; Zhou et al. 2015). In *D. radiodurans*, visualizing this splitting process was more difficult, since the cells do not undergo any substantial morphological changes upon cytokinesis. Instead the separation appears to be slower and progressive, most likely catalyzed by the enzymatic processing of the cell wall in this region of the cell.

In every organism, nucleoid organization and cell division are intimately linked. The present study presents the first morphological characterization of the nucleoids of a coccus bacterium. The nucleoids of *D. radiodurans* were found to display a remarkable plasticity, adopting multiple, distinct conformations as the cells progress through their cell cycle. Our single-molecule and ensemble measurements suggest that the dynamic nature of these nucleoids may be facilitated by the loose binding of the major *D. radiodurans* NAP, the histone-like protein HU, to the genomic DNA. To our knowledge, this is the first report of such a wide diversity of nucleoid structures in bacteria. In addition to the previously reported toroid-shape, the nucleoid was also found to adopt an elongated branched structure that aligned parallel to the central septum. This arrangement perpendicular to the newly growing septum provides clear evidence that

nucleoid organization and chromosome segregation are tightly coupled to the cell division process. In many model bacteria including *S. aureus*, *E. coli* and *B. subtilis*, nucleoid occlusion (NO) systems, typically composed of sequence specific DNA-binding proteins, play a central role as spatial and temporal regulators of cell division by preventing the assembly of the divisome over the nucleoid (Wu & Errington 2012). Interestingly, in *D. radiodurans* Phase 3 cells in which septal growth is starting, three major conformations of nucleoids can be observed: toroids, squares and crescent-shaped nucleoids formed by the opening of the ring-like structures prior to their elongation and alignment with the central septum in Phase 4. Changes in the cell morphology and in particular start of septal growth, thus seem to precede the major rearrangements of the nucleoid, which suggests that the nucleoid is not the major determinant of the division site in *D. radiodurans*. Although no NO system has so far been identified in *D. radiodurans* (Pinho et al., 2013), we cannot exclude that such a system might also be at play in the regulation of cell division in this organism.

The Min system that prevents the formation of the Z-ring in aberrant locations (Lutkenhaus 2007), might be the main factor ensuring that cytokinesis occurs at midcell in *D. radiodurans*. Many spatial features have been proposed as key determinants of pole-to-pole oscillations of Min in *E. coli*, such as the highly negative membrane curvature at the poles (Renner & Weibel 2011), the longest axis of confinement (Schweizer et al. 2012), the longest possible distance for the diffusion of MinD (Corbin et al. 2002) or the symmetry axes and scale of the cell shape (Wu et al. 2015). *D. radiodurans* diads do not possess any poles per se. In Phase 1, cell ellipticity is close to 1 and cells possess an infinite number of symmetry planes (i.e. every plane orthogonal to the central septum). It is only when the cells start growing in Phase 2 (with a major change in the length of the major axis and no change in minor axis length leading to a decrease in the ellipticity of the cells), that the number of symmetry planes is reduced to two, both orthogonal to the central septum, one having its normal vector parallel to the long axis of the cell and the other with its normal vector parallel to the second short axis. A possible oscillation of MinCDE along the long axis of the ellipsoidal shaped cell, parallel to the central septum, could be the basis for the precise placement and angle of growth of the dividing septum, orthogonal to the central septum and along the short axis of the cell. In such a scenario, the Min system would sense the geometry of the cell and start to oscillate in Phase 2.

As bacterial nucleoids fill a large fraction of the total cell volume, a common hypothesis suggests that the cell size and shape may play a major role in chromosome positioning and sizing. It was recently proposed that cell shape and size were “sensed” indirectly by chromosomes via the pressure exerted by depletion forces induced by cytosolic crowders (Jun & Mulder 2006; Wu et al. 2018), which would promote the compact shape and central localization of nucleoids in cells. In the case of *D. radiodurans*, several studies have described its nucleoid as being highly condensed (Englander et al. 2004; Levin-

Zaidman et al. 2003; Minsky et al. 2006; Minton & Daly 1995; Zimmerman & Battista 2005), but this visual impression is in part due to the relatively large size of *D. radiodurans* cells that have a mean volume of $\sim 2.6 \mu\text{m}^3$. We therefore assessed the volume occupied by the nucleoids of *D. radiodurans* and compared them to that of *E. coli*, which had previously been reported to occupy $\sim 70\%$ of the cell volume (Fisher et al. 2013). Our measurements revealed that the mean volume of *D. radiodurans* nucleoids is very similar to that of *E. coli* (0.7 vs $0.8 \mu\text{m}^3$), but because of the larger cell volume, the fraction of the cell occupied by the nucleoid is significantly lower in the case of *D. radiodurans* and was found to vary from 25 to 40% depending on the phase of the cell cycle. This fraction even decreased to $\sim 18.5\%$ in stationary phase cells, which are smaller and present highly condensed nucleoids. Such small cell fractions occupied by the nucleoid suggest either that depletion forces do not play a major role in nucleoid positioning and compaction in *D. radiodurans* or that *D. radiodurans* cells possess an unusually high concentration of crowders.

Because *D. radiodurans* possesses multiple copies of its genome, compared to a single copy in *E. coli*, the average DNA density in *D. radiodurans* nucleoids is thus significantly higher than in *E. coli*, thereby confirming the impression that *D. radiodurans* nucleoids are particularly condensed. Interestingly, the nucleoids were found to be most compact in Phases 4 and 5, during the final stages of chromosome segregation. The specific positioning of the nucleoids in the center of cells and parallel to the central septum, together with their increased levels of compaction during these late stages of the cell cycle are reminiscent of metaphase chromosomes in eukaryotic cells that align at midcell prior to segregation of each one of the two chromosomes into the two daughter cells.

Finally, we compared the number and distribution of the *ori* and *ter* loci of chromosome 1 as a function of the cell cycle. As previously reported (Passot et al. 2015), there were significantly more *ori* foci in cells than *ter* sites irrespective of the stage of the cell cycle. This difference has been proposed to result from either a difference in transient cohesion periods of sister chromatids just after replication, this period being longer for *ter* and/or a very late replication of *ter* compared to *ori* (Passot et al. 2015). Our cartography of the localizations of *ori* and *ter* loci in *D. radiodurans* at each phase of the cell cycle also revealed very distinct distribution patterns for the two loci and allow us to propose a first model for nucleoid organization and choreography in a coccus bacterium possessing a complex, multicopy genome (Fig. 7). Chromosome arrangement in *D. radiodurans* is neither longitudinal nor transversal, but instead radial with *ori* sites distributed all around centrally located *ter* sites. The *ter* loci were clearly retained and clustered by a yet unknown mechanism in the central region of the cells until just before cytokinesis (Fig. 7B and C). *ter* foci could indeed be seen in the small gap formed by the closing septal doors in Phase 5 cells. Segregation of replicated *ter* loci occurred at a very late stage of the cell cycle (Phase 5; Fig. 7C) and the duplicated *ter* loci rapidly migrated to the centre of the two new sister cells in Phase 6. In contrast, *ori* loci localized

throughout the cell, with the exclusion from membrane proximal regions, ruling out any direct anchoring of *ori* loci to the cell walls as has been observed in some bacteria (Ben-Yehuda et al. 2005; Thanbichler & Shapiro 2006; Yamaichi et al. 2012). Further work will be needed to understand the detailed choreography of this complex genome and how it relates to the various nucleoid structures observed in this study.

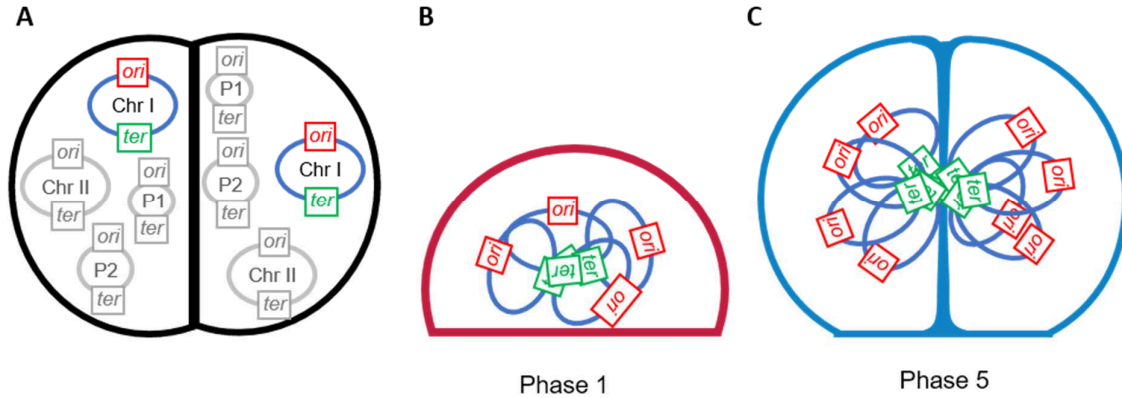


Figure 7: Radial organization and segregation of chromosome 1 in *D. radiodurans* (A) *D. radiodurans* possesses multiple copies (4 to 10) of four replicons (2 chromosomes: Chromosome 1, Chr1 and chromosome 2, Chr 2, and two plasmids, P1 and P2), each of which possess an origin of replication (*ori*) and a termination site (*ter*). For Chr1, the *ori* and *ter* loci are represented respectively in red and in green. (B)-(C) Proposed arrangement of Chr1 in Phase 1 and 5 cells. The centrally located *ter* loci surrounded by radially distributed *ori* loci seen in Phase 1 cells are maintained for most of the cell cycle. It is only in Phase 5 that this arrangement changes as a result of the late duplication and segregation of *ter* sites. Chr1 is present in at least 4 copies in Phase 1, and this number doubles by the end of the cell cycle (Phase 5). The *ori* loci are dispersed throughout the cytoplasm, but are excluded from regions in vicinity to the peripheral cell membrane. The number of *ter* foci remains constant and close to 1 for most of the cell cycle, most likely as a result of their clustering by an unknown mechanism. During septal growth, fewer *ori* loci are found in the vicinity of the growing septa, while the *ter* loci remain in the center of the cell throughout the cell cycle and progressively drift away from the central septum after cytokinesis to relocate in the center of the daughter cells.

5. Methods

Bacterial cultures

All *Deinococcus radiodurans* strains (wild-type, HU-mCherry, HU-PAmCherry GY17031, and *ori/ter* labelled strains GY15787 and GY15800) were grown at 30°C with shaking in TGY2X supplemented with the appropriate antibiotics. *Escherichia coli* strain BL21 (DE3) was grown at 37°C with shaking in LB medium. For microscopy experiments, *D. radiodurans* cells were pre-grown the day before and then diluted for an overnight growth until reaching exponential (OD₆₅₀ ~0.3-0.5) or stationary phase (OD₆₅₀ >5). To establish the growth curve of wild-type *D. radiodurans* cells, cultures inoculated at different cell densities were measured every 2h and then combined to obtain a complete growth curve. The final growth curve corresponds to the mean of three independent experiments.

Sample preparation for microscopy

General sample preparation: Glass coverslips used for PALM/PAINT imaging of *D. radiodurans* were treated in an ozone oven for at least 10 minutes. 1.75% low-melting agarose (Biorad) pads dissolved in minimal medium (Floc'h et al. 2018) (for PALM) or TGY2X (for spinning-disk microscopy) were poured on a cover slide inside a frame made with double-faced tape. A glass coverslip was placed on top of the agarose pad in order to flatten the surface of the agarose while hardening. This coverslip was removed once the agarose had solidified. For imaging, bacterial cultures were centrifuged 3 min at 3000 x g and were resuspended in 10 µl of medium or washed in high purity PBS (GIBCO). 1 µl of this cell suspension was deposited on the pads. The drop was spread over the surface of the pad by rotating the coverslip. A second coverslip was placed over the agarose pad containing the sample, thereby immobilizing the bacteria on the pad.

Nucleoid and cell membrane staining: To determine the growth phase and cell volumes, cells in exponential phase were incubated with Nile Red for 15 min at 30°C, with agitation and then placed on an TGY agarose pad. For single timepoint images acquired with the spinning disk microscope, the Nile Red was used at a concentration of 30 µM. For correlative spinning-disk microscopy and PAINT imaging the concentration was 300 nM. For PAINT imaging alone, the concentration was 15 nM. To determine nucleoid volumes, cells in exponential phase were incubated with Nile Red (30 µM) and Syto9 (150 nM) for 15 min at 30°C, with agitation and then placed on a TGY2X agarose pad. In all cases, the cells were rinsed to remove excess dye prior to imaging.

Peptidoglycan labeling: Cells in exponential growth phase were stained with the fluorescent BADA dye (Pilhofer et al. 2013) at a concentration of 31 µM, incubated at 30°C with agitation for 15 min. Then Nile Red was added (15 µM) for another 15 min

at 30°C with agitation. The cells were then rinsed in TGY2X at 30°C in order to remove unbound dyes. Cells were then returned to the incubator and at different timepoints (T=0 and T=130min), cells were deposited on TGY2X agarose pads for imaging.

Timelapse imaging: Cells in exponential growth phase were incubated with Nile Red (15 μ M) for 15 min at 30°C, with agitation. Cells were then rinsed in TGY2X and placed on an TGY2X agarose pad designed with air holes to oxygenate the cells (Jong et al. 2011). The samples were maintained at 30°C during image acquisition. Single plane image sets were acquired every 10 min, for a total period of 4h, using very low 561 nm laser power (few micro-Watts) and 100 ms exposure times.

Foci acquisition: A saturated pre-culture of *ori* or *ter* labelled HU-mCherry expressing *D. radiodurans* cells was diluted 60X in fresh TGY2X and grown for a further 5h until reaching an OD₆₅₀ between 0.3 and 0.5. Cells were then stained with HADA (30 μ M) for 30 min and deposited on a TGY2X agarose pad.

Image acquisition

PALM/PAINT imaging: Wide-field illumination was achieved by focusing the laser beams to the back focal plane of a 100x 1.49-numerical-aperture (NA) oil immersion apochromatic objective lens (Olympus). The intensity and time sequence of laser illumination at the sample were tuned by an acousto-optical tunable filter (AOTF; Quanta Tech). Near circular polarization of the laser beams was ensured by inserting a polychromatic quarter-wave plate downstream the AOTF. 8 to 20 cells were imaged per field of view. Typically, for each sample 2 or 3 fields of view on the same agarose pad were imaged and at least three independent experiments were performed on different days. Sample drift was corrected in ImageJ using gold nanobeads (Sigma) deposited on the agarose pads nearby the bacteria.

Single particle tracking: Data were acquired with continuous 561 nm light illumination, at low power (130 W/cm²) using a framerate of 30 ms. The Trackmate plugin for ImageJ was used to localize the particles in each frame and to connect the coordinates into trajectories (Tinevez et al. 2017). Simple LAP (Linear Assignment Problem) Tracker generated the tracks, with a maximal allowed linking distance set to 200 nm and a maximal frame interval between two spots to be bridged set to 2. Only tracks that contained more than four points were exported into MATLAB for further processing. The TrackArt MATLAB software (Matysik & Kraut 2014) was used to analyze trajectories and determine cumulative probability distributions and apparent diffusion coefficients. Trajectories shorter than 10 frames or with a minimal individual mean square displacement (MSD) fit “R²” values below 0.9 were filtered out.

Spinning disk imaging: Spinning-disk confocal microscopy was performed on the M4D cell imaging platform at IBS using an Olympus IX81 microscope and Andor iXon Ultra

EMCCD Camera with the laser beams focused to the back focal plane of a 100X 1.49-numerical-aperture (NA) oil immersion apochromatic objective lens (Olympus). The intensity and time sequence of laser illumination at the sample were tuned by an acousto-optical tunable filter. For cell and nucleoid volume analyses, series of Z-planes were acquired every 100 nm, whereas 200 nm was used for the multiplex imaging of *ori* and *ter* labelled *D. radiodurans* strains.

FRAP measurements: A time-lapse acquisition of the fluorescence channel (mCherry) was performed for 60 timepoints at the fastest acquisition speed (10 timepoints before and 50 timepoints after photobleaching). Photobleaching (Andor FRAPPA module) was set at the wavelength used for imaging, targeting a single point (crosshair) of the analyzed nucleoid. Bleaching was performed using a low intensity setting (2% of the nominal maximum laser power), for 160 μ s dwell time and 12 repeats to achieve a sufficiently small bleached region and with a loss of at least 50% of the original signal intensity. FRAP analysis was performed using EasyFRAP after measuring intensities using (Schindelin et al. 2012), as described in the original publication (Rapsomaniki et al. 2012).

Analysis

For cell volume measurement: To calculate the volume of each cell, an ellipse was fitted to the cellular membrane of Nile Red-labelled cells in 2D images. Measurements of the shorter (L_{short} in Fig. S4A) and longer (L_{long} in Fig. S4A) axes of these ellipses were extracted from such fits. The distance between the central septum and the extremity of the exterior of the ellipse along the short axis was measured (P in Fig. S4A), to retrieve the distance between the septum and the center of the ellipse along the short axis (w value in Fig. S4A). With all these values, the total volume of the cell was computed using the equations presented in Supplementary Fig. S4A with the cells approximated as prolate ellipsoids. The length and width of the elongated and toroid shaped nucleoids were measured as described in Supplementary Fig. S4C and D.

For peptidoglycan ratio: To determine the extent of BADA (green) versus Nile Red (red) staining in Phase 1 cells, the perimeter of each cell was measured by fitting an ellipse to the Nile Red-labelled cell membrane. The fraction of cell wall labelled with BADA was then determined by measuring the two angles as shown in Supplementary Fig. S4B. The perimeter of Nile Red only stained membranes (without any BADA labeling) for an angle α , is retrieved from the equation (1). The BADA labelled perimeter was then determined by computing the lengths of the two sections of cell wall devoid of BADA labeling and subtracting them from the whole perimeter of the ellipse.

$$l = \int_0^\alpha \sqrt{(L_{short} * \cos(\theta))^2 + (L_{long} * \sin(\theta))^2} d\theta \quad (1)$$

Nucleoid volume measurements: The Syto9 fluorescence signal corresponding to the nucleoids was deconvoluted in Volocity using 7 iterative cycles and a calculated PSF (488nm/520nm). Cropped images in which the fluorescence signal was homogeneous throughout the full field of view were then exported to the Imaris (Bitplane) software, where surfaces were created based on the automatic thresholding of the fluorescence signal. The same settings in Imaris were used to extract nucleoid volumes from all our samples, including *E. coli* nucleoids.

Foci distribution: Using the Volocity software, Z-stacks of the GFP signal were iteratively deconvoluted using a calculated PSF (488nm/520nm). In the case of *ter*, Z-projection for each channels were concatenated into multi-channel stacks. In the case of *ori*, the same multi-channel stacks were assembled, but we also verified that fluorescent foci were not lost by the Z projection. Fluorescent foci were manually marked in ImageJ to extract their xy coordinates as well as the dimensions and phase of the cells in which they were found. The number of foci and their distribution were then automatically determined with respect to the average cell dimension of *D. radiodurans* cells at each phase of the cell cycle derived from PAINT imaging.

Statistical analysis: The non-parametric Mann-Whitney tests were performed with GraphPad Prism 6 in order to assess the difference in cell dimensions and nucleoid volumes during the cell cycle. P values below 0.01 were considered as significant and were indicated with asterisks: **P 0.01, ***P 0.001, **** P 0.0001.

Acknowledgements

We thank Prof. Yves Brun and Prof. Michael Van Nieuwenhze for providing us with the BADA dye. This work was supported by CEA Radiobiology grant (A-IRBIO-01-19) and the CEA Irtélis program (PhD grant of KF). This work used the M4D imaging platform of the Grenoble Instruct-ERIC Center (ISBG: UMS 3518 CNRS-CEA-UGA-EMBL) with support from FRISBI (ANR-10-INBS-05-02) and GRAL (ANR-10-LABX-49-01) within the Grenoble Partnership for Structural Biology (PSB).

Contributions

KF, FL, DB and JT designed the research. KF, FL and JPK performed the microscopy experiments. PS provided the genetically modified strains of *D. radiodurans*. YSW synthesized the HADA dye. KF, FL, JPK and JT analyzed the data. KF, DB and JT wrote the manuscript and all authors discussed the results and approved the manuscript.

6. References

- Badrinarayanan, A., Le, T.B. & Laub, M.T., 2015. Bacterial chromosome organization and segregation. *Annual review of cell and developmental biology*, 31, pp.171–199.
- Battista, J.R., 1997. Against all odds: the survival strategies of *Deinococcus radiodurans*. *Annual Reviews in Microbiology*, 51(1), pp.203–224.
- Blasius, M., Hübscher, U. & Sommer, S., 2008. *Deinococcus radiodurans*: what belongs to the survival kit? *Critical reviews in biochemistry and molecular biology*, 43(3), pp.221–238.
- Corbin, B.D., Yu, X.-C. & Margolin, W., 2002. Exploring intracellular space: function of the Min system in round-shaped *Escherichia coli*. *The EMBO journal*, 21(8), pp.1998–2008.
- Daly, M.J., 2009. A new perspective on radiation resistance based on *Deinococcus radiodurans*. *Nature Reviews Microbiology*, 7(3), pp.237–245.
- Daly, M.J. et al., 2004. Accumulation of Mn (II) in *Deinococcus radiodurans* facilitates gamma-radiation resistance. *Science*, 306(5698), pp.1025–1028.
- Dame, R.T. & Tark-Dame, M., 2016. Bacterial chromatin: converging views at different scales. *Current opinion in cell biology*, 40, pp.60–65.
- Dillon, S.C. & Dorman, C.J., 2010. Bacterial nucleoid-associated proteins, nucleoid structure and gene expression. *Nature Reviews Microbiology*, 8(3), p.185.
- Englander, J. et al., 2004. DNA toroids: framework for DNA repair in *Deinococcus radiodurans* and in germinating bacterial spores. *Journal of bacteriology*, 186(18), pp.5973–5977.
- Fisher, J.K. et al., 2013. Four-dimensional imaging of *E. coli* nucleoid organization and dynamics in living cells. *Cell*, 153(4), pp.882–895.
- Floc'h, K. et al., 2018. Bacterial cell wall nanoimaging by autoblanking microscopy. *Scientific reports*, 8(1), p.14038.
- Gao, Y. et al., 2017. Charged residues in the H-NS linker drive DNA binding and gene silencing in single cells. *Proceedings of the National Academy of Sciences*, p.201716721.

- Jong, I.G. de et al., 2011. Live cell imaging of *Bacillus subtilis* and *Streptococcus pneumoniae* using automated time-lapse microscopy. *Journal of visualized experiments: JoVE*, (53).
- Jun, S., 2015. Chromosome, cell cycle, and entropy. *Biophysical Journal*, 108(4), p.785.
- Jun, S. & Mulder, B., 2006. Entropy-driven spatial organization of highly confined polymers: lessons for the bacterial chromosome. *Proceedings of the National Academy of Sciences*, 103(33), pp.12388–12393.
- Kumar, M., Mommer, M.S. & Sourjik, V., 2010. Mobility of cytoplasmic, membrane, and DNA-binding proteins in *Escherichia coli*. *Biophysical journal*, 98(4), pp.552–559.
- Le, T.B. et al., 2013. High-resolution mapping of the spatial organization of a bacterial chromosome. *Science*, 342(6159), pp.731–734.
- Levin-Zaidman, S. et al., 2003. Ringlike structure of the *Deinococcus radiodurans* genome: a key to radioresistance? *Science*, 299(5604), pp.254–256.
- Luijsterburg, M.S. et al., 2006. The architectural role of nucleoid-associated proteins in the organization of bacterial chromatin: a molecular perspective. *Journal of structural biology*, 156(2), pp.262–272.
- Lutkenhaus, J., 2007. Assembly dynamics of the bacterial MinCDE system and spatial regulation of the Z ring. *Annu. Rev. Biochem.*, 76, pp.539–562.
- Makarova, K.S. et al., 2001. Genome of the extremely radiation-resistant bacterium *Deinococcus radiodurans* viewed from the perspective of comparative genomics. *Microbiology and Molecular Biology Reviews*, 65(1), pp.44–79.
- Marbouty, M. et al., 2015. Condensin-and replication-mediated bacterial chromosome folding and origin condensation revealed by Hi-C and super-resolution imaging. *Molecular cell*, 59(4), pp.588–602.
- Matysik, A. & Kraut, R.S., 2014. TrackArt: the user friendly interface for single molecule tracking data analysis and simulation applied to complex diffusion in mica supported lipid bilayers. *BMC research notes*, 7(1), p.274.
- Minsky, A., Shimoni, E. & Englander, J., 2006. Ring-like nucleoids and DNA repair through error-free nonhomologous end joining in *Deinococcus radiodurans*. *Journal of bacteriology*, 188(17), pp.6047–6051.

- Minton, K.W. & Daly, M.J., 1995. A model for repair of radiation-induced DNA double-strand breaks in the extreme radiophile *Deinococcus radiodurans*. *Bioessays*, 17(5), pp.457–464.
- Monteiro, J.M. et al., 2015. Cell shape dynamics during the staphylococcal cell cycle. *Nature communications*, 6, p.8055.
- Murray, R., Hall, M. & Thompson, B., 1983. Cell division in *Deinococcus radiodurans* and a method for displaying septa. *Canadian journal of microbiology*, 29(10), pp.1412–1423.
- Passot, F.M. et al., 2015. Nucleoid organization in the radioresistant bacterium *Deinococcus radiodurans*. *Molecular microbiology*, 97(4), pp.759–774.
- Pelletier, J. et al., 2012. Physical manipulation of the *Escherichia coli* chromosome reveals its soft nature. *Proceedings of the National Academy of Sciences*.
- Pilhofer, M. et al., 2013. Discovery of chlamydial peptidoglycan reveals bacteria with murein sacculi but without FtsZ. *Nature communications*, 4, p.2856.
- Rapsomaniki, M.A. et al., 2012. easyFRAP: an interactive, easy-to-use tool for qualitative and quantitative analysis of FRAP data. *Bioinformatics*, 28(13), pp.1800–1801.
- Renner, L.D. & Weibel, D.B., 2011. Cardiolipin microdomains localize to negatively curved regions of *Escherichia coli* membranes. *Proceedings of the National Academy of Sciences*, 108(15), pp.6264–6269.
- Schindelin, J. et al., 2012. Fiji: an open-source platform for biological-image analysis. *Nature methods*, 9(7), pp.676–682.
- Schweizer, J. et al., 2012. Geometry sensing by self-organized protein patterns. *Proceedings of the National Academy of Sciences*, 109(38), pp.15283–15288.
- Shendruk, T.N. et al., 2015. Simulating the entropic collapse of coarse-grained chromosomes. *Biophysical journal*, 108(4), pp.810–820.
- Slade, D. & Radman, M., 2011. Oxidative stress resistance in *Deinococcus radiodurans*. *Microbiology and molecular biology reviews*, 75(1), pp.133–191.
- Stracy, M. et al., 2015. Live-cell superresolution microscopy reveals the organization of RNA polymerase in the bacterial nucleoid. *Proceedings of the National Academy of Sciences*, 112(32), pp.E4390–E4399.

- Thanbichler, M. & Shapiro, L., 2006. MipZ, a spatial regulator coordinating chromosome segregation with cell division in *Caulobacter*. *Cell*, 126(1), pp.147–162.
- Thornley, M.J., Horne, R. & Glauert, A.M., 1965. The fine structure of *Micrococcus radiodurans*. *Archiv für Mikrobiologie*, 51(3), pp.267–289.
- Tian, B. et al., 2007. Evaluation of the antioxidant effects of carotenoids from *Deinococcus radiodurans* through targeted mutagenesis, chemiluminescence, and DNA damage analyses. *Biochimica et Biophysica Acta (BBA)-General Subjects*, 1770(6), pp.902–911.
- Tinevez, J.-Y. et al., 2017. TrackMate: An open and extensible platform for single-particle tracking. *Methods*, 115, pp.80–90.
- Touelle, M. et al., 2012. A comparative proteomic approach to better define *Deinococcus* nucleoid specificities. *Journal of proteomics*, 75(9), pp.2588–2600.
- Umbarger, M.A. et al., 2011. The three-dimensional architecture of a bacterial genome and its alteration by genetic perturbation. *Molecular cell*, 44(2), pp.252–264.
- Veiga, H., Jorge, A.M. & Pinho, M.G., 2011. Absence of nucleoid occlusion effector Noc impairs formation of orthogonal FtsZ rings during *Staphylococcus aureus* cell division. *Molecular microbiology*, 80(5), pp.1366–1380.
- Wang, P. & Schellhorn, H.E., 1995. Induction of resistance to hydrogen peroxide and radiation in *Deinococcus radiodurans*. *Canadian journal of microbiology*, 41(2), pp.170–176.
- Wang, X. et al., 2006. The two *Escherichia coli* chromosome arms locate to separate cell halves. *Genes & development*, 20(13), pp.1727–1731.
- Wang, X., Llopis, P.M. & Rudner, D.Z., 2013. Organization and segregation of bacterial chromosomes. *Nature Reviews. Genetics*, 14(3).
- Wu, F. et al., 2018. Cell boundary confinement sets the size and position of the *E. coli* chromosome. *bioRxiv*, p.348052.
- Wu, F. et al., 2015. Symmetry and scale orient Min protein patterns in shaped bacterial sculptures. *Nature nanotechnology*, 10(8), p.719.
- Wu, L.J. & Errington, J., 2012. Nucleoid occlusion and bacterial cell division. *Nature Reviews Microbiology*, 10(1), p.8.

- Yamaichi, Y. et al., 2012. A multidomain hub anchors the chromosome segregation and chemotactic machinery to the bacterial pole. *Genes & development*, 26(20), pp.2348–2360.
- Ben-Yehuda, S. et al., 2005. Defining a centromere-like element in *Bacillus subtilis* by identifying the binding sites for the chromosome-anchoring protein RacA. *Molecular cell*, 17(6), pp.773–782.
- Zhou, X. et al., 2015. Mechanical crack propagation drives millisecond daughter cell separation in *Staphylococcus aureus*. *Science*, 348(6234), pp.574–578.
- Zimmerman, J.M. & Battista, J.R., 2005. A ring-like nucleoid is not necessary for radioresistance in the Deinococcaceae. *BMC microbiology*, 5(1), p.17.

7. Supplementary Material

Supplementary Figures S1-S9

Supplementary Movies S1-S4

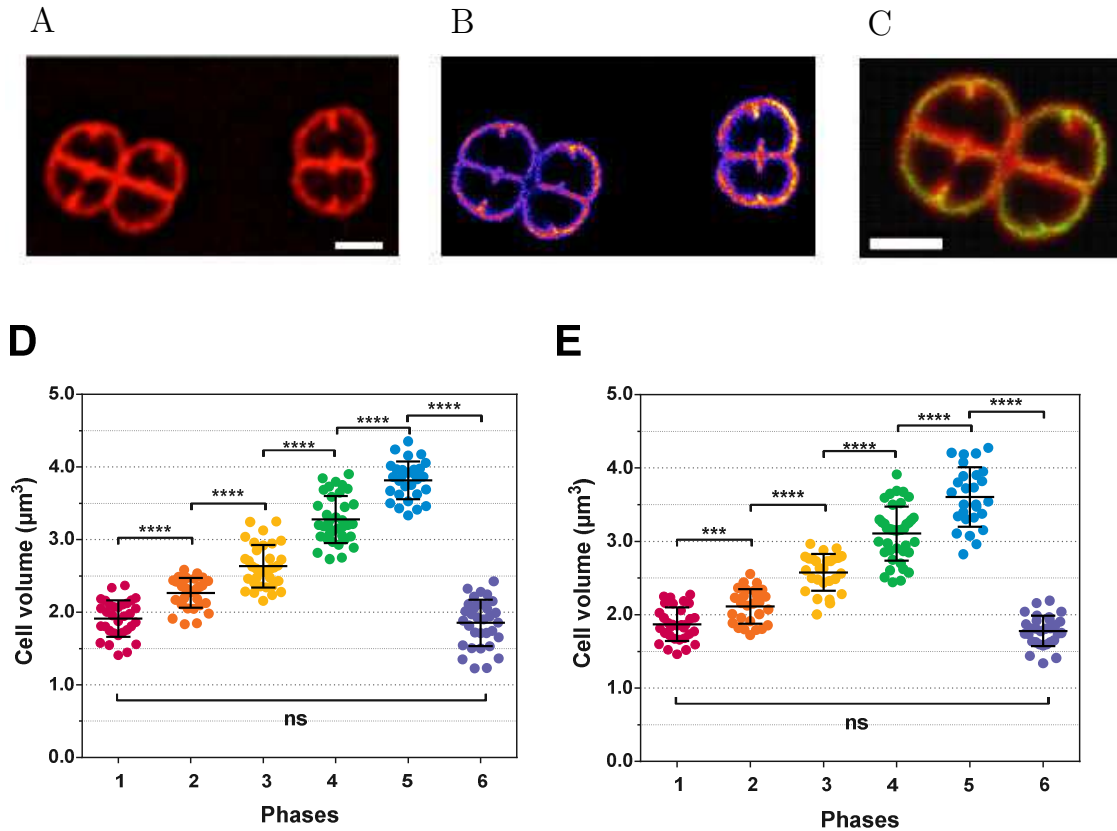


Figure S1: Comparison of spinning-disk and PAINt images of *D. radiodurans* cells stained with membrane dye Nile Red. (A) Spinning-disk image and (B) PAINt image of the same Nile Red stained *D. radiodurans* cells. (C) Overlay of images (A) and (B). Scale bar: 1 μm . (D)-(E) Changes in cell volume as a function of the cell cycle retrieved from either super-resolved, PAINt images (D), or from spinning-disk confocal images (E) of Nile Red stained *D. radiodurans*. The same three independent populations of cells were observed with the two imaging techniques. Cell volumes were calculated by measuring the cell parameters as described in Fig. S4. Only very small differences in cell volumes were observed between the two imaging methods. (***: $P < 0.001$, ****: $P < 0.0001$, ns: not significant).

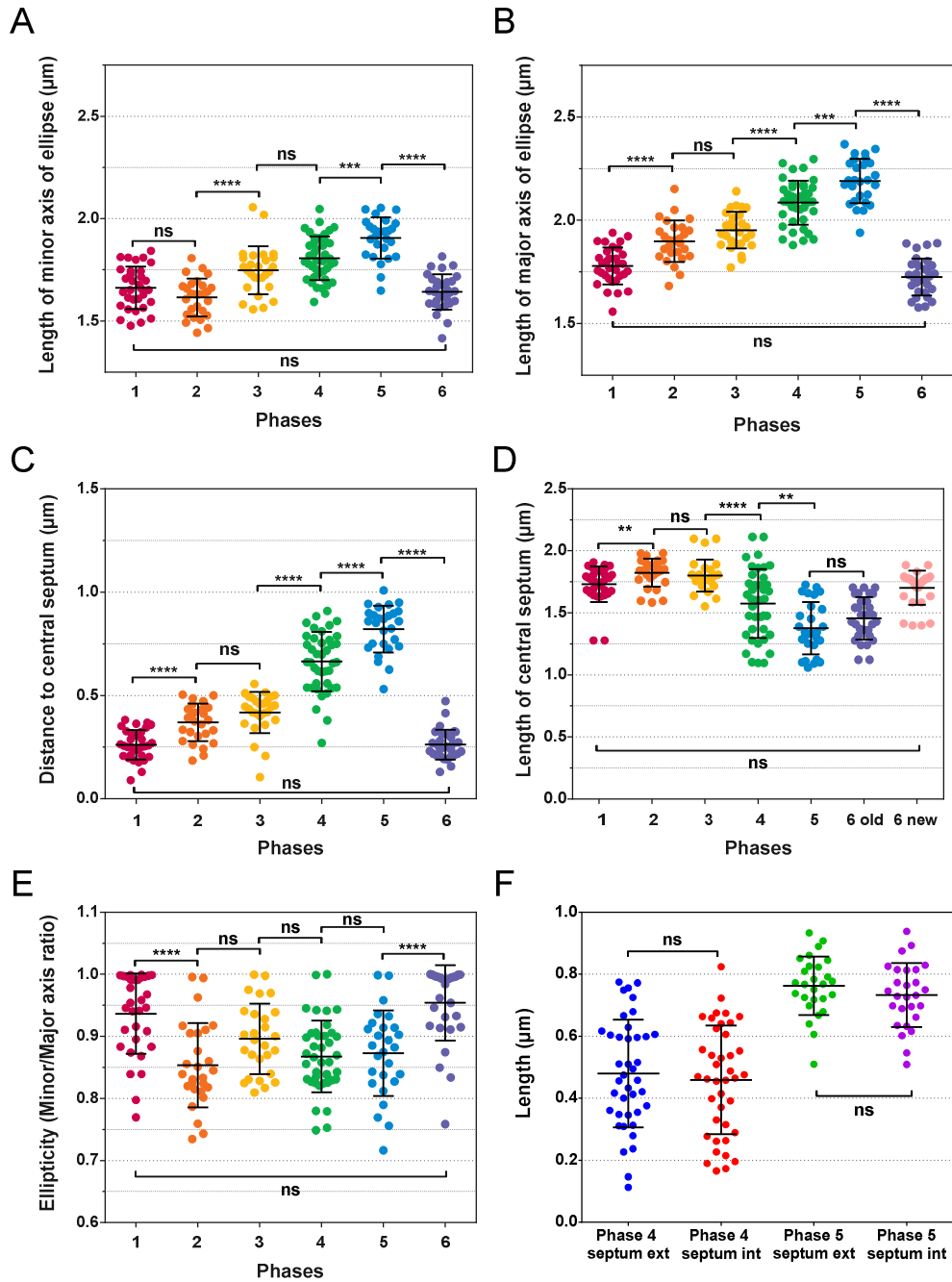


Figure S2: Cell parameters of *D. radiodurans* cells extracted from PAINT images of Nile Red stained, exponentially growing cells. (A)-(B) Length of the minor (A) and major (B) axes of the fitted ellipses used to measure cell volumes (see Fig. S4). (C) Distance of the ellipse centre to the central septum of the cell. (D) Length of the central septum. In Phase 6 cells, there are two central septa: the old septum originating from the previous cell cycle and the new one that has just closed. (E) Ellipticity of the cells (ratio between the length of the minor and major axes). (F) Lengths of the outer (growing from the peripheral cell wall) and inner (growing from the central septum) septa in Phases 4 and 5 (*: $P < 0.05$, **: $P < 0.01$, ***: $P < 0.001$, ****: $P < 0.0001$, ns: not significant).

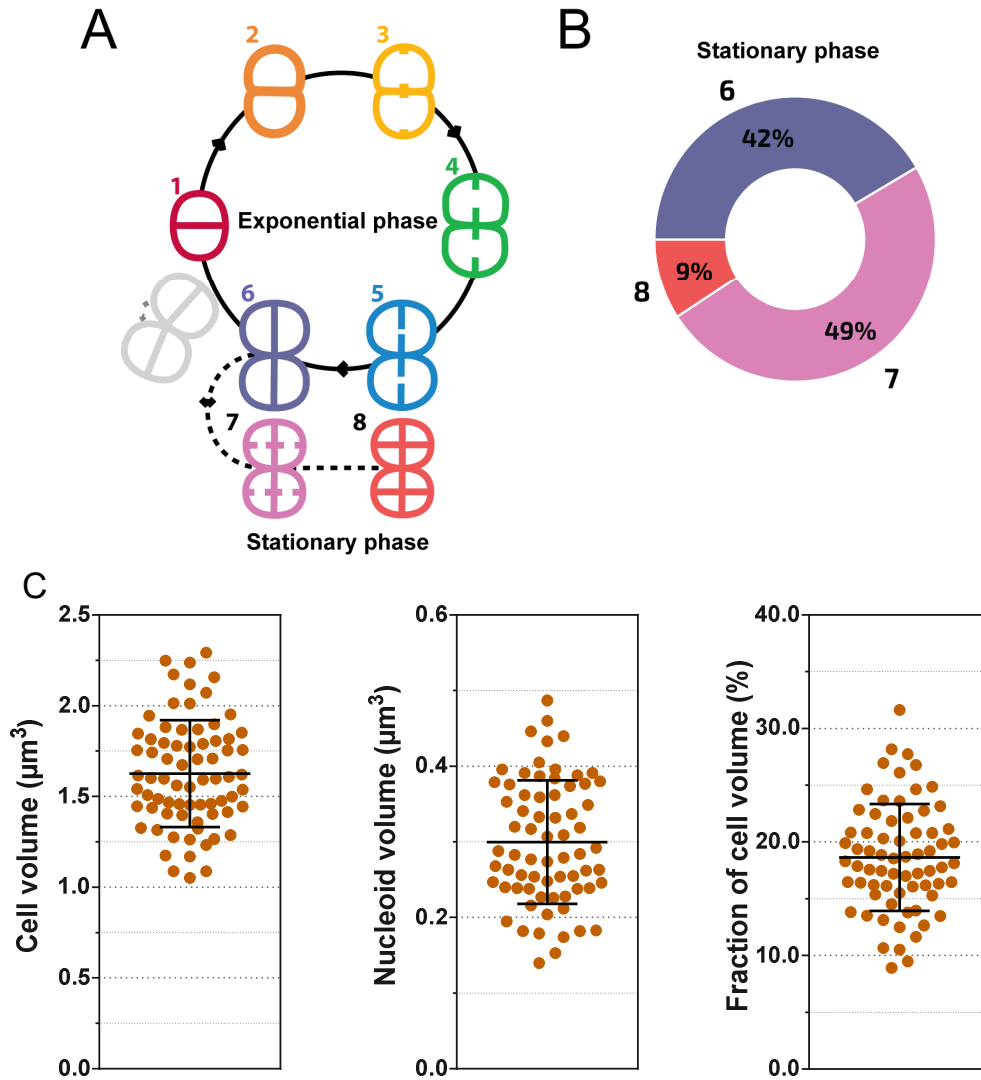


Figure S3: Changes in cell morphology during the stationary phase of *D. radiodurans* cell growth. (A) Schematic representation of the cell cycle, for one diad. In stationary phase, two additional phases can be seen: Phase 7 corresponds to tetrads engaging in a new cell cycle without dissociation into diads, and Phase 8 cells are octads. (B) Distribution of phases in the population of stationary cells (24h of growth) when observed at a given time point ($N > 600$). All data were collected from at least 2 independent experiments. (C) Mean cell and nucleoid volumes, and fraction of the cell volume occupied by the nucleoid in stationary phase tetrads ($N = 70$ cells). Cell volumes were calculated by measuring the cell parameters presented in Fig. S4 on spinning-disk images. Nucleoid volumes were measured as described for exponentially growing cells (see Methods).

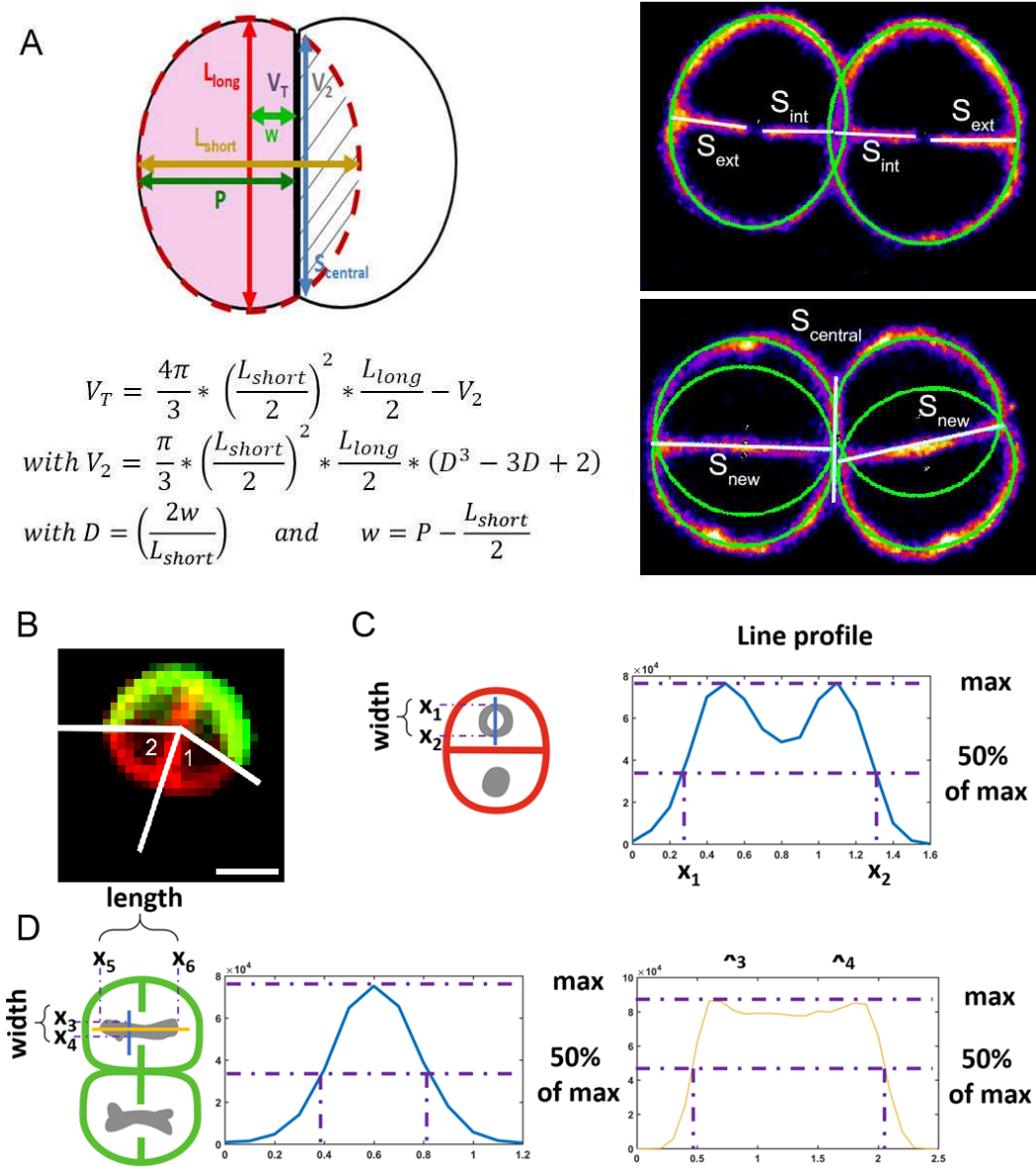


Figure S4: Cell and nucleoid measurements used in this study. (A) Schematic diagram illustrating the mode of calculation of the volumes of *D. radiodurans* cells based on the fitting of ellipses (dotted red line) to individual cells and the equations used for these calculations. L_{long} = length of major axis of the fitted ellipse; L_{short} = length of minor axis of the fitted ellipse; P = distance between central septum and the opposite side of the ellipse; w = distance from center of ellipse to central septum ($=P - [L_{short}/2]$); S_{ext} = length of exterior septum of cells in Phases 4 and 5; S_{int} = length of interior septum of cells in Phases 4 and 5; S_{new} = length of the newly formed central septum in Phase 6; $S_{central}$ = length of the old division septum originating from the previous cell cycle. (B) Illustration of the two angle measurements made to determine the lengths of the BADA (green) and Nile Red (red) labelled cell perimeters in Phase 1 diads at $T = 130$ min. Scale bar: 1 μm . (C)-(D) Illustration of the measurements made to determine the width of the toroidal-shaped nucleoids (C) and the length and width of the elongated nucleoids (D).

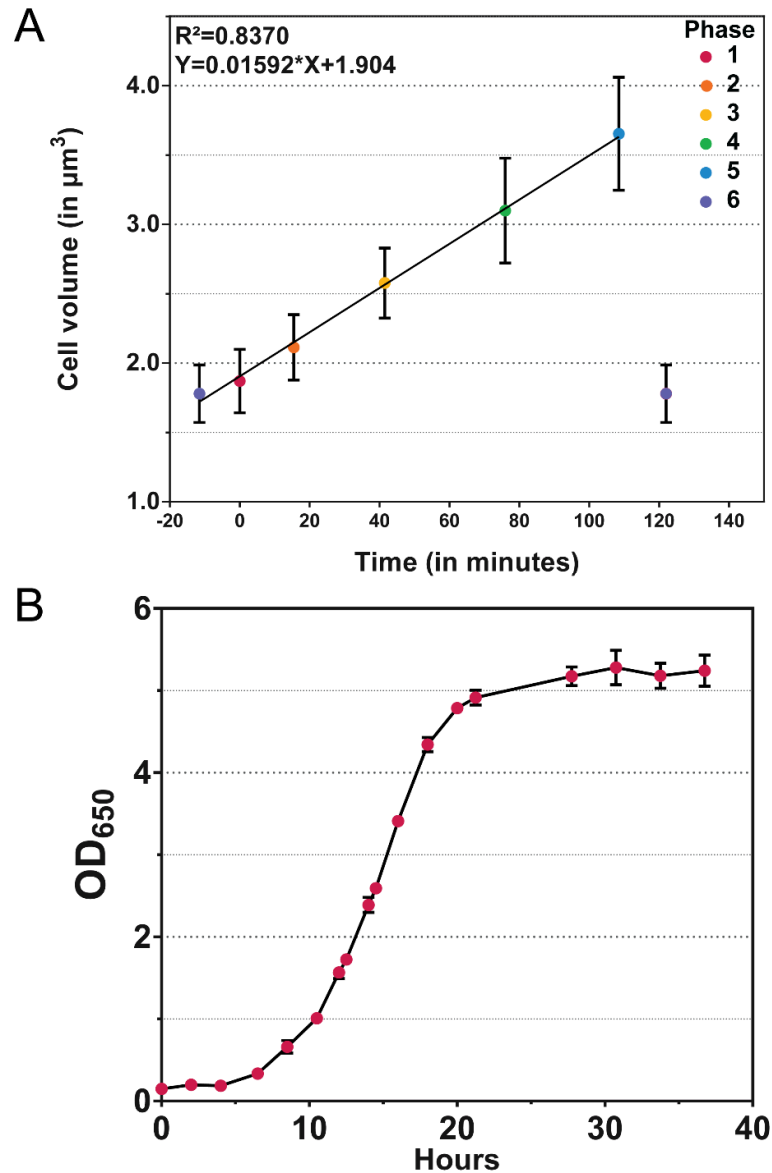


Figure S5: Changes in cell size and optical density as a function of incubation time. (A) Linear increase of *D. radiodurans* cell volume with time during the cell cycle, derived from measurements of Nile Red stained exponentially growing cells imaged with PAINT. (B) Growth curve of wild-type *D. radiodurans* cells grown in TGY2X medium at 30°C in a shaking incubator. The curve was established using data points from at least three independent experiments. The doubling time in exponentially growing cells extracted from this curve (by fitting the linear part of the curve in log scale as a function of time to a linear regression) was estimated to be 122 minutes.

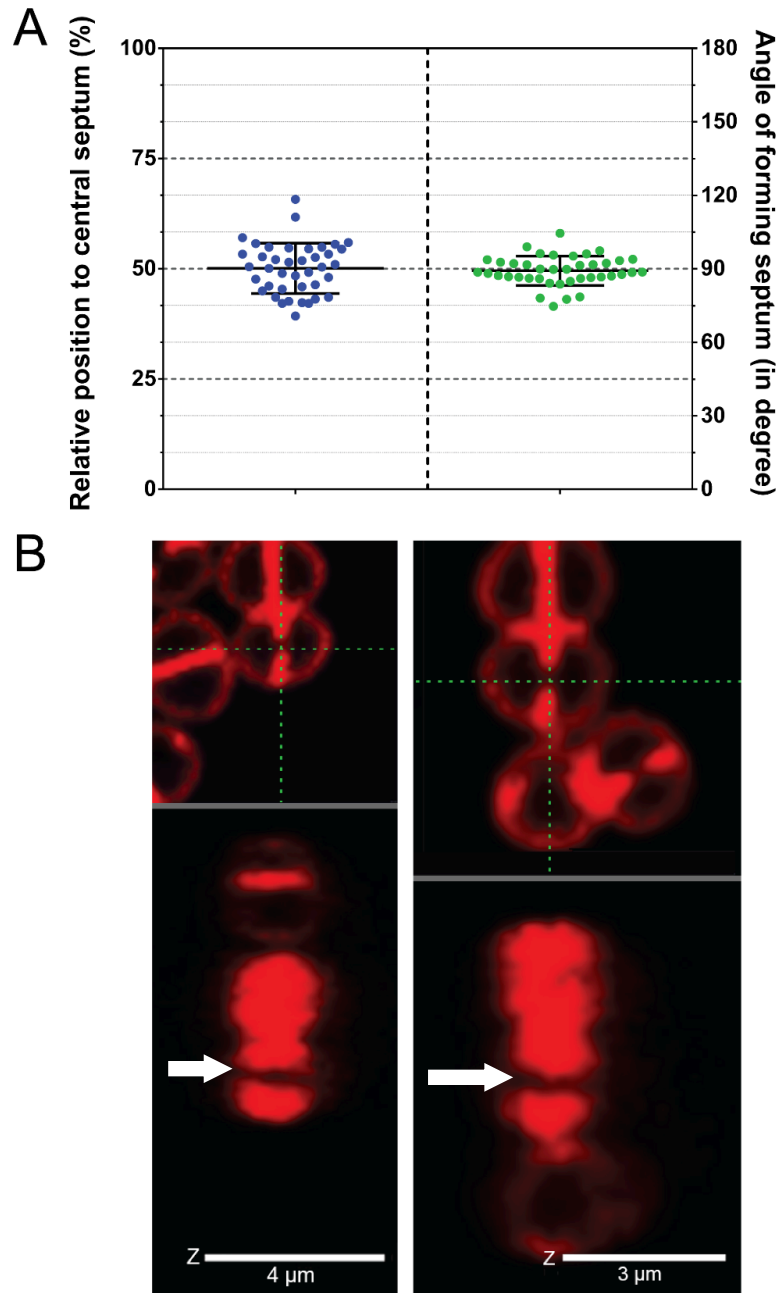


Figure S6: Septal growth and closure mechanism in *D. radiodurans*.(A) Position and angle of newly forming septa relative to the central septum ($N > 40$ cells). (B) Two examples (left and right) of 3D spinning-disk images of Nile Red stained *D. radiodurans* cells in which septal closure is in progress. The top panel represents the observed cells, in the XY plane, with the observation cross superimposed in green. The bottom panel is the XZ orthogonal view along the X direction defined by the green cross in the top panel. Septal growth from both sides of the cells leaves a gap stretching all away across the height of the cell, as seen in the XZ projection and indicated with white arrows. These images support a closing door mechanism rather than a diaphragm.

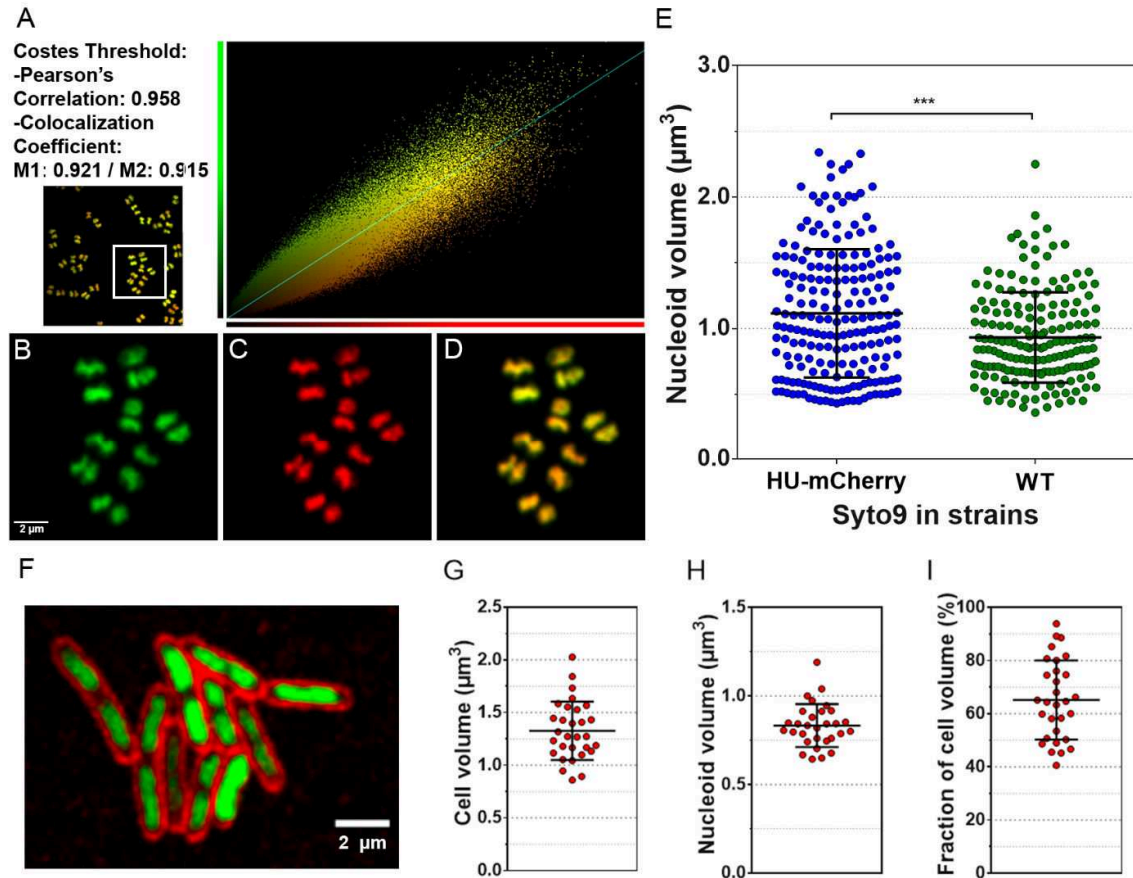


Figure S7: Nucleoid labelling in exponentially growing *D. radiodurans* and *E. coli* BL21 cells. (A) Colocalization statistics (analysis with Velocity software) of HU-mCherry and Syto9 fluorescence signals in *D. radiodurans* cells expressing HU-mCherry and stained with Syto9. The colocalization analysis was performed on the full Z-stack of untreated raw images. (B)-(D) Close-up insets of white box in (A), showing nucleoids stained with both Syto9 (B) and HU-mCherry (C). (D) Overlay of the two fluorescence signals. Similar shapes and structures are seen using both labelling methods. The images correspond to raw images, shown in extended focus (all Z-planes are superimposed into a single, final image). (E) Nucleoid volumes of Syto9 stained exponentially growing wild-type (WT) and HU-mCherry expressing *D. radiodurans* cells ($N > 200$; ***: $P < 0.001$). (F) Image of exponentially growing *E. coli* BL21 cells stained with Syto9 and Nile Red. (G) Cell volume, (H) nucleoid volume and (I) fraction of the cell volume occupied by the nucleoid ($N > 30$) in *E. coli* cells. The fraction consists of the ratio of the nucleoid volume divided by the volume of the associated cell. The cell volume was computed from measurements of the length and width of individual cells, assuming *E. coli* cells were cylinders capped with two semi-spheres. The nucleoid volumes were extracted as for *D. radiodurans* nucleoids (see Methods).

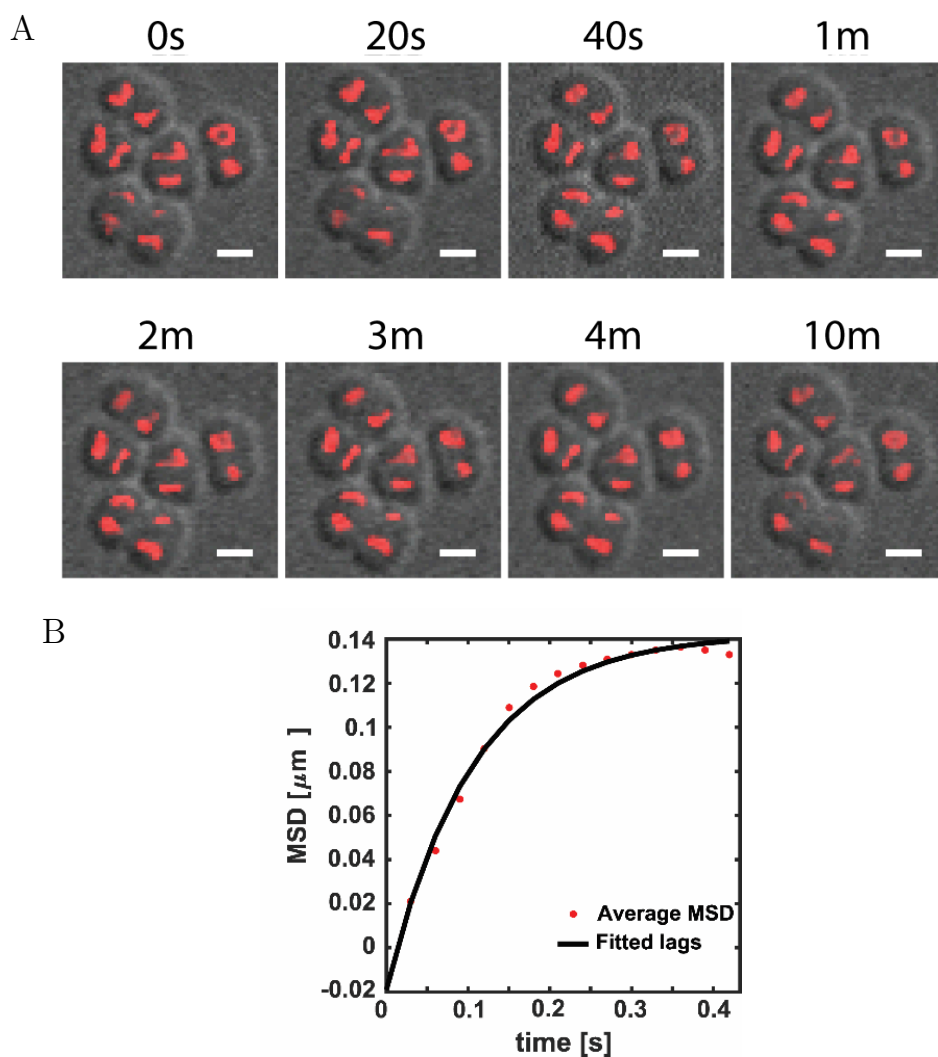


Figure S8: Nucleoid dynamics in live *D. radiodurans*. (A) Snapshots of spinning-disk microscopy time-lapse images (acquired every 20 seconds) of HU-mCherry expressing *D. radiodurans* cells overlaid on brightfield images, taken at various time points: 0, 20, 40, 60, 120, 180, 240 and 600 sec. Nucleoids are dynamic and change shape on the minute timescale. (B) Mean square deviation (MSD) plot of the population of HU-PAmCherry molecules tracked by sptPALM in live *D. radiodurans* ($\Delta t = 30$ ms). The curve indicates that the molecules are confined with a confinement radius of 400nm.

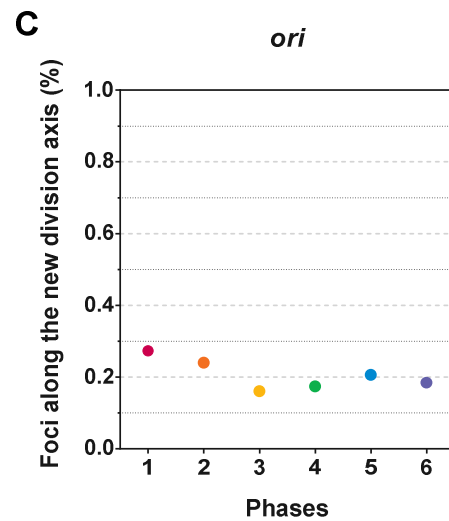
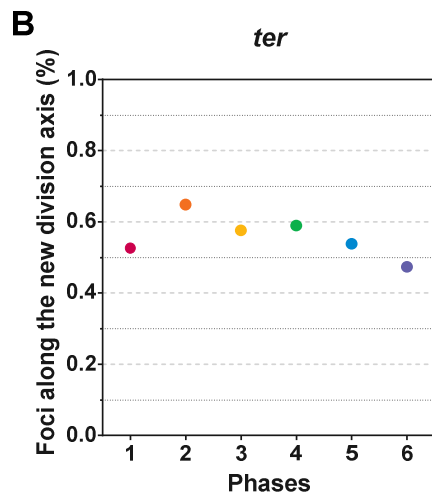
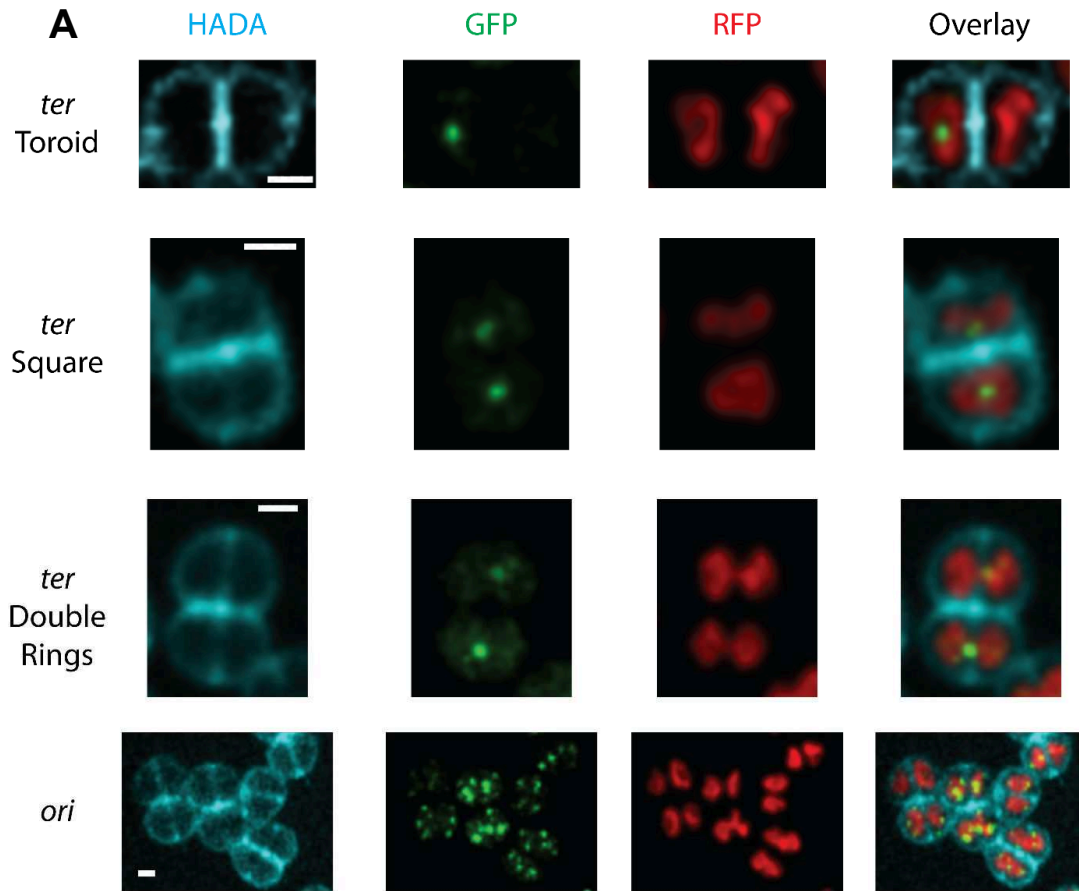


Figure S9: Localization of *ter* and *ori* foci with respect to HU-mCherry labelled nucleoids in exponentially growing *D. radiodurans* cells. (A) Examples of *ter* and *ori* foci localization relative to the different nucleoid conformations of *D. radiodurans*, expressing HU-mCherry (red) and ParB-GFP (green), and stained with the cell wall dye HADA (blue). Scale bar: 1 μ m. (B) Fraction of *ter* and (C) *ori* foci localized along the new division axis where septal growth occurs as a function of the cell cycle. ($N > 300$ foci for both *ter* and *ori*).

Movie S1: <https://www.youtube.com/watch?v=AUA1WVcRy5s>

Timelapse movie of growing *D. radiodurans* cells, deposited on an agarose pad, stained with membrane dye Nile Red. Scale bar: 2 μ m.

Movie S2: <https://www.youtube.com/watch?v=q4RWx-BrwP0>

Timelapse movie of growing *D. radiodurans* cells, deposited on an agarose pad, stained with the intercalating dye Syto9. Scale bar: 5 μ m.

Movie S3: <https://www.youtube.com/watch?v=ki8KX7eVy8>

Timelapse movie of growing HU-mCherry expressing *D. radiodurans* cells, deposited on an agarose pad. Scale bar: 5 μ m.

Movie S4: <https://www.youtube.com/watch?v=rItXQfhwzGA>

On-scale (size and timing) simulation of *D. radiodurans* cell cycle, illustrating the coordination of the morphological changes of the nucleoids with septal growth during the cell cycle. Scale bar: 1 μ m.

CHAPTER

VI

Discussion and perspectives

1. Autoblinking

In this work, we have studied the autoblinking phenomenon that has been observed in different bacteria. We have confirmed that many of them are prone to autoblinking, and more particularly two *Deinococcus* species, *D. radiodurans* and *D. deserti*. We showed that autoblinking should be considered as a new type of artifact in SMLM. At present, no clear and easy-to-apply filter can trustfully distinguish PTFPs signals from autoblinking ones. Our data show that autoblinking is not endogenous but originates from the transient binding of exogenous molecules to the cell wall, coming mostly from the growth medium, in a PAINT-based regime. Agarose pads were also shown to constitute another possible source of autoblinking, unlike the lack of cleanliness of the coverslips. We also demonstrated that the aging of the different chemicals and their storage conditioning influence the autoblinking levels. These observations lead us to hypothesize that the molecules responsible for autoblinking could originate from residues of plastic although we currently have not been able to test this hypothesis.

In our publication (Floc'h et al. 2018), one of our main conclusions is that the high autoblinking levels in *D. radiodurans* and *D. deserti*, probably result from the unusual cell wall composition of these bacteria. In addition, the autoblinking molecules seem to preferentially bind to the plasma membrane. Moreover, our results suggest some level of heterogeneity in the plasma membrane of *D. radiodurans*, although we cannot rule out that the observed heterogeneities may arise from a heterogeneous nature of the molecules themselves, as we are not able to precisely define their nature.

Differences in properties observed between autoblinking in *D. radiodurans* and the autoblinking reported in the literature, strengthen the suggestion that the autoblinking may be caused by a heterogeneous pool of molecules:

- In (Liao et al. 2015), the autoblinking in *E. coli* is excited by the 405 nm laser, which is not the case for autoblinking in *D. radiodurans*. It is also reported that cleaning the coverslips in an oxygen etcher decreases the autoblinking levels. We showed that cleaning in a UV oven did decrease the impurities present on the coverslips, but did not decrease the autoblinking in *D. radiodurans*.
- In (Tuson et al. 2016), the autoblinking is not excited by the 488 nm laser, unlike in our case. Again, the cleaning of coverslips in an oxygen etcher was reported as a means to reduce the levels of autoblinking.
- In (Leon et al. 2017), only the trajectories of the autoblinking molecules were studied. Nevertheless, it is reported that the spatial distribution of the tracks was distributed uniformly in cells. In contrast, we showed that the autoblinking distribution in *E. coli* (as in all bacteria studied in this thesis) was largely restricted to the cell wall. It is possible that the relatively small size of *E. coli*, which is

comparable to the depth of field of the objectives, makes it difficult to unambiguously locate the autoblinking signal to the cell wall due to projection on a 2D plane of a 3D object. In this study, the authors observed only one population of diffusing autoblinking molecules, in contrast to our study, in *D. radiodurans*, where two populations of diffusing autoblinking molecules were seen. The processing of sptPALM data with multiple populations of diffusing molecules, especially with some levels of confinement, is complicated and is often ambiguous. So far no software can efficiently process such data. For example, we performed a simulation of a single population of diffusing molecules in a very confined membrane-like space and depending on the input parameters (level of confinement, diffusion coefficients etc.), we could find either one or two populations of diffusing molecules. Therefore, sptPALM results relying on weak signals (low-photon budget) with some degree of confinement should be considered with extreme care.

Anyway, on a lighter note, something that amuses me: if one had had the idea of observing *D. radiodurans* with a good camera under high laser power before 2006, one could have discovered single-molecule localization microscopy without even using any specific fluorescent markers.

2. D. radiodurans cell and nucleoid dynamics

In all bacteria, genomic DNA must fit into the restricted space of the cell cytoplasm while remaining accessible for essential DNA-related processes including DNA replication, repair and transcription. This packaging/organization of the nucleoid can be analyzed at different levels: at the molecular level (through NAPs), at the micro/macro-domain level (with DNA supercoiling for example) or on a more global level (with the depletion force induced by macromolecular crowding). Currently, limited knowledge is known on the mechanisms responsible for the nucleoid organization, compaction, segregation or on the bacterial cell morphology during division, which all actually appear intimately interlinked. This is in part due to the diversity of bacteria, which is reflected in the variety of proteins and mechanisms involved in these processes. This diversity actually prevents the definition of universal mechanisms. This is also due to the relative small size of bacteria and of their nucleoids ($<1\mu\text{m}^3$), which has limited their studies by conventional microscopy. Moreover, most of the studies of bacterial nucleoids have focused on rod- or crescent-shaped bacteria. In contrast, little is known on cocci nucleoid organization, compaction or segregation and on their mode of division.

In this thesis, using advanced imaging techniques, we studied the morphological changes of *D. radiodurans* that occur both at the cellular and nucleoid level. Briefly, our data enable assessing the levels of compaction of the nucleoid through the cell cycle. The nucleoids appear dynamic, adopting multiple distinct shapes. We also showed that nucleoid organization and segregation are coupled with the cell division and septal growth. In addition to the discussions, presented in “Chapter V: *D. radiodurans* cell and nucleoid dynamics” the following points can also be raised.

2.1. Cell morphology definition

We have followed the morphological changes that occur during the growth of *D. radiodurans* by either time-lapse imaging on a spinning-disk confocal microscope or super-resolution imaging using PAINT microscopy. Super resolution imaging enabled us to define 6 different phases during the cell cycle of *D. radiodurans* while the duration of the various stages of the cell cycle was derived from time-lapse imaging.

The “representative” phases of the cell cycle were manually determined, based on visual cues, that were definable as unambiguously as possible. In phase 1, cells appear particularly round, compared to other cells that were more elliptical. Phase 2 cells were close in size to phase 1 cells, but with a slight invagination at the junctions between the central septum and the cell periphery. Phase 3 cells displayed bright foci corresponding to the start of the growth of the new septa. Phase 4 cells correspond to cells with partial septal growth. Phase 5 cells have their newly formed septum almost closed. Phase 6 cells are tetrads, with complete septal growth. These visual cues were thus subjective by

construction. One could wonder if our phase definition was too restrictive. For example, the spread of the different measurements we have for phase 4 cells might indicate that phase 4 could have been further subdivided into new phases (or possibly that the different phases are in fact wrongly defined). It would have been interesting to define the phases with a more objective/automatized process. We could have imagined that feeding an unsupervised machine learning algorithm with thousands of our cell images could have resulted in a different definition of phases. Unsupervised machine learning algorithms, independent of user interaction, thus try to recognize patterns, groups, structures in the input data, without any user definition of what the output should be like. Moreover, once we had defined the phases, the sorting of the cells was performed manually, which in addition to being time-consuming, also introduced another layer of subjectivity that could also have been automatized.

All the quantitative measurements manually extracted from super-resolution images (length of the central septum, the fit of an ellipse on the cells etc.) could also have been algorithmically measured, according to the computer-chosen phases. Such automatic measurement extractions would have been of high interest. Indeed, solid statistics are very important for the studies we performed. Manually, we were able to analyze a couple of hundred cells during our different experiments. However, the analysis of hundreds of cells, as requested by journals such as Nature or Science, would greatly benefit from the use of automated analyses. Altogether, our measurements would have been more robust with some degree of automatization in the image processing (i.e. more cells). We also observed a biological variability of our cells and therefore decided to “normalize” our protocols. For example, we decided not to plate our cells on Petri dishes and instead, for each experiment, to start from a -80°C stock.

Due to limitations in our computer-science manpower, we had to limit ourselves to already available solutions instead of inhouse development. Moreover, no machine learning software could be found for the classification of the phases. In the case of cell measurements, using software like MicrobeJ (Ducret et al. 2016) or BacStalk (Hartmann et al. 2018), I was not able to retrieve cell measurements from our different PALM or SD images. Unfortunately, neither softwares were suited for the detection of cellular contours using membrane stained images. Moreover, the complex shape of *D. radiodurans* diads (or even tetrads) was not correctly recognized during the segmentation step by such software.

2.2. Cell growth

In this work, we determined that *D. radiodurans* grows throughout its cell cycle while dividing in alternate orthogonal planes. The dividing septal growth occurred through a closing door mechanism (Murray et al. 1983), at least for the plasma membrane layer of the septal cell wall: one side originating precisely from the middle of the central septum, the other from the middle of the opposite peripheral cell wall, both growing at 90° angle

to the central septum. Such a closing door mechanism has never been reported before for other bacteria. In *ovocci* for example, the dividing septum usually resembles an aperture (Touhami et al. 2004; Wheeler et al. 2011).

A very preliminary experiment showed puzzling results concerning the PG growth during the dividing septal growth. Sites of PG synthesis were labeled with the BADA dye and showed a very different staining than that of the plasma membrane labelled with Nile Red (Figure 6.1). In particular, in phase 1 cells, a disk devoid of any BADA dye but not of Nile Red is visible in the middle of the central septum. In phase 2, this disk seems to reduce in size. In phase 3 the disk is no longer visible. Actually, the space previously occupied by the disk is now the site with the highest BADA signal in the central septum. In phases 4 and 5, we can observe the growth of the dividing septum, appearing as a closing door mechanism for the Nile Red (and hence plasma membrane) and more like an aperture for the PG (ring-like staining). In phase 6, the cytoplasmic membrane of the dividing septum now appears closed, whereas for the PG, a disk devoid of any BADA dye is visible again.

Currently, we have no hypothesis to explain these observations. One could argue that the image of sliding doors retrieved from the plasmic membrane staining with Nile Red (561 nm), may result from microscopy artifacts, mainly due to the axial resolution (which depends on the wavelength). Indeed, even in confocal microscopy, the signal collected at a Z-position originates from signals that are contained in a thick optical section, above and below the observed Z-position. Thus, the collected signal which is 2D, will be affected by the 3D of the observed object.

Let us consider a labelled vertical aperture object observed by confocal microscopy. At a Z-plane at the center of the object, the image retrieved will result from the collected signals just above and below this Z plane (i.e. the signals are still originating from the labelled object). But, at the extremities of the aperture, for example the Z “top” position, the image will result from the collected signal below the Z-top (still in the object), and signal collected above the Z-top (i.e. signals that are not from the object anymore but from the medium). At the Z-top, the collected signal will appear weaker than signal retrieved at the center of the object. Thus, the image retrieved from an aperture may appear as sliding doors if the signal collected at the poles is weak enough. As we show in Figure 6.1, we are actually able to visualize rings of PG with BADA labeling (488 nm), which should strengthen the idea that the resolution should not transform the appearance of an aperture into sliding doors. However, as mentioned earlier, the resolution increases with the wavelength. Therefore, we cannot totally rule out that the difference in resolving power might disturb sufficiently enough the signal at 561 nm and not at 488 nm and transform an aperture into sliding doors.

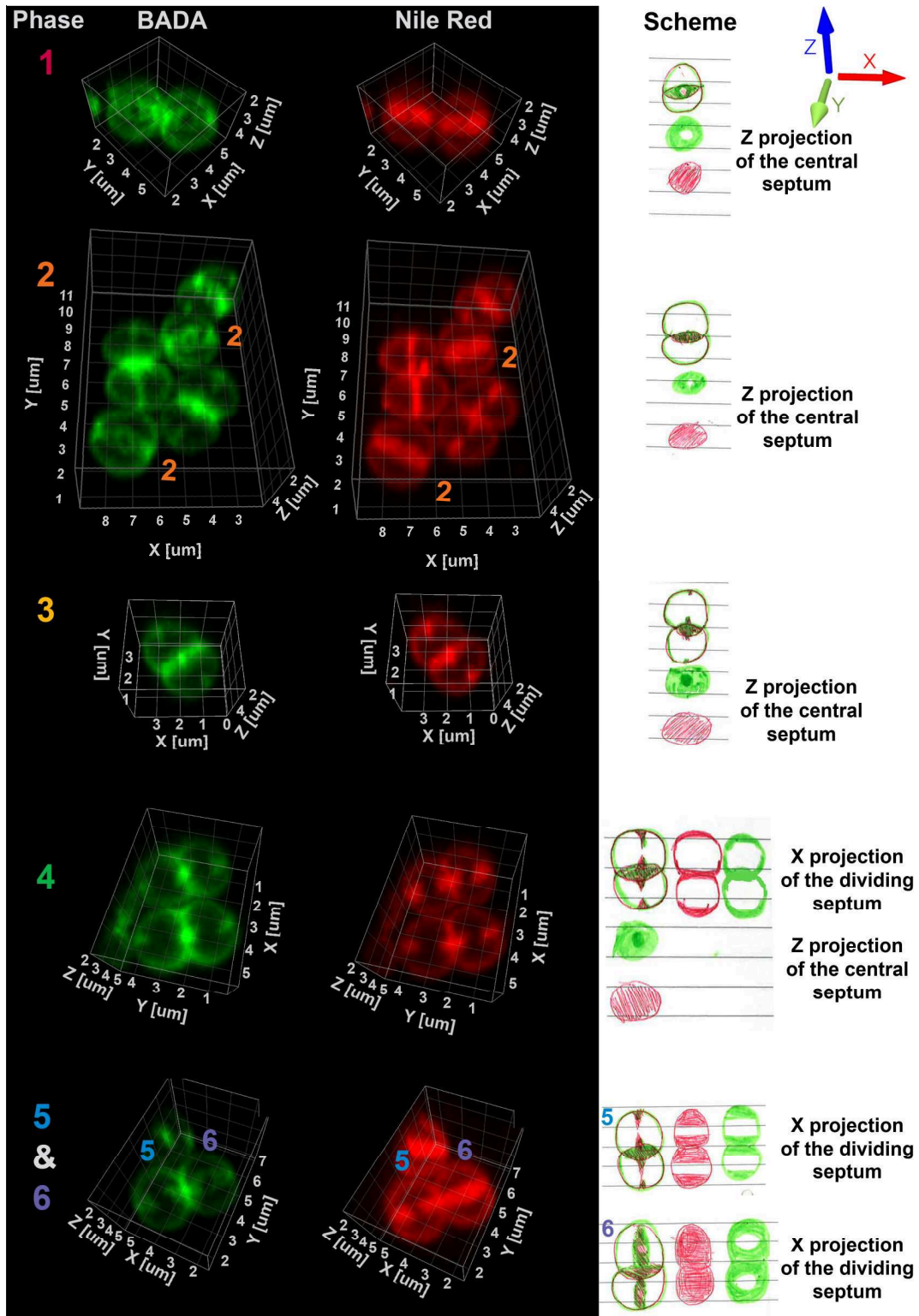


Figure 6.1: BADA and Nile Red staining of *D. radiodurans* cell walls. Images of *D. radiodurans* cells at different phases (1 to 6), imaged immediately after 15 min of BADA (31 μM) labelling followed by another 15 min of BADA and Nile Red labelling (15 μM) and a washing step to remove the excess dyes. See text for more details. BADA: green staining of sites of PG synthesis. Nile Red: red staining of plasma membrane. Raw images acquired on a spinning-disk microscope, on live cells, stacks of 25 Z-images per channel (200nm Z-sampling).

One of our future steps to further investigate this intriguing observation could be to investigate it in 3D SMLM. If Nile Red turns out to be inappropriate for 3D SMLM, possibly not bright enough, we could use the brighter dye “Potomac” (still as a PAINT method) (Spahn et al. 2018). BADA/HADA dyes are not compatible with SMLM. However, one of our collaborators has recently developed an alternative that also labels sites of PG synthesis and that is fully compatible with 3D SMLM (data not yet published), which we could maybe use in future experiments.

Currently, we have not studied any of the underlying mechanisms of PG synthesis. Still, we can compare our observations of *D. radiodurans* growth to those made in other bacteria (see “Chapter I: 4. Bacterial cell division”). Briefly, the latest model in *S. aureus*, (Monteiro et al. 2018), proposes that *S. aureus* possesses only one type of PG synthesis machinery, the synthesis occurring at two different locations. During initial stages of the cell cycle, it continuously incorporates PG at the periphery of the cell. Then the PG synthesis machinery is diverted from the cell periphery to the midcell in preparation for division. There, the PG machinery will synthesize the dividing septum.

We showed that in *D. radiodurans*, like in *S. aureus*, the PG synthesis occurs throughout both the septal and the peripheral cell walls. Unlike in *S. aureus*, during the phases of dividing septum synthesis, we showed that the peripheral growth does not seem to be negligible compared to the PG synthesis in the septal cell. Thus, we could hypothesize that the growth in *D. radiodurans* may be similar to the growth in *S. aureus*, but, with a less pronounced diversion of the PG machinery to the midcell during division. Further studies will be needed to determine whether there is a unique PG synthesis machinery in *D. radiodurans* that is responsible for synthesis in both the peripheral and septal cell wall as in *S. aureus* or whether these two processes are performed by distinct complexes.

2.3. Nucleoid organization, segregation and compaction

As the nucleoids of bacteria fill a large fraction of the total cell volume, it has been hypothesized that the cell size and shape may play the major role in the chromosome positioning and sizing. In a recent study (Wu, Swain, et al. 2018), different compaction behaviors in *E. coli* were explained by modeling the nucleoid as a polymer, on which inward pressure was exerted by depletion forces induced by cytosolic crowders at constant density along the cell cycle. In these experiments, the volumes of *E. coli* nucleoids scaled non-linearly with the cell volume. These studies were performed on live mutant *E. coli* cells that were prevented from both dividing and initiating new rounds of DNA replication while being confined in channels. Thus, it is rather difficult to compare these results to our studies of live wild-type *D. radiodurans* cells that were not confined. Still, in the case of *D. radiodurans*, we also observed that the nucleoid volume

scaled non-linearly with the cell volume along the cell cycle. For example, in the early/mid stage of growth (half of the cell cycle, phases 1 to 3), we observed that while the volume of *D. radiodurans* cells significantly increased, their nucleoids did not expand. In contrast, in *E. coli*, in the early/mid stage of growth both the cell volume and the nucleoid volume increased. According to the model proposed by Wu et al., in *E. coli*, when the cell volume increases with a constant density of cytosolic crowders, then the nucleoid expands as it “senses” the polar cell walls. However, this proposed model does not hold or must be refined for *D. radiodurans*. It is possible that changes (likely an increase) in cytosolic crowder density must be taken into account (the newly synthesized crowders could enhance the force already exerted on the nucleoid, preventing it from expanding), or alternatively other factors impacting nucleoid organization (NAPs, domains etc.) may also take part in *D. radiodurans* nucleoid compaction.

The morphology of the nucleoid of *D. radiodurans*, and its changes, is also puzzling and seems incompatible with a compaction mostly due to inward pressure exerted by depletion forces induced by cytosolic crowders. Indeed, it seems easier to imagine that an inward pressure on such a complex nucleoid (it possesses multiple copies (4 to 10) of 4 different replicons), could result on a compact non-defined shape instead of the observed toroidal shape during almost half of the cell cycle or to the elongated or branched shape observed in phases 4 and 5. Thus, it is likely that molecular crowding is just one of the factors affecting nucleoid organization. Recent simulation models, shows that a large molecule like a chromosome, when approximated as a ring-like, soft-spring polymer, made of a string of beads and confined in a small volume such as a cylinder, will collapse into a donut shape (Jung et al. 2012; Youngren et al. 2014). Japaridze et al., (Japaridze et al. 2017), while simulating the effect of the attractive DNA-DNA potential on long supercoiled circular plasmid (16 kb), showed that it could result in the formation of toroidal condensates. Still, to our knowledge, no model can explain the diversity and sequential order of nucleoid forms observed in *D. radiodurans*.

In some bacteria the chromosome partitioning system, the ParABS complex, has been identified as playing an active role in the segregation of the nucleoid *ori*-proximal region. It is noteworthy that *D. radiodurans* chr I appears to encode for a complete ParABS system with 3 possible *parS* sequences (Charaka & Misra 2012). However, chr I *ori* as well as the entire nucleoid, never appeared to be tethered to the cell periphery during the cell cycle. However, we do observe that at midcell, at the end of the cell cycle (phase 5), *ter* sites are in close proximity to the dividing septum. We currently do not know if *ter* sites are actually tethered (and to what) to the growing septum or not. The *ori* loci also present a broad distribution of localization. These last two observations are the opposite of what is observed in bacteria where their origins are segregated by the ParABS system. Thus, the mode of action of the partition system in *D. radiodurans* remains unclear. *D. radiodurans* encodes the DivIVA protein (Maurya et al. 2016). Among the possible functions of DivIVA, it has been found to play a role in *ori* anchoring to the

cell wall in *B. subtilis* (Badrinarayanan et al. 2015) and *S. pneumoniae* (Fadda et al. 2007). Since we never saw any anchoring of the *ori* to the cell periphery in *D. radiodurans*, it would be interesting to study the distribution of this protein.

Using previously established strains of *D. radiodurans*, we followed the choreography of the chromosomal loci, *ori* and *ter*, during its cell cycle. The choreography of such loci has been well studied in model bacteria (see Chapter I: 2.3 Spatial organization of the nucleoid). We have proposed a model for the nucleoid choreography for *D. radiodurans* (in Fig. 7 of Chapter V). The late segregation of *ter* sites suggests that FtsK may play an important regulatory role. FtsK is a highly conserved protein located on the dividing septum and is known to promote the decatenation of chromosomes by stimulating Topo IV as well as their segregation via its translocase activity. Thus the FtsK protein is able to disentangle unresolved DNA and pump it away from the center of the cell, towards daughter cell compartments, just before the final scission. As *D. radiodurans* possesses a complex nucleoid, composed of multiple copies (4 to 10) of four different replicons, we could imagine that recently replicated *Ter* regions may be unresolved to a certain degree and may require sister chromosome disentangling by FtsK-stimulated Topo IV. FtsK is thus likely to play an important role at the end of the cell cycle (phase 5) for the late segregation of *ter* sites, but we do not know whether it may also play a role in earlier phases (1 to 4). Interestingly, *ter* sites are never positioned at the “poles” of the cells but are instead located at the center of cells, and thus do not seem to migrate as much as in other bacteria (where *ter* are seen to migrate from pole to midcell at some point during the cell cycle). Here again, the FtsK translocase activity may be implicated in this step: the pumping of the DNA away from the new septum may constitute the main driving force for the relatively short migration of *ter* sites from the center of the division site to the center of the new daughter cells.

In *E. coli*, the *ter* loci are clustered at midcell thanks to the action of MatP protein which also delays the segregation of the *ter* loci until the end of the cell division. As stated in Passot & al. (Passot et al. 2015), other bacteria lacking MatP also present segregation delay of their *ter* (*C. crescentus* and *B. subtilis*). Thus, the long-lasting clustering of *ter* in *D. radiodurans* also suggests the existence of a MatP/matS equivalent, or of another system. Globally, chromosome segregation mechanisms in *D. radiodurans* remain unclear. We can imagine that our future studies will concentrate on understanding the choreography of the 3 other replicons as well as their spatial relationships with the different structures of nucleoids that we identified.

2.4. Perspectives

D. radiodurans possesses exceptional radiation resistance capabilities, but little is known about the effect of irradiation on chromosome segregation and more generally on nucleoid organization and compaction. In Passot & al. (Passot et al. 2015), the loci positions of *ter* and *ori* were studied in cells 120 min after irradiation. They observed

that after irradiation, the nucleoid organization was modified, with some transient alignment of the loci and an even greater delay of *ter* segregation. However, in this study, the cell cycle was less detailed and precise than in ours mostly because it relied only on phase contrast images for the definition of the cell shape. Also, the nucleoid was not analyzed in terms of shape or in 3D as in our results and quantification in this paper was limited to foci numbers. In our work, we have now developed a framework for studying *D. radiodurans* cell cycle, as well as protocols for staining and measuring cell properties. Thus, it would now be of interest to study these processes after irradiation to monitor the changes until *D. radiodurans* resumes its “normal” cell cycle.

Interestingly, we noticed that we have never been able to perform 2 color timelapse imaging of *D. radiodurans*, despite using low laser power and low concentrations of DNA and membrane dyes. Cells seem to sense the combination of lasers and stop growing during such experiments, entering a kind of quiescent state, but were able to resume their growth when the lasers were switched off and cells were left to grow on the agarose pad. It would be interesting to explore the mechanisms underlying this behaviour.

Overall, our results showed that studying bacteria that are different from the model ones is interesting to better understand the mechanisms involved in coordinating nucleoid organization and segregation with the cell cycle. The relatively large coccus, *D. radiodurans*, ($\sim 3\mu\text{m}^3$), which possesses a complex genome could potentially be a relevant model for the study of nucleoids and cell division in cocci. All the presented results provide a framework for numerous and diverse further studies in *D. radiodurans*. It would be particularly interesting to identify the proteins that play key roles in these mechanisms (organization and dynamics of the nucleoids/their coordination with the cell cycle). As discussed above, the exact roles of the Min system, the putative NO system, FtsK, the ParABS system or NAPs in these processes in *D. radiodurans* (and more generally in cocci) are still unclear and their interplay are yet to be defined. After their identification, we would need to follow their localizations during the cell cycle as well as understand their molecular mechanisms of action. Moreover, because *D. radiodurans* possesses exceptional radiation resistance capabilities, studying the organization and the compaction of the nucleoid may lead to a better understanding of how these may affect DNA damage and DNA repair processes.

3. D. radiodurans imaging

Thanks to its relatively large size and unusual properties, *D. radiodurans* is an interesting bacterium for fluorescence imaging. In this work we have shown that different strategies and approaches could be used to successfully image *D. radiodurans*, with each technique having its advantages and disadvantages. The choice of which approach to use is largely dictated by the available microscopy techniques (in our case, spinning-disk and PALM) and suitable fluorescent markers, and also the question that one tries to address. For example, to study the dynamics of specific proteins sptPALM would be the most suited, whereas studying the organization/assembly of the divisome in *D. radiodurans* does not necessarily require super-resolution microscopy (right now) as lots of “basic” data can already be extracted from conventional microscopy (the large field of view of this technique is a major asset for statistics in this case). So in the next paragraphs we will mainly focus the discussion on *D. radiodurans* imaging on a more methodological/autoblinking related aspect.

Firstly, as we have shown, several studies can be performed by confocal microscopy and many properties are yet to be studied by conventional microscopy (see above discussion that states the different studies that we think will be interesting to do in the near future, on the subject of cell morphology and nucleoid organization). Moreover, conventional microscopy is not affected by the autoblinking phenomenon: the laser power is low, the cameras may not be sensitive enough and the acquisition time might be long enough to smooth out the autoblinking, etc.

Secondly, ensemble SR microscopy (SIM, STED) should not be affected by the autoblinking. As autoblinking is PAINT based, it is the duration of an acquisition that almost directly determines the number of autoblinking events recorded. The longer the acquisition, the more autoblinking events. Due to the stochastic and pointillist nature of PALM/dSTORM, it requires up to several minutes of recording, at a given position, to retrieve an image of a cell, thus promoting the collect of numerous autoblinking events. However, ensemble techniques are much faster, and require only seconds of recording per cell. In SIM or STED, the autoblinking signals will thus be negligible compared to the signals of interest.

Thirdly, in the case of SMLM, we have also shown that its study might be impaired by the presence of strong levels of autoblinking in cells grown in standard TGY. The imaging of highly expressed non-membrane associated proteins should enable reducing the impact of the autoblinking in the retrieved signals. Membrane associated proteins or low copy number proteins will most likely be drowned in the autoblinking signal. Moreover, we have shown several data collection strategies in our paper in order to use the autoblinking as an asset for PALM imaging. Based on state-of-the-art microscopy, there are other possibilities for SMLM studies of *D. radiodurans*:

- Improvements to PTFP-based SMLM techniques. 3D single-molecule techniques might enable to spatially distinguish the autoblinking from the signal of PTFPs. Currently, the most widespread 3D technique is the astigmatism method (Huang et al. 2008). This technique relies on the reshaping of the PSF by introducing “controlled” astigmatism. However, this introduced astigmatism is contaminated by other aberrations (due for example to refractive index mismatch between the immersion medium and the objective, to the sample itself or to the microscope components). This leads to a reduction of detected photons and in the degradation of the PSF quality. 3D astigmatism can be combined with expensive adaptive optics, which can introduce “perfect astigmatism” which will not be contaminated by other aberrations (Clouvel et al. 2013). Preliminary results using our PALM microscopy set-up without adaptive optics showed that the autoblinking and a PTFP like PAmCherry were currently out of scope for 3D localization by the astigmatism method. But we can imagine that new 3D techniques or adaptive optics would be good enough to 3D localize the autoblinking. We also performed a preliminary experiment to try to 3D localize the autoblinking with a more advanced 3D technique, Single-objective selective-plane illumination microscopy, soSPIM (Galland et al. 2015). This technique enables illuminating selectively a plane of a sample with a light sheet, thus only a thin slice of the sample is illuminated, reducing the background signal. Thanks to micro cavities displaying 45° mirrors combined with a laser beam-steering unit, soSPIM is capable of retrieving the Z position of PTFPs in cells (with a displacement of the excitation-beam in the X direction). In this first test, we were not able to detect any autoblinking using this set-up, but new trials should be performed. Improvements in spectral imaging (which should be concomitant to 3D improvements) could also enable distinguishing labelled proteins of interest from autoblinking if they have different spectral properties (Mlodzianoski et al. 2016; Zhang et al. 2015).
- *D. radiodurans* cells can be washed several times in ultra-pure medium, thus reducing the autoblinking levels, but this may disturb the cells and needs to be controlled. An alternative would be to fix the cells before the washes. However, fixation may generate significant artifacts (Schnell et al. 2012). Fixation in *D. radiodurans* by formaldehyde has been used in some studies (Li et al. 2017; Nguyen et al. 2009; Toueille et al. 2012). We have tried different fixation strategies, varying the chemical agent (paraformaldehyde, formaldehyde, methanol, toluene) as well as the fixation time and the fixing agent concentration. In all cases, we observed severe morphological changes of *D. radiodurans* nucleoid, but no visible changes in the overall morphology of the cell. Thus, further protocol optimization work may be needed to find new fixation schemes/molecules for the study of *D. radiodurans* nucleoids (such as glyoxal, (Richter et al. 2018), not yet tested in *D. radiodurans*). A promising technology is the combination of cryo-EM and PALM

imaging. Indeed, the cells will then be cryo-fixed, which might reduce the number of artifacts compared to conventional chemical fixation (Chang et al. 2014).

- Another strategy would be to rely on the use of newly engineered brighter PTFPs (e.g. the mutant Dendra2-T69A, (Berardozzi et al. 2016)) or on synthetic dyes for the imaging of proteins of interest. The difference in photon budget between the autoblinking and these brighter markers would enable distinguishing them more readily. The most common way to use synthetic dyes relies on immunochemistry which requires the fixation and the permeabilization of the cells in order to immunolabel the proteins of interest inside the cells. Several studies using immunochemistry in *D. radiodurans* have been published (La Tour et al. 2009; Nguyen et al. 2009). However, early results on fixation of *D. radiodurans* showed severe nucleoid morphological artifacts for example. The permeabilization step also tended to result in some morphological changes of the bacterial shape. Thus, we still need to optimize the fixation/permeabilization steps of the immunochemistry protocols in *D. radiodurans*. Alternatives with no needs for permeabilization exist. For example, the fusion of self-labeling tags (HaloTag or SNAP-tag) to proteins of interest can be combined with membrane-permeable dyes (Barlag et al. 2016). However, *D. radiodurans* possesses a rather unusual cell wall which may result in difference in membrane-permeability for dyes. Another strategy relies on “click-chemistry”, typically a copper-catalyzed reaction of an azide with an alkyne. For example, *E. coli* nucleoids were studied with click-chemistry: *E. coli* cells were incubated with the thymidine analogue, 5-ethynyl-20 -deoxyuridine which was incorporated into the DNA of live cells, and cells were then fixed, permeabilized and labelled with an azide-substituted fluorophore (Alexa Fluor 647) via click-chemistry (Spahn et al. 2014).

Thus, the autoblinking might continue to impair the study of membrane associated proteins as well as low copy number proteins by SMLM. But, in the future, many improvements (ranging from protocol optimization to set-up enhancement or new techniques) may provide means of circumventing the autoblinking issue.

CHAPTER

VII

Appendices

1. Codes used for analyses

1.1. Density graph of foci

```

1  %% Coordinates (x,y) of 2 ter in the 1st phases
2  foci_ter_x{1}=[0.059947242 0.254778325]
3  foci_ter_y{1}=[-0.035530585 0.150916892]
4
5  %% parameter graph of phase 1, to adapt with cell size, aim for 200nm
6  foci_ter_x{1,1}(1,2)=-0.26090625
7  foci_ter_x{1,1}(1,3)=0.862
8  foci_ter_x{1,1}(1,4)=0.831265
9
10
11 %% Graphs of ter density
12 for i=1:1%loop trough phases
13     x=foci_ter_x{i}(:,1)'
14     y=foci_ter_y{i}(:,1)'
15
16     % Bin the data:
17     pts = linspace(-1.5, 1.5, 12);
18
19     %raw histogram
20     N = histcounts2(y(:), x(:), pts, pts,'Normalization','probability')
21
22     % normalization of the histogram and saving
23     fig=figure
24     imagesc(pts, pts, N);
25     axis equal;
26     set(gca, 'XLim', [-foci_ter_x{1,i}(1,3) foci_ter_x{1,i}(1,3)], 'YLim',
27         [foci_ter_x{1,i}(1,2) foci_ter_x{1,i}(1,4)], 'YDir', 'normal');
28     caxis manual
29     caxis([0 0.35]);
30     colormap (myparula)%color map array, user defined
31     colorbar
32
33     hold on
34
35     s1 = 'foci_ter';
36     chr = int2str(i)
37     filename = strcat(s1,chr)
38     print(fig,filename,'-dtiff')
39     hold off
40
41     % extraction of data
42     % sum of probability for the axis of the dividing septum, projected on the central
43     septum
44     foci_ter_x{i}(1,5)=sum(N(:,6))
45     % sum of probabilities along the the dividing septum axis
46     for j=1:11
47         foci_ter_x{i}(j,6)=sum(N(j,:))
48     end
49
50     % graph of sum of probabilities
51     for ii=1:1%loop trough phases
52         y_ter(ii)=foci_ter_x{ii}(1,5)
53     end
54     figure
55     plot (y_ter)
56
57     for iii=1:1%loop trough phases
58         figure
59         plot (foci_ter_x{iii}(:,6))
60         set(gca, 'XLim', [0 11])
61     end

```

1.2. Perimeter fraction of a phase 1 diad

```

1  %Inputs:
2  % fit an ellipse on the diads, retrieve the long and hsort axis
3  % retrieve the two desired angles
4  long=[15.89 14.82]/2
5  court=[13.782 14.038]/2
6  angle1=[59.47 82.875]*pi/180
7  angle2=[71.896 66.161]*pi/180
8
9  % transform angle1 into the end of the ellipse arc for the integral calculation
10 limitupinteg1=[atan(long.*tan(angle1)./court)]
11 % trigonometry operation to correct the trick of negative angles
12 if any(limitupinteg1<0)
13 limitupinteg1(limitupinteg1<0)=
14 [atan(long(limitupinteg1<0).*tan(90*pi/180)./court(limitupinteg1<0))+atan(long(limitupin
15 teg1<0).*tan(90*pi/180)./court(limitupinteg1<0))-atan(long(limitupinteg1<0).*tan(pi-angle
16 1(angle1>90*pi/180))./court(limitupinteg1<0))]]
17 end
18
19 %transform angle1 into the end of the ellipse arc for the integral calculation
20 limitupinteg2=[atan(long.*tan(angle2)./court)]
21 % trigonometry operation to correct the trick of negative angles
22 if any(limitupinteg2<0)
23 limitupinteg2(limitupinteg2<0)=
24 [atan(long(limitupinteg2<0).*tan(90*pi/180)./court(limitupinteg2<0))+atan(long(limitupin
25 teg2<0).*tan(90*pi/180)./court(limitupinteg2<0))-atan(long(limitupinteg2<0).*tan(pi-angle
26 2(angle2>90*pi/180))./court(limitupinteg2<0))]]
27 end
28
29 % Implementation of th calculation of the arc length for both sides
30 syms t
31 fun1 =@(t)-sin(t)
32 fun2 =@(t)cos(t)
33
34 for i=1:length(long)
35 funtotal= @(t) sqrt((long(i)*fun1(t))^2+(court(i)*fun2(t))^2);
36
37 Arclength1 = integral(funtotal,0,limitupinteg1(i),'ArrayValued',true)
38 Arclength2 = integral(funtotal,0,limitupinteg2(i),'ArrayValued',true)
39
40 Arc_length1(i)=Arclength1
41 Arc_length2(i)=Arclength2
42 end
43
44 perimeterellipse=(2*pi*sqrt((long.^2+court.^2)/2))
45 length_red=(Arc_length1+Arc_length2)
46 length_green=(perimeterellipse-length_red)
47 fraction= (Arc_length1+Arc_length2)./perimeterellipse'*100
48

```


2. Video material

The video simulating the growth and division of *D. radiodurans* and the accompanying reorganization of the nucleoid was made as follows.

Cell dimensions were first extracted from PALM images of hundreds of cells in order to retrieve the mean dimensions needed for a reconstitution of the different phases of the cells. SD images were used to extract nucleoid shapes and sizes.

Cells were then reconstructed as 2D vectors in Illustrator. The 6 vector shapers of the phases of the cell cycle were then transferred into After Affect. The different phases were then used as patterns in order to recreate the cell cycle, combining the different notion/effects that are present in these different tutorials:

- Cell division:

<https://www.youtube.com/watch?v=jYyA9Bhr3IY>

<https://www.youtube.com/watch?v=9aBw5LqUT5w>

- Textures:

<https://www.youtube.com/watch?v=AEbLfkrEC7g>

- Countdown:

<https://www.youtube.com/watch?v=jmRd1dmbTcI>

3. Résumé de la thèse en Français

3.1. Introduction

Le premier chapitre du manuscrit se concentre sur l'état de l'art des sujets abordés durant cette thèse.

Au cours de ce projet, nous nous sommes intéressés à une bactérie, *D. radiodurans*. La première partie de l'introduction est une description de celle-ci. *D. radiodurans* a été découverte en 1950 et est particulièrement connue pour ces extraordinaires capacités de résistance à différents facteurs de stress. Cependant, à cause de ces capacités cette bactérie a surtout été étudiée dans cette optique. Certaines caractéristiques de son cycle cellulaire restent méconnues, notamment (i) sa morphologie au cours de sa division ainsi que (ii) l'organisation et (iii) la ségrégation de son nucléoïde.

Les parties suivantes de cette introduction se concentrent alors sur ces trois sujets, chez des bactéries mieux caractérisées, les « bactéries modèles ». Brièvement, au cours de la division cellulaire, les chromosomes contenus dans les bactéries doivent être d'abord copiés, puis séparés dans chacune des cellules filles. Étant donné la petite taille des bactéries, le nucléoïde de celles-ci est particulièrement organisé. Au niveau moléculaire, le nucléoïde semble organisé par des NAPs, « nucleoid associated proteins », en des microdomaines, mais aussi en macrodomaines. Le nucléoïde présente également différentes macro-organisations dont les plus connus sont les organisations longitudinales et transversales. Cette organisation permet aux bactéries d'avoir un nucléoïde à la fois compact, mais accessible aux différentes protéines des processus nécessitant la lecture de l'ADN. La ségrégation des chromosomes peut se faire alors grâce à plusieurs mécanismes, actifs, ou passifs. La ségrégation est alors coordonnée avec la fin de la division de la bactérie, afin d'éviter la fermeture du septum de division sur les chromosomes, ce qui pourrait être fatal aux bactéries.

Au cours de cet état de l'art, nous avons montré que la grande diversité des bactéries se traduit en un grand nombre de différentes protéines et mécanismes impliqués dans la morphologie de la bactérie, l'organisation du nucléoïde et sa ségrégation au cours du cycle cellulaire. Cette diversité nous empêche pour l'instant de définir des processus universels pour ces bactéries.

Comme montré dans ces parties, peu de connaissances sur ces sujets sont disponibles pour les bactéries de types coques, et encore moins chez *D. radiodurans*. Pourtant, certaines propriétés de sa morphologie (sa paroi cellulaire particulière) ou de son nucléoïde (sa forte compaction, sa forme toroïdale, la multiplicité de ses chromosomes) ont été proposées comme facteurs pouvant jouer un rôle dans sa radiorésistance. Il apparaît alors intéressant de mieux connaître le cycle cellulaire de *D. radiodurans* afin

d'éventuellement mieux comprendre sa radiorésistance, ainsi que d'approfondir nos connaissances sur les bactéries sphériques.

Dans cette partie du manuscrit, nous montrons également que la petite taille relative des bactéries a été un frein pour leurs études en microscopie photonique. Nous avons alors montré les différents apports récents de la microscopie de super-résolution pour l'étude des bactéries. En effet, ce nouveau type de microscopie permet de s'affranchir de la limite de résolution de 200nm, pour atteindre les 20nm de résolution. Comme différentes techniques de microscopie sont utilisées au cours de ce projet, leurs fonctionnements sont aussi brièvement expliqués.

3.2. Autoblinking

La microscopie de fluorescence peut être affectée par l'autofluorescence de l'objet étudié. Il existe plusieurs sources d'autofluorescence qui se manifestent lorsqu'un échantillon est illuminé à certaines longueurs d'onde. Par exemple, certaines molécules comme la chlorophylle ou encore des protéines comme la flavoprotéine peuvent contribuer à cette autofluorescence.

L'autofluorescence peut affecter le signal sur bruit lors d'une acquisition et ainsi interférer avec la détection des fluorochromes utilisés pour imager des structures. La microscopie de super-résolution est aussi affectée par l'autofluorescence. En effet, la localisation d'évènement de scintillement des fluorochromes peut se retrouver noyée dans un signal d'autofluorescence trop fort en comparaison du scintillement. Les évènements seront alors difficilement identifiables par les différents algorithmes qui rechercheront le profil gaussien des scintillements.

Par analogie avec l'autofluorescence, nous avons attribué le terme d'« autoblinking » à un phénomène qui apparait seulement en microscopie de super-résolution. Lors de l'observation des bactéries *D. radiodurans* sauvages sans marquage, nous pouvons observer la présence de scintillement, d'origine inconnue et très similaire au scintillement de protéines fluorescentes phototransformables, mais moins intense que celui des fluorochromes synthétiques. Comme l'autofluorescence, l'autoblinking peut affecter grandement l'acquisition d'images de super-résolution. En effet, même si en soi l'autoblinking ne diminue pas le signal sur bruit de l'échantillon, les scintillements de l'autoblinking peuvent être identifiés comme du signal provenant de fluorochrome.

Ce phénomène d'autoblinking a assez peu été décrit dans la littérature sauf dans 2 bactéries, *B. subtilis* et *E. coli* (Leon et al. 2017; Tuson et al. 2016). Dans ces articles, les auteurs ont proposé différentes méthodes pour le diminuer. Ils ont également caractérisé certaines de ces propriétés physiques, mais n'ont pas montré de pistes concernant son origine. L'autoblinking qui est présent chez les espèces de *Deinococcus* atteint des niveaux bien supérieurs à ceux décrits dans la littérature. Nous avons ainsi

procédé à une étude approfondie de ce phénomène afin d'essayer de mieux le maîtriser, connaître son origine et comprendre en quoi il pouvait être éventuellement une force ou une faiblesse pour l'imagerie en super-résolution des bactéries *Deinococcus*.

Ainsi, il ressort que l'autoblinking est dû à des molécules principalement présentes dans les milieux riches (TGY), qui se lieraient de façon temporaire (i.e un phénomène similaire à du PAINT, Point Accumulation for Imaging in Nanoscale Topography) à la membrane plasmique dans *D. radiodurans* (voir figure 2 de (Floc'h et al. 2018)). Nous avons aussi montré que l'agarose était également une source d'autoblinking. Nous avons montré que la façon d'entreposer le TGY ou l'agarose influence aussi le niveau d'autoblinking dans nos bactéries. L'autoblinking s'est montré utile pour l'imagerie de la formation du septum dans les bactéries au cours de leurs divisions cellulaires. Nous avons aussi procédé à l'imagerie deux couleurs de certaines souches de *D. radiodurans*, en combinant l'imagerie des parois de bactéries par l'autoblinking avec l'image du signal provenant de PAmCherry exprimé par les bactéries dans le cytoplasme.

3.3. Dynamique du cycle cellulaire et du nucléoïde

D. radiodurans est une bactérie sphérique, relativement grande, avec des capacités exceptionnelles de résistance à différents stress, avec un nucléoïde particulièrement compacté, pouvant adopter une forme toroïdale. Ces deux dernières propriétés ont été proposées comme facteur pouvant avoir un rôle dans la radiorésistance de la bactérie.

De par ses propriétés extraordinaires de radiorésistance, la plupart des études sur *D. radiodurans* se sont concentrées sur les facteurs impliqués dans cet étonnant phénotype. De fait, peu de choses à ce jour sont connues sur le cycle cellulaire de cette bactérie, que ce soit au niveau de ses changements morphologiques ou de la dynamique de son nucléoïde. De plus, la plupart des résultats connus sur ces deux points dans les bactéries en général sont issus d'étude sur des bactéries en forme de bâtonnet ou de croissant. La taille de ces bactéries, proche de la limite de résolution des microscopes optiques, a limité leurs études au niveau de leurs changements morphologiques ou de leurs dynamiques de leurs nucléoïdes. Par exemple, ce n'est que récemment, grâce à la microscopie de super-résolution, le 3D-SIM, qu'il a été montré que *S. aureus* possède plusieurs phases de croissance, dont une phase de croissance de la périphérie de la bactérie qui précède la formation du septum central (Monteiro et al. 2015).

Nous avons donc utilisé la microscopie de fluorescence de super-résolution pour étudier la forme de *D. radiodurans* ainsi que de son nucléoïde complexe, formé de plusieurs copies de ses chromosomes, au cours de son cycle cellulaire.

Nous avons ainsi montré que, *D. rad* grossit tout au long de son cycle par une croissance de toute la périphérie de la bactérie et se divise dans deux plans orthogonaux

successifs. Son nucléoïde est hyper compact pendant tout son cycle, mais reste très dynamique, et adopte 6 différentes configurations, comprenant le nucléoïde de forme toroïdale décrit dans la littérature (voir figure 7.1). La technique de sptPALM montre que la protéine HU, qui couvre tout le génome de *D. radiodurans* n'est pas fortement liée à l'ADN, mais au contraire est mobile, ce qui pourrait aider les réarrangements structuraux du nucléoïde. De plus, le marquage fluorescent des loci oriC et Ter du chromosome 1 a montré que ceux-ci possédaient des distributions très différentes au fur et à mesure du cycle. Tous ces résultats montrent que le nucléoïde de *D. radiodurans* est une structure complexe, dont la synchronisation avec la progression du cycle cellulaire est très contrôlée.

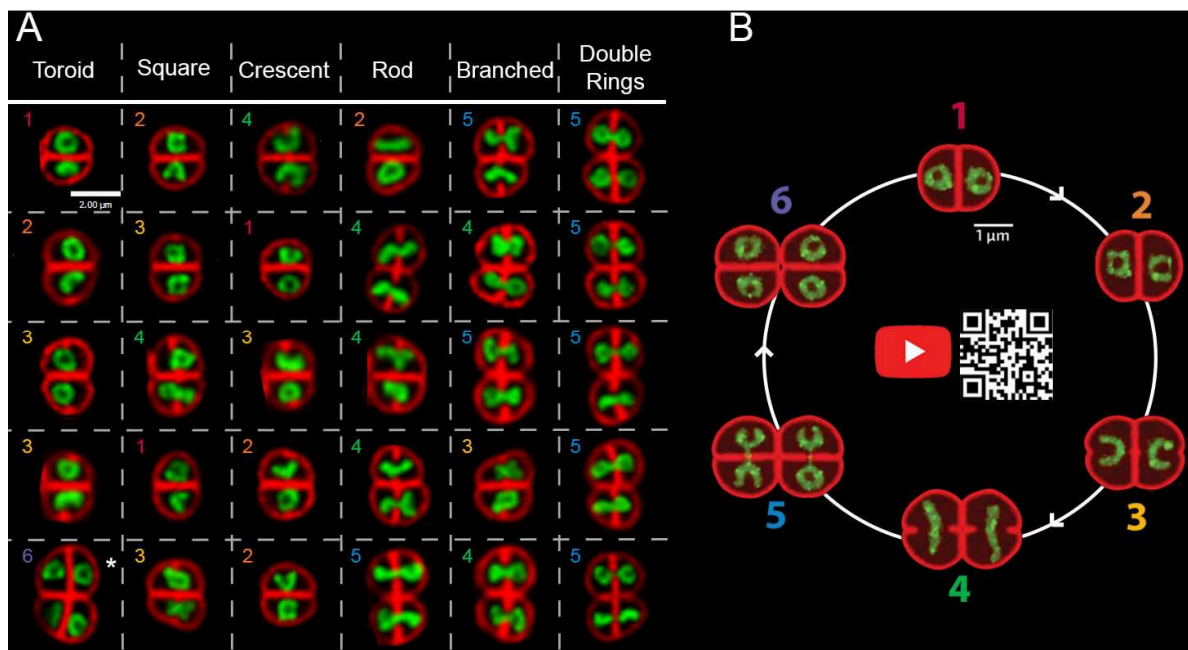


Figure 7.1: Coordination des changements morphologiques du nucléoïde avec le cycle cellulaire de *D. radiodurans*. A) Tableau représentant les différentes formes du nucléoïde de la souche sauvage de *D. radiodurans*. Le nucléoïde est en vert, marqué par du Syto9 et la membrane plasmique en rouge, marqué par du Nile Red. Dans chaque case du tableau, la forme représentative du nucléoïde concerne la cellule du haut. Dans le cas d'une tétrade, la cellule représentative est marquée par une étoile. Les nombres dans chaque case représentent la phase dans laquelle la cellule du haut de la case est. Échelle : 2µm. B) Reconstitution à l'échelle d'un cycle de *D. radiodurans*. Échelle : 1µm.

3.4. Conclusion et perspectives

Au cours de cette thèse, nous avons utilisé des techniques avancées de microscopie pour étudier l'organisation du nucléoïde ainsi que les changements morphologiques de la bactérie *D. radiodurans*.

L'analyse des images que nous avons acquises a été faite manuellement. L'ensemble du cycle cellulaire a été découpé en plusieurs phases (ou archétypes), afin de définir les différentes étapes du cycle cellulaire de la bactérie. Nous pouvons imaginer que cette définition subjective aurait pu être rendue plus robuste par un algorithme de machine-learning non supervisé afin qu'il détermine des phases sans nos aprioris. Ensuite, la mesure des différentes dimensions de cellules a également été faite de façon manuelle. Avec plus de ressources/compétences, cette étape aurait également pu être automatisée afin d'augmenter le nombre de cellules analysées.

Nous avons montré durant nos travaux que le nucléoïde de *D. radiodurans* est particulièrement compact, comparé à *E. coli* par exemple. De plus, de façon surprenante, ce nucléoïde adopte de façon successive des formes de nucléoïde, à différents moments de son cycle cellulaire. Actuellement, nous ne pouvons expliquer ces changements morphologiques du nucléoïde. De plus, les différents mécanismes présentés dans les bactéries "modèles" (telles que la compaction induite par des forces de déplétions ou par des protéines associées au nucléoïde) ne semblent pas pouvoir expliquer ces changements morphologiques du nucléoïde. Nos résultats ont également montré qu'étudier une bactérie différente des bactéries "modèles" est intéressant pour la compréhension plus générale des mécanismes impliqués dans l'organisation du nucléoïde et de sa ségrégation au cours du cycle cellulaire. Nous avons aussi montré que *D. radiodurans* pourrait être une bactérie modèle pour l'étude des bactéries de type coque. Les différents résultats présentés dans cette thèse pourraient servir de fondation pour de plus amples études futures.

Au cours de ce projet, nous nous sommes intéressés à *D. radiodurans*, particulièrement connue pour ces extraordinaires capacités de résistance à différents facteurs de stress. Cependant, à cause de ces capacités de radiorésistance, cette bactérie a surtout été étudiée dans cette optique. Certaines caractéristiques de son cycle cellulaire restent à ce jour méconnues, ce que nous avons étudié durant cette thèse. Logiquement, après avoir observé et caractérisé le cycle cellulaire de cette bactérie, il serait maintenant intéressant d'étudier l'évolution de ce cycle après irradiation de la bactérie, afin d'observer de potentiels changements jusqu'au retour au cycle « normal » de la bactérie. De plus, comme *D. radiodurans* possède des capacités extraordinaires de résistance à différents facteurs de stress, étudier l'organisation et la compaction de son nucléoïde pourrait conduire à mieux comprendre comment ceux-ci pourraient jouer un rôle dans la réponse aux dommages de l'ADN.

Bibliography

- Anderson, A.W. et al., 1956. Studies on a radioresistant *Micrococcus*. I. Isolation, morphology, cultural characteristics, and resistance to gamma radiation. *Food Technol*, 10, pp.575–577.
- Badrinarayanan, A., Le, T.B. & Laub, M.T., 2015. Bacterial chromosome organization and segregation. *Annual review of cell and developmental biology*, 31, pp.171–199.
- Balandina, A., Kamashev, D. & Rouviere-Yaniv, J., 2002. The bacterial histone-like protein HU specifically recognizes similar structures in all nucleic acids: DNA, RNA and their hybrids. *Journal of Biological Chemistry*.
- Barlag, B. et al., 2016. Single molecule super-resolution imaging of proteins in living *Salmonella enterica* using self-labelling enzymes. *Scientific reports*, 6, p.31601.
- Battista, J.R., 1997. Against all odds: the survival strategies of *Deinococcus radiodurans*. *Annual Reviews in Microbiology*, 51(1), pp.203–224.
- Berardozi, R. et al., 2016. Arginine 66 controls dark-state formation in green-to-red photoconvertible fluorescent proteins. *Journal of the American Chemical Society*, 138(2), pp.558–565.
- Berardozi, R., 2016. *Photophysical study of photoconvertible fluorescent proteins used as markers in super-resolution microscopy*. Université Grenoble Alpes. Available at: <https://tel.archives-ouvertes.fr/tel-01498997>.
- Bernhardt, T.G. & De Boer, P.A., 2005. SlmA, a nucleoid-associated, FtsZ binding protein required for blocking septal ring assembly over chromosomes in *E. coli*. *Molecular cell*, 18(5), pp.555–564.
- Betzig, E. et al., 2006. Imaging intracellular fluorescent proteins at nanometer resolution. *Science*, 313(5793), pp.1642–1645.
- Blasius, M., Hübscher, U. & Sommer, S., 2008. *Deinococcus radiodurans*: what belongs to the survival kit? *Critical reviews in biochemistry and molecular biology*, 43(3), pp.221–238.
- Boer, P.A. de, Crossley, R.E. & Rothfield, L.I., 1989. A division inhibitor and a topological specificity factor coded for by the minicell locus determine proper placement of the division septum in *E. coli*. *Cell*, 56(4), pp.641–649.
- Bourgeois, D., Regis-Faro, A. & Adam, V., 2012. Photoactivated structural dynamics of fluorescent proteins.

- Bretschneider, S., Eggeling, C. & Hell, S.W., 2007. Breaking the diffraction barrier in fluorescence microscopy by optical shelving. *Physical review letters*, 98(21), p.218103.
- Brim, H. et al., 2000. Engineering *Deinococcus radiodurans* for metal remediation in radioactive mixed waste environments. *Nature biotechnology*, 18(1), pp.85–90.
- Chang, Y.-W. et al., 2014. Correlated cryogenic photoactivated localization microscopy and cryo-electron tomography. *Nature methods*, 11(7), p.737.
- Charaka, V.K. & Misra, H.S., 2012. Functional characterization of the role of the chromosome I partitioning system in genome segregation in *Deinococcus radiodurans*. *Journal of bacteriology*, 194(21), pp.5739–5748.
- Chou, F. & Tan, S., 1991. Salt-mediated multicell formation in *Deinococcus radiodurans*. *Journal of bacteriology*, 173(10), pp.3184–3190.
- Cisse, I.I. et al., 2013. Real-time dynamics of RNA polymerase II clustering in live human cells. *Science*, 341(6146), pp.664–667.
- Clouvel, G. et al., 2013. Dual-color 3D PALM/dSTORM imaging of centrosomal proteins using MicAO 3DSR. In *Single Molecule Spectroscopy and Superresolution Imaging VI*. International Society for Optics and Photonics, p. 85900Z.
- Corbin, B.D., Yu, X.-C. & Margolin, W., 2002. Exploring intracellular space: function of the Min system in round-shaped *Escherichia coli*. *The EMBO journal*, 21(8), pp.1998–2008.
- Daly, M.J., 2009. A new perspective on radiation resistance based on *Deinococcus radiodurans*. *Nature Reviews Microbiology*, 7(3), pp.237–245.
- Daly, M.J. et al., 2004. Accumulation of Mn (II) in *Deinococcus radiodurans* facilitates gamma-radiation resistance. *Science*, 306(5698), pp.1025–1028.
- Daly, M.J. & Minton, K.W., 1996. An alternative pathway of recombination of chromosomal fragments precedes recA-dependent recombination in the radioresistant bacterium *Deinococcus radiodurans*. *Journal of Bacteriology*, 178(15), pp.4461–4471.
- Dame, R.T. & Tark-Dame, M., 2016. Bacterial chromatin: converging views at different scales. *Current opinion in cell biology*, 40, pp.60–65.

- Danilova, O. et al., 2007. MukB colocalizes with the oriC region and is required for organization of the two Escherichia coli chromosome arms into separate cell halves. *Molecular microbiology*, 65(6), pp.1485–1492.
- Dempsey, G.T. et al., 2011. Evaluation of fluorophores for optimal performance in localization-based super-resolution imaging. *Nature methods*, 8(12), p.1027.
- Dempwolff, F. et al., 2011. Bacillus subtilis MreB orthologs self-organize into filamentous structures underneath the cell membrane in a heterologous cell system. *PloS one*, 6(11), p.e27035.
- Dillon, S.C. & Dorman, C.J., 2010. Bacterial nucleoid-associated proteins, nucleoid structure and gene expression. *Nature Reviews Microbiology*, 8(3), p.185.
- Doolittle, R. et al., 1986. Domainal evolution of a prokaryotic DNA repair protein and its relationship to active-transport proteins. *Nature*, 323(6087), p.451.
- Ducret, A., Quardokus, E.M. & Brun, Y.V., 2016. MicrobeJ, a tool for high throughput bacterial cell detection and quantitative analysis. *Nature microbiology*, 1(7), p.16077.
- Duigou, S. & Boccard, F., 2017. Long range chromosome organization in Escherichia coli: The position of the replication origin defines the non-structured regions and the Right and Left macrodomains. *PLoS genetics*, 13(5), p.e1006758.
- Dupaigne, P. et al., 2012. Molecular basis for a protein-mediated DNA-bridging mechanism that functions in condensation of the E. coli chromosome. *Molecular cell*, 48(4), pp.560–571.
- Eltsov, M. & Dubochet, J., 2005. Fine structure of the Deinococcus radiodurans nucleoid revealed by cryoelectron microscopy of vitreous sections. *Journal of bacteriology*, 187(23), pp.8047–8054.
- Englander, J. et al., 2004. DNA toroids: framework for DNA repair in Deinococcus radiodurans and in germinating bacterial spores. *Journal of bacteriology*, 186(18), pp.5973–5977.
- Espinosa, E., Barre, F.-X. & Galli, E., 2017. Coordination between replication, segregation and cell division in multi-chromosomal bacteria: lessons from Vibrio cholerae. *International Microbiology*, 20(3), pp.121–129.
- Fadda, D. et al., 2003. Characterization of divIVA and other genes located in the chromosomal region downstream of the dcw cluster in Streptococcus pneumoniae. *Journal of bacteriology*, 185(20), pp.6209–6214.

- Fadda, D. et al., 2007. Streptococcus pneumoniae DivIVA: localization and interactions in a MinCD-free context. *Journal of bacteriology*, 189(4), pp.1288–1298.
- Farci, D. et al., 2015. Purification and characterization of DR_2577 (SlpA) a major S-layer protein from Deinococcus radiodurans. *Frontiers in microbiology*, 6, p.414.
- Farci, D. et al., 2016. The S-layer protein DR_2577 binds deinoxanthin and under desiccation conditions protects against UV-radiation in Deinococcus radiodurans. *Frontiers in microbiology*, 7.
- Ferreira, A.C. et al., 1997. Deinococcus geothermalis sp. nov. and Deinococcus murrayi sp. nov., two extremely radiation-resistant and slightly thermophilic species from hot springs. *International Journal of Systematic and Evolutionary Microbiology*, 47(4), pp.939–947.
- Fisher, J.K. et al., 2013. Four-dimensional imaging of E. coli nucleoid organization and dynamics in living cells. *Cell*, 153(4), pp.882–895.
- Floc'h, K. et al., 2018. Bacterial cell wall nanoimaging by autoblanking microscopy. *Scientific reports*, 8(1), p.14038.
- Fürstenberg, A. & Heilemann, M., 2013. Single-molecule localization microscopy–near-molecular spatial resolution in light microscopy with photoswitchable fluorophores. *Physical Chemistry Chemical Physics*, 15(36), pp.14919–14930.
- Le Gall, A. et al., 2016. Bacterial partition complexes segregate within the volume of the nucleoid. *Nature communications*, 7, p.12107.
- Galland, R. et al., 2015. 3D high-and super-resolution imaging using single-objective SPIM. *Nature methods*, 12(7), p.641.
- Gelles, J., Schnapp, B.J. & Sheetz, M.P., 1988. Tracking kinesin-driven movements with nanometre-scale precision. *Nature*, 331(6155), p.450.
- Ghedira, K. et al., 2016. Insights into Ionizing-Radiation-Resistant Bacteria S-Layer Proteins and Nanobiotechnology for Bioremediation of Hazardous and Radioactive Waste. In *Management of Hazardous Wastes*. InTech.
- De Groot, A. et al., 2005. Deinococcus deserti sp. nov., a gamma-radiation-tolerant bacterium isolated from the Sahara Desert. *International journal of systematic and evolutionary microbiology*, 55(6), pp.2441–2446.
- Grove, A., 2011. Functional evolution of bacterial histone-like HU proteins. *Current issues in molecular biology*, 13(1), p.1.

- Gupta, P. et al., 2016. MDP: A Deinococcus Mn²⁺-decapeptide complex protects mice from ionizing radiation. *PloS one*, 11(8), p.e0160575.
- Gustafsson, M.G., 2000. Surpassing the lateral resolution limit by a factor of two using structured illumination microscopy. *Journal of microscopy*, 198(2), pp.82–87.
- Hansen, M.T., 1978. Multiplicity of genome equivalents in the radiation-resistant bacterium *Micrococcus radiodurans*. *Journal of bacteriology*, 134(1), pp.71–75.
- Harms, A. et al., 2013. Tracking of chromosome and replisome dynamics in *Myxococcus xanthus* reveals a novel chromosome arrangement. *PLoS genetics*, 9(9), p.e1003802.
- Hartmann, R. et al., 2018. BacStalk: a comprehensive and interactive image analysis software tool for bacterial cell biology. *bioRxiv*, p.360230.
- Hashimoto, M. et al., 2003. HU protein of *Escherichia coli* has a role in the repair of closely opposed lesions in DNA. *Journal of Biological Chemistry*, 278(31), pp.28501–28507.
- Heilemann, M. et al., 2008. Subdiffraction-resolution fluorescence imaging with conventional fluorescent probes. *Angewandte Chemie International Edition*, 47(33), pp.6172–6176.
- Hell, S.W. & Wichmann, J., 1994. Breaking the diffraction resolution limit by stimulated emission: stimulated-emission-depletion fluorescence microscopy. *Optics letters*, 19(11), pp.780–782.
- Hess, S.T., Girirajan, T.P. & Mason, M.D., 2006. Ultra-high resolution imaging by fluorescence photoactivation localization microscopy. *Biophysical journal*, 91(11), pp.4258–4272.
- Hirsch, P. et al., 2004. *Deinococcus frigens* sp. nov., *Deinococcus saxicola* sp. nov., and *Deinococcus marmoris* sp. nov., low temperature and draught-tolerating, UV-resistant bacteria from continental Antarctica. *Systematic and applied microbiology*, 27(6), pp.636–645.
- Hofmann, M. et al., 2005. Breaking the diffraction barrier in fluorescence microscopy at low light intensities by using reversibly photoswitchable proteins. *Proceedings of the National Academy of Sciences*, 102(49), pp.17565–17569.
- Huang, B. et al., 2008. Three-dimensional super-resolution imaging by stochastic optical reconstruction microscopy. *Science*, 319(5864), pp.810–813.

- Hud, N.V. & Downing, K.H., 2001. Cryoelectron microscopy of λ phage DNA condensates in vitreous ice: the fine structure of DNA toroids. *Proceedings of the National Academy of Sciences*, 98(26), pp.14925–14930.
- Hud, N.V. & Vilfan, I.D., 2005. Toroidal DNA condensates: unraveling the fine structure and the role of nucleation in determining size. *Annu. Rev. Biophys. Biomol. Struct.*, 34, pp.295–318.
- Huisman, O. et al., 1989. Multiple defects in Escherichia coli mutants lacking HU protein. *Journal of bacteriology*, 171(7), pp.3704–3712.
- Izeddin, I. et al., 2014. Single-molecule tracking in live cells reveals distinct target-search strategies of transcription factors in the nucleus. *Elife*, 3, p.e02230.
- Japaridze, A. et al., 2017. Hyperplectonemes: a higher order compact and dynamic DNA self-organization. *Nano letters*, 17(3), pp.1938–1948.
- Jensen, E.C., 2012. Types of imaging, Part 2: an overview of fluorescence microscopy. *The Anatomical Record: Advances in Integrative Anatomy and Evolutionary Biology*, 295(10), pp.1621–1627.
- Jones, L.J., Carballido-López, R. & Errington, J., 2001. Control of cell shape in bacteria: helical, actin-like filaments in Bacillus subtilis. *Cell*, 104(6), pp.913–922.
- Joshi, H.M. & Toleti, R.S., 2009. Nutrition induced pleomorphism and budding mode of reproduction in Deinococcus radiodurans. *BMC research notes*, 2(1), p.123.
- Juette, M.F. et al., 2008. Three-dimensional sub-100 nm resolution fluorescence microscopy of thick samples. *Nature methods*, 5(6), pp.527–529.
- Jun, S., 2015. Chromosome, cell cycle, and entropy. *Biophysical Journal*, 108(4), p.785.
- Jun, S. & Wright, A., 2010. Entropy as the driver of chromosome segregation. *Nature Reviews Microbiology*, 8(8), p.600.
- Jung, Y. et al., 2012. Ring polymers as model bacterial chromosomes: confinement, chain topology, single chain statistics, and how they interact. *Soft Matter*, 8(7), pp.2095–2102.
- Kennedy, S.P., Chevalier, F. & Barre, F.-X., 2008. Delayed activation of Xer recombination at dif by FtsK during septum assembly in Escherichia coli. *Molecular microbiology*, 68(4), pp.1018–1028.

- Kitayama, S. & Matsuyama, A., 1981. Genome multiplicity and radiation resistance in *Micrococcus radiodurans*. *The Journal of Biochemistry*, 90(3), pp.877–880.
- Klar, T.A. et al., 2000. Fluorescence microscopy with diffraction resolution barrier broken by stimulated emission. *Proceedings of the National Academy of Sciences*, 97(15), pp.8206–8210.
- Le, T.B. et al., 2013. High-resolution mapping of the spatial organization of a bacterial chromosome. *Science*, 342(6159), pp.731–734.
- Leaver, M. & Errington, J., 2005. Roles for MreC and MreD proteins in helical growth of the cylindrical cell wall in *Bacillus subtilis*. *Molecular microbiology*, 57(5), pp.1196–1209.
- Lecoite, F. et al., 2004. Vectors for regulated gene expression in the radioresistant bacterium *Deinococcus radiodurans*. *Gene*, 336(1), pp.25–35.
- Lemon, K.P. & Grossman, A.D., 2001. The extrusion-capture model for chromosome partitioning in bacteria. *Genes & development*, 15(16), pp.2031–2041.
- Leon, F.G. de et al., 2017. Tracking low-copy transcription factors in living bacteria: the case of the lac repressor. *Biophysical journal*, 112(7), pp.1316–1327.
- Levin-Zaidman, S. et al., 2003. Ringlike structure of the *Deinococcus radiodurans* genome: a key to radioresistance? *Science*, 299(5604), pp.254–256.
- Li, T. et al., 2017. *Deinococcus radiodurans* Toxin–Antitoxin MazEF-dr Mediates Cell Death in Response to DNA Damage Stress. *Frontiers in microbiology*, 8, p.1427.
- Liao, Y. et al., 2015. Single-molecule motions and interactions in live cells reveal target search dynamics in mismatch repair. *Proceedings of the National Academy of Sciences*, 112(50), pp.E6898–E6906.
- Lieberman-Aiden, E. et al., 2009. Comprehensive mapping of long-range interactions reveals folding principles of the human genome. *science*, 326(5950), pp.289–293.
- Lim, H.C. et al., 2014. Evidence for a DNA-relay mechanism in ParABS-mediated chromosome segregation. *Elife*, 3.
- Linton, K.J. & Higgins, C.F., 1998. The *Escherichia coli* ATP-binding cassette (ABC) proteins. *Molecular microbiology*, 28(1), pp.5–13.
- Lioy, V.S. et al., 2018. Multiscale Structuring of the *E. coli* Chromosome by Nucleoid-Associated and Condensin Proteins. *Cell*, 172(4), pp.771–783.

- Liu, Z., Lavis, L.D. & Betzig, E., 2015. Imaging live-cell dynamics and structure at the single-molecule level. *Molecular cell*, 58(4), pp.644–659.
- Livny, J., Yamaichi, Y. & Waldor, M.K., 2007. Distribution of centromere-like *parS* sites in bacteria: insights from comparative genomics. *Journal of bacteriology*, 189(23), pp.8693–8703.
- Luijsterburg, M.S. et al., 2006. The architectural role of nucleoid-associated proteins in the organization of bacterial chromatin: a molecular perspective. *Journal of structural biology*, 156(2), pp.262–272.
- Lutkenhaus, J., 2007. Assembly dynamics of the bacterial MinCDE system and spatial regulation of the Z ring. *Annu. Rev. Biochem.*, 76, pp.539–562.
- Madabhushi, R. & Mariani, K.J., 2009. Actin homolog MreB affects chromosome segregation by regulating topoisomerase IV in *Escherichia coli*. *Molecular cell*, 33(2), pp.171–180.
- Makarova, K.S. et al., 2001. Genome of the extremely radiation-resistant bacterium *Deinococcus radiodurans* viewed from the perspective of comparative genomics. *Microbiology and Molecular Biology Reviews*, 65(1), pp.44–79.
- Manley, S. et al., 2008. High-density mapping of single-molecule trajectories with photoactivated localization microscopy. *Nature methods*, 5(2), pp.155–157.
- Marbouty, M. et al., 2015. Condensin-and replication-mediated bacterial chromosome folding and origin condensation revealed by Hi-C and super-resolution imaging. *Molecular cell*, 59(4), pp.588–602.
- Marenduzzo, D., Finan, K. & Cook, P.R., 2006. The depletion attraction: an underappreciated force driving cellular organization. *J Cell Biol*, 175(5), pp.681–686.
- Marsh, R.J. et al., 2018. Artifact-free high-density localization microscopy analysis. *Nature methods*, 15(9), p.689.
- Mattimore, V. & Battista, J.R., 1996. Radioresistance of *Deinococcus radiodurans*: functions necessary to survive ionizing radiation are also necessary to survive prolonged desiccation. *Journal of bacteriology*, 178(3), pp.633–637.
- Maurya, G.K., Modi, K. & Misra, H.S., 2016. Divisome and segrosome components of *Deinococcus radiodurans* interact through cell division regulatory proteins. *Microbiology*, 162(8), pp.1321–1334.

- Mera, P.E., Kalogeraki, V.S. & Shapiro, L., 2014. Replication initiator DnaA binds at the *Caulobacter* centromere and enables chromosome segregation. *Proceedings of the National Academy of Sciences*, 111(45), pp.16100–16105.
- Mercier, R. et al., 2008. The MatP/matS site-specific system organizes the terminus region of the *E. coli* chromosome into a macrodomain. *Cell*, 135(3), pp.475–485.
- Minnen, A. et al., 2016. Control of Smc coiled coil architecture by the ATPase heads facilitates targeting to chromosomal ParB/*parS* and release onto flanking DNA. *Cell reports*, 14(8), pp.2003–2016.
- Minsky, A., Shimoni, E. & Englander, J., 2006. Ring-like nucleoids and DNA repair through error-free nonhomologous end joining in *Deinococcus radiodurans*. *Journal of bacteriology*, 188(17), pp.6047–6051.
- Minton, K.W., 1994. DNA repair in the extremely radioresistant bacterium *Deinococcus radiodurans*. *Molecular microbiology*, 13(1), pp.9–15.
- Minton, K.W. & Daly, M.J., 1995. A model for repair of radiation-induced DNA double-strand breaks in the extreme radiophile *Deinococcus radiodurans*. *Bioessays*, 17(5), pp.457–464.
- Misra, C.S., Basu, B. & Apte, S.K., 2015. Surface (S)-layer proteins of *Deinococcus radiodurans* and their utility as vehicles for surface localization of functional proteins. *Biochimica et Biophysica Acta (BBA)-Biomembranes*, 1848(12), pp.3181–3187.
- Mlodzianoski, M.J. et al., 2016. Super-resolution imaging of molecular emission spectra and single molecule spectral fluctuations. *PloS one*, 11(3), p.e0147506.
- Mohl, D.A. & Gober, J.W., 1997. Cell cycle-dependent polar localization of chromosome partitioning proteins in *Caulobacter crescentus*. *Cell*, 88(5), pp.675–684.
- Monteiro, J.M. et al., 2015. Cell shape dynamics during the staphylococcal cell cycle. *Nature communications*, 6, p.8055.
- Monteiro, J.M. et al., 2018. Peptidoglycan synthesis drives an FtsZ-treadmilling-independent step of cytokinesis. *Nature*, 554(7693), p.528.
- Murray, R., Hall, M. & Thompson, B., 1983. Cell division in *Deinococcus radiodurans* and a method for displaying septa. *Canadian journal of microbiology*, 29(10), pp.1412–1423.

- Nguyen, H.H. et al., 2009. The essential histone-like protein HU plays a major role in *Deinococcus radiodurans* nucleoid compaction. *Molecular microbiology*, 73(2), pp.240–252.
- Nolivos, S. et al., 2016. MatP regulates the coordinated action of topoisomerase IV and MukBEF in chromosome segregation. *Nature communications*, 7, p.10466.
- Ormö, M. et al., 1996. Crystal structure of the *Aequorea victoria* green fluorescent protein. *Science*, 273(5280), pp.1392–1395.
- Otomo, K. et al., 2015. STED microscopy—super-resolution bio-imaging utilizing a stimulated emission depletion. *Microscopy*, 64(4), pp.227–236.
- Pang, T. et al., 2017. The nucleoid occlusion factor Noc controls DNA replication initiation in *Staphylococcus aureus*. *PLoS genetics*, 13(7), p.e1006908.
- Passot, F.M. et al., 2015. Nucleoid organization in the radioresistant bacterium *Deinococcus radiodurans*. *Molecular microbiology*, 97(4), pp.759–774.
- Pelletier, J. et al., 2012. Physical manipulation of the *Escherichia coli* chromosome reveals its soft nature. *Proceedings of the National Academy of Sciences*.
- Pinho, M.G., Kjos, M. & Veening, J.-W., 2013. How to get (a) round: mechanisms controlling growth and division of coccoid bacteria. *Nature reviews microbiology*, 11(9), p.601.
- Raaphorst, R. van, Kjos, M. & Veening, J.-W., 2017. Chromosome segregation drives division site selection in *Streptococcus pneumoniae*. *Proceedings of the National Academy of Sciences*, 114(29), pp.E5959–E5968.
- Raskin, D.M. & De Boer, P.A., 1999. Rapid pole-to-pole oscillation of a protein required for directing division to the middle of *Escherichia coli*. *Proceedings of the National Academy of Sciences*, 96(9), pp.4971–4976.
- Richter, K.N. et al., 2018. Glyoxal as an alternative fixative to formaldehyde in immunostaining and super-resolution microscopy. *The EMBO journal*, 37(1), pp.139–159.
- Rothfuss, H. et al., 2006. Involvement of the S-layer proteins Hpi and SlpA in the maintenance of cell envelope integrity in *Deinococcus radiodurans* R1. *Microbiology*, 152(9), pp.2779–2787.
- Rowlett, V.W. & Margolin, W., 2013. The bacterial Min system. *Current Biology*, 23(13), pp.R553–R556.

- Rust, M.J., Bates, M. & Zhuang, X., 2006. Sub-diffraction-limit imaging by stochastic optical reconstruction microscopy (STORM). *Nature methods*, 3(10), pp.793–795.
- Salje, J. et al., 2011. Direct membrane binding by bacterial actin MreB. *Molecular cell*, 43(3), pp.478–487.
- Schermelleh, L. et al., 2008. Subdiffraction multicolor imaging of the nuclear periphery with 3D structured illumination microscopy. *Science*, 320(5881), pp.1332–1336.
- Schnell, U. et al., 2012. Immunolabeling artifacts and the need for live-cell imaging. *Nature methods*, 9(2), p.152.
- Sharma, A. et al., 2017. Across the tree of life, radiation resistance is governed by antioxidant Mn²⁺, gauged by paramagnetic resonance. *Proceedings of the National Academy of Sciences*, 114(44), pp.E9253–E9260.
- Sharonov, A. & Hochstrasser, R.M., 2006. Wide-field subdiffraction imaging by accumulated binding of diffusing probes. *Proceedings of the National Academy of Sciences*, 103(50), pp.18911–18916.
- Shendruk, T.N. et al., 2015. Simulating the entropic collapse of coarse-grained chromosomes. *Biophysical journal*, 108(4), pp.810–820.
- Shimomura, O., Johnson, F.H. & Saiga, Y., 1962. Extraction, Purification and Properties of Aequorin, a Bioluminescent Protein from the Luminous Hydromedusan, Aequorea. *Journal of Cellular and Comparative Physiology*, 59(3), pp.223–239. Available at: <https://onlinelibrary.wiley.com/doi/abs/10.1002/jcp.1030590302>.
- Shivanandan, A. et al., 2014. Challenges in quantitative single molecule localization microscopy. *FEBS letters*, 588(19), pp.3595–3602.
- Slade, D. et al., 2009. Recombination and replication in DNA repair of heavily irradiated *Deinococcus radiodurans*. *Cell*, 136(6), pp.1044–1055.
- Slade, D. & Radman, M., 2011. Oxidative stress resistance in *Deinococcus radiodurans*. *Microbiology and molecular biology reviews*, 75(1), pp.133–191.
- Spahn, C., Endesfelder, U. & Heilemann, M., 2014. Super-resolution imaging of *Escherichia coli* nucleoids reveals highly structured and asymmetric segregation during fast growth. *Journal of structural biology*, 185(3), pp.243–249.
- Spahn, C.K. et al., 2018. A toolbox for multiplexed super-resolution imaging of the *E. coli* nucleoid and membrane using novel PAINT labels. *Scientific reports*, 8(1), p.14768.

- Sullivan, N.L., Marquis, K.A. & Rudner, D.Z., 2009. Recruitment of SMC by ParB-*parS* organizes the origin region and promotes efficient chromosome segregation. *Cell*, 137(4), pp.697–707.
- Surovtsev, I.V. & Jacobs-Wagner, C., 2018. Subcellular organization: a critical feature of bacterial cell replication. *Cell*, 172(6), pp.1271–1293.
- Thanbichler, M., 2010. Synchronization of chromosome dynamics and cell division in bacteria. *Cold Spring Harbor perspectives in biology*, 2(1), p.a000331.
- Thanbichler, M. & Shapiro, L., 2006. MipZ, a spatial regulator coordinating chromosome segregation with cell division in *Caulobacter*. *Cell*, 126(1), pp.147–162.
- Thornley, M.J., Horne, R. & Glauert, A.M., 1965. The fine structure of *Micrococcus radiodurans*. *Archiv für Mikrobiologie*, 51(3), pp.267–289.
- Tian, B. et al., 2007. Evaluation of the antioxidant effects of carotenoids from *Deinococcus radiodurans* through targeted mutagenesis, chemiluminescence, and DNA damage analyses. *Biochimica et Biophysica Acta (BBA)-General Subjects*, 1770(6), pp.902–911.
- Timmins, J. & Moe, E., 2016. A Decade of Biochemical and Structural Studies of the DNA Repair Machinery of *Deinococcus radiodurans*: Major Findings, Functional and Mechanistic Insight and Challenges. *Computational and structural biotechnology journal*, 14, pp.168–176.
- Toro, E. et al., 2008. *Caulobacter* requires a dedicated mechanism to initiate chromosome segregation. *Proceedings of the National Academy of Sciences*.
- Toro, E. & Shapiro, L., 2010. Bacterial chromosome organization and segregation. *Cold Spring Harbor perspectives in biology*, p.a000349.
- Touelle, M. et al., 2012. A comparative proteomic approach to better define *Deinococcus* nucleoid specificities. *Journal of proteomics*, 75(9), pp.2588–2600.
- Touhami, A., Jericho, M.H. & Beveridge, T.J., 2004. Atomic force microscopy of cell growth and division in *Staphylococcus aureus*. *Journal of bacteriology*, 186(11), pp.3286–3295.
- La Tour, C. Bouthier de et al., 2015. The abundant and essential HU proteins in *Deinococcus deserti* and *Deinococcus radiodurans* are translated from leaderless mRNA. *Microbiology*, 161(12), pp.2410–2422.

- La Tour, C.B. de et al., 2009. The *Deinococcus radiodurans* SMC protein is dispensable for cell viability yet plays a role in DNA folding. *Extremophiles*, 13(5), pp.827–837.
- Tuson, H.H. et al., 2016. Addressing the Requirements of High-Sensitivity Single-Molecule Imaging of Low-Copy-Number Proteins in Bacteria. *ChemPhysChem*, 17(10), pp.1435–1440.
- Umbarger, M.A. et al., 2011. The three-dimensional architecture of a bacterial genome and its alteration by genetic perturbation. *Molecular cell*, 44(2), pp.252–264.
- Valens, M. et al., 2004. Macrodomain organization of the *Escherichia coli* chromosome. *The EMBO journal*, 23(21), pp.4330–4341.
- Valens, M., Thiel, A. & Boccard, F., 2016. The MaoP/maoS site-specific system organizes the Ori region of the *E. coli* chromosome into a macrodomain. *PLoS genetics*, 12(9), p.e1006309.
- Veiga, H., Jorge, A.M. & Pinho, M.G., 2011. Absence of nucleoid occlusion effector Noc impairs formation of orthogonal FtsZ rings during *Staphylococcus aureus* cell division. *Molecular microbiology*, 80(5), pp.1366–1380.
- Wang, P. & Schellhorn, H.E., 1995. Induction of resistance to hydrogen peroxide and radiation in *Deinococcus radiodurans*. *Canadian journal of microbiology*, 41(2), pp.170–176.
- Wang, W. et al., 2011. Chromosome organization by a nucleoid-associated protein in live bacteria. *Science*, 333(6048), pp.1445–1449.
- Wang, X. & Rudner, D.Z., 2014. Spatial organization of bacterial chromosomes. *Current opinion in microbiology*, 22, pp.66–72.
- Wang, X. & Sherratt, D.J., 2010. Independent segregation of the two arms of the *Escherichia coli* Ori region requires neither RNA synthesis nor MreB dynamics. *Journal of bacteriology*, 192(23), pp.6143–6153.
- Westphal, V. & Hell, S.W., 2005. Nanoscale resolution in the focal plane of an optical microscope. *Physical review letters*, 94(14), p.143903.
- Wheeler, R. et al., 2011. Super-resolution microscopy reveals cell wall dynamics and peptidoglycan architecture in ovococcal bacteria. *Molecular microbiology*, 82(5), pp.1096–1109.

- White, O. et al., 1999. Genome sequence of the radioresistant bacterium *Deinococcus radiodurans* R1. *Science*, 286(5444), pp.1571–1577.
- Wilson, T., 2011. Resolution and optical sectioning in the confocal microscope. *Journal of microscopy*, 244(2), pp.113–121.
- Wu, F., Swain, P., et al., 2018. Cell boundary confinement sets the size and position of the *E. coli* chromosome. *bioRxiv*, p.348052.
- Wu, F., Japaridze, A., et al., 2018. Direct Imaging of the circular chromosome of a live bacterium. *bioRxiv*, p.246389.
- Wu, L.J. & Errington, J., 2012. Nucleoid occlusion and bacterial cell division. *Nature Reviews Microbiology*, 10(1), p.8.
- Yamaichi, Y. et al., 2007. Distinct centromere-like *parS* sites on the two chromosomes of *Vibrio* spp. *Journal of bacteriology*, 189(14), pp.5314–5324.
- Yamaichi, Y. & Niki, H., 2004. *migS*, a cis-acting site that affects bipolar positioning of *oriC* on the *Escherichia coli* chromosome. *The EMBO journal*, 23(1), pp.221–233.
- Yang, F., Moss, L.G. & Phillips Jr, G.N., 1996. The molecular structure of green fluorescent protein. *Nature biotechnology*, 14(10), p.1246.
- Yildiz, A. et al., 2003. Myosin V walks hand-over-hand: single fluorophore imaging with 1.5-nm localization. *science*, 300(5628), pp.2061–2065.
- Youngren, B. et al., 2014. The multifork *Escherichia coli* chromosome is a self-duplicating and self-segregating thermodynamic ring polymer. *Genes & development*, 28(1), pp.71–84.
- Zahradka, K. et al., 2006. Reassembly of shattered chromosomes in *Deinococcus radiodurans*. *Nature*, 443(7111), pp.569–573.
- Zapun, A., Vernet, T. & Pinho, M.G., 2008. The different shapes of cocci. *FEMS microbiology reviews*, 32(2), pp.345–360.
- Zhang, Z. et al., 2015. Ultrahigh-throughput single-molecule spectroscopy and spectrally resolved super-resolution microscopy. *Nature methods*, 12(10), pp.935–938.
- Zimmerman, J.M. & Battista, J.R., 2005. A ring-like nucleoid is not necessary for radioresistance in the *Deinococcaceae*. *BMC microbiology*, 5(1), p.17.

Zimmerman, S.B. & Trach, S.O., 1991. Estimation of macromolecule concentrations and excluded volume effects for the cytoplasm of *Escherichia coli*. *Journal of molecular biology*, 222(3), pp.599–620.

Acknowledgment

First of all, I would like to thank my advisors, Joanna Timmins and Dominique Bourgeois, without whom, everything done during this PhD would not have been possible. It was very instructive to work with them, as they gave me the freedom of research in the different aspects of my projects, while remaining available for advices.

Then, I would like to thank all the people that I've annoyed/worked with, in particular former and present members of the VIC group, of Pixel team and of M4D platform.

Many thanks go to Remy, Corey and Jean-Baptiste, for our collaboration on the autoblanking spectrum acquisition.

I am also grateful to Franz Bruckert, François-Xavier Barre, Christian Lesterlin, Ulrike Endesfelder, Mariana Gomes de Pinho and Irina Gutsche to have been part of my defense committee, Laurence Blanchard and Martial Balland for being part of my CSI.

During this PhD I also had the opportunity to attend for 3 years an Advanced Master in Biotechnology and Pharmaceutical Management. For that I thank the labex GRAL for the funding, and Arsia for the acceptance into his program. I also thank my fellow masochist colleagues Mariam, Sara and Maud, as well as the regular students of these different years of master.

As writing a PhD was not particularly an exciting work for me, I've to thank people that enlighten these "dreadful" days: Rana, my fellow writing-prisoner Lynda, the perfect -except for the gray mop-like hair Rida, Guillaume for his inspiring thrive for the Clariostar, Momo for his titters in front of the Tunisian team aka the best team in Africa aka the team that never passed the group stage aka les chèvres and Kaiyao (cio ni ma). A special thanks to the Ranouna who mistook me for Simon during 2 months.

I also thank all my family for their support and my non-PhD friends that reminded me that work was not important. Arbitrarily, in terms of hair remaining on the skull: Benga (bien sûr), Julien (implantation haute depuis tes 12 ans, ça passe), Momo & Toto (ça sonne bien ensemble), Jerem (trop grand, personne voit ton crâne), DJ Jerem (à 35 ans, respect), Marion & Marion (ou l'inverse), Anaëlle, Caca, Claire (merci encore pour l'hébergement sur Bordeaux), Vanessa. A special thanks to the Kazakh/source of inspiration Anton (thanks again for the stay in Zurich)!

Resumé

Durant ce projet, nous nous sommes intéressés à une bactérie, *D. radiodurans*, un coque particulièrement connu pour ces extraordinaires capacités de résistance à différents facteurs de stress. Cependant, à cause de ses capacités de radiorésistance, cette bactérie a surtout été étudiée dans cette optique. Certaines caractéristiques de son cycle cellulaire restent méconnues, notamment (i) sa morphologie au cours de sa division ainsi que (ii) l'organisation et (iii) la ségrégation de son nucléoïde. Ces méconnaissances touchent aussi de façon plus générale toutes les bactéries de types coques, notamment de par la petite taille relative des bactéries qui a été un frein pour leurs études en microscopie photonique.

Le but du projet de thèse est donc de mieux comprendre comment les bactéries sont capables d'avoir un nucléoïde très compacté, mais en même temps, dynamique et restant accessible pour les différents mécanismes tels que la réplication de l'ADN, sa transcription ou sa réparation. Dans ce but, nous avons exploré l'organisation en 4D ainsi que la dynamique du nucléoïde de *D. radiodurans*, en fonction du cycle de vie de la bactérie, de sa phase de croissance. Afin de réaliser ces objectifs, plusieurs stratégies ont été poursuivies : (i) des timelapses en 3D par microscopie confocale (ii) l'étude dynamique du nucléoïde par FRAP et par SptPALM, et (iii) la cartographie des protéines associées au nucléoïde réalisé par microscopie de super-résolution (PALM).

Summary

During this PhD work, we have studied on *D. radiodurans*, a coccus, known for its intriguing outstanding resistance to different stress factors. Studies on *D. radiodurans* have been mainly focusing on its tremendous radioresistance. 52 years after its discovery, its nucleoid organization/segregation as well as its cell morphology during its cell cycle still remain elusive. Most of our knowledge on the bacteria shape during division and on the nucleoid organization/segregation arises from the study of a small number of “model bacteria”, that are mainly rod-shaped or ovoid. In contrast, little is known on the nucleoid organization/segregation of cocci. Moreover, the small relative size of bacteria and of their nucleoids ($<1\mu\text{m}^3$) has limited their studies by conventional microscopy.

Thus, one of the aims of this PhD project is to contribute to a better understanding of the cell morphology and the nucleoid organization/segregation in cocci. For that matter, we explored the 4D organization and the dynamics of *D. radiodurans* nucleoids, as a function of the cell cycle progression and growth phase. In order to achieve the objective of this PhD, several strategies were undertaken: (i) timelapse 3D stacks by spinning confocal microscopy (ii) dynamics studies with FRAP analysis and SptPALM acquisitions, and (iii) cartographies of nucleoid associated proteins using super-resolution microscopy (PALM).